XAFS characterization of disordered nanoclusters and augmentation of Indus-2 XAFS beamlines for extreme thermodynamic conditions

By

NITYA RAMANAN

PHYS01200904022

Bhabha Atomic Research Centre

A thesis submitted to the
Board of Studies in Physical Sciences
In partial fulfillment of requirements
for the Degree of
DOCTOR OF PHILOSOPHY
of
HOMI BHABHA NATIONAL INSTITUTE

February, 2015

Homi Bhabha National Institute

Recommendations of the Viva Voce Board

As members of the Viva Voce Board, we certify that we have read the dissertation prepared by **Nitya Ramanan** entitled **"XAFS characterization of disordered nanoclusters and augmentation of Indus-2 XAFS beamlines for extreme thermodynamic conditions"** and recommend that it may be accepted as fulfilling the thesis requirement for the Degree of Doctor of Philosophy.

Surinder M Sharma **Date:** 22.09.2015

Chairman- **Prof. S. M. Sharma**

Date: 22/09/2015

Guide / Convener- **Prof. M.N. Deo**

Date: 22/9/2015

Member 1- **Prof. N.K. Sahoo**

Date: 22/09/2015

Member 2- **Prof. S.K. Dhar**

Final approval and acceptance of this dissertation is contingent upon the candidate's submission of the final copies of the dissertation to HBNI.

I hereby certify that I have read this dissertation prepared under my direction and recommend that it may be accepted as fulfilling the thesis requirement.

Date: 22/09/2015
Place: HBNI, A.Nagar

Dr. M.N.Deo
(Guide)

STATEMENT BY AUTHOR

This dissertation has been submitted in partial fulfillment of requirements for an advanced degree at Homi Bhabha National Institute (HBNI) and is deposited in the Library to be made available to borrowers under rules of the HBNI.

Brief quotations from this dissertation are allowable without special permission, provided that accurate acknowledgement of source is made. Requests for permission for extended quotation from or reproduction of this manuscript in whole or in part may be granted by the Competent Authority of HBNI when in his or her judgment the proposed use of the material is in the interests of scholarship. In all other instances, however, permission must be obtained from the author.

Nitya Ramanan

DECLARATION

I hereby declare that the investigation presented in the thesis has been carried out by me. The work is original and has not been submitted earlier as a whole or in part for a degree / diploma at this or any other Institution / University.

Nitya Ramanan

List of Publications arising from the thesis

A. **Publications in peer reviewed Journals**

1. Nitya Ramanan, Debdutta Lahiri, Parasmani Rajput, Ramesh Chandra Varma, A. Arun, T.S. Muraleedharan, K.K. Pandey, Nandita Maiti, S.N. Jha and Surinder M. Sharma, 'Investigating structural aspects to understand the putative/claimed non-toxicity of Hg-based Ayurvedic drug "*Rasasindura*", using XAFS', *Journal of Synchrotron Radiation,* **22**, 1233 (2015).
2. Nitya Ramanan, Debdutta Lahiri, Ashwani Kumar, Parasmani Rajput, K. Thankarajan, D. Bhattacharyya and S.N. Jha, 'First phase commissioning of High Pressure XAFS setup at ED-XAFS beamline, Indus-2 Synchrotron Radiation Source, India', *Journal of Optics (Optical Society of India)*, **44**, 182 (2015).
3. Nitya Ramanan, Parasmani Rajput, S.N. Jha and Debdutta Lahiri, 'Assessing the feasibility of Low temperature XAFS experiments at Indus-2, India: first results', *Nuclear Instruments and Methods in Physics Research A*, **782**, 63 (2015).
4. Nitya Ramanan, Sumalay Roy, Debdutta Lahiri, Surinder M. Sharma and B.N. Dev, 'Ascertaining the nano-cluster formation within ion-irradiated Pt/Ni/C multi-trilayer, with X-ray Absorption Spectroscopy', *Journal of Synchrotron Radiation*, **20**, 137 (2013).
5. Debdutta Lahiri, Yongseong Choi, Amit Kumar, Nitya Ramanan, Soma Chattopadhyay, Surinder M. Sharma, Daniel Haskel and S.M. Yusuf, "Understanding temperature and magnetic-field actuated magnetization polarity reversal in the Prussian blue analogue $Cu_{0.73}Mn_{0.77}[Fe(CN)_6].zH_2O$, using XMCD", under review, Materials Research Express.

B. Publications in Conferences

1. Nitya Ramanan, Sumalay Roy, Debdutta Lahiri, Surinder M. Sharma and B.N. Dev, 'XSW-XAFS characterization of ion-irradiated Pt/Ni/C Multilayer', *Journal of Physics: Conference Series*, **430**, 012063 (2013).
2. Debdutta Lahiri, Tomohiro Shibata, Soma Chattopadhyay, Nitya Ramanan, Swati Pandya, P D Kulkarni, A Thamizhavel, A K Grover, S Ramakrishnan and Surinder M. Sharma, 'XAFS understanding of "repeated" magnetic compensation in $Nd_{0.8}Tb_{0.2}Al_2$' *Journal of Physics: Conference Series*, **430**, 012106 (2013).*
3. Nitya Ramanan, Debdutta Lahiri, Nandini Garg, D. Bhattacharyya, S.N. Jha, N K Sahoo and Surinder M Sharma, 'High Pressure experiments at the XAFS beamline, Indus-2', *Journal of Physics: Conference Series*, **377**, 012011 (2012).

C. Technical Publications

1. N. Ramanan, D. Lahiri, D. Bhattacharyya and S. N. Jha, 'Calibration of standard Ni foil XAFS data recorded at the EXAFS Beamline, INDUS-2 SRS', BARC report, *BARC/2012/E/009* (2012).
2. N. Ramanan, D. Lahiri, S.M. Sharma, N.C. Das, D.V. Udupa and A.D. Patil, 'Development of a bendable mirror for studying materials under high pressure using EXAFS beamline at INDUS-2 SRS', BARC report, *BARC/2010/E/12* (2010).

D. Under Preparation

1. "Investigating alloying/de-alloying of Ag/Pt and Ag/Au nanorods under Swift Heavy-ion Irradiation", *manuscript under preparation*.

* Not included in thesis

Nitya Ramanan

To my grandfather, who taught me the power of words

ACKNOWLEDGEMENTS

It is my pleasure to thank several people who have been instrumental to the realization of this work.

First of all, I would like to thank Dr. S.M. Sharma for giving me an opportunity to be a part of his esteemed group. Despite his busy schedule and countless responsibilities, he always guided me and lent me words of wisdom whenever I went astray.

Next, I would like to thank Dr. M.N. Deo for his constant encouragement, good wishes and support. My Ph.D. journey would not have been half as smooth, had it not been for him.

Next, and very importantly, I am greatly indebted to Dr. Debdutta Lahiri, without whom this Ph.D. would not have been possible. I could not have asked for a more knowledgeable, thorough person to work with. She has been the guiding force of my Ph.D. I know that supervising me can be a real test of patience! She, very selflessly and unflinchingly, guided me in every step of my Ph.D. She has constantly encouraged me to push my limits farther and farther. I thank her for her expert guidance and her invaluable time.

I thank the members of my doctoral committee – Dr. N.K. Sahoo and Dr. S.K. Dhar for their valuable suggestions during the course of my Ph.D.

I thank Dr. D. Bhattacharyya and Dr. S.N. Jha for their expert guidance and supervision during my experiments at Indus-2.

I am deeply indebted to Dr. Parasmani Rajput for all the support she has given me during my trips to Indore. She was ever-ready for motivational discussions and always had valuable advice to give me.

I thank Mr. K. Thankarajan from the workshop for teaching me basic designing, which helped me understand complicated drawings and also to design my own sample holders.

I thank Dr. R.S. Ningthoujam from Chemistry Division, BARC, for his ‘anytime’ help. He always connected me to the right people whenever I needed equipment/reagents etc.

I take this opportunity to thank my senior, Himal Bhatt, for proofreading parts of this thesis. He has helped me both professionally and personally in so many different ways that words are insufficient to express my gratitude. I also thank Dr. Susy Thomas for all the moral support and encouragement that she has given me. I am thankful to my

labmates – Shivkumar, Naini and Ashok for creating a lively environment for me to work in. I am also grateful to Shivkumar and Naini for helping me type the index pages of this thesis.

I thank my friends at BARC - Mitali, Sohini, Suresh, Priyanka, Naveen, Anita, Arundhati, Chandrani, Dipti, Shuvendu, for several stimulating and fruitful discussions and also for lending me mental support whenever I was in dire need of it.

I would like to thank Ms. Megha Sanjesh and Mr. Rajiv Sinha for helping out with all my official paperwork.

I would like to thank my friends outside BARC: Rishabh, for standing by me through the good times and the bad times and eternally reminding me to believe in myself; Puja, for her overwhelming belief in my abilities and for constantly reminding me of the greener sides of life and Amit for being the morale booster that he always is during the darkest of times.

Finally, I acknowledge with deepest regards the sustained support of my family- my grandmother, Lakshmi, my parents, Ramanan and Geetha, and my brother, Vaikunt who have stood by me through all these years, and believed, in the first place, that I have the capability to complete this Ph.D. Without them, I would be nothing.

CONTENTS

LIST OF FIGURES

LIST OF TABLES

Homi Bhabha National Institute

SYNOPSIS OF PH.D. THESIS

1. **Name of the student**: Ms. Nitya Ramanan
2. **Name of the Constituent Institution**: Bhabha Atomic Research Centre
3. **Enrolment Number**: PHYS01200904022
4. **Title of the thesis**: XAFS characterization of disordered nanoclusters and augmentation of Indus-2 XAFS beamlines for extreme thermodynamic conditions
5. **Board of Studies**: Physical Sciences (08)

SYNOPSIS

Nanoclusters, i.e. clusters having diameter ~ 1-100nm, have immense technological importance in both fundamental science and industry due to their small size and ability to exhibit intriguing size-dependent properties. For many applications, small size is a necessity, for eg. (i) Electronic Device Industry: In electronic devices, where the idea is to accommodate maximum possible structures on a single chip, small individual elements would come in handy; (ii) Nanodrugs: Drugs have maximum potency when their size is comparable to the size of the target cell. The average size of human cell constituents is ~ 10-100nm. Therefore, to achieve good bioavailability, in vivo stability, solubility, intestinal absorption, sustained and targeted delivery to site of action, therapeutic effectiveness and low generalized side effects, nano-sized drugs are required. (iii) Plasmon Band: Several opto-electronic devices function on the basis of Surface Plasmon Resonance (SPR). SPR occurs due to scattering of conduction electrons by the nanocluster surface when the nanocluster diameter is less than the mean free path of the conduction electrons in the bulk metal. (iv) Sensors: Small size improves the efficiency and specificity of sensors.

Due to their small size, nanoclusters possess large surface to volume ratio, making them extremely reactive (since more surface is available to react) and hence potential candidates for catalysts. In fact, the reactivity becomes so remarkably high that even the so called noble metals (Au, Ag, Pt etc.) cease being noble in the nano-regime! Moreover, the high aspect ratio further simplifies the task of functionalizing nanocluster surfaces for various applications (from drug delivery to clothing insulation) simple.

In the nano-size regime, quantum size effects rule the properties of clusters. As a result, size becomes an additional degree of freedom, strongly influencing the optical, electric, magnetic, thermal and electronic properties. At this small size, nanoclusters are prone to various defects, mainly surface defects and vacancy. The strain induced by these defects makes the nanoclusters prone to disorder, resulting in a variety of interesting consequences, like alloying, de-alloying and segregation. X-ray Absorption Fine Structure (XAFS) is the only technique that can be used to obtain structural information on such highly disordered systems, and we have employed the same to investigate disordered clusters in different configurations. Due to the weak nature of XAFS oscillations, continuous energy spectrum, having high flux, high intensity and high resolution is required to override statistical noise and obtain good quality XAFS data. Synchrotron, due to its energy tunability, high brilliance and polarization represents the ideal source for XAFS experiments.

In parallel, we have also undertaken the task of augmentation of the XAFS beamlines at the Indus-2 synchrotron source for studying such systems at extreme thermodynamic conditions. Pressure and temperature offer additional control parameters to derive insights into the phase diagram of nanoclusters.

This dissertation is divided into two parts: (i) XAFS characterization of disordered nanoclusters and (ii) augmentation of Indus-2 XAFS beamlines for extreme thermodynamic conditions. In the former part, we have characterized disordered nanoclusters in different configurations, viz. embedded nanoclusters in thin films, bimetallic nanorods synthesized via swift heavy ion irradiation and nanomedicine. In the latter part, we present the newly installed low temperature and high pressure XAFS facilities at Indus-2. The dissertation is organized into nine chapters, which are summarized as follows:

Chapter 1: Introduction

In this chapter, we present a basic introduction to nanoclusters. Their various possible applications and the size dependence of their properties are discussed. We then move on to discuss one important consequence of small size – the presence of disorder in these clusters. The various techniques that can be used for characterization of such disordered clusters are discussed. Finally we emphasize the need for XAFS for characterization and highlight the new information that can be extracted using the same. The various systems studied in this dissertation are presented.

Chapter 2: Theory of XAFS

In this chapter, the underlying physics of XAFS is explained. The XAFS equation is derived and each of the terms in the equation is described in detail. The approximations used for derivation of the equation are summarized. The equation is extended to include effects due to multiple scattering. A brief overview of XANES (X-ray Absorption Near Edge Structure) phenomenon is also given. Finally, the strengths and limitations of XAFS in comparison with other techniques are discussed.

Chapter 3: Experimental Apparatus for XAFS

In this chapter, we describe the instrumentation required for carrying out XAFS experiments. The experimental setup for XAFS is broadly classified into source and beamline instrumentation. Synchrotrons are the ideal source for XAFS experiments, and we discuss their strengths. The different generations of synchrotron sources, viz. bending magnet, insertion devices and free electron lasers are described. XAFS experiments require streamlined optics for getting good quality data. We describe in detail the optical components of XAFS beamlines and detectors for transmission and fluorescence mode XAFS, sample holders for various XAFS experiments and the sample preparation method for XAFS. Finally, we discuss the methods to eliminate noise in XAFS data.

Chapter 4: XAFS data analysis

In this chapter, we explain the method of analysis of XAFS data using the IFEFFIT fitting package. XAFS data analysis breaks up into (i) data processing, (ii) data modelling and (iii) data fitting. We discuss each of these steps in detail.

Chapter 5: Augmentation of Indus-2 XAFS beamlines for extreme thermodynamic conditions.

The synchrotron source in India, Indus-2, is a second generation source operating at 2.5 GeV ring energy and 300mA current. Presently two XAFS beamlines are operational at Indus-2 – one operates in energy dispersive mode and the other operates in energy scanning mode. Recently, we have upgraded these beamlines to accommodate experiments under extreme conditions, viz. low temperature and high pressure. This chapter describes (i) installation displex closed cycle cryostat and assessment of the possibility of performing experiments using the same by measuring XAFS on standard Au foil, and (ii) modification of optical layout of dispersive XAFS beamline for experiments under high pressure.

Chapter 6: XAFS characterization of embedded bimetallic nanoclusters in multilayer film

In this chapter, we characterize bimetallic clusters embedded in C matrix. These clusters were formed following ion irradiation of a Pt/Ni/C multilayer film. TEM, X-ray Reflectivity and X-ray Fluorescence measurements on the film pre- and post- irradiation provided information on layer periodicity and roughness, and also revealed cluster formation with irradiation. But they could not ascertain the composition and configuration of these clusters; neither could they determine the nature of the formed clusters. We have used XAFS in X-ray Standing Wave mode to derive this information. With rigorous XAFS coordination analysis, we have de-coupled the interfacial and layer contributions and derived the structure of the clusters to be Ni centered Ni/Pt bimetallic alloy clusters, highly disordered beyond first nearest neighbour. The possible applications of the same are discussed.

Chapter 7: XAFS characterization of bimetallic nanorods synthesized via Swift Heavy Ion Irradiation

In this chapter, we characterize bimetallic nanorods in silica matrix synthesized via Swift Heavy Ion Irradiation (SHII) of co-sputtered metal/metal//silica film. Although several methods have been previously used for synthesis of such nanorods, this is the first time they have been synthesized by SHII. We present two systems – Ag/Pt (bulk immiscible) and Ag/Au (bulk miscible). These are amorphous and crystalline respectively pre-SHII. We attempt to understand the relative effect of SHII on these two systems by deriving their composition and configuration using XAFS.

Chapter 8: XAFS characterization of Ayurvedic nanomedicine

In the absence of scientific evidence towards their claimed non-toxicity, Ayurvedic drugs are facing a world-wide ban due to their heavy metal content. In this chapter, we investigate the structure of Hg based ayurvedic drug, ‘Rasasindura’, with the objective of finding evidence towards its putative non-toxicity. Our results establish that the system contains HgS nanocrystals in stable α-HgS configuration and that metallic Hg^0 is completely absent, ensuring absence of Hg-based toxicity. With rigorous, novel XAFS analysis strategies, we have estimated the number and nature of defects, confirming the robust structure of the HgS nano-crystals (<3% defects). This ensures integrity of the nano-crystals during the drug-delivery process.

Chapter 9: Conclusions and future directions

In this chapter, we summarize the main conclusions of this dissertation. (i) The utility of XAFS to deduce the structure of disordered nanoclusters has been clearly demonstrated. XAFS successfully helped in understanding the composition and configuration of these clusters. Additionally, XANES characterization of these clusters led us to understand the chemical nature of cluster formation. (ii) The XAFS beamlines at Indus-2 have been augmented for performing experiments under low temperature and high pressure. We have assessed the feasibility of performing experiments using these new setups.

This Chapter is concluded by bringing out the future scope of the work.

Publication in Refereed Journals:

b. Published

1. Nitya Ramanan, Sumalay Roy, Debdutta Lahiri, Surinder M. Sharma and B.N. Dev, ‘Ascertaining the nano-cluster formation within ion-irradiated Pt/Ni/C multi-trilayer, with X-ray Absorption Spectroscopy’, *Journal of Synchrotron Radiation*, **20**, 137 (2013).
2. Nitya Ramanan, Sumalay Roy, Debdutta Lahiri, Surinder M. Sharma and B.N. Dev, ‘XSW-XAFS characterization of ion-irradiated Pt/Ni/C Multilayer’, *Journal of Physics: Conference Series*, **430**, 012063 (2013).
3. Debdutta Lahiri, Tomohiro Shibata, Soma Chattopadhyay, Nitya Ramanan, Swati Pandya, P D Kulkarni, A Thamizhavel, A K Grover, S Ramakrishnan and Surinder

M. Sharma, 'XAFS understanding of "repeated" magnetic compensation in $Nd_{0.8}Tb_{0.2}Al_2$' *Journal of Physics: Conference Series*, **430**, 012106 (2013).

4. Nitya Ramanan, Debdutta Lahiri, Nandini Garg, D. Bhattacharyya, S.N. Jha, N K Sahoo and Surinder M Sharma, 'High Pressure experiments at the XAFS beamline, Indus-2', *Journal of Physics: Conference Series*, **377**, 012011 (2012).

c. Accepted

1. Nitya Ramanan, Parasmani Rajput, S.N. Jha and Debdutta Lahiri, 'Assessing the feasibility of Low temperature XAFS experiments at Indus-2, India: first results', in press, *Nuclear Instruments and Methods in Physics Research A.*

d. Under review

1. Nitya Ramanan, Debdutta Lahiri, Parasmani Rajput, Ramesh Chandra Varma, A. Arun, T.S. Muraleedharan, K.K. Pandey, Nandita Maiti, S.N. Jha and Surinder M. Sharma, 'Investigating structural aspects to understand the putative/claimed non-toxicity of Hg-based Ayurvedic drug "*Rasasindura*", using XAFS', under review, *Journal of Synchrotron Radiation*.
2. Nitya Ramanan, Debdutta Lahiri, Ashwani Kumar, Parasmani Rajput, K. Thankarajan, D. Bhattacharyya and S.N. Jha, 'First phase commissioning of High Pressure XAFS setup at ED-XAFS beamline, Indus-2 Synchrotron Radiation Source, India', under review, *Journal of Optics (Optical Society of India).*

e. Other publications

1. ‘Investigating alloying/de-alloying of Ag/Pt and Ag/Au nanorods under Swift Heavy-ion Irradiation’, manuscript under preparation.
2. N. Ramanan, D. Lahiri, D. Bhattacharyya and S. N. Jha, ‘Calibration of standard Ni foil XAFS data recorded at the EXAFS Beamline, INDUS-2 SRS’, BARC report, *BARC/2012/E/009* (2012).
3. N. Ramanan, D. Lahiri, S.M. Sharma, N.C. Das, D.V. Udupa and A.D. Patil, ‘Development of a bendable mirror for studying materials under high pressure using EXAFS beamline at INDUS-2 SRS’, BARC report, *BARC/2010/E/12* (2010).

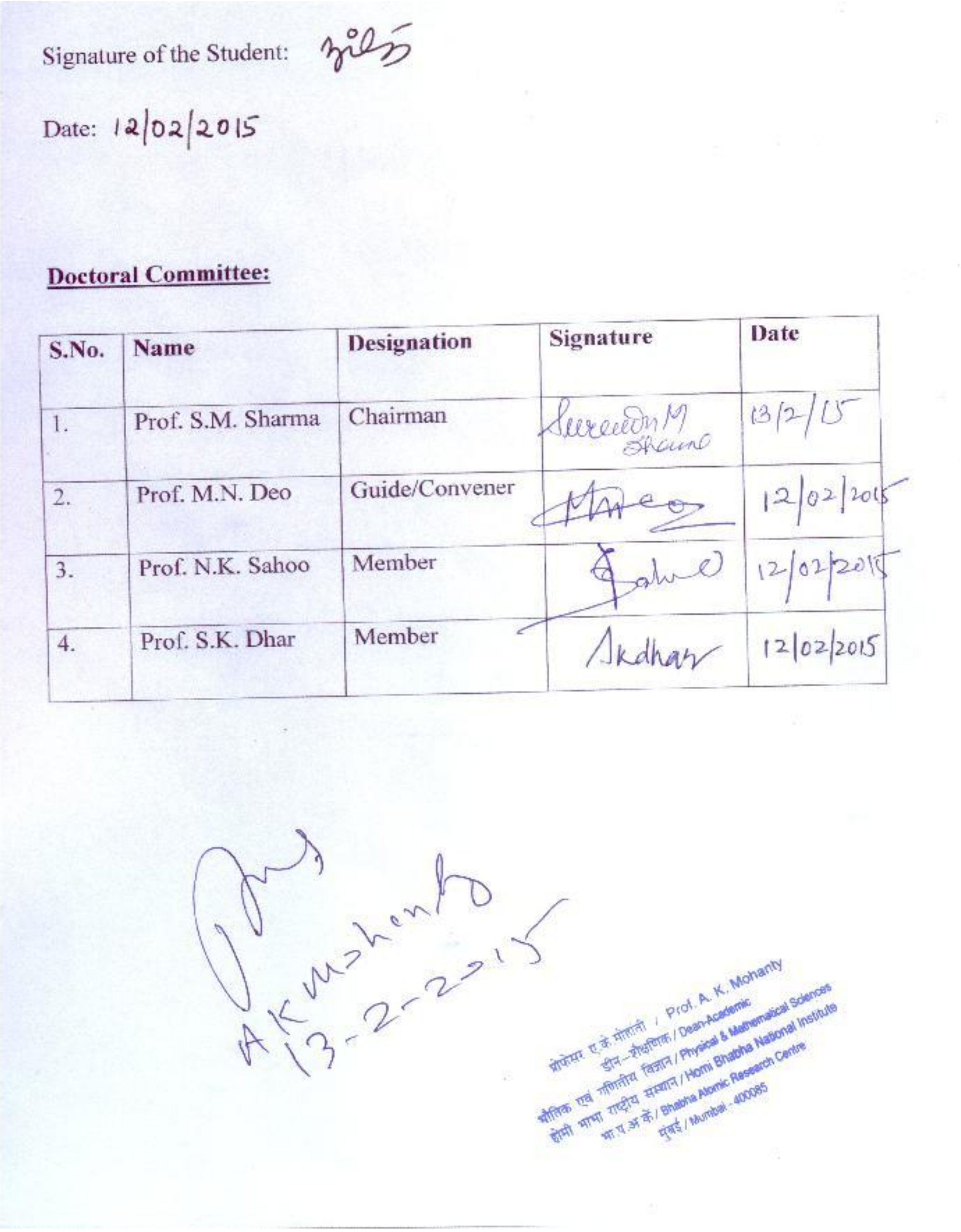

Signature of the Student:

Date: 12/02/2015

Doctoral Committee:

S.No.	Name	Designation	Signature	Date
1.	Prof. S.M. Sharma	Chairman	Surendra M Sharma	13/2/15
2.	Prof. M.N. Deo	Guide/Convener		12/02/2015
3.	Prof. N.K. Sahoo	Member	Sahoo	12/02/2015
4.	Prof. S.K. Dhar	Member	Skdhar	12/02/2015

A K Mohanty
13-2-2015

प्रोफेसर ए.के. मोहान्ती / Prof. A. K. Mohanty
डीन–शैक्षणिक / Dean-Academic
भौतिक एवं गणितीय विज्ञान / Physical & Mathematical Sciences
होमी भाभा राष्ट्रीय संस्थान / Homi Bhabha National Institute
भा.प.अ.कें / Bhabha Atomic Research Centre
मुंबई / Mumbai - 400085

CHAPTER 1

INTRODUCTION

Nanoclusters (NCs) are of immense technological importance in fundamental science and industry due to their small size (<100nm) and ability to exhibit intriguing size-dependent properties.[1] Over the past decade or so, development and synthesis of NCs has gained impetus primarily due to the growing need for smaller sized materials. There are several cases wherein small size is a prerequisite, for e.g.: (i) Electronic devices: In the device industry, where the perpetual aim is to accommodate more and more components on a single small chip, resulting in faster operation, lower cost and lesser power consumption, designing smaller, more compact individual components holds the key.[2-3] (ii) Nanodrugs: Since the sizes of human cell constituents are ~ 10-100nm, use of large sized materials for drug delivery has serious drawbacks in terms of poor bioavailability, in vivo stability, solubility, intestinal absorption, sustained and targeted delivery to site of action, therapeutic effectiveness and generalized side effects.[4] Furthermore, small size is also a necessity for gene sequencing.[5-6] (iii) Sensors: Surface Plasmon Resonance (SPR) occurs due to scattering of conduction electrons by the NC surface. SPR band occurs only when the NC diameter is less than the mean free path of the conduction electrons in the bulk metal.[7] This phenomenon is extensively utilized in optical sensors. Additionally, smaller size improves the efficiency and specificity of sensors.[8-9]

NCs possess large surface-to-volume ratio owing to their small size, which makes them highly reactive (since more surface is available to react), and hence potential candidates for catalysts. [10] In fact, the reactivity becomes so remarkably high that even the so called noble metals (Au, Ag, Pt etc.) cease being noble in the nano-regime![11] Besides this, they are also ideal candidates for water treatment and desalination.[12] The high aspect ratio further simplifies the task of functionalizing NC surfaces for various diverse applications (from drug delivery to clothing insulation) simple.

In the nano-size regime, quantum size effects rule the properties of clusters.[13] Size becomes an additional degree of freedom, strongly influencing the following properties: (a) Band Gap: NCs exhibit size dependent tunability of band gap. As a result, their interaction with light and hence their 'color' is size-dependent.[14] Band gap tunability is particularly profitable for photovoltaics[15] wherein band structure and energy level alignment hold the key to device performance. (b) Thermal Properties (e.g. Melting Point): NCs have large number of surface atoms, facilitating lower melting point as compared to bulk, which can even lower down to room temperature in some cases.[16] (c) Electrical Properties (e.g. conductivity): In composite materials, small particle size favors formation of conduction pathway, hence resulting in high conductivity.[17] (d) Magnetic Properties: The saturation magnetization in NCs is size dependent.[18-20] Such size controlled magnetism has interesting applications in spintronics.[21-22] (e) Control of Negative Thermal Expansion (NTE) is correlated with NC size control in the case of polymer/NTE composites, wherein uniform dispersion is the main requirement.[23]

Due to their small size, nanoclusters are prone to various defects, mainly surface defects and vacancy. The strain induced by these defects makes the nanoclusters prone to disorder, resulting in a variety of interesting consequences, like alloying, de-alloying and segregation. In this dissertation, we have attempted to characterize disordered NCs in different configurations, namely (a) Ion irradiation generated embedded Ni/Pt clusters in Pt/Ni/C multilayer films, (b) Ag/Pt and Ag/Au nanorods synthesized via Swift Heavy Ion Irradiation, (iii) Nano-medicine. All of these possess only short range order. Several techniques can be used for characterization of NCs, including X-ray Diffraction (XRD), Transmission Electron Microscopy (TEM), Selective Area Electron Diffraction (SAED), Scanning Electron Microscopy (SEM), UV-Visible Absorption Spectroscopy (UV-Vis), Vibrational Spectroscopy (infrared (IR) and Raman). XRD and SAED can be used to detect crystal structure within the NCs. TEM and SEM give information on size, shape and distribution of the NCs. UV-Vis is used for size estimation and also to detect alloying. Vibrational spectroscopy can be used to understand the surface interaction of the NCs with the environment. However, for very small clusters with large degree of amorphous character, these techniques are incapable of deriving the complete structure.

XAFS is the only technique that can be used for characterization of highly disordered clusters of size < 2 nm. Due to the “local” nature of XAFS information and its elemental specificity, XAFS can be used to derive detailed structure around selected atoms of interest. In the present work, with the aid of rigorous XAFS coordination analysis, we provide unambiguous characterization of clusters in terms of their composition, configuration (segregated / alloyed / core-shell / icosahedra etc.), degree and nature of disorder (orientation disorder / amorphous). In conjunction with XAFS, the exhaustive local structure details pertaining to chemical origin of NC formation have been derived through X-ray Absorption Near Edge Structure (XANES).

While investigating these systems, it was realized that external stimuli in the form of extreme thermodynamic conditions could provide an additional parameter for tuning the properties of NCs. Therefore, in parallel, we have undertaken the task of augmentation of the XAFS beamlines at the Indus-2 synchrotron source for studying such systems at extreme thermodynamic conditions, viz. low temperature and high pressure.

This dissertation is therefore divided into two parts: (i) X-ray Absorption Fine Structure (XAFS) characterization of Disordered Nanoclusters, and (ii) Augmentation of Indus-2 XAFS beamlines for extreme thermodynamic conditions.

1.1 XAFS characterization of disordered nanoclusters

1.1.1 Embedded bimetallic Ni/Pt clusters in Pt/Ni/C multilayer film synthesized by ion irradiation

Bimetallic Ni/Pt clusters embedded in C (dielectric) matrix were synthesized via ion irradiation of a Pt/Ni/C multilayer.[24] In contrast with other fabrication methods, viz. sol-gel synthesis, colloidal synthesis, ion irradiation is a dry synthesis method, and therefore helps in overcoming the 'wetting' issue in electronic devices. Moreover, the composition and configuration of the generated clusters is not dictated by thermodynamics alone, but depends on collision kinetics, the initial layer thickness and the interfacial integrity as well. TEM, X-ray Reflectivity (XRR), X-ray Fluorescence (XRF) gave information on roughness, ion-irradiation induced inter-layer mixing and cluster formation, but could not determine the composition and configuration of the clusters. XAFS in Standing Wave mode[25] was employed to (i) determine degree and nature of interfacial mixing leading to cluster formation, (ii) understand the relative susceptibility of the interfaces and its role in cluster formation, (iii) determine whether Ni and Pt exist as isolated or alloyed clusters and the configuration of the clusters. Additionally, we have determined the nature of the clusters to be Ni centered Ni/Pt bimetallic alloy clusters. Novel and non-trivial XAFS coordination analysis was used in this work. We have directly established the correlation between cluster composition and chemical / physical nature of the interfaces of the multilayer. These results have utmost significance in the design of spintronic devices, with magnetic clusters (Ni/Pt) on non-magnetic matrix (C) and where cluster composition is crucial to ferromagnetic character.

1.1.2 Ag/Pt and Ag/Au nanorods synthesized by Swift Heavy Ion Irradiation

Ag/Pt nanorods in silica matrix were synthesized by Swift Heavy Ion Irradiation (SHII) of Ag/Pt/silica film [prepared by atom beam co-sputtering]. Several methods have been used previously for synthesis of bimetallic nanorods; however, to the best of our knowledge, this is the first time bimetallic nanorods have been synthesized by SHII – a technique objected at generating aligned nanorods, uniformly distributed in the matrix both in terms of size and separation. Alignment is of utmost importance, since the high sensing capabilities of nanorods are best realized when they are parallel aligned. Ag/Pt is bulk immiscible due to the large positive heat of mixing of Ag and Pt. These are potential economic catalysts for methanol oxidation in Fuel Cells, considering the lower cost of Ag as compared to Pt.[26-27] Transmission Electron Microscopy revealed formation of nano-rods, following critical ion-flux. X-ray Diffraction and Optical Absorption Spectroscopy confirmed highly disordered structure that could not be resolved; SAED suggested crystalline phase locally though it could not determine whether Ag and Pt are alloyed or segregated. Degree of alloying is the defining parameter for the use of these nanorods as fuel cell catalysts. We have used XAFS coordination analysis to quantitatively determine the degree and nature of alloying. Further, we have compared our results on this system with bulk miscible Ag/Au system to evaluate the relative role of thermodynamics, diffusion etc. on the alloying abilities of these systems.

1.1.3 HgS nanoclusters in Ayurvedic nanodrug

Hg is one of the most toxic elements known to humans and Hg contamination in water, soil and environment is of worldwide concern. For this reason, the use of Hg in ayurvedic drugs in concentrations higher than WHO prescribed limits is questionable. In the absence of scientific evidence of their non-toxicity, Ayurvedic drugs are facing a world-wide ban.

The system chosen was Hg-based Indian ayurvedic drug, "*Rasasindura*". We have investigated this system using XAFS with the objective of providing evidence towards the claimed non-toxicity of this drug. Our results establish that the system contains HgS nanocrystals in stable α-HgS configuration and that metallic Hg^0 is completely absent, ensuring absence of Hg-based toxicity. With rigorous, novel XAFS analysis strategies, we have estimated the number and nature of defects, confirming the robust structure of the HgS nano-crystals (<3% defects). This ensures integrity of the nano-crystals during the drug-delivery process. Our results provide significant lead that the chemical form of heavy metal, rather than its content, is the correct parameter to evaluate toxicity of Ayurvedic drugs.

1.2 Augmentation of XAFS beamlines at Indus-2 for extreme thermodynamic conditions

Indus-2 is a 2.5GeV/300mA third generation synchrotron source at the Raja Ramanna Centre for Advanced Technology (RRCAT), India. Presently, Indus-2 houses two XAFS beamlines – one operates in energy dispersive mode (BL-08) and the other operates in energy scanning mode (BL-09). Although both these beamlines were initially designed for ambient conditions, to cater to the increasing demand for experiments under extreme conditions, we have augmented these beamlines to accommodate experiments under low temperature and high pressure.

1.2.1 High Pressure XAFS experiments at Indus-2

Structural changes of materials under high pressure have direct bearing on practical applications, where they could be in nano-size and subject to high surface pressure. In this regard, there are several problems which are of prominent interest to the high pressure community: Negative Thermal Expansion (NTE) materials[28-30], Fe-based superconductors[31-32], perovskites (e.g. $BiFeO_3$[33], $BaLiF_3$[34], Sr_2MgWO_6 [35]), pyrochlores (e.g. $Yb_2Ti_2O_7$[36], $LaHf_2O_7$ [37], Rare earth oxides (e.g. Dy_2O_3[38], CeO_2[39], $CeVO_4$[40], Nd_2O_3[41]), metal-filled carbon nanotubes[42] etc.

High Pressure (HP) experiments are Diamond Anvil Cell (DAC) based and have stringent spot size requirements, considering the small sample size in DAC (~50-120µm). Therefore, highly focused, stable beam is a necessity for such experiments. In the Energy Dispersive geometry, there is zero mechanical movement (of optics, etc.) during the course of the experiment. Sharp focusing, short acquisition time (~ 300ms) and reduced cost make it the ideal choice for HP experiments.

In the energy dispersive XAFS beamline (BL-08), the present experimental spot size (at 10 keV) is ~ 192 µm × 460 µm (H × V). To reduce the vertical spot size to DAC compatible values, additional focusing element had to be installed at BL-08. To achieve this goal without disturbing the current setup, an additional bendable elliptical post-mirror has been designed and installed prior to sample position.

1.2.2 Low temperature XAFS experiments at Indus-2

Low temperature XAFS experiments have gained impetus over the years, due to the growing importance of understanding short-range-order (SRO) changes across magneto-electronic phase transitions that generally occur at low temperature ($T_C << 300K$). In several cases, paradoxes which could not be explained by studying temperature evolution of Long Range Order (non-coincident superconducting and phase transition temperatures[43], pairing mechanism[44]) could be solved by XAFS detection of disorder on local scale.

To cater to the increasing demand for low-temperature XAFS, low-temperature XAFS-compatible cryostat (low vibration; Temperature range = 4.2-300K) has been commissioned at Indus-2. The cryostat was tested down to 5K. We have assessed the feasibility of XAFS experiments using this cryostat in terms of data quality, possible temperature range, temperature calibration and temperature resolution by measuring XAFS of standard Au foil. Debye Model based method of calibration was adopted in this case.[45]

CHAPTER 2

THEORY OF XAFS

2.1 Introduction

The X-ray absorption spectrum of any material around the absorption edge of any of its constituent atoms exhibits a series of oscillatory fine features that modulate the monotonically decreasing atomic absorption coefficient μ_o by a few percent. This is known as X-ray absorption fine structure (XAFS).[46] XAFS has been attributed to the presence of other atoms around the excited atom. By analyzing XAFS, detailed structural information about the "local" environment of the absorbing atom can be derived.

Fig. 2.1 shows a typical XAFS spectrum (Au L3 edge, 11,919 eV). The spectrum can be divided into two main regions: X-ray Absorption Near Edge Structure (XANES) and Extended X-ray Absorption Fine Structure (EXAFS). XANES refers to the region close to the absorption edge ($\leq 30eV$) and contains information about the chemical state (oxidation state, site symmetry, etc.) of the absorbing atom. EXAFS refers to the oscillations well above the edge ($> 30eV$) and contains local structural information (near neighbor coordination number, bond lengths, Debye Waller Factors). The only real distinction between the physics of XANES and EXAFS is in terms of resolution and in the complexity of the spectra. The most important strength of XAFS is the ability to simultaneously measure chemical state and local structure. XAFS has wide ranged applications in several fields ranging from basic physics/chemistry/biology to catalysis, environmental science, device physics, optoelectronics etc.

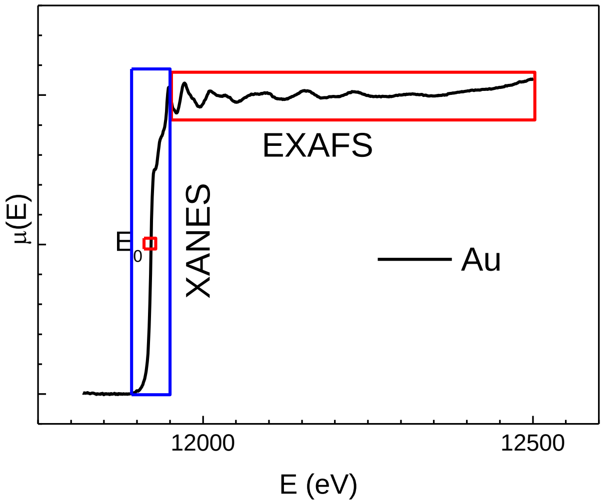

Fig. 2.1: Typical XAFS spectrum

2.2 Physics of XAFS

When an atom absorbs an x-ray of energy $E \cong E_0$, where E_0 is the binding energy, a photo-electron with energy $(E - E_0)$ is ejected (Fig. 2.2). If the x-ray energy is large enough to promote a core-level electron to the continuum, there is a sharp increase in absorption. For an isolated atom, μ(E) resembles typical resonance spectrum i.e. rises sharply at and then monotonically drops with increasing energy (Fig. 2.3(a)). Quantum mechanically, this is due to the fact that the probability of the photon being absorbed by the electron depends on the initial and the final state of the electron, which includes the superposition of the outgoing and all incoming, backscattered waves and the potential energy difference between the atomic state and the Fermi energy. In real material, one observes oscillatory features superimposed on the mean background. The origin of these oscillations could be understood considering wave-form of the ejected photo-electron and scattering phenomenon. In real material, atoms are not isolated but surrounded by neighboring atoms. The ejected photo-electron wave back-scatters from neighboring atoms (Fig. 2.3 (b)) and interferes with itself. Thus, the final state electron wave-function is not decaying anymore; instead it is oscillatory as function of energy. The oscillations of the final electron wave are reflected as oscillations in μ(E), called XAFS.

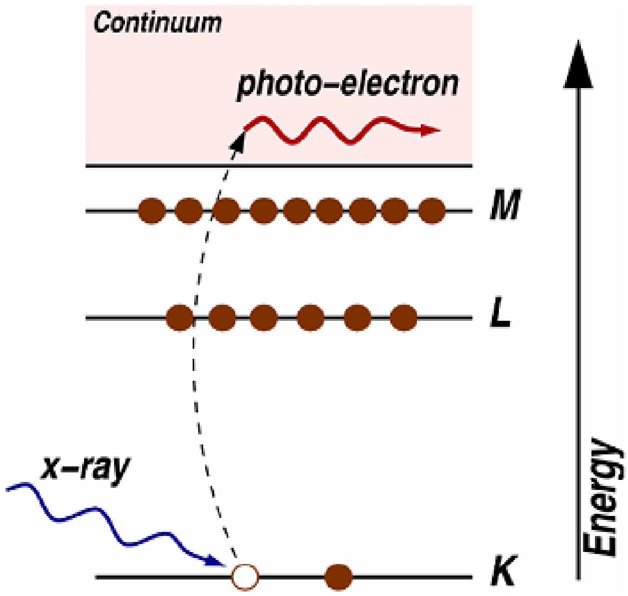

Fig. 2.2: Physics of X-ray Absorption (Newville, 2004)

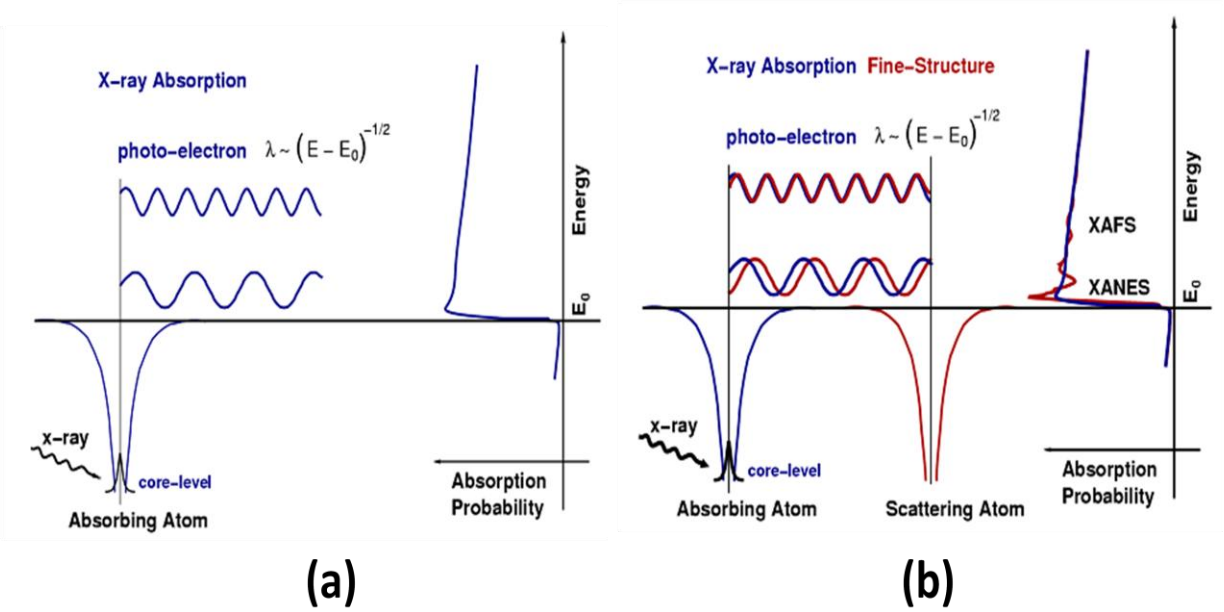

Fig. 2.3: (a) X-ray absorption by a free atom, (b) X-ray absorption in the presence of neighboring atoms (Newville, 2004)

Being electron wave scattering phenomenon, XAFS information is inherently local in nature and hence can be used for studying local-scale defects. Over the years, understanding of local-scale defects (for example, their role on electronic structure) has gained importance, as long-range-order (LRO) could not adequately explain many of the phase transitions.[47-52] The other strengths of XAFS are (i) due to the "local" nature of information, crystalline samples are not required. This makes XAFS the unique structural tool for both crystalline and amorphous systems (e.g. disordered nanoparticles, metallic glass, soil, liquid) [53-59] which lack Long Range Order, and hence structural tools such as X-ray Diffraction are insufficient to decode the structure. (ii) Tunability: In a multi-component system, XAFS, being an element-specific probe, can extract site-resolved structural information.[60-64] This is useful to understand the exact role of each component in the scientific problem of interest. (iii) Since XAFS is not inherently surface sensitive, penetration depth can be controlled to carry out both bulk and surface measurements by changing the angle of incidence of x-rays on the sample. (iv) XAFS has ppm range detection limit, and hence can be applied to even very dilute dopants. (v) XAFS can be measured under extreme thermodynamic conditions – low temperature, high pressure, high temperature.

2.3 The XAFS Equation

XAFS is defined as:

$$\chi(E) = \frac{\mu(E) - \mu_0(E)}{\Delta\mu_0(E_0)} \tag{2.1}$$

where, $\mu(E)$ is the measured absorption coefficient; $\mu_0(E)$ is the slowly varying background absorption from isolated absorbing atom and other processes; $\Delta\mu_0(E_0)$ is the measured jump in absorption coefficient at threshold energy E_0.

XAFS is an interference effect and depends on the wave-nature of the photo electron. Therefore it is convenient to think of XAFS in terms of the photo-electron wave number rather than the X-ray energy. The XAFS oscillations are hence conventionally described *wrt* the photo-electron wave number, k.

$$k = \sqrt{\frac{2m(E-E_0)}{\hbar^2}}\,, \tag{2.2}$$

where m=electron mass, $E = \hbar w$ is the energy of the absorbed x-ray photon.

X-ray absorption is a transition between two quantum states. The initial state contains an x-ray photon and a core-electron and no photo-electron. The final state contains no x-ray photon, a core-hole and a photo-electron. Therefore, $\mu(E)$ can be described using Fermi's Golden Rule[65]:

$$\mu(E) \sim \left|\langle i|H|f\rangle\right|^2, \tag{2.3}$$

where, $\langle i|$: The initial state (x-ray photon + core electron). This is not altered by the neighboring atom.

H: the interaction. In the dipole approximation,

$$H = e^{ikr} \approx 1. \tag{2.4}$$

$|f\rangle$: The final state (core-hole + photo-electron).This is altered by the neighboring atom. Hence the absorption is modulated.

Now, $|f\rangle = |f_0\rangle + |\Delta f\rangle$, i.e. sum of the bare atom $|f_0\rangle$ and the effect of the neighboring atom $|\Delta f\rangle$.

Then, the bare atom absorption,

$$\mu_0 = \left|\langle i|H|f_0\rangle\right|^2 \tag{2.5}$$

and the fine structure,

$$\chi(E) \propto \left|\langle i|H|\Delta f\rangle\right|^2. \tag{2.6}$$

H represents the process of interchange of two energy and momentum states.

The absorption is proportional to the amplitude of the photo electron at the origin. Consider an outgoing photo-electron described by a spherical wave number k ($k = {}^{2\pi}\!/\!_{\lambda}$; $\lambda = {}^{h}\!/\!_{p}$) and amplitude A:

$$A \propto \frac{e^{ikr}}{r} \tag{2.7}$$

The neighboring atoms scatter this spherical wave into a new spherical wave. This backscattered wave is proportional to the amplitude of the incident wave and the backscatter type-dependent backscattering amplitude $F(2k)$, i.e.

$$F(2k)\frac{e^{ikr}}{r}\frac{e^{ik|r-r_i|}}{|r-r_i|}$$

The backscattered wave emanates from r and not from the point of origin of the outgoing spherical wave. However, it is the intensity of the backscattered wave at the origin (r~0) which is of interest to us. This is because the initial state is an s-state, which is non-zero close to the origin, therefore $\langle i|H|\Delta f\rangle \neq 0$ only close to the origin. Amplitude of the backscattered wave at the origin is proportional to

$$F(2k)\frac{e^{i2kr}}{r^2}.$$

The factor $2kr_i$ is the phase shift introduced by a wave of wave number $k = {}^{2\pi}\!/\!_{\lambda}$ in traveling distance $2r_i$ from the origin and back from the backscatterer. However, since the electron is not traveling in constant potential, a phase shift δ(k) must be incorporated to account for the varying potentials of the absorber and backscattering atoms.

$$\delta(k) = 2\delta_a(k) - l\pi + \delta_b(k), \tag{2.8}$$

where $\delta_a(k)$ and $\delta_b(k)$ denote the phase shifts due to absorber and backscatterer respectively (Fig. 2.4); l=1 for K-edge. [Note that $\delta_a(k)$ has to be counted twice in the sum].

Therefore, $$\chi(k) \propto F(2k)\frac{e^{i[2kr+\delta(k)]}}{2r^2} = \frac{F(2k)\sin(2kr+\delta(k))}{r^2} \tag{2.9}$$

The backscattered wave modifies the absorption as it interferes with the outgoing wave, and this modification is, by definition, the EXAFS.

Since the absorber atom usually has more than one neighboring atom, the above equation must be summed over the scattering contributions from all neighboring atoms. In the single scattering approximation, the effect of many scatterers can be obtained simply by adding the effects of each scatterer, and the total EXAFS becomes

$$\chi(k) = K\sum_j \frac{F_j(2k)\sin(2kr_j+\delta_j(k))}{r_j^{\ 2}} \tag{2.10}$$

where K is a constant of proportionality.

$$KF_j(2k) = \frac{m}{2\pi\hbar^2} f_j(2k) \tag{2.11}$$

In any coordination shell, all the atoms will not be exactly at the same distance because of thermal vibrations or structural disorder. Thus the contributions of these atoms will not all exactly be in phase. If this disorder is small, and has a Gaussian distribution about the average distance R_i, i.e. it has a probability of deviating from the average by

$$\left(2\pi\sigma_j^2\right)^{-1}\exp\left(-\frac{\left(r_j-R_i\right)^2}{2\pi\sigma_j^2}\right),$$

the de-phasing produced by it adds a factor $N_j \exp(-2k^2\sigma_j^2)$ to the EXAFS expression instead of N_j, where N_j is the number of atoms of type j in the shell and σ_j is the RMS deviation from the average distance R_j. The EXAFS expression in equation 2.10 is modified as

$$\chi(k) = \frac{m}{2\pi\hbar^2}\sum_j \frac{f_j(2k)N_j \exp(-2k^2\sigma_j^2)\sin(2kr_j + \delta_j(k))}{r_j^{\,2}} \tag{2.12}$$

So far, this derivation has left out an important physical effect: the lifetime τ_0 of the photo-electronic states. This has two contributions: (i) the time taken for the core-hole to be filled by another electron and (ii) the lifetime of the photo-electron itself. These two lifetimes contribute to determine the finite lifetime of the excited state consisting of the photo electron together with the core-hole from which it came. The lifetime is important because in order for the backscattered wave to interfere with the outgoing wave, the two must be coherent, i.e. the phase difference between the two must be well defined. This depends on λ, the mean free path of the electron, which defines the distance upto which an electron can travel before being inelastically scattered. λ ~ 8-10Å, which is responsible for the local nature of XAFS. Therefore, another exponential decay factor $\exp(-{}^{2r_j}\!/_{\lambda})$ is introduced into equation 2.12, which accounts for the inelastic losses suffered by the electron during the scattering process. The equation now becomes:

$$\chi(k) = \frac{m}{2\pi\hbar^2}\sum_j \frac{f_j(2k)N_j \exp(-2k^2\sigma_j^2)\exp(-\frac{2r_j}{\lambda})\sin(2kr_j + \delta_j(k))}{r_j^{\,2}} \tag{2.13}$$

Further, an additional factor, called the amplitude reduction factor or S_0^2, is introduced, which accounts for relaxation of all other electrons in the absorber atom due to creation of the core-hole. It has element-specific constant value.[66] Usually, $0.7 < S_0^2 < 1$. The equation is then modified as:

$$\chi(k) = \frac{m}{2\pi\hbar^2}\sum_j \frac{S_0^2 f_j(2k)N_j \exp(-2k^2\sigma_j^2)\exp(-\frac{2r_j}{\lambda})\sin(2kr_j + \delta_j(k))}{r_j^{\,2}} \tag{2.14}$$

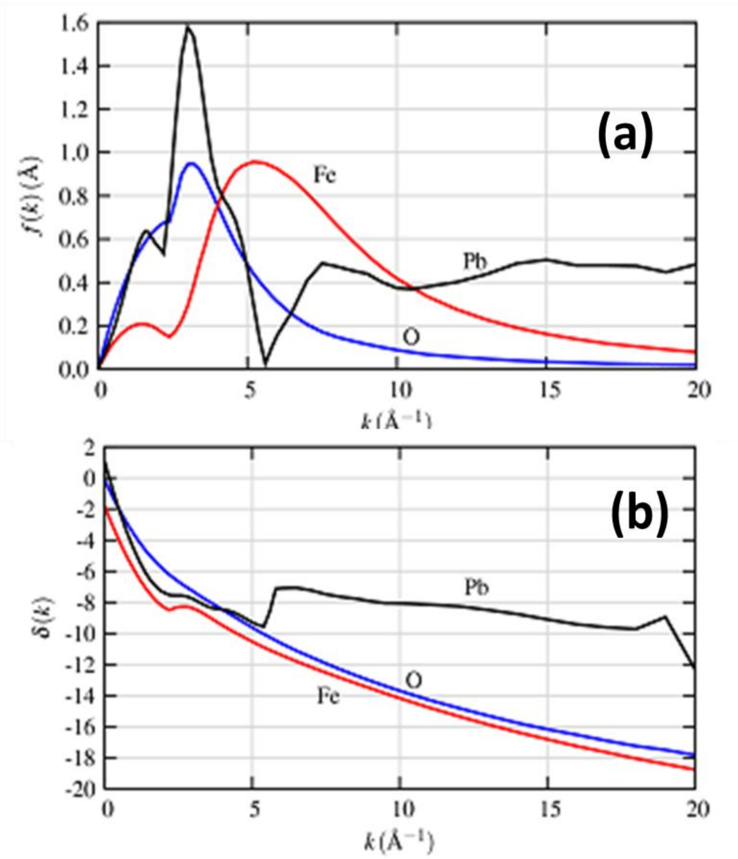

Fig. 2.4: Dependence of (a) scattering amplitude f(k) and (b) phase shift δ(k) on scatterer type (Newville, 2004)

The XAFS equation is the superimposed result of the structural information from different atoms at different distances. From equation 2.14, it is clear that the period of XAFS oscillations is given by r_j, the radial coordinates of the neighboring atoms, and the amplitude is proportional to N_j, the coordination number of the neighboring atoms. To decouple this information, the oscillations are Fourier transformed to yield a radial distribution function (corrected phase shifts) of atoms. The positions of the peaks in the distribution correspond to the different radial distances from the absorbing atom at which the surrounding atoms are located and the amplitudes of the peaks correspond to the number of these atoms. Each of these peaks is then fitted using the structural parameters (coordination number, atomic type, bond length, Debye Waller Factor) as variables. The theoretical accuracy with which these parameters can be determined are $r = \pm 0.01 Å$, $\sigma^2 = 0.002$ $Å^2$, $N = \pm 1$, $Z = \pm 5$.

The following is the summary of approximations used while deriving the XAFS equation:

1. Dipole Approximation: The Electric Field over the electromagnetic wave is assumed to be constant over the dimensions of the K-shell, so that the interaction Hamiltonian,

   $$H = e^{ikr} \approx 1. \tag{2.15}$$

   This selection rule ($\Delta l = \pm 1$) implies that (a) if the initial core has s-symmetry (l=0, edges K and L_I), the final state has p symmetry (l=1); (b) if the initial core-state has p symmetry (l=1, edges L_{II} and L_{III}, the final state can have s or d symmetry (l=0 or l=2 respectively). However, sometimes, dipole-forbidden transitions become 'allowed' due to hybridization between states, giving non-negligible contributions to XAFS.

2. Muffin-tin approximation: The muffin-tin potential is a spherical scattering potential centered on each atom, with a constant value of potential in the interstitial region between the atoms. In the EXAFS domain, the kinetic energy of the photo-electron is large; therefore the electron is less sensitive to details of the potential at the outer edges of the atom and in the region between the atoms. As a result, the electron is mainly scattered by the inner parts of the atomic potential and it moves more-or-less freely in the average potential within the flat interstitial region. Therefore, the muffin-tin potential approximation works well in the EXAFS regime. However, the details of the potential are much more important for XANES calculations where the photoelectron has low kinetic energy.

3. Plane wave approximation: The plane wave approximation is valid if the effective size of the atom in backscattering is small compared with the distance between the atom and the center atom. At low k, this is not case, because the effective atomic size is about the same as inter-atomic distance. As the k of the photoelectron increases, the effective size of the atom decreases as the photoelectron penetrates deeper into the atom before scattering. The electron will scatter significantly only when the spatial variation of the atomic potential has a significant fractional change in the distance of 1/*k*. At high k the diminishing effective size of the backscattering atom makes the small-atom approximation satisfactory.

   The effect of the breakdown of the small-atom approximation on the phase of EXAFS can be approximately compensated for by a shift of E_0. Here E_0 is the binding energy of the photoelectron and is related to k: $k = \sqrt{\frac{2m(E - E_0)}{\hbar^2}}$. However, E_0 shifts cannot correct for amplitude error introduced by the small atom approximation. Eliminating the small-atom approximation makes EXAFS less convenient because *f(2k)* and $\delta(k)$ then depend on r_j in addition to *k*, and their tabulation would become prohibitive because of the additional parameter of r_j.

4. Quasi-independent particle approximation: While deriving the XAFS equation, we have initially ignored the fact that the remaining (N-1) states will no longer have the same wave function as the core-electron is rejected and correspondingly a hole is created. This incomplete overlap reduces the measured XAFS amplitudes. To compensate for this, the term S_0^2 is introduced in the equation.

5. Single scattering approximation: The derivation of XAFS equation was based only on single scattering process of the photo-electron. Multiple scattering effects, which are important for XANES and also in the EXAFS regime in certain cases,

have been ignored. The multiple scattering effects are discussed in the following section.

6. The equation was derived for 1s initial state (K-edge) for which there is only one possible final state (p-state). For a p or d initial state (L or M edge), there will be two possible final states and hence the equation will have a more complicated angular dependence.

2.4 Multiple Scattering

As mentioned above, the derivation of the EXAFS equation (2.14) was based on the single scattering approximation – that the outgoing wave is backscattered from the surrounding atom only once before combining with the unscattered wave. This approximation is valid only so long as the scattering is small. For further scatterings such as scattering from one neighbor to the next before combining with the unscattered wave, the equation must be modified further.

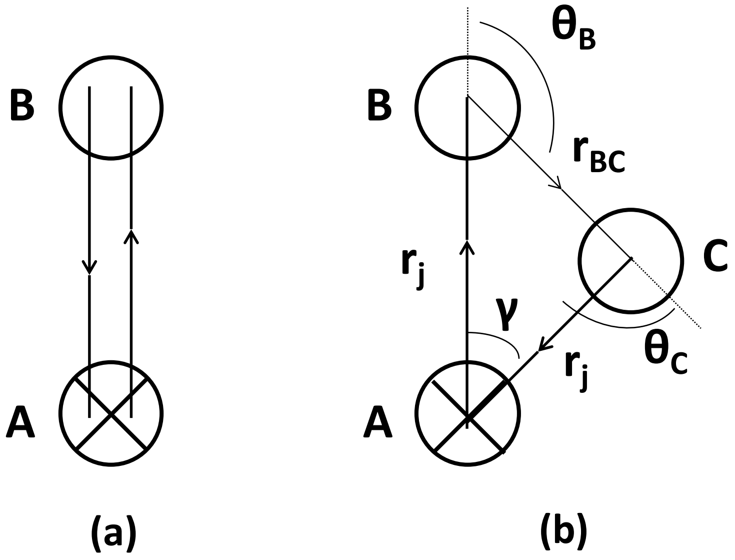

Fig. 2.5: (a) Single Scattering path for photo electron, (b) Double scattering path for photo electron

Consider the three atom systems shown in Fig. 2.5, with atom A being excited by absorbing the x-ray photon. We compare two processes. Fig. 2.5 (a) is the single scattering case wherein the photo-electron is back scattered from atom B and interferes with the outgoing state at atom A. Fig. 2.5(b) is the double scattering case wherein the photoelectron scatters from atom B and then atom C before returning to atom A and interfering with the outgoing state. This double scattering contribution produces a backscattered wave of the form

$$\frac{F(\theta_B)F(\theta_C)\exp i[k(2r_j + r_{BC}) + \delta_m(k) - \pi/2]}{kr_j^2 r_{BC}}\cos\gamma \tag{2.16}$$

where $\delta_m(k) = 2\delta_1 + \beta_B + \beta_C$, $F(\theta_B)$ is the amplitude of scattering from atom B through an angle θ_B, and β_B is the phase introduced by that scattering. γ is the angle between the first and last scattering paths. $\cos\gamma$ measures the overlap of the p state of the final incoming electron with the p-state excited by the x-ray. A Fourier Transform of equation 2.16 will peak at the larger distance $R \cong {r_j + r_{BC}}/{2}$, neglecting the shift caused by the k dependence of the phase δ_m. The magnitude of the backscattering amplitude is F/r_{BC} times that of single scattering. For θ_B, θ_c >40°, $F(\theta)/r_{BC} \cong F(\pi)/r_{BC}$, which is small for $r_{BC} \geq 2$ Å. However, for $\theta \cong 0°$, $F(0)$ peaks and becomes much larger (see Fig. 2.4(a)). $F(\theta)/r_{BC} \cong 1$ and double scattering becomes important. This forward scattering configuration is called the focusing or shadowing effect and is the only case where double scattering is important relative to single scattering in the same shell.

Forward multiple scattering has been used to determine atomic configurations where three atoms are aligned or almost aligned.[67] It has also been used to determine unit cell tilt angles in several cases.[43,55,68]

It is to be noted that all multiple scatterings peak in the Fourier Transform only at distances larger than that of the single scattering first neighbor. Thus the first neighbor peak in the Fourier Transform has rigorously no multiple scattering contributions.

2.5 Brief overview of XANES

XANES is a region of x-ray absorption spectrum within 30eV of the absorption edge. Although the basic physics of XANES is same as that of EXAFS, the low kinetic energy of the photo-electron in the XANES region results in a different phenomenon. Since the De-Broglie wavelength of the photo-electron is very large (~100Ǻ) in the XANES region, it spills over several bondlengths; therefore the local structural resolution is lost. However, due to low kinetic energy, the photo-electron wave becomes very sensitive to the chemical potential so that it can recognize chemical state of the atom. Because of low kinetic energy, it is susceptible to multiple scattering so that it can detect site symmetry (tetrahedral vs. octahedral). Hence, important information such as charge transfer/oxidation state/site symmetry can be obtained from XANES

Fig. 2.6 shows a typical XANES spectrum. It can be divided into the following regions:

(i) Pre-edge refers to the region just before the edge step. Pre-edge features are caused by electronic transitions to empty bound states, the transition probability being governed by dipole selection rules. The pre-edge contains information pertaining to local geometry around absorbing atom and shows strong dependence on oxidation state and bonding characteristics (chemical shift) of absorbing atom.

(ii) Edge refers to the absorption edge. It defines the ionization threshold for transition to continuum states. It shows strong oxidation state dependence as well.

(iii) Whiteline refers to a sharp peak in the spectrum just above the edge. Its intensity is proportional to the density of unoccupied states and it is strongly dependent on the oxidation state as well.

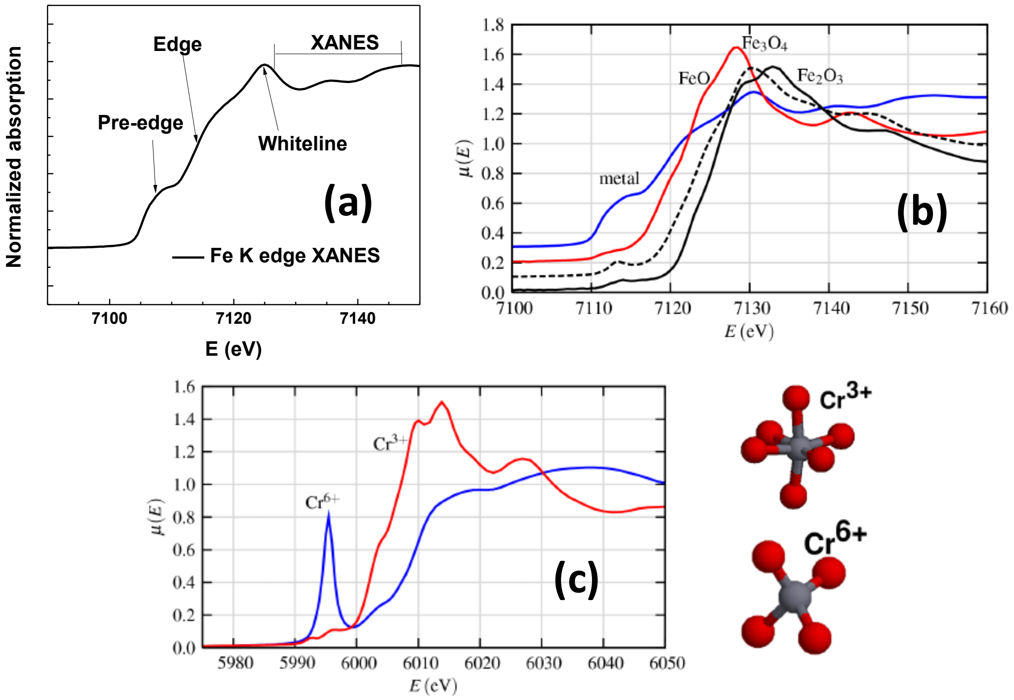

Fig. 2.6: (a) Typical XANES spectrum. XANES can be used to qualitatively detect (b) oxidation state, (c) site symmetry. (Newville, 2004)

(iv) XANES features arise due to multiple scattering resonances of photo electrons ejected at low kinetic energy. They contain information on inter-atomic distances and bond angles.

A lot of chemical information is obtainable from XANES, particularly the valence (very difficult to experimentally determine in a non-destructive way) state of the absorbing atom and its coordination environment. Since the edge position and shape are sensitive to formal valence state, ligand type, and coordination environment, the same are reflected in the edge features.

2.5.1 Oxidation State: Change in oxidation state is reflected as: (i) shift in absorption edge position (positive shift = higher oxidation state). Increase in oxidation state is equivalent to an increase in the attractive potential of the nucleus following loss of an electron. (ii) change in "whiteline" intensity. Whiteline intensity is proportional to the density of unoccupied final states, which is related to the oxidation state of the sample. Higher the oxidation state, sharper is the whiteline intensity. The determination of exact oxidation state from whiteline intensity is complicated by the effect of coordination geometry on the transition probabilities. But, the systematic change in whiteline intensity can be used to monitor relative charge-transfer related phenomena as a function of dopant concentration for eg. in intermetallics or the time evolution of species during a chemical reaction by time-resolved in-situ experiments. This leads to important applications of XANES in two important fields – environmental science and catalysis.

2.5.2 Site symmetry: Coordination geometry of nearest neighbors around the absorbing atom lays its signature in XANES through orbital hybridization of unoccupied states. Although X-ray absorption is dominated by dipole transition rule ($l=\pm1$), weak pre-edge features result if there is hybridization between orbitals of suitable symmetry. For eg. in K-edge XANES, although the transition is from 1s→p state, there could be pre-edge features resulting from p-d mixing. For octahedral symmetry, no p-d mixing is allowed and only a weak pre-edge feature may be present from quadrupole transition. For tetrahedral symmetry, pre-edge feature has highest intensity. Distorted octahedral also result in pre-edge features. Therefore, pre-edge intensity is a qualitative mark of distortion from octahedral symmetry.

2.6 Strengths and Limitations of XAFS

Just like every other technique, XAFS has its own advantages and limitations. The main advantage is the "local" nature of XAFS information, making it possible to determine accurate structures for non-crystalline samples. Several important length scales in science, e.g. coherence length of charge carriers in high T_c superconductors, length scales of magnetic interactions, chemical interactions, interface binding, fall in the “local” structure regime. This local structure is at times significantly different from the average Long Range Order detected by conventional structural techniques like diffraction. Local structural information, for e.g. nanoscale phase separation, local structural inhomogenities, dopant induced disorder, can provide the key to understanding several material properties and novel phenomena like Metal-insulator transition, persistence of superconductivity beyond crystallographic transition, switching phenomena, luminescence stability, glass forming ability etc..[49,51,53-69]

In ideal circumstances, EXAFS data can be analyzed to determine the absorber-scatterer distance with an accuracy of at least ~ 0.02 Å. Coordination numbers can be determined with an accuracy of ~ 25% and scatterer identity can typically be defined to the nearest row of the periodic table.

XANES analysis provides oxidation state and spin-state information that can be difficult or sometimes even impossible to extract from crystallographic measurements. In comparison with other spectroscopic methods, XAFS has the decided advantage that it is always detectable, without the need for specific spin states or isotopic substitution, and that it is element specific.

There are, of course, some limitations of EXAFS. Firstly, it provides only limited chemical resolution - scattering atoms that differ by $\Delta Z \leq 5$ (e.g. C, O, N, and F) typically cannot be resolved. Secondly, the finite k range of the EXAFS spectrum limits the bond-length resolution of the method. Two scattering shells can only be resolved if they differ sufficiently in frequency to cause a detectable change in the EXAFS amplitude. Finally, it only gives the bond distances and not the actual coordinates of the neighboring atoms.

CHAPTER 3

EXPERIMENTAL APPARATUS FOR XAFS

Experimental apparatus for XAFS maybe sub-divided into the following sections: synchrotron source, beamline optics, detectors and sample holders.

3.1 Source

The XAFS signal is typically only 1% of the absorption coefficient, and is measured over an extended energy range over a wide range of atomic species. Therefore, x-ray source with continuous energy spectrum, high intensity and high resolution is required to override statistical noise and obtain good quality XAFS data (Signal-to-Noise ratio ~ 10^4). Any noise in the data can be misinterpreted as a sharp oscillation, which, when Fourier Transformed, gives rise to spurious peaks in R-space and interferes with the real structure. Laboratory X-ray sources are limited by poor counting statistics and resolution. Synchrotrons fulfill all of the above criteria, and hence are ideal sources for XAFS.

3.1.1 History of synchrotrons

A synchrotron is a machine that accelerates charged particles such as electrons in circular paths to extremely high energies (2-8 GeV), generating electron beam that travels at almost the speed of light. The circular motion is driven by strong magnetic field under Lorentz force ($F = e(E + v \times B)$, where *e* and v are the charge and velocity of the electron respectively; E and B are the electric and magnetic fields). Powerful electromagnets are used to focus and steer the beam inside ring-shaped vacuum chamber (~10^{-10} Torr vacuum) called “storage ring” and allows storage of the beam at high energy levels for many hours (Fig. 3.1).

Synchrotron radiation (SR) was first observed in Betatron in 1947, though its properties had been predicted much earlier. It was initially thought of as nuisance, sapping energy from circulating electron beams and upsetting calculations. Gradually physicists learned that the tangential fan of synchrotron radiation 'waste' from high energy electron rings could be used to probe the structure of a wide range of samples, and parasitic synchrotron radiation studies began to be carried out at machines built to supply electrons for particle physics studies. This represented the *first generation SR facilities.*

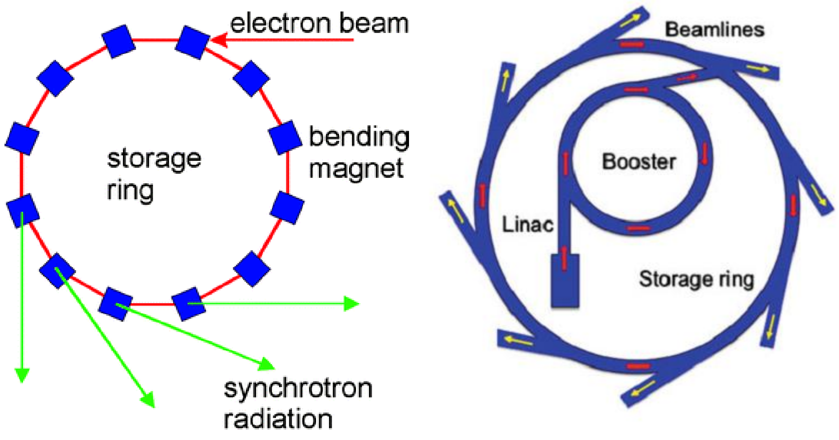

Fig. 3.1: Synchrotron radiation from Bending Magnet source

In the late-1970s, the world’s first dedicated Synchrotron Radiation Source was built at Daresbury in the UK, which started user experiments in 1981. This was followed up with the completion of the National Synchrotron Light Source (NSLS) at the Brookhaven National Laboratory, USA in 1981. During the same period, the Photon Factory was completed in 1982 at the KEK laboratory in Tsukuba, Japan, and the BESSY facility at Berlin, Germany, began serving users in 1982. These early-dedicated facilities, in which SR was mainly produced by bending magnets, are called *second generation sources*. Later, magnetic field devices called “insertion devices”, such as wigglers and undulators were placed in straight sections and made possible the realization of very low-divergence and very bright SR beam. This is the so-called *third generation source* [ESRF

(France), APS (USA) and SPRING-8 (Japan)] that has made new experiments (micro-imaging, XMCD, dilute environmental samples etc.) feasible. The comparison of flux for different generations of SR is shown in Fig. 3.2.

While improvements in third generation synchrotron radiation sources are still possible, *fourth generation sources* are being developed, based on free electron lasers (FELs) able to produce very short coherent light pulses of very high peak intensity and brightness.

The path of the electrons: Electrons are accelerated by a linear accelerator (linac) till their energy ~ MeV, and then by a booster ring that boosts their energy to ~GeV. At this point they are transferred to a storage ring. Storage rings consist of circular evacuated pipes where electrons are forced to follow a circular path under the action of bending magnets placed along the circumference (Fig. 3.1). Electrons traveling at a speed close to c, the speed of light, are forced to change the direction of their motion under the effect of magnetic fields (perpendicular to the direction of their motion) and emit SR.

Synchronization of electrons: The electrons are further accelerated to higher fields by Radio Frequency (RF) electric fields. After reaching the expected energy, the electrons are forced to follow circular paths by the magnetic fields of the bending magnets. At each turn they lose a part of their energy, emitting SR. The energy lost this way is regained while passing through the RF cavity (Frequency ~ 500 MHz). So, basically, it is the RF cavities which accelerate the particles.

The main advantage of synchrotron over cyclotron is that in a synchrotron, particles can be accelerated to much higher velocities. The upper bound on energy obtainable from the cyclotron is set by relativistic effects. Since the cyclotron frequency of the RF accelerating voltage depends upon the particle mass, the effects of relativistic mass cause the particle to get progressively more out of step with the accelerating voltage as its speed increases. In contrast, in synchrotrons, the frequency of the accelerating voltage is varied to track the relativistic effects.

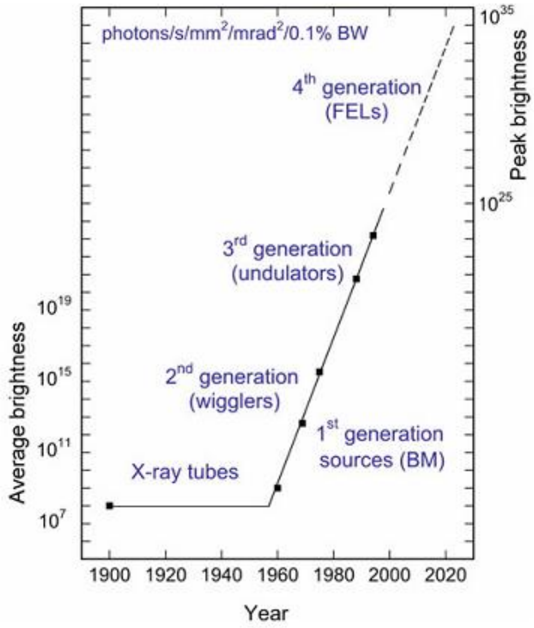

Fig. 3.2: Generations of synchrotron sources

3.1.2 Properties of synchrotron radiation from Bending Magnets (BM)

SR[70-71] emitted by electrons in particle accelerators is extremely intense and extends over a broad energy range from the infrared through the visible and ultraviolet, into the soft and hard x-ray regions of the electromagnetic spectrum (120 eV to 120 keV). Due to these and other characteristics, SR is used to study many aspects of the structure of matter at the atomic and molecular scale, from surface properties of solids to the structure of protein molecules.

The properties of SR making it the ideal source for XAFS experiments are:

1. *Wide spectral range*, including photon energies in the infrared (~10meV to 1eV), visible (~1eV to 10eV), ultraviolet (~10eV to 120eV), soft x-ray (120 eV to 10 keV) and hard x-ray (10 keV to 120 keV), facilitating a high degree of energy tunability.

2. *High intensity*, allowing rapid experiments even on weakly scattering samples.

3. *Collimation*- The emission of SR from bending magnets is confined to a narrow range of vertical angles, centered at the plane of the reference electron orbit (spatial coherence), making it easier to concentrate the intense photon beam into a small area of the specimen in the experimental chamber. This also leads to *high brilliance,* i.e. the flux per unit area per unit opening angle.

4. *Polarization*, which is linear for emission in the plane of the orbit and elliptical outside the plane. This is often used to resolve the structure of the sample into two directions – along the axis and perpendicular to the axis by simply orienting the sample axis along and perpendicular to the plane of polarization respectively. This is particularly useful for detection of anisotropic structural changes (e.g. Jahn Teller Distortion).

5. *Time structure*, which consists of short *pulses* (electron bunches) of femto-second width and separated by longer intervals (pico-second), allowing resolution of processes on the same time scale.

6. *High beam stability* (submicron level).

3.1.2.1 Storage ring operation and Power Spectrum of Synchrotron:

Storage rings consist of circular evacuated pipes where the electrons are forced to follow circular paths under the action of magnets placed along the circumference (bending magnets). The array of magnets, connected by straight linear sections, focuses and bends the beam. In one or more of these linear sections, RF cavities are installed in order to accelerate the particles.

The first step in the operation of a storage ring is the injection of new electrons into the ring (produced and pre-accelerated by the injection system). There are two possible ways to do this: (i) Top-up mode – The injector brings the electrons to energy equal to the final desired energy for circulation in the storage ring. (ii) Bunch mode – The electrons are pre-accelerated to energy lower than the final desired energy. The electrons are stacked in the ring and then accelerated to their final energy by the combined action of the RF cavity and the magnetic lattice.

The electrons pre-accelerated by the injection system are brought into the vacuum chamber of the storage ring by an injection line equipped with a suitable magnet system. Once inside the storage ring, bending magnets keep the electrons moving in a closed trajectory applying a magnetic field perpendicular to their velocity.[72] The acceleration of such particles is given by the Lorentz equation:

$$\frac{dp}{dt} = e(E + \frac{v \times B}{c}) , \tag{3.1}$$

where p, *e* and v are respectively the particle momentum, charge and velocity of the electron; E and B are the electric and magnetic fields.

The *power radiated*[73] by a relativistic electron forced to move along a circular orbit, with a radius of curvature, R, is given by Schwinger's formula[72]:

$$P_e = \int P(\lambda, \psi) d\lambda d\psi = \frac{2}{3} \frac{e^2 c}{R^2} \left[\frac{E}{mc^2} \right]^4 , \tag{3.2}$$

where λ is the wavelength of the emitted radiation, ψ is the azimuthal or vertical half-opening angle perpendicular to the orbital plane. $P(\lambda,\psi)$ is the power radiated by an electron in a unit wavelength interval centered at λ and in a unit vertical angular aperture centered at ψ. E is the electron energy, m its mass, c is the speed of light. mc^2 is the electron rest mass energy. E^4 dependence implies that to increase the energy of the storage ring, it is necessary to increase their radius, so that the radiated power is kept at reasonable values. Further, due to the dependence on m^{-4}, the radiation produced by proton accelerators is negligible.

The energy lost per turn by the charged particle, taking into account a revolution time of $2\pi R/c$, is given by:

$$\Delta E_e = \frac{4\pi}{3}\frac{e^2}{R}\left[\frac{E}{mc^2}\right]^4 \tag{3.3}$$

To compensate for the energy loss and keep the electrons at a constant energy, RF cavities are used. In a RF cavity, a longitudinal electric field accelerates the electrons. RF fields have an accelerating effect during one half of their period and a decelerating action during the other half; so effectively the RF restores the electron energy only for one half of the time. Additional considerations have to be performed, regarding the stability of the electron orbit. Let us suppose that at the time t_0 an electron passing through the RF finds exactly the electric field needed to fully restore the energy lost during a turn. This electron is called a “synchronous” electron (Fig. 3.3).

Synchronous electrons continue their motion along the ring returning in the RF again in time to regain the exact amount of energy lost along the circular path. So, the synchronous electrons are in a stable condition. Let us now consider electrons arriving in the RF slightly later than the synchronous electrons. They are slower than the first ones, i.e. they have lower energy. In order to restore the energy, they have to find an electric field higher than that found by the synchronous electrons; otherwise they will continue to lose energy with respect to them. In the next turn they will arrive later, and after some turns they will enter the RF during the decelerating semi-period and will be lost. Similarly, electrons arriving before the synchronous ones must find a lower electric field, otherwise their energy will increase with respect to the synchronous electrons. These considerations show that only one half of the accelerating semi-period (i.e. one fourth of the period) is effective in maintaining the electrons on the orbit (Fig. 3.3). Actually, the stability condition is much more stringent – only 5–10 % of the RF period is effective in restoring the electron energy. Those electrons which pass through the RF out-of-phase with this effective time deviate from the ideal circular orbit of the ring, and are therefore lost. As a consequence, the electrons in the storage ring are grouped in *bunches* with time lengths that are typically 5–10 % of the RF period. Additionally, the radiation appears in pulses with the same time duration and separation (Fig. 3.4).

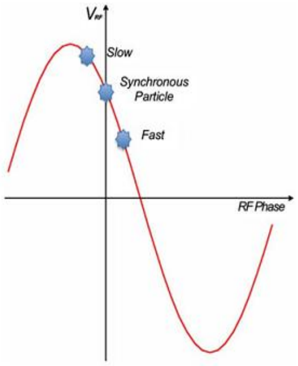

Fig. 3.3: Time dependence of voltage of RF cavity

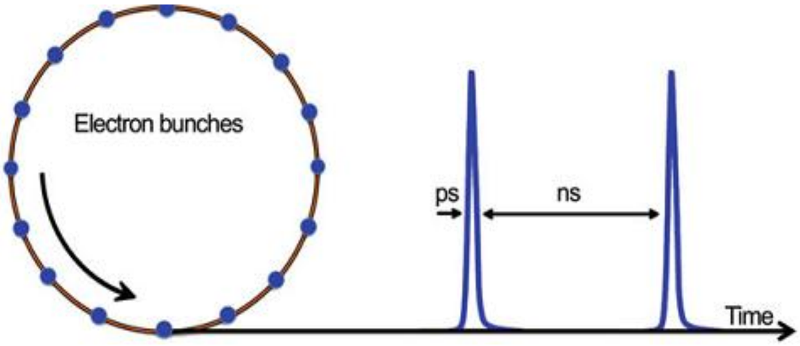

Fig. 3.4: Electron bunches moving in the storage ring produce radiation peaks having the same bunch length (ps) and separation (ns)

Multiple bunches can be distributed along the storage ring. The time interval between them is an integer multiple of the RF period (called *harmonic number* of the ring). The maximum separation between two pulses is obtained in the single bunch mode, i.e. when only one bunch in the full ring is present. In this case the time interval is equal to the period of revolution, typically of the order of microseconds. When more bunches are present the time interval is lower; the minimum possible time interval between bunches is equal to the RF period. The filling of bunches in a machine is a parameter that can be completely controlled; it is possible to choose how many and which bunches to have in the ring. This flexibility is often used to relate different time dependence characteristics to the photon source. The total current depends on the number of filled bunches. The current is lower when few bunches are filled, because the total amount of current that can be stored in a single bunch is limited.

3.1.2.2 Angular, spectral and intensity distribution of synchrotron

For a classical electron moving at a speed, $v \ll c$, the emitted radiation pattern is similar to that of an oscillating dipole with its maximum of intensity in the direction perpendicular to the acceleration and is independent of v. However, for $v \approx c$, the radiation pattern gets compressed into a narrow cone in the direction of motion, resulting in an emission tangential to the particle orbit. The vertical half-opening angle, ψ, is given by:

$$\psi = \frac{mc^2}{E} = \gamma^{-1} = 1957E \text{ (For an electron)} \tag{3.4}$$

This implies that for a storage ring of energy E=2.5GeV, ψ=0.204mrad = 0.012°, i.e. synchrotron radiation is highly collimated. In a bending magnet the horizontal collimation is lost because the electrons move along a circular orbit emitting the radiation along the tangent. The radiation is collected, for experiments, through a horizontal slit (S) of width, w, at a distance, D, from the electron orbit (see Fig. 3.5); this corresponds to an angular collection angle, $\Delta\theta = w/D \gg \psi$. This means that the natural narrow collimation, ψ, is preserved only in the direction perpendicular to the plane of the orbit (Fig.3.5). Using undulators results in collimation in both directions.

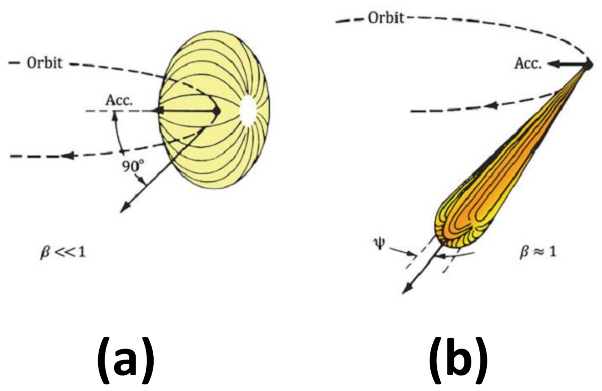

Fig. 3.5 Radiation pattern for electron in circular orbit when (a) v<<c and (b) v~c

The spectral distribution of the bending magnet SR flux, is a continuous function (x-ray to infra-red) (see Fig. 3.6) and is characterized by a critical wavelength, λ_c, which divides the power spectrum (of the emitted radiation) into two equal parts, i.e. half the total emitted power is due to photons with energy greater than λ_c and half is emitted by photons with frequency below λ_c.

$$\lambda_c = \frac{4\pi\rho}{3\left(\frac{E}{m_0c^2}\right)^3}. \tag{3.5}$$

The corresponding critical energy,

$$E_c = \frac{3\hbar c}{2\rho}\left(\frac{E}{m_0c^2}\right)^3 \tag{3.6}$$

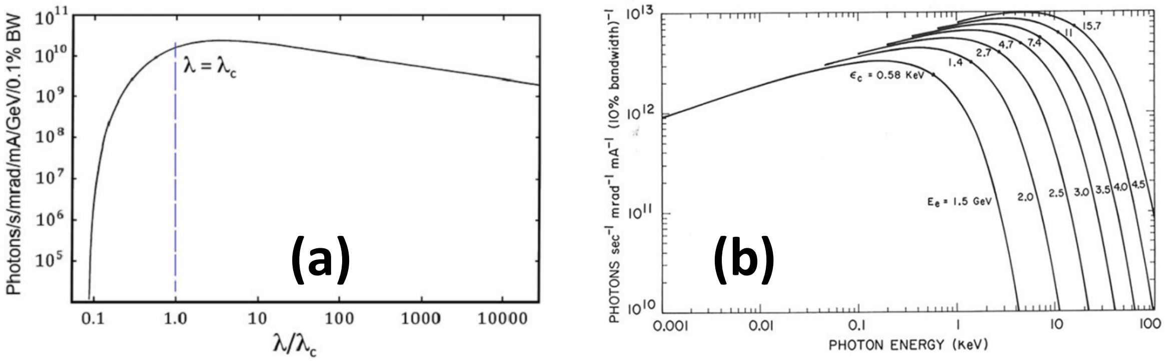

Fig. 3.6: Spectral flux vs (a) wavelength and (b) photon energy of synchrotron.

3.1.2.3 Polarization

The radiation emitted by a bending magnet is mostly linearly polarized. When observed in the horizontal plane, the electric field is parallel to the plane of the electron orbit (horizontal). Observing the radiation above and below this plane at finite vertical angles, a polarization component perpendicular to the plane of the electron orbit is present.

3.1.2.4 Spectral Brightness and Emittance

Spectral Brightness is defined as the number of photons emitted per second, in a spectral bandwidth $\Delta E/E = 0.1\%$ in a unit source area and per unit of solid angle. Brightness is preserved by focusing, such that brightness of the source is equal to the brightness of focused beam on the sample. The brightness is determined by the size of the source, which is given by the convolution of the angular distribution of synchrotron radiation, $\Delta\psi$, with the angular divergence of the electron beam. Therefore brightness of the photon source is determined by the characteristics of the electron beam source.

Table 3.1 Comparison of Indus-2 Source parameters with popular sources across the world

	Indus 2	Elettra	ESRF	APS	Petra III	Spring 8
Energy (GeV)	2.5	2	6	7	6	8
Current (mA)	300	300	200	100	100	100
Critical wavelength	1.986Å	3.872Å	1.29Å (3.5 mrad opening angle) and 0.604Å (10.5 mrad opening angle)	0.635Å	0.592Å	0.429Å

In a storage ring the product of the electron beam transverse size and angular divergence is a constant along the ring and is called *emittance*. Emittance is measured both in horizontal and vertical directions, and the vertical emittance is normally a few percent of the horizontal one. Machines with smaller emittance have higher brightness.

3.1.5 Insertion Devices

Insertion devices (ID) are periodic magnetic structures installed in the straight sections of a storage ring. Passing through such structures, electrons are accelerated perpendicularly to the direction of their motion and therefore emit SR (Fig. 3.7). The primary effects of IDs are (i) the shift of the critical energy to higher values due to the smaller bending radius with respect to the bending magnets, (ii) the increase of the intensity of the radiation by a factor related to the number of wiggles induced by the many poles of the magnetic structure, (iii) increase in spectral brilliance with respect to that achievable with bending magnets. IDs are of two kinds, wigglers and undulators. The electron beam is periodically deflected only *inside* both these devices.

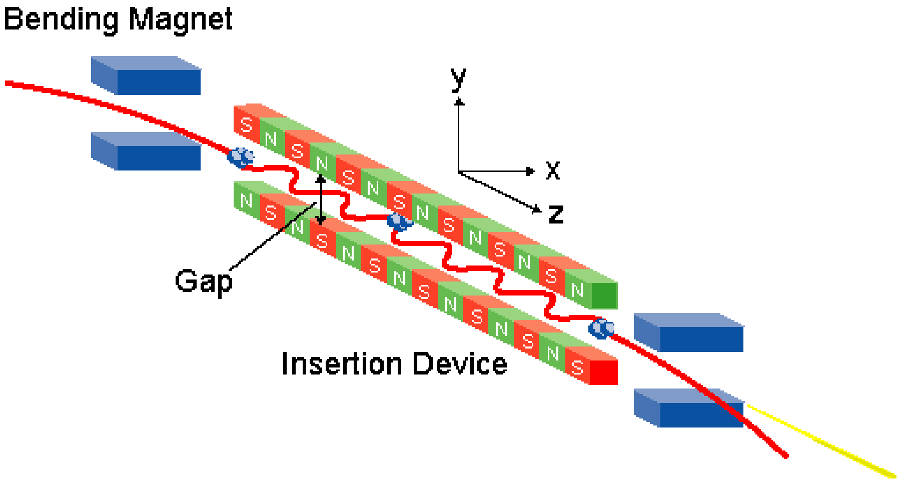

Fig. 3.7: Schematic of insertion devices

.

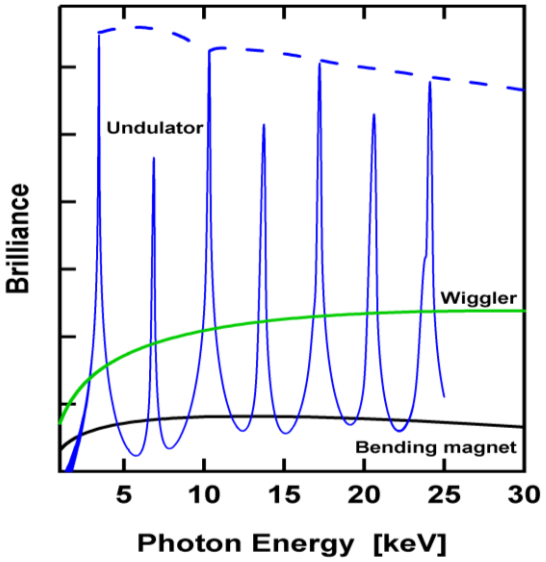

Fig. 3.8: Comparison of spectra from Bending Magnet, Undulator and Wiggler.

(a) **Wigglers**: Wigglers produce a spectrum similar to that of bending magnet radiation. A wiggler or a ‘wavelength shifter’, is a multi pole magnet comprising of a periodic series of magnets (N periods of length λ_u, the overall length being $L = N\lambda_u$), whose magnetic field forces the electrons to wiggle around their otherwise straight trajectory. The alternating magnetic field is applied in the vertical direction so that the sinusoidal trajectory of the electron beam lies in the horizontal plane. This causes the electrons to follow a curved trajectory with a smaller local radius of curvature with respect to the one of the dipole-bending magnet, because in a wiggler magnetic fields higher than those in bending magnet can be used. The use of higher magnetic fields increases the critical energy with respect to the values achievable with bending magnets and extends the spectral range of a storage ring towards higher energies.

The radiation observed is the incoherent sum of the radiation emitted by each individual pole. Therefore the overall characteristics of the beam are the same as those of a bending magnet with the same magnetic field but with an intensity enhanced by the factor N, the number of poles.

The basic parameter used to distinguish between wiggler from undulator is a dimensionless parameter, called the deflection parameter, which is the ratio of the wiggling angle of the trajectory, α, to the natural angular aperture of SR, γ^{-1} .

$$K = \alpha\gamma . \tag{3.7}$$

This K parameter measures the angular (horizontal) deflection of the beam from its original straight path in the magnet array. For an electron moving in a sinusoidal magnetic field,

$$K = \frac{e}{2\pi mc}\lambda_u B . \tag{3.8}$$

In a wiggler the transverse oscillations of the electrons are very large and the angular deviations, α, much wider than the natural opening angle $\psi = \gamma^{-1}$, therefore K >> 1. In these large K devices, the interference effects between the emissions from the different poles can be neglected and the overall intensity is obtained by summing the contribution of the individual poles.

(b) **Undulators**: An undulator consists of a periodic structure of dipole magnets. Electrons traversing the periodic structure are forced to undergo oscillation, thus emitting radiation.

Undulators are very similar to wigglers, but their K < 1, i.e., the wiggling angle, $\alpha \leq \gamma^{-1}$. The interference occurs between the radiation emitted by electrons at different points along the trajectory. Considering the phase differences between the photons emitted at different points along the sinusoidal orbit, if one observes the radiation in a direction forming an angle θ with the axis of the undulator, constructive interference occurs at the wavelength

$$\lambda = \frac{\lambda_u}{2\gamma^2}\left(1 + \frac{K^2}{2} + \gamma^2\theta^2\right) \tag{3.9}$$

In addition to the fundamental wavelength, higher harmonics of shorter wavelength are also emitted. Their number and intensity increases with K; on the axis (θ = 0) only odd harmonics are emitted. K^2 dependence allows for variation of the energy of photon emission.

In an undulator, the amplitudes of the fields radiated by each individual period (N) of the undulator add up coherently, so the intensity increases with N^2 while it increases only as 2N in a wiggler. Each harmonic has a limited wavelength bandwidth approximately given by:

$$\Delta\lambda/\lambda = 1/nN \cdot \tag{3.10}$$

Therefore the bandwidth decreases with the number, N, of periods of the undulator and with the harmonic number, n.

The angular distribution, of the n^th^ harmonic is concentrated in a narrow cone in both the horizontal and vertical directions whose half width is given by:

$$\sigma^2 = \sqrt{\frac{3}{4\pi}(1+\frac{K^2/2}{\gamma^2 nN})} = \frac{1}{\gamma\sqrt{nN}} \tag{3.11}$$

Hence it is always smaller than the natural emission angle of bending magnet. This very narrow angular distribution together with the N^2 dependence of the intensity radiated in the ‘undulator’ regime explain why the spectral brightness achievable with undulators exceeds by several order of magnitude that of bending magnets and of wigglers.

At present, undulators are in operation at several synchrotron facilities including APS (USA), Petra III (Germany), ESRF (France), Spring 8 (Japan), BESSY (Germany). Currently, undulator has also been installed at Indus-2 (India).

3.1.6 Free Electron Lasers (FELs)

FELs represent the next generation of light sources. FELs produce extremely high brightness, transversely coherent radiation by inducing a bunch-density modulation of the electron beam at the optical wavelength. This is achieved by the interaction of a bright electron beam with an intense optical field in the spatially periodic magnetic field of an undulator.

Electron beam from an undulator is incoherent, because the electromagnetic waves from randomly distributed electrons interfere constructively and destructively in time, and the resulting radiation power scales linearly with the number of electrons. An external laser causes interaction of the transverse electric field of the radiation beam with the transverse electron current created by the sinusoidal wiggling motion, causing some electrons to gain and others to lose energy to the optical field. This energy modulation evolves into electron density (current) modulations with a period of one optical wavelength. The electrons are thus clumped, called *micro-bunches*, separated by one optical wavelength along the axis. The radiation emitted by the bunched electrons are in phase and hence coherent. The FEL radiation intensity grows, causing additional micro-bunching of the electrons, which continue to radiate in phase with each other. This process continues until the electrons are completely micro-bunched and the radiation reaches a saturated power several orders of magnitude higher than that of the undulator radiation.

The wavelength of the emitted radiation, λ_{FEL}, is given by

$$\lambda_{FEL} = \frac{\lambda_u}{2\gamma^2}(1+K^2) \tag{3.12}$$

3.2 Beamline Optics

3.2.1 Energy selection from the beam

As mentioned earlier, XAFS data are recorded as a function of energy. To extract each energy point, white beam from the source needs to be filtered out to the desired energy/energy band. This is achieved with the help of monochromator /polychromator (Fig. 3.9 (a-b)).

The working principle for both the monochromator and the polychromator is Bragg's law, which states that a lattice plane will diffract x-ray only of a particular wavelength (λ) [or its higher harmonics, n] at a particular angle (θ). If d is the lattice spacing,

$$2d\sin\theta = n\lambda \qquad (3.13)$$

The desired wavelength (energy) of incident x-ray is obtained by tuning θ.

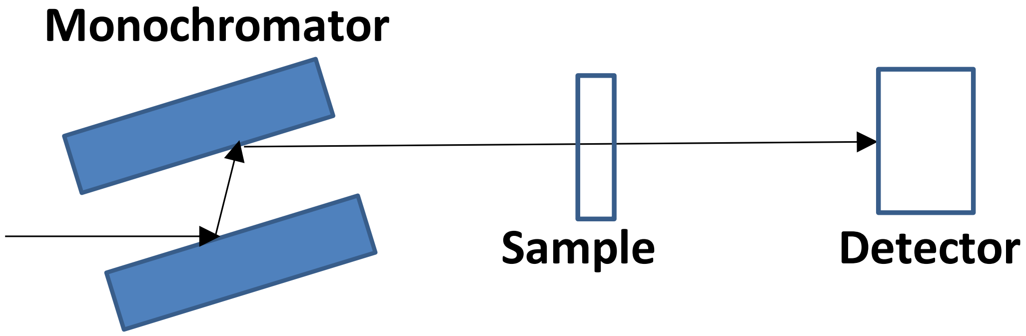

Fig. 3.9 (a) Schematic of XAFS experiment using monochromator

Typically, a monochromator consists of a pair of crystals, usually Si or Ge, cut at (111), (220) or (311) planes, in parallel arrangement. The first crystal diffracts the x-ray with a certain wavelength towards the second crystal. The second crystal further reflects the beam into the experimental station. The primary requirement for a monochromator is rapid tunability, since the monochromator has to be scanned to vary the x-ray photon energy. Besides, the energy resolution should be comparable to lifetime broadening of the absorption edges of interest.

One common drawback associated with monochromators is the origin of "glitches". When the rotation of the monochromator leads to additional oblique lattice planes coming into the reflecting position for the same wavelength as the main lattice planes, a spill into the intensity in the main channel takes place, with several complex geometry-determined effects on the measured signal. These can usually be eliminated during data processing.

Alternatively, a bent crystal polychromator can be used to focus a broad bandwidth beam onto the sample (Fig. 3.9(b)). A position sensitive detector behind the sample then receives x-rays whose position is then correlated with their energy. In that case, the x-ray absorption spectrum can be recorded in a short time, without any scanning required. When a polychromator is used, the geometry is such that it forms an arc of the ellipse in which the source and the sample form the two foci.

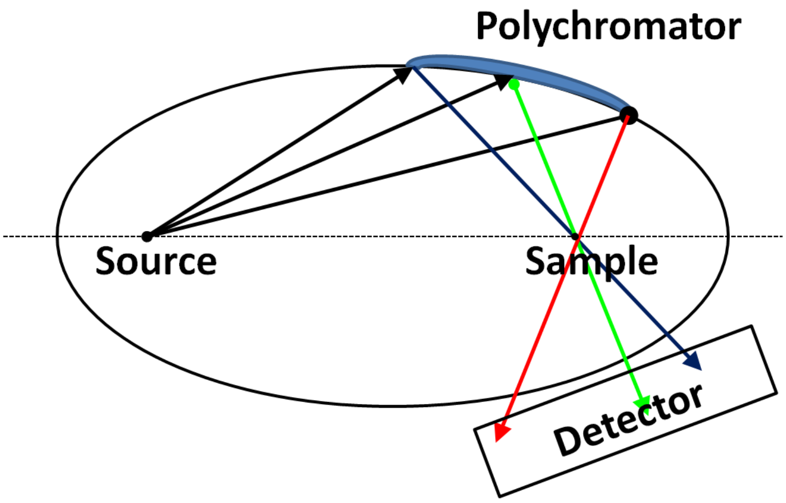

Fig. 3.9 (b) Schematic of XAFS experiment using polychromator

The material for the monochromator/polychromator crystal should have the following properties: (i) It should not have absorption edges in the energy range of interest. (ii) It should have low coefficient of thermal expansion so that it gives stable output energy. (iii) It should have good thermal conductivity to minimize thermal gradients underhigh thermal and radiation loads. For this reason, monochromators are generally kept cooled by liquid nitrogen. (iv) It should have long lifetime.

3.2.2 Higher harmonic rejection from the beam

The beam from the monochromator contains higher harmonics of the desired fundamental energy. For the most commonly used Si (111) crystal, the second order reflection is forbidden so that the most intense high order harmonic is the (333) reflection at three times the energy. These harmonics can seriously distort the XAFS amplitude, if not removed. An illustration of the same is shown in Fig. 3.10 for Ga K edge of Ga foil obtained using Si (111) monochromator.[74] Fig. 3.10a is the absorption spectrum measured at one third the energy of the K-edge ($\frac{10.368}{3} = 3.458 eV$), due to the third order harmonic contamination. Fig. 3.10b is the "true" absorption spectrum.

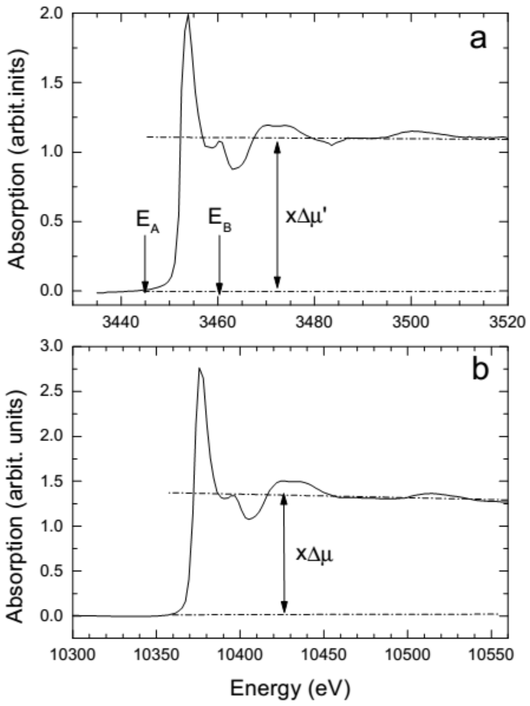

Fig. 3.10: Absorption spectrum of Ga foil at Ga K edge (10.368 keV) obtained with the Si(111) monochromator (a) set within one third the energy region of Ga K-edge. This is clearly due to third harmonic contamination, (b) true absorption spectrum.[76]

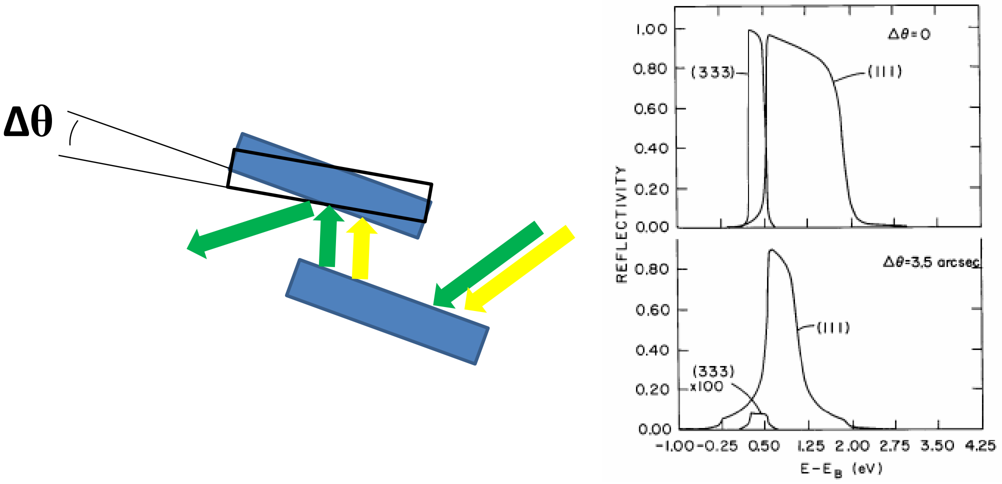

Fig. 3.11: Detuning of monochromator to eliminate higher energy harmonics[76]

One way to eliminate the high energy harmonics in practice is to adjust the pair of crystals in such a way that these two crystals are slightly off from parallel alignment. The harmonics passed by the first crystal are then outside the rocking curve of the second crystal and are hence prevented from being reflected. This process is called detuning (Fig. 3.11).

Alternately, higher harmonic rejection is performed using a ‘harmonic rejection mirror’. The refractive index of a material,

$$n = 1 - \delta - i\beta \ , \tag{3.14}$$

where δ and β are proportional to the electron density and the linear absorption coefficient of the material respectively. The absorption in a material is accounted for by the negative part of the refractive index. Since the refractive index in the x-ray regime is less than one, total external reflection occurs for angle of incidence less than the critical angle. For a particular energy, the critical angle (Fig. 3.12)

$$\theta_c \approx \sqrt{\rho\hbar} / E \tag{3.15}$$

Therefore, beam will be reflected only for angles $\theta < \theta_c$, and there will be a sharp drop in intensity for $\theta > \theta_c$. Since $\theta_c \propto 1/E$, θ_c for the first harmonic is much higher than that for higher harmonics. Thus by placing the mirror at angle $(\theta_c)_{\text{higher harmonic}} < \theta < (\theta_c)_{\text{first harmonic}}$, higher harmonics can be avoided in the beam.

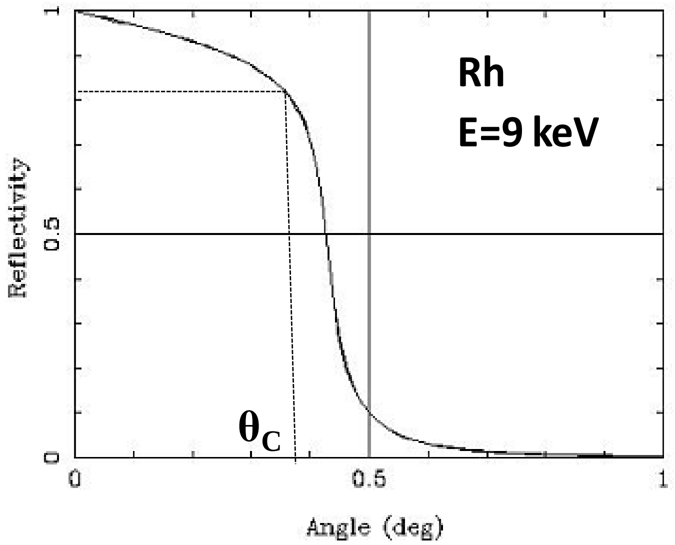

Fig. 3.12: Reflectivity of Rh as function of angle[76]

3.2.3 Experimental Geometry for XAFS

Two geometries are widely used for XAFS experiments: transmission and fluorescence. In a transmission experiment (Fig. 3.13 (a)), the absorption is directly measured by the attenuation of the x-ray as it passes through the sample. The absorption is then obtained from the equation

$$\mu(E) = \ln \frac{I_0}{I_t}, \tag{3.16}$$

where I_0 and I_t are the intensities of the beam before and after the sample respectively. Fluorescence mode (Fig. 3.13(b)) measures the absorption indirectly through the fluorescence photons emitted from the excited atom, such that the absorption is given by

$$\mu(E) = \frac{I_f}{I_0}, \tag{3.17}$$

where I_f is the fluorescence intensity from the sample. In this mode, the sample and the fluorescence detector are aligned at 45° and 90° respectively *wrt* the beam. This geometry minimizes the background from the elastically scattered photons. The two modes are compared in Table 3.2. The choice of mode of XAFS measurement is determined by the sample in question and the energy edges to be measured.

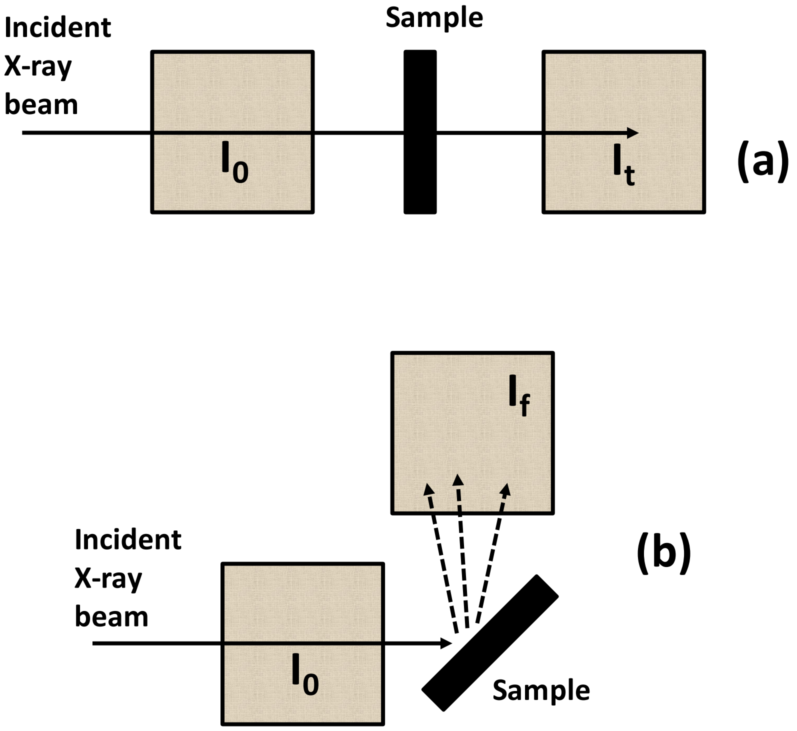

Fig. 3.13: Experimental geometry for (a) Transmission mode and (b) Fluorescence mode XAFS

Table 3.2 Choice of experimental geometry for XAFS

	Transmission	Fluorescence
Sample requirements	Uniform and concentrated samples	Dilute samples, Thin films
Energy range	No limitations	Low fluorescence yield for Z<30. Therefore possible energy range E > 2keV
Information obtained	Bulk	Surface or bulk depending on the angle of incidence of beam on the sample.

3.2.4 Detectors

The most important factors to be considered while selecting a detector for XAFS measurements are count rate, energy resolution, linearity and noise. Different detectors are used for measuring transmitted and fluorescence intensities. Two detectors were mainly used for transmission mode XAFS measurements reported in this thesis – ionization chamber and Charge Coupled Device (CCD). These are described in detail below. Additionally, fluorescence detectors, viz. Lytle detector and Solid State Detector are also described.

3.2.4.1 Ionization Chambers

The ionization chamber is a gas-filled radiation detector, widely used for x-ray detection. It measures the charge from the number of ion pairs created within a gas caused by incident radiation. It consists of a gas-filled chamber with two parallel conducting plates. A voltage potential is applied between the plates to create an electric field in the fill gas. When this gas is ionized by the incident radiation, ion-pairs are created which move towards oppositely charged plates under the influence of the electric field. This generates an ionization current which is measured by an electrometer circuit. Each ion pair created deposits or removes a small electric charge to or from a plate, such that the accumulated charge is proportional to the number of ion pairs created, and hence the radiation dose. This continual generation of charge produces an ionization current, which is a measure of the total ionizing dose entering the chamber.

The incident intensity monitor in front of the sample is optimized for absorption of around 20% of the incident flux so that the major fraction of the beam falls on the sample, while the post sample detector should absorb 80-90% of the transmitted beam or the fluorescence photons from the sample for good statistics. The absorbing gas is selected based on the energy of the x-rays to be detected. At lower edges, I_0 chamber usually contains 80% He and 20% N_2 gas while at higher edges, 100% N_2 gas is used. The post-sample detectors are usually filled with heavier gases like N_2, Ar or Kr.

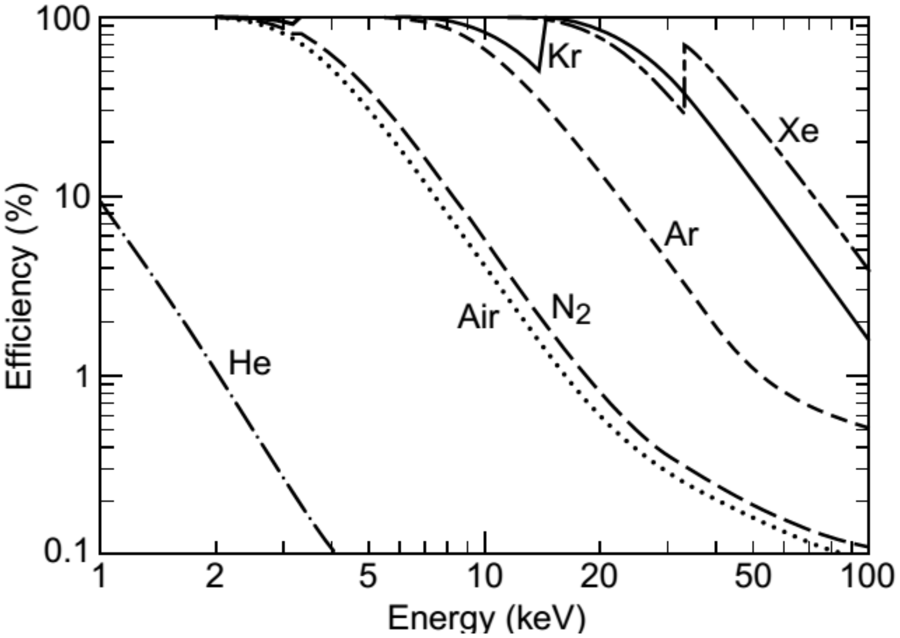

Fig. 3.14: Efficiency of an ionization chamber as a function of energy for different gases at normal pressure.[76]

Calculation of a suitable choice of fill gases is usually straightforward. The probability of a photon of energy E being absorbed by the fill gas is $1-\exp(-\mu_{fg}(E)l)$, where l is the length of the electrode along the direction of beam travel, and $\mu_{\mathrm{fg}}(E)$ is the energy dependent fill gas absorption coefficient in the chamber. This can be calculated from the cross section values available at http://csrri.iit.edu/mucal.html. Fig. 3.14 shows the efficiency of an ionization chamber (10 cm length) for different fill gases as a function of energy.

3.2.4.2 Charge Coupled Device (CCD) detector

CCD is a position sensitive detector commonly used for transmission XAFS measurements.

An X-ray photon entering the CCD, it is captured by photoelectric absorption, thereby generating a primary charge cloud in which the number of electrons is proportional to the incident X-ray energy. The primary charge cloud expands through diffusion as it travels through the depletion region of the CCD to the buried channel, where the charge is collected into pixel structures defined by electric fields near the surface of the CCD. The incident X-ray energy is estimated by summing up the signal contained inside the event.

The CCD used for XAFS measurements in this thesis has an area of 25 x 25 mm^2 area with 2048 x 2048 pixels, each of 13.5mm x 13.5mm size. A strip of a material, known as phosphor or scintillator, coupled to the CCD by means of a fibre-optic taper [Phosphor is deposited onto one end of the taper and the CCD sensor is coupled to the other end] is used to convert the x-ray photons into visible photons, which are then detected by the CCD. This phosphor absorbs x-ray photons and emits visible photons predominately at 545nm (2.28eV), with approximately 15% conversion efficiency, i.e. 15% of the absorbed x-ray photon energy is converted into visible photons.

The CCD detector is cooled to -40°C, which results in a very low dark count (without the synchrotron beam), approximately a few counts per pixel. A vertical column of few hundred pixels is binned at each horizontal pixel to capture the full vertical beam and hence total dark count at each horizontal pixel is approximately a few hundred counts. This integrated count goes up to $\sim 10^6$ with the synchrotron beam on, which enables a reasonably good signal to noise ratio. It may be mentioned that in a dispersive setup, the band width covered by the CCD and hence the energy per pixel value depends on the particular settings of the bent crystal, sample and detector, which are again defined by the photon energy range of interest. The energy resolution of the beamline at a particular energy can also be improved by restricting the band width by moving the detector away from the sample.

3.2.4.3 Lytle Detector

Fluorescence XAFS experiments requires detectors of large area, or atleast large solid angle, for which transmission ionization chambers are not optimal. By modifying the geometry of the transmission ionization chamber, so that the x-rays pass through one or more of the electrodes and are absorbed by the fill gas, Stern and Heald developed a detector for fluorescence XAFS measurements.[75] The through-plate geometry, combined with use of suitable filters and slits, permits collection of photons over a large area and the rejection of elastically scattered background from the sample. The electrodes can be made of any electrically conductive but X-ray transparent material, such as tightly stretched aluminized mylar, Ni mesh, or electrically conductive polymers. It is very important that the electrodes be mechanically stable, otherwise vibrations and sound waves can introduce excessive noise. Detectors of this type, known as "Lytle Detectors", with 3 or 5 electrodes of alternating polarity (to increase the sensitive volume of fill gas) are available on many beamlines.[76]

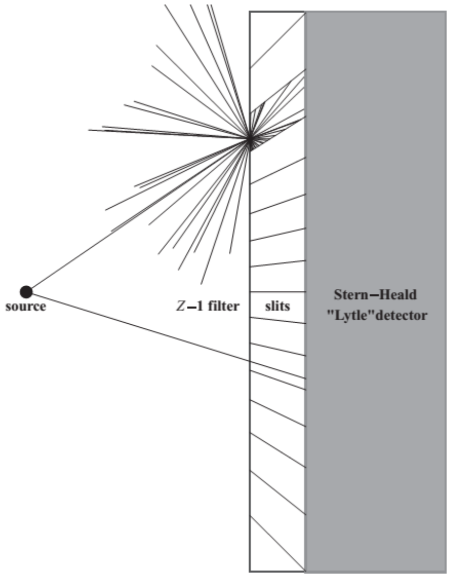

Fig. 3.15: Concept of usage of Lytle detectosr. $Z-1$ filters preferentially absorb elastic scatter above the filter's absorption edge. The slits transmit the sample fluorescence, but block most of the filter re-fluorescence.[76]

In most cases the effective use of such detectors requires the use of "$Z - 1$" filters and slits to reject elastically scattered background, i.e. scattered x-rays that are at the energy of the incident beam. The concept of such filters is illustrated in Fig. 3.15. The X-ray filters usually are composed of a thin support with a uniform coating consisting mostly of the element one atomic number lower than that of the element of interest in the sample. This places the absorption edge of the filter between the $K\alpha$ fluorescence peak and the absorption edge of the element of interest, resulting in low absorption by the filter of the fluorescence, but high absorption for the elastically scattered background, which is at the energy of the incident beam.

Table 3.3: Summary of Detectors

Detector	**Energy Range (keV)**	**Resolution (ΔE/E)**	**Applications**
Ionization chamber	0.2-50	n/a	Transmission
CCD	1-70	n/a	Transmission
Solid state detector	1-10,000	150 eV at 5.9 keV	Fluorescence
Lytle detector	0.2-50	n/a	Fluorescence of very dilute samples

3.2.4.4 Solid State detector

Si and Ge detectors can make excellent energy-resolving detectors of single photons (about 150 eV at 5.9 keV). These are large, reverse-biased n^+–i–p^+ diodes. When a photon interacts in the intrinsic region, tracks of electron-hole pairs are produced (analogous to electron– positive ion pairs in a counting gas). These pairs separate in the presence of electric field and rapidly drift to the detector contacts. The average energy required to generate an electron-hole pair is 3.6 eV for Si and 2.98 eV for Ge. To keep the leakage current low, the detector must have very few electrically active impurities. For example, Ge detectors are made from zone-refined crystals that have fewer than 10^{10}

electrically active impurities/cm^3. They are usually cooled to reduce the thermal leakage current. The count rate capability with an energy resolution of <200 eV is limited to about 2 × 10^5 per second. To handle the high counting rates available at synchrotrons, multielement arrays of 4–30 elements have been developed for fluorescence EXAFS experiments.[77]

3.3 Sample preparation for XAFS

As mentioned earlier, XAFS measurements can be performed on several different types of samples, viz. powder, liquid, metal foil, thin film. XAFS data quality is also very much dependent on the quality and uniformity of the samples.

Sample requirements for XAFS experiments are dependent on the mode in which the experiment is to be carried out – transmission mode or fluorescence mode.

For transmission XAFS experiments, the concentration of the element of interest in the sample should be one weight % or more. A thin, uniformly thick sample, free of pin holes is a requirement for production of high quality absorption signal.

For a uniform, homogeneous sample of thickness t,

$$\frac{I}{I_0} = \exp(-\mu(E)t)\,. \tag{3.18}$$

$\mu(E)$, the linear absorption coefficient, decreases as $1/E^3$ between absorption edges. Now the absorption length ($1/\mu$) is the distance over which x-ray intensity decreases by a factor of 1/E (~37%). It determines the basic length scale for selection of sample thickness, particle size, and sample homogeneity. For a single substance,

$$\mu(cm^{-1}) = \rho(g/cm^3) \times \sigma(cm^2/g)\,, \tag{3.19}$$

where ρ and σ are the density and absorption cross section of the material respectively. σ

values can be obtained from Ref.78-79. For compounds, the absorption coefficient is approximately given by

$$\mu \approx \sum \rho_i \sigma_i = \rho_M \sum \frac{m_i}{M} \sigma_i = \rho_N \sum \frac{n_i}{N} \sigma_i , \tag{3.20}$$

where ρ_M is the mass density of the material as a whole, ρ_N is the number density of the material as a whole, and m_i/M and n_i/N are the mass fraction and number fraction of element *i*.

The thickness should be optimized such that the partial absorption due to the absorber atoms is approximately one absorption length ($\Delta\mu x = 1$) and the total absorption from all atoms in the sample is less than 2.5 absorption lengths ($\mu x = 2.5$). Amount of sample required is calculated using the following equation:

$$w = \frac{2.5}{\sum \left(\frac{\mu}{\rho}\right)_i \times w_i} , \tag{3.21}$$

where w_i is the weight of element *i* in the sample.

The calculated sample is weighed out and sieved using a mesh. It is then ground to fine powder using a mortar and pestle. The ground powder is placed in a non-reactive liquid (e.g. isopropyl alcohol) and allowed to stand for several hours. Once the large particles settle down, the supernatant liquid is decanted into a petridish and left undisturbed for a prolonged period of time. The liquid eventually evaporates, leaving uniformly sized fine (5 µm) particles behind. The particle size is checked with microscope. These particles are brushed onto scotch tape. The tape can be folded to 4-6 folds to minimize the effect of holes on the XAFS spectrum of the sample.

An alternate method is to press the fine particles obtained via evaporation of the decanted liquid into pellets. For this the particles are mixed with light, non-reactive, non-absorbing material like cellulose, boron nitride, etc. The absorption length is then recalculated by considering the amount of filler.

3.4 Sample holders for XAFS

Different types of samples require different sample holders. Additionally, specific conditions like low temperatures, high pressures, high temperatures etc. require special sample holders.

3.4.1 Powder samples: Powder samples are commonly brushed onto scotch tape or pressed into a pellet. The tape/pellet is mounted onto a sample holder. The most common type of sample holder is a simple Aluminium plate with a slot in the centre for mounting samples prepared as pellets or tapes (Fig. 3.16(a)). These can also be used for studying thin film samples in fluorescence mode. However, for more complicated experimental conditions (and for more complicated samples), different sample holders are used.

3.4.1.1 Low temperature: For XAFS experiments at lower temperatures, cryostat sample holder is used. Typically, a Cu sample holder with multiple slots for samples is mounted onto a cryostat (open or closed cycle, depending on the availability of supply Helium at the beamline). The cryostat is then pumped down to lower temperatures. This type of sample holder is described in detail in chapter 5.

3.4.1.2 High Pressure: XAFS experiments at high pressures are performed using a diamond anvil cell (DAC). A DAC consists of two opposing diamonds with a sample compressed between the culets (tips). Pressure is monitored using a reference material whose behavior under pressure is known. Common pressure standards include ruby[80] fluorescence, and various structurally simple metals, such as copper, gold or platinum.[81] The uniaxial pressure supplied by the DAC is transformed into uniform hydrostatic pressure using a pressure transmitting medium, such as argon, xenon, hydrogen, helium, paraffin oil or a mixture of methanol and ethanol.[82] The pressure-transmitting medium is enclosed by a gasket and the two diamond anvils. The sample is viewed through the diamonds.

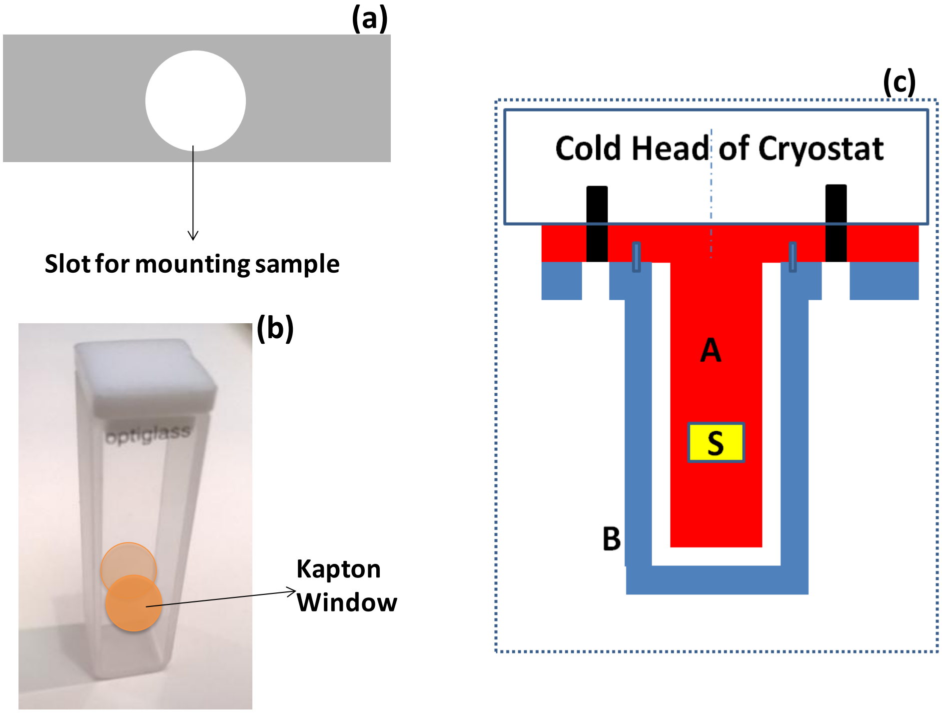

Fig. 3.16 (a) Aluminium sample holder for powder pellets/tapes; (b) Liquid sample holder; (c) Schematic of moisture proof sample holder for measurements under low temperature

The operation of the diamond anvil cell relies on a simple principle:

$$p = \frac{F}{A}, \tag{3.22}$$

where p is the pressure, F the applied force, and A the area.

Therefore high pressure can be achieved by applying a moderate force on a sample with a small area.

3.4.1.3 Moisture Proof Sample Holder: This is a special type of sample holder designed to study moisture-sensitive samples under low temperature. The trouble with such samples is that they cannot be in contact with the cryostat vacuum.

Schematic of the holder is shown in Fig. 3.16 (c). The sample holder assembly consists of two parts: an inner sample holder (part A) and an outer vacuum shroud (part

B), both made of non-magnetic Al 6061 alloy instead of the usual Cu, so that Cu K edge XAFS can also be measured for Cu containing samples. The central part of part A is milled down to create a mounting surface, which has a slot long enough to accommodate three sample tapes. Part B is a hollow cylinder with kapton sealed window for beam entry and exit. Parts A and B are sealed together inside a He filled glove box. Indium wire wrapped around Part A serves as cryogenic seal (Indium cold welds and creates a hermetic seal). Part B completely isolates the samples from the cryostat vacuum.

3.4.2 Liquid samples

Liquid samples are generally filled into special cells made of quartz (Fig. 3.16(b)). The cells have kapton windows for entry and exit of the beam. They are mounted upright at sample position.

3.5 Obtaining good quality data

Good quality data, with low noise, can be obtained by maximizing the signal to noise ratio. Noise in EXAFS experiments has a number of sources, among them unavoidable random fluctuations in the number of photons absorbed by the detectors (“photon counting noise”), electronic noise, and noise that arises from sensitivity to fluctuations of the x-ray beam. In the typical EXAFS experiment, one acknowledges the fact that the incident x-ray intensity varies with time, and attempts to compensate for it by dividing the measured signal by the measured incident flux, each integrated over the same time interval. A number of experimental problems often interfere with exact compensation for such beam intensity fluctuations (Fig. 3.17). Most of these problems can be avoided if sufficient care is taken, but they can (and often do) cause glitches, noise, and distorted amplitudes if they are ignored. The most important of these problems can be summarized in the mnemonic *HALO: Harmonics, Alignment, Linearity, Offsets.*[76]

3.5.1. Harmonics: In order to precisely compensate for the incident intensity fluctuations, it is necessary that the incident (I_0) and transmitted/fluorescence (I_t/I_f) intensity detectors "see" exactly the same beam, in the same way. If harmonics are present in the incident beam, both the detectors will in general measure different proportions of the harmonic radiation and the fundamental, even if the detectors are identical. This is because the I_t/I_f detector senses the transmitted/fluorescence photons, plus scattered background (most of which is elastic scattering at the excitation energy, but some of which is inelastically scattered radiation at lower energies), plus scattered harmonic radiation. The I_0 detector measures the x-ray intensity at the excitation energy (the fundamental), and also some small fraction of the harmonic radiation. Thus the two detectors, in effect, see different beams, and as a result, the fluctuations in the incident beam intensity do not divide out perfectly. For this reason it is essential to minimize the harmonic content of the beam, either by detuning the monochromator, or by using a harmonic reject mirror.

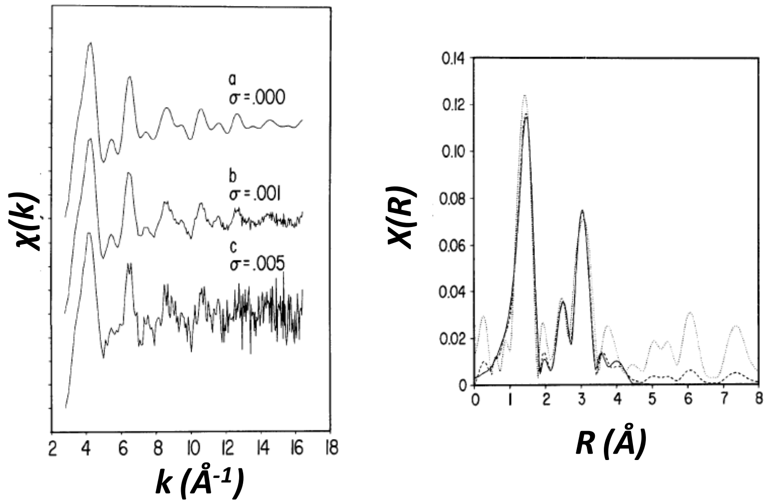

Fig. 3.17: Example of noise in XAFS data

3.5.2. Alignment: The second major reason why the two detectors may "see different beams" is that the sample alignment may be incorrect. The x-ray beam size and shape should be defined by a slit placed before the I_0 detector, and nothing except for spatially uniform objects such as smooth windows and a homogeneous sample should intercept the beam after that point. Even a small clip in the beam between I_0 detector and the sample (from the edge of the exit aperture of the front ion chamber or the edge of a cryostat entrance window, or even a wrinkled cryostat entrance window) can lead to small fluctuations in beam position, causing noise, glitches, or other distortions. Therefore alignment is a major factor contributing to the quality of experimental data.

3.5.3. Linearity: The intensity fluctuations will divide out only if the detectors and electronics are linear, that is, their outputs are proportional to the inputs. If ion chambers are used, the applied voltage must be high enough that they are in their “plateau region”, where the output for a given x-ray flux is independent of high voltage. The value of the plateau voltage depends on the construction of the ion chamber, the photon flux, the fill gas (es), and other variables. If other types of detectors are used, it is crucial that their linearity also be checked. The electronics (e.g. amplifiers, voltage to frequency converters) should be operated over their linear ranges by suitably adjusting the gains and offsets. Any amplifier offset must be subtracted out during data collection.

3.5.4. Offset: “Offsets” (i.e. the signal produced when the x-ray beam is off) should be periodically measured and subtracted out. Fluctuations in incident intensity will not divide out between I_0 and I_t/I_f if the proper offsets have not been subtracted.

Typically the amplitude of the EXAFS over the data range is only a few percent of the size of the edge step. In order to have signal to noise ratio (S/N ratio) of 1–10%, relative to the edge step, we must obtain a signal to noise ratio of .01–.1%, i.e. S/N~ 10^3. Attaining such a signal to noise ratio requires 10^6–10^7 effective counts total per energy point. If the time required exceeds the time available, the energy range of the scan can be reduced.

CHAPTER 4

XAFS DATA ANALYSIS

In practice, the XAFS data is recorded as a function of energy. In most XAFS experiments, the exact concentration of the absorbing atom and the sample thickness is not precisely known. Besides, a variety of materials such as kapton windows and the sample matrix enter into the beam path before reaching the detector. This causes the observed signals to be multiplied by energy dependent absorption factors. To compensate for this, in transmission experiments, a logarithm of the ratio of the incident and transmitted intensities is taken so that the multiplicative factor is converted into an additive background which slowly varies with energy. However, in fluorescence experiments, no logarithm is taken and the energy dependent factors are carried through the entire analysis. The elastically and inelastically scattered x-ray photons from the incident beam contribute an additive background to the fluorescence data. Therefore,

$$[\mu(E)]_{Transmission} = \ln\left(\frac{I_0}{I_t}\right); \tag{4.1}$$

$$[\mu(E)]_{Fluorescence} = \frac{I_f}{I_0} \tag{4.2}$$

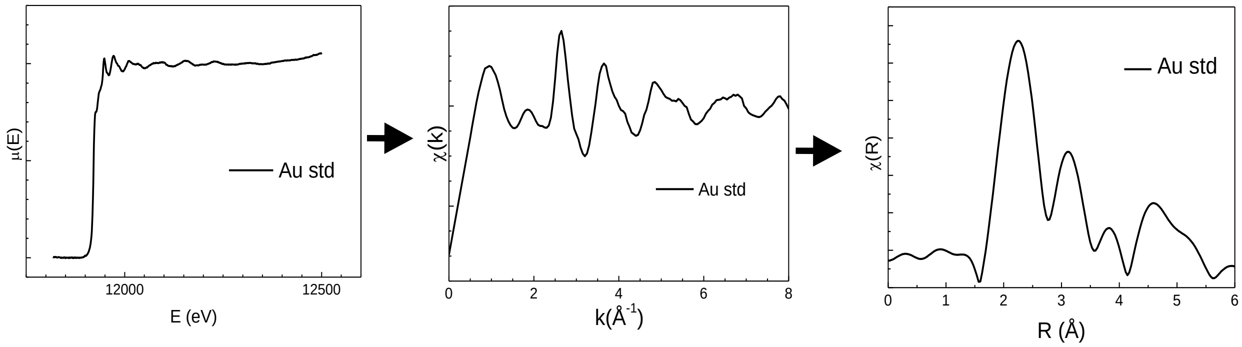

Fig. 4.1: Schematic of XAFS data analysis

The collected data is then converted to wave-number (k), which is Fourier Transformed to yield radial distribution about the absorbing atom. Fig. 4.1 shows the schematic of XAFS data analysis.

XAFS data analysis is non-trivial and proceeds via two main steps: (1) Data Processing, (2) Data Modeling and Fitting. (Fig. 4.2)

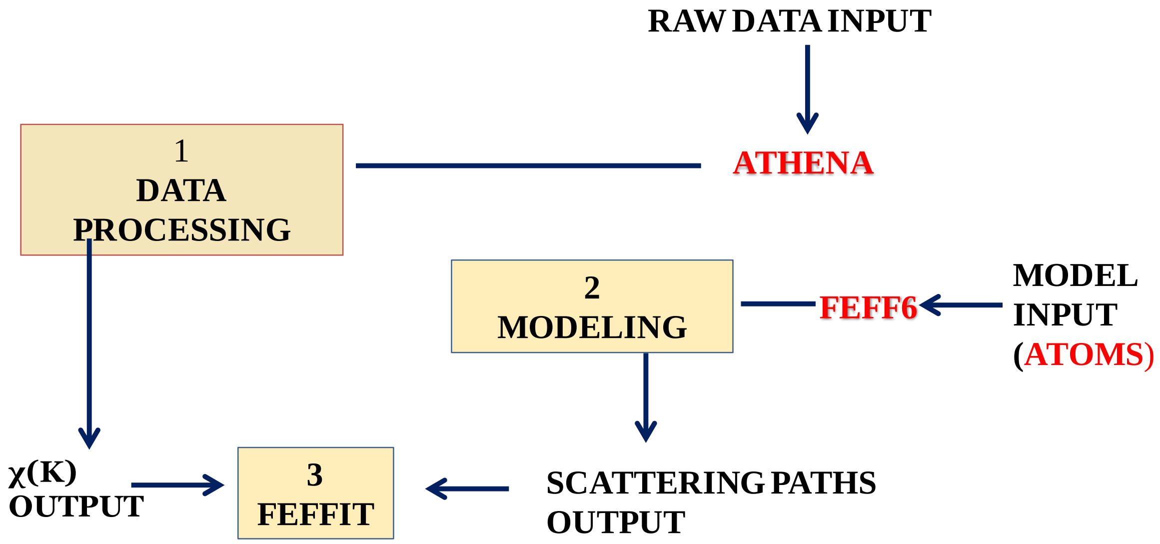

Fig. 4.2: Data Analysis Flowchart

4.1. Data Processing

Data processing is the most challenging step in XAFS data analysis. The most popular software for data processing is ATHENA.[83] Data processing involves several steps:

(i) Merging of scans: XAFS oscillations are very weak in nature and hence very high signal-to-noise ratio $\left({}^{S}\!/_{N} \sim 10^{3}\right)$ is required to get meaningful information from the data. Due to the effect of radiation on the sample and due to oxidation of the sample, the XAFS spectrum may vary from scan to scan. Moreover, there could be noise arising from instrumental errors. Therefore, in practice, several data scans are taken to check data reproducibility. The scans are merged to reduce statistical noise.

(ii) Determining of threshold energy E_0: *k*, the photoelectron wave number in the EXAFS equation, is defined with respect to threshold energy E_0 (binding energy of the electron) as $k = \sqrt{\frac{2m(E - E_0)}{\hbar^2}}$. E_0 for the onset of absorption depends on the chemical state of the central atom and the structural symmetry of its surroundings. So, for the same absorbing atom in different samples, E_0 may vary upto a few eV. The purpose of E_0 determination is to correctly and quantitatively account for any edge shift observed in the different samples. In practice, E_0 is chosen to be the energy at half of the edge step. Only relative shift in E_0 between standard and unknown samples is very important: if both are shifted by the same amount, the answer will be the same to a good approximation. Relative E_0 shifts primarily affect the data at low values of k which are distinguishable from changes in other structural parameters. Thus, ambiguities in absolute E_0 position, and small (~3 eV) differences in relative E_0 position, do not introduce corresponding ambiguities in structure determination by EXAFS. The choice of E_0 does pose significant uncertainties for k-space analysis in the XANES region, however.

After the edge energy E_0 is fixed, the whole data gets divided into the pre-edge and the post-edge regions.

(iii) Deglitching of the data: Absorption and fluorescence data often include sharp points, called glitches, which may be many times larger than the EXAFS signal. Although they have a small energy width, because of the finite data content, upon Fourier transformation, they may be magnified manifold and have a small effect on the data. The background subtraction may also be incorrect because of the presence of these spiky glitches and can change the chi-space spectrum. So these must be removed in the initial stages of data processing. In order to distinguish a glitch from a data point, one must look at the plot for I_0. A glitch in the μ(E) plot corresponds to a dip in energy in the I_0 plot.

(iv) Pre-edge background subtraction: The removal of pre-edge background involves fitting of a functional form to the data before the edge and extrapolation of this function to the XAFS data region. Since the pre-edge background is a slowly varying function of energy, it can be fitted to a linear function between 200 eV and 50 eV below the edge and then extrapolated to the post-edge region.

(v) Post-edge background subtraction: Extracting the post-edge background function, μ_0, is the most critical step of background removal, as this function can affect the final conclusions for the structural information. Incorrect background removal leads to leakage of the background peak into the nearest neighbor peak of interest and distorts the latter's structural information (particularly coordination number).

The XAFS oscillations should be even about the background line.

The background is approximated by a single cubic least-squares-spline polynomial[84] over the energy region of interest, with the first and last data points respectively at the beginning and end of the energy range defined. The polynomial function is solved using these data points. If the background subtraction using this method does not look good, then the background may be approximated by a series of cubic polynomial functions that are joined at “knots” where the functions and their first derivative are continuous. It must be ensured that the data is not distorted by background removal process. Too few knots might not approximate the background oscillation well enough and might show as a low-*r* peak in the Fourier transform. On the other hand, too many knots might tend to follow the true XAFS oscillations and distort the analysis. The position of the knots can be varied and the background may also be forced to pass through a certain point in cases of a complicated background fitting. Once the fitting parameters are fixed, the fitting program tries to adjust the ordinates for the minimization of the mean square error between the data and the polynomial.

Alternately, a program called AUTOBK[85] is popularly used to remove the "background function" from a measured XAFS spectrum, using an automated algorithm based on the Fourier content of the XAFS spectrum. AUTOBK considers the background function to be that part of the measured absorption which does not contain any structural information. Salient features of this method of background subtraction are (1) No point on the absorption curve is assumed to be on the background curve, (2) AUTOBK chooses a smooth spline to best fit only the low-frequency components of $\mu(E)$, (3) The number and the abscissas of knots in the AUTOBK method are explicitly determined because of the restrictions put on the background spline from the information content of $\tilde{\chi}(r)$.

$$N_{knots} = \frac{2 r_{bkg} \Delta k}{\pi}, \tag{4.3}$$

where Δk is the *k*-range of useful data and r_{bkg} is the upper limit of the low-*R* region over which the background is to be fit. r_{bkg} is typically about half the distance of the first shell peak. The knots are set to be equally spaced in *k*-space while the ordinates of the knots are determined by minimizing the difference between data and standard $\tilde{\chi}(r)$ in the low-*r* region.

Difficulty in using AUTOBK arises when leakage from the first shell causes substantial low-r component of $\tilde{\chi}(r)$. In such cases, a suitable standard may be measured to give an estimate of the leakage into the low-*r* region from the first shell.

For very noisy data, the first background subtraction method tends to do a better job. Mostly, background subtractions from the two methods are comparable. However, AUTOBK tends to give slightly more even oscillations about the background line in *k*-space.

(vi) Transformation to k-space: This involves extracting the oscillations $\chi(k)$ and interpolating them to an equally spaced grid in photoelectron wave number k. The extraction to k-space (from energy space) is essential to derive the structural parameters since (k,R) are the conjugate variables, not (E,R).

(vii) Fourier Transform to r-space: Fourier transform of the data is taken over a finite range from k_{min} to k_{max}.

$$\tilde{\chi}(r) = \frac{1}{2\pi}\int_{k_{\min}}^{k_{\max}} \chi(k) e^{2ikr} dk \tag{4.4}$$

In order to increase the data content, *k* is chosen upto a long range (at least upto 12 Å^{-1}). The choice of *k* is such that good quality data exists upto the value of $k_{max.}$ k_{min} is chosen in the region where the background doesn't change rapidly.[86]

A practical problem associated with the Fourier transforming technique here is due to the finite range. Truncation ripples often interfere with physical features of interest. For a limited range of k as in our case, $\chi(k)$ may be replaced by

$W(k)\chi(k)$ where $W(k) = \begin{cases} 1, & k_{\min} < k < k_{\max} \\ 0, & otherwise \end{cases}$

The transform $\tilde{A}(r) = W(r) * A(r-R)$,

where $\tilde{W}(r) = \exp(ik_0 r)\dfrac{\sin \Delta k r}{r}$,

k_0 is the center of transform range and Δk is the width. This is a damped sine function with a peak at $r = 0$. The convolution of this $\tilde{A}(r)$ with $\tilde{W}(r)$ results in peak broadening as well as truncation ripples on the sides of the main transform peak. These ripples can contaminate neighboring peaks.

It is possible to reduce the amplitude of truncation ripple at the expense of further peak broadening by using a tapered windowing function of the form

$$W(k) = \cos^2(\frac{k-k_0}{\Delta k}),\ for |k-k_0| < \Delta k \qquad (4.5)$$

where k_0 and Δk are as defined before. The $\cos^2$ window is often referred to as Hanning function. The transform of this function is given by

$$\tilde{W}(r) = \exp(2ik_0 r)\frac{\sin(\Delta k r)}{r}\frac{\pi^2}{2(\pi^2 - 2\Delta k^2 r^2)} \qquad (4.6)$$

Comparing this with the result of that without window, it is apparent that the truncation ripples die out much faster at large $(r - r_0)$ using the smooth window, but the central peak is significantly broader. It is often useful to combine a flat region over the middle of the data range with a Hanning function at the ends, that is:

$$W(k) = \begin{cases} \sin^2\left(\dfrac{\pi(k-k_1)}{2(k_2-k_1)}\right), & k_1 < k < k_2 \\ 1 & ,k_2 < k < k_3 \end{cases}$$

$$= \cos^2\left(\frac{\pi(k-k_3)}{2(k_4-k_3)}\right), k_3 < k < k_4$$

where k_1, k_2, k_3, k_4 delimit three different ranges corresponding to the two end regions and the flat central region.

To sum up, window functions are used to weigh different portions of the data, truncate the data smoothly at the ends of the transform range and make data from two samples appear as close as possible.

After selecting appropriate k-range, the data is exported as a chi (k) file. Further analysis is performed on this exported data as described in the following section.

4.2. Data Modeling and Fitting

This step involves the following sub-steps:

4.2.1 Construction of the appropriate structural model using FEFF6[87]

Suitable structural model is simply based on physical intuition. The scattering phase shifts and amplitudes corresponding to the input model are generated *ab initio* by program FEFF6. FEFF6 calculates wave phase shifts, effective scattering amplitudes and single and multiple scattering curved XAFS spectra, including polarization dependence, for clusters of atoms ($Z<95$). FEFF6 requires atomic coordinates for the input model and physical information about the system such as absorbing atom and excited core level for its calculation. For crystalline systems, the program ATOMS[88] is used to generate list of atomic coordinates. ATOMS generates the required coordinates starting from a crystallographic description of the system, for e.g., lattice type, lattice parameters and space group. For a disordered system, the model bond lengths are assumed from the peak positions of the Fourier transformed data.

FEFF6 calculates EXAFS using four internal modules:

1. POTPH (Potentials and Phases): This module calculates the scattering potentials for each type of atom by overlapping their wave functions based on their geometric distribution. To calculate free atomic potentials, the inputs required by this module are the atomic numbers of all the atoms and the type of core-hole being considered.
2. PATHS (Path enumeration): This module identifies all significant single and multiple scattering paths for an arbitrary cluster of atoms, in order of increasing path length, based on a list of atomic coordinates. Different paths are weighed on the basis of scattering amplitudes and subsequently the low amplitude paths are neglected.
3. GENFMT (Scattering amplitude and other XAFS parameters calculation): For each path the code calculates the effective scattering amplitude (F_{eff} from which FEFF gets its name), total scattering phase shift and other XAFS parameters and writes the result to a corresponding file feffnnnn.dat.
4. FF2CHI (XAFS spectrum calculation): This module constructs the XAFS spectrum chi (k) using the XAFS parameters from one or more paths. Single and multiple scattering Debye-Waller factors are calculated using a correlated Debye model. Output from this module is the total XAFS spectrum and optionally, the contribution to the XAFS from each path individually.

4.2.2 Fitting the peaks in *r*-space using least squares fitting method and FEFFIT[89]

FEFFIT compares the experimental XAFS data to theoretical calculations. It fits the calculations from FEFF to XAFS chi (k) data, hence aiding in the determination of local structure around an atom. It can determine inter-atomic distances, co-ordination numbers and atomic species of neighboring atoms. Finer details of atomic configurations, including detailed descriptions of two-body distribution functions and certain aspects of three-body correlations, are also measurable with FEFFIT.

FEFFIT fits the XAFS data using FEFFnnnn.dat files output from FEFF as the basis. The XAFS contribution of each scattering path (read from each feffnnnn.dat file) is adjusted by applying standard XAFS parameters such as co-ordination number, change in distance, Debye Waller Factor, and shift in energy origin) until the best-fit to the data is found. Standard numerical techniques are used to find the set of variables that minimizes the sum of squares of the difference between model and data and to estimate the uncertainties in the variables. Fitting can be done in either *r*-space or back-transformed k-space, with Fourier Transforms done by FEFFIT on both the XAFS data and the calculated model during the fitting process. However, *r*-space is preferred because in that case, any difference between the fit and the data is a direct measure of the quality of fit. On the other hand, in *k*-space there is no limit to the number of multiple scattering paths required, which increases the number of variable parameters. Because of the finite content of an XAFS signal, so many parameters cannot all be independently measured as indicated from the equation

$$N_{idp} \approx \frac{\Delta k \Delta r}{\pi} \tag{4.7}$$

Therefore, if k-space fitting is considered, difference between data and fit has two contributions – one from the accuracy of the model used and the other from the neglect of higher order multiple scattering paths; there is no reliable way to separate the two. Thus, in order to limit the number of paths used, *r*-space fitting is considered.

Conversion to *r*-space is undertaken via equation 4.4. *k*-range should be selected such that data of good quality exists in *k*-space upto the maximum value of k_{max} and k_{min} is beyond 2 Å^{-1}, in order to avoid multiple scattering and other effects. The *r*-range is defined by the peaks (bonds) of interest.

4.3 Error Analysis

4.3.1 χ^2 as an estimate of goodness of fit

The best set of variables in FEFFIT will minimize the sum of the squares of the difference of model and data XAFS. The statistic called chi-square (χ^2), which is a scaled measure of the sum of squares of a function, is generally considered the best figure of merit to judge the quality of the fit. By definition,

$$\chi^2 = \sum_{i=1}^{N} \left(\frac{f_i}{\varepsilon_i} \right)^2 , \qquad (4.8)$$

where f_i is the function to be minimized, N is the number of function evaluations and ε_i are the uncertainties in f_i approximated by a constant value due to random fluctuations.

FEFFIT[90] allows the fit to be performed in *r*- or *k*-space, but there is no conceptual difference in the way the fit is done. When fitting in *r*-space, the function to minimize is

$$f(r_i) = \tilde{\chi}_{data}(r_i) - \tilde{\chi}_{\mathrm{mod}el}(r_i), r_{\min} \le r_i \le r_{\max} , \qquad (4.9)$$

and when fitting in *k*-space, the function to minimize is

$$f(k_i) = \tilde{\chi}_{data}(k_i) - \tilde{\chi}_{\mathrm{mod}el}(h_i), k_{\min} \le k_i \le k_{\max} \qquad (4.10)$$

There is one real and one imaginary evaluation for each data point. Therefore the number of evaluations is

$$N = \frac{2(r_{\max} - r_{\min})}{\delta r} \qquad (4.11)$$

when fitting in *r*-space. Likewise, when fitting in *k*-space,

$$N = \frac{2(k_{\max} - k_{\min})}{\delta k} \qquad (4.12).$$

δr and δk are the grid spacings in *r* and *k* space respectively. N has no physical significance, since δr and δk are chosen arbitrarily. The more important number is the number of relevant independent measurements:

$$N_{idp} = \frac{2(k_{\max} - k_{\min})(r_{\max} - r_{\min})}{\pi} + 2 \tag{4.13}$$

The explanation for the above equation is as follows: (a) the conjugate variables considered are k and $2r$, (b) since we are measuring real and imaginary parts of $\tilde{\chi}(r)$ the information must be an even number of points, (c) even for an infinitesimally small r-range, we must have atleast one pair of points.

This implies that $\chi^2 = \sum_{i=1}^{N_{idp}} \left(\frac{f_i}{\varepsilon_i} \right)^2 = \frac{N_{idp}}{N} \sum_{i=1}^{N} \left(\frac{f_i}{\varepsilon_i} \right)^2$ (4.14)

FEFIT uses a single value of ε for all values of ε_i for the sake of simplicity. Assuming a reasonable estimate for ε,

$$\chi^2 = \frac{N_{idp}}{N\varepsilon^2} \sum_{i=1}^{N} \{[\mathrm{Re}(f_i^{\,2})] + [\mathrm{Im}(f_i^{\,2})]\}. \tag{4.15}$$

This is the definition of χ^2 used by FEFFIT, and it is the primary figure of merit to characterize the goodness of fit. There is a related figure of merit, χ_v^2 or reduced chi-square.

$$\chi_v^2 = \frac{\chi^2}{v}, \tag{4.16}$$

where v = no. of degrees of freedom in the fit = $N_{idp} - N_{\mathrm{var}}$, N_{var} being the number of variables in the fit.

$\chi^2$and χ_v^2 are useful quantities for comparing the quality of different fits. The general rule is that the fit with lower χ_v^2 is the best. χ_v^2 is lowered for useful variables. If addition of a variable causes decrease in χ^2 but increase in χ_v^2 then the fit does not improve.

In principle, a good fit should have χ_v^2~1. However, practically, χ_v^2>>1! Specifically, it is unclear from the value of χ_v^2 alone if hard-to-estimate systematic errors are drowning out the random measurement errors or if the fit is truly bad. To distinguish between these two very different conclusions, R-factor is introduced which is scaled to the magnitude of the data itself.

$$R = \frac{\sum_{i=1}^{N}\{[\mathrm{Re}(f_i)]^2 + [\mathrm{Im}(f_i)]^2\}}{\sum_{i=1}^{N}\{[\mathrm{Re}(\chi_{data})_i]^2 + [\mathrm{Im}((\chi_{data})_i]^2}. \tag{4.17}$$

This number is directly proportional to χ^2, and gives a sum-of-squares measure of the fractional misfit. As long as the measurement uncertainty is not a significant fraction of the measurement itself, any fit with R-factor greater than a few percent is not a good fit. General acceptable values are $R \leq 0.02$, $\chi_v^2 > 10$. Such fits are considered as good fits as the theory and data agree within a percent.

4.3.2 Measurement Uncertainty

Estimating systematic errors in $\tilde{\chi}(r)$ is the main difficulty in error analysis in FEFFIT. ε contains both random fluctuations and systematic error in the data.

4.3.2.1 Systematic Uncertainty

Systematic errors are dominated by (i) leakage of imperfect background into the first few shells, (ii) systematic errors in the measurement of μ(E). It is possible to estimate the size of the systematic errors by trying different reasonable background removals. Analyzing different data scans taken under different experimental conditions could give an estimate of (ii). A third source of systematic errors in the fit comes from the FEFF calculation itself. Such errors are important as they contribute to the small amount of misfit expected in a good fit.

4.3.2.2 Statistical uncertainty

The scale of ε depends on the Fourier Transform parameters used. Assuming that the noise is dominated by random fluctuations, the measurement uncertainty in k-space data is linearly related to ε_k, i.e. the unfiltered fluctuations in χ(k) data:

$$\varepsilon_k = \varepsilon_R \sqrt{\frac{\pi(2\omega+1)}{\delta k(k_{\max}^{2\omega+1} - k_{\min}^{2\omega+1}}}, \tag{4.18}$$

where ω is the k-weighting.

4.3.3 Error estimation for the variables

FEFFIT estimates the uncertainties in the variables once the best-fit values of the variables are found. The uncertainties are estimated using standard χ^2 minimization technique. The goal of the fit is to minimize χ^2 in each of its N_{var} dimensions. Generally the Levenberg-Marquardt non-linear least squares fitting algorithm[91] is used (For details about the algorithm, see Appendix A). The first and second derivatives of χ^2 are found *wrt* each of the variables. These are used for finding the next estimate of the best variables, and are found to be useful for estimating the uncertainties in the variables after the best fit has been found.

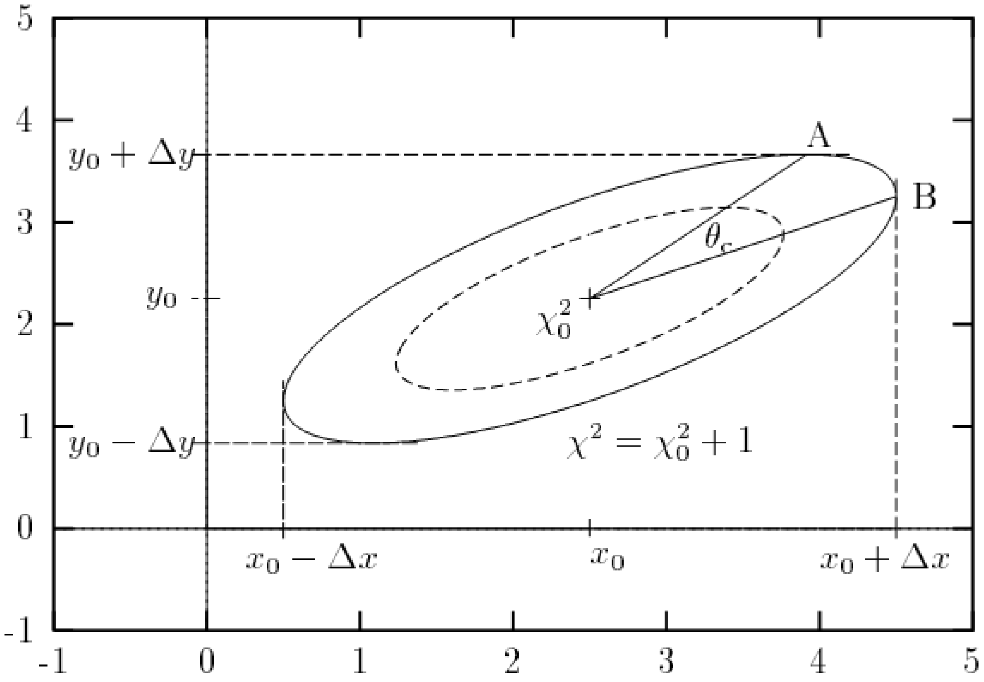

Fig. 4.3: Contour map of χ^2 as a function of two variables x and y

At the best fit solution, χ^2 is roughly parabolic in each of its N_{var} dimensions. The curvature of the χ^2 is given by the ($N_{\text{var}} \times N_{\text{var}}$) matrix of the second derivatives around the solution. Fig. 4.3 shows a contour plot of the χ^2 surface for a two variable problem. The surface is elliptical since the errors in the variables are not equal. At the solution, the variables x and y have values x_0 and y_0 respectively and $\chi^2 = \chi_0^2$. As x or y move away from their best fit solution, χ^2 increases. For normally distributed uncertainties, the contour of χ^2 is elliptical for two dimensions. The uncertainty in the value of a variable is the amount by which it can be increased and still have χ^2 below some limit. FEFFIT uses the $\chi_0^2 + 1$ criterion (same as the one commonly used for randomly distributed errors). The uncertainties in x and y are Δx and Δy respectively, and these ensure that χ^2 is increased by 1 from its best value.

While evaluating the uncertainty in a variable, all the other variables are allowed to vary, so that the correlations between variables can be taken in to account. The correlation is a measure of how much the best-fit value of one of the variables changes in response to changing another variable away from its best-fit value. In Fig. 4.3, the correlation between the variables x and y is equivalent to the projection of x on y, i.e. $\cos\theta_c$. If x and y had been completely correlated, the ellipse in Fig. 4.3 would have had its major and minor axes parallel to the x and y axes. If we ignore the correlations and hold y constant, then the uncertainty in x would be estimated to be Δx'. This is considerably smaller than Δx, and is a worse estimate of the uncertainty in x

Algebraically, the uncertainties in the variables are given by the inverse of the curvature matrix (the matrix of the second derivatives), called the correlation matrix. The uncertainties in the variables are the square roots of the diagonal terms, and the correlations between pairs of variables are given by the off-diagonal terms of this matrix.

The uncertainties of the variables and the correlations between variables are estimated at the best fit condition. Needless to say, each analysis requires its own assessment of uncertainties, including estimation of the relative importance of systematic and random errors; therefore it is not possible to state universal values for these uncertainties. Since the fits involve simultaneously varying several variables, it is possible that a local minimum may be found instead of a global minimum. Another possibility is that the initial structural model considered is very far away from the correct model, and the model does not have the freedom required to allow the necessary variation for reaching the correct model. Yet another possibility is that there exists some correlation between the variables employed and with the available data, it is not possible to unambiguously determine these correlated variables.

Before stating conclusive results, several models must be considered and accounted for by applying appropriate error bars. One particularly useful way to reduce error bars is by simultaneously fitting different datasets. Sometimes, choice of appropriate k-weight for the data is also important for obtaining low error bars.

Therefore, XAFS data analysis is largely non-trivial and rigorous, and arriving at the correct conclusion significantly depends on the ability of the analyst to judge the quality of fit.

CHAPTER 5

AUGMENTATION OF INDUS-2 XAFS BEAMLINES FOR EXTREME THERMODYNAMIC CONDITIONS

5.1 Background

The Indian Synchrotron, Indus-2, is a 2.5GeV third generation synchrotron source at the Raja Ramanna Centre for Advanced Technology (RRCAT)[92], presently working at 200mA beam current (designed for 300mA current). Currently, two bending magnet port-XAFS beamlines (BL-08&09) are operational at Indus-2. While BL-08 is a polychromator-based beamline which operates in *energy-dispersive* mode, BL-09 is a monochromator-based beamline which operates in *energy-scanning* mode. Schematic of the two modes is shown in Fig. 5.1.

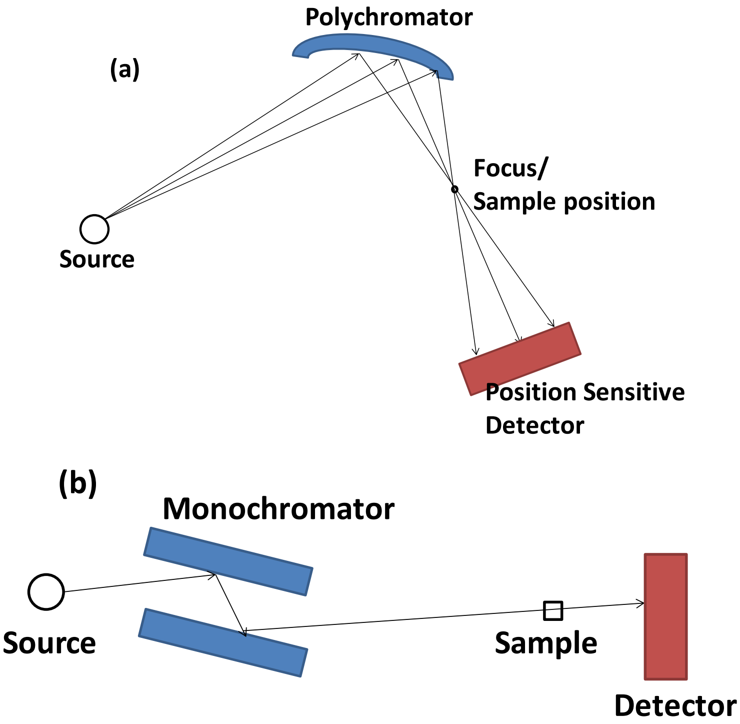

Fig. 5.1: Schematic of beamline operating in (a) energy dispersive mode and (b) energy scanning mode.

Both these beamlines were initially designed for ambient conditions. To cater to the increasing demand for experiments under extreme conditions, we have augmented these beamlines to accommodate experiments under low temperature and high pressure. Data from dispersive beamlines often suffer from non-linearity due to non-linearity of the CCD or erroneous bending of the polychromator. Critical assessment of linear calibrated BL-08 XAFS data[93] revealed that it required non-linear correction. We therefore developed an algorithm for correction.

This chapter is divided into three parts: (i) non-linear correction of dispersive XAFS data (ii) modification of BL-08 for high pressure XAFS experiments. (iii) low temp setup for XAFS experiments.

5.2 Non-Linear Correction of Dispersive XAFS Data

The Energy Dispersive EXAFS beamline, BL-08 [Fig. 5.2], at Indus-2 works in the energy range 5-20 keV. The heart of this beamline is a bent Si (111) polychromator crystal, which functions as the energy dispersive-cum-focusing element. White synchrotron beam, emerging from the bending magnet port of the storage ring, is first incident on a Rhodium coated harmonic rejection mirror (M) (kept at 0.2° *wrt* the incident beam) at grazing angle of incidence, which also functions as the vertically focusing element. Reflected beam from this mirror undergoes Bragg reflection from the bent crystal (CC) and is, eventually, dispersed with a certain bandwidth around the central x-ray photon energy. The crystal focuses the beam (horizontally) at the sample position (S). Transmitted radiation from the sample is incident on a position sensitive CCD detector (D) having 2048×2048 pixels (1pixel=13.5μm). This detector records the whole EXAFS spectrum in millisecond time scale [94-95]. Table 5.1 summarizes the optical elements of this beamline and their focusing characteristics.

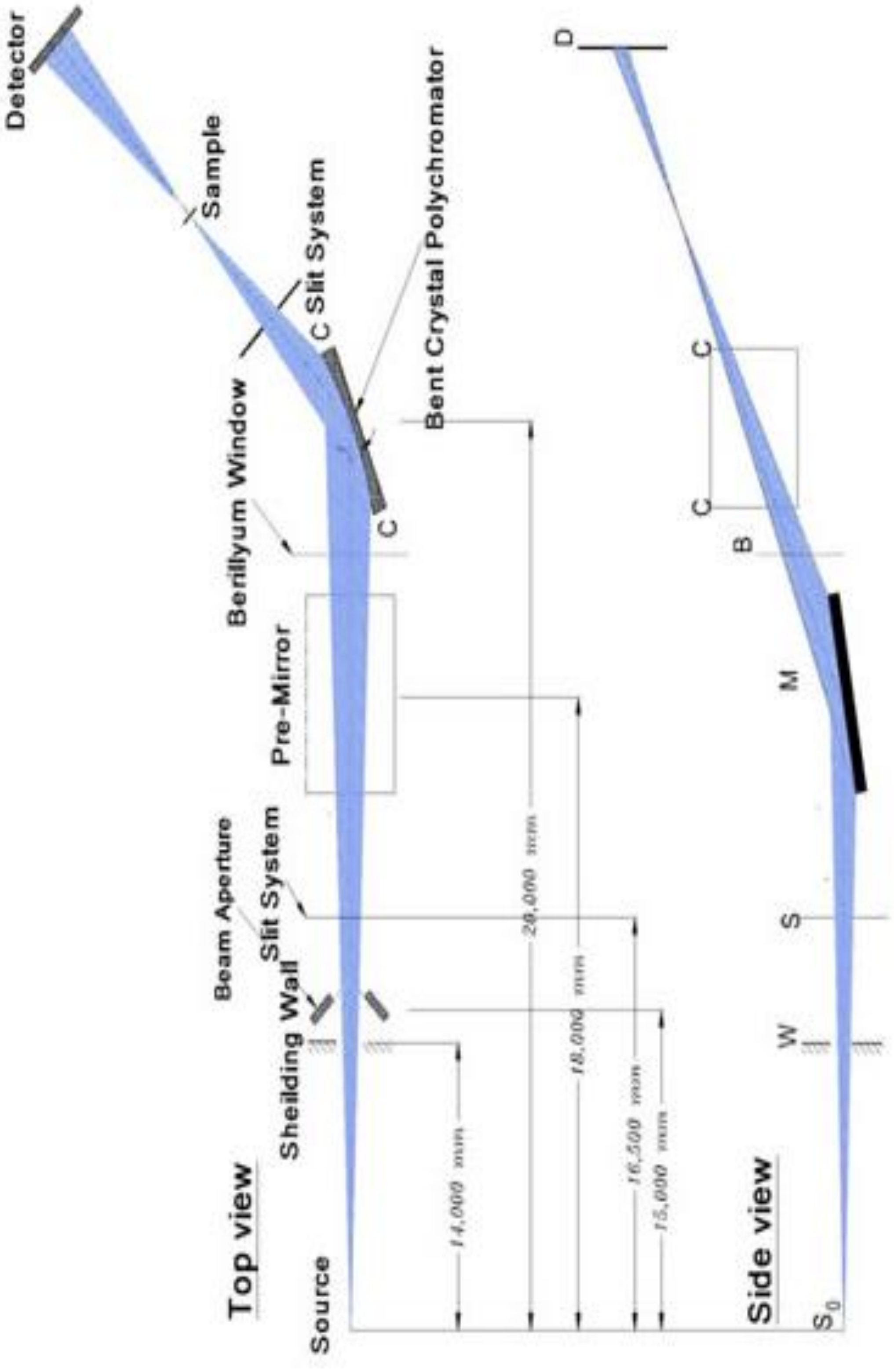

Fig. 5.2: Optical layout of the BL-08

Table 5.1: Optical Elements of BL-08

1.	**Harmonic Rejection Mirror**	
	Coating	Rhodium
	Length	1000 mm
	Radius, R (fixed)	1.32 km
	Angle (fixed), θ_M	0.2°
	Distance from Source (p) (Fixed)	18000mm
	Focusing Direction	Vertical
2.	**Bent crystal polychromator (CC)**	
	Material	Si (111)
	Bending	Elliptical
	Radius, R_{CC} (variable)	0.028-0.265 km
	Bragg angle, θ_0 (variable)	5.67°-23.29°
	Focus direction	Horizontal
	Focus distance, q_H (variable)	570-1404mm
	Distance from M (fixed)	2000 mm
	Energy Band around central energy (E_0), ΔE (variable)	300-2000 eV
3.	**Detector**	Position sensitive CCD 2048×2048 pixels

The raw data is recorded on the CCD as a function of pixel number. To extract μ (E), the pixel number has to be converted into energy point. For this purpose, reference data on two standard foils are recorded.[96] The values of CCD channel numbers corresponding to the edge energy positions of these two foils are noted. The dispersion (i.e. the linear calibration factor) is obtained by dividing the difference of these two energies by the difference in the corresponding channel numbers. The conversion to energy is carried out using:

$$E(\mathrm{eV}) = \text{channel number} \times \text{dispersion} + E_0, \tag{5.1}$$

where E_0 is the energy of the desired edge.

EXAFS at Ni *K* edge (8.333 keV) was recorded on standard Ni foil at 74mA beam current, 2 GeV ring energy. The data recorded (in pixels, μ (pixel)) was first converted to μ(E) using the method described in the previous paragraph, using Ni foil and Tm_2O_3 as calibration standards. The linear calibration factor was determined to be 0.29 eV/ pixel, following our previous method of linear calibration. Fig. 5.3 shows the comparison of linear-calibrated Ni foil data from BL-08 (Indus-2 data) with standard Ni foil data from NSLS beamline X18B, USA. NSLS storage ring parameters are comparable to those of Indus-2. Clearly, the calibration is not linear and needs further refinement.

The data were processed using ATHENA and the extracted XAFS oscillations, χ (*k*), were Fourier transformed into real space for fitting. An initial structural model was reasonably constructed, for which the theoretical scattering amplitudes and phase shifts were generated by FEFF 6.l. The model parameters were allowed to vary while fitting (using FEFFIT) to yield the best-fit values for bond lengths (*r)*, coordination numbers (*N),* and Debye-Waller factors (DWF). The *R*-factor was considered as an estimate of the quality of fit.[89,97]

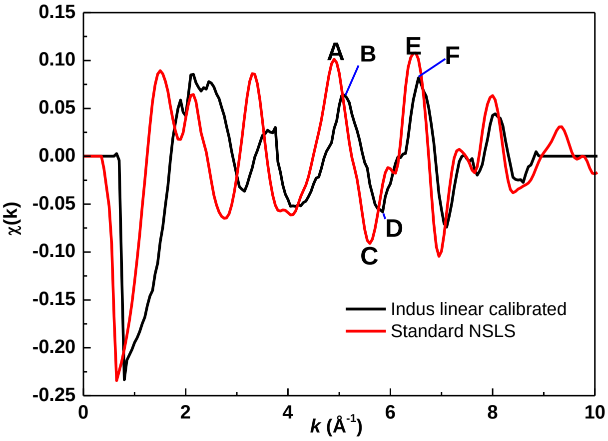

Fig. 5.3: Comparison (*k*-space) linearly calibrated Indus-2 Ni foil data with data from NSLS

The fitting plan includes fitting the following: (I) NSLS data, (II) linear calibrated Indus-2 data, (III) Non-linear calibrated Indus-2 data obtained using a mathematical algorithm, employing least squares minimization method, described in section 5.2.1.

5.2.1. Determination of EXAFS parameters for Standard Ni foil from NSLS and calibrated Ni foil data from Indus-2:

Table 5.2: Structural parameters obtained from XAFS data fitting

Fitting	*k*-range(Å^{-1})	R-range (Å)	R-factor	N	DWF (Å^{2})	R(Å)
Standard NSLS data						
N= variable	2.5-8 Or 3.9-8	1-2.8	0.0097	12	0.006 (1)	2.473 (7)
Linear calibrated Indus-2 data						
N= variable	2.5-8	1-2.8	0.007	7.7 (5)	0.005 (1)	2.482 (5)
N= variable	3.9-8	1.2-3	0.013	8.2 (9)	0.005 (2)	2.49 (1)
N=12	2.5-8	1-2.8	0.026	12	0.0106(6)	2.49 (8)
Non-linear calibrated Indus-2 data						
N= variable	3.9-8	1.2-3	0.029	12.79±1.88	0.012 (3)	2.50 (2)

(i) Simultaneous fitting of standard Ni foil data from NSLS for k^w (w=1,2) [to reduce error bars] over *k*-range 2.5-8Å^{-1}, *r*-range 1-2.8 Å. The results obtained are summarized in Table 5.2.

(ii) Simultaneous fitting of Ni foil Indus-2 data for k^w(w=1,2) [to reduce error bars] over *k*-range 2.5-8Å^{-1}, R-range 1-2.8 Å. The results obtained are summarized in Table 5.3. Clearly there is a difference in the structural parameters compared to standard NSLS data. The value of N is significantly lower than that for standard Ni foil. On the other hand, fixing the N value for Indus-2 data yields high DWF.

5.2.2 Calibration of Indus-2 data in *k*-space using range of data points

One possible method to non-linearly calibrate dispersive XAFS data is by using the ‘Calibrate dispersive XAS’ option in ATHENA. In this method, the recorded data is compared with international standard data to determine the mapping of μ(pixel) to μ(E). This mapping function can then be presumed constant for all data measured under that experimental geometry. ATHENA assumes that the function mapping μ(pixel) to μ(E) is quadratic in pixel position. Thus

$$E_i = C_0 + C_1 p_i + C_2 p_i^2 . \tag{5.2}$$

Each energy value is thus a quadratic function of pixel position. To calibrate μ (pixel), the polynomial coefficients, C_0, C_1 and C_2 are adjusted manually. The parameters are refined by optimizing the difference between the international standard and the converted μ(E) of the dispersive data.

However, this calibration method is very tedious and fragile as it is extremely sensitive to very minute changes to C_2 (as much as fifth decimal place). A starting value for the linear term C_1 that is too far away from the best value will almost certainly result in the refinement finding a false minimum. Besides, this calibration works best when the data being compared are recorded under the same conditions. We therefore devised a more general method, which leads to direct, part-by-part calibration of the data.

The data were first converted to k-space. Let k denote the *k* values for the standard (NSLS) spectrum and k' denote the corresponding *k* values for the experimental (Indus-2) spectrum. The spectra were divided into segments, each segment containing the part of the spectrum between an antinode and a node. Referring to Fig. 5.3, point A in the standard NSLS spectrum corresponds to point B in the linear calibrated Indus-2 spectrum, point C in the standard NSLS spectrum corresponds to point D in the linear calibrated Indus-2 spectrum and so on. The first segment corresponds to the region between point A and point C for Standard NSLS spectrum and between point B and point D for linear calibrated Indus-2 spectrum. Similarly, segments CE and DF correspond to the second segment for Standard NSLS and Indus-2 data respectively The points with low values of k’ (< 4 Å^{-1}, i.e. before point C in Indus-2 spectrum) were not used for calibration due to poor resolution and noise (Ref. Fig. 5.3). Amplitude difference for the Indus-2 data (w.r.t. NSLS data) had to be corrected for. The amplitude ratios for corresponding points in the two spectra were calculated and the Indus-2 spectrum was multiplied by these values. The amplitude ratios for different *k*-ranges of the spectrum have been plotted in Fig. 5.4.

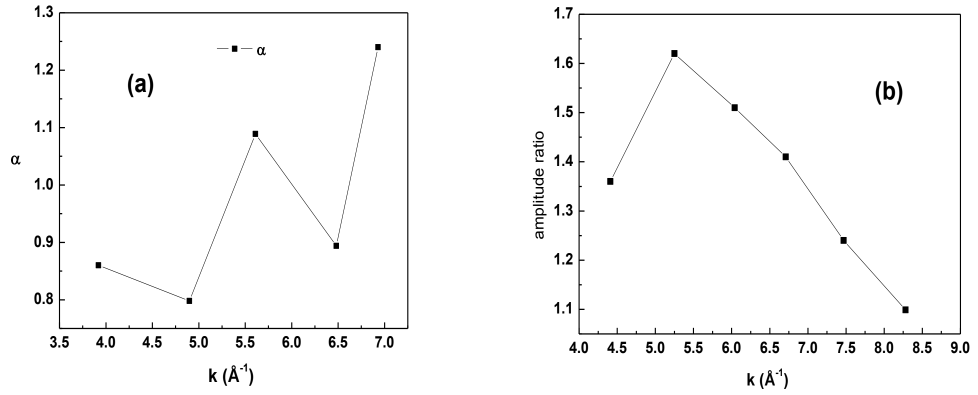

Fig. 5.4. Plot of (a) α vs *k*; (b) amplitude ratios (for Indus-2 data w.r.t. NSLS data) vs *k*.

Assuming linear correlation between corresponding data points in *k* –space between standard NSLS data and Indus-2 data (to first order), for each of the segments

$$k = (k' - A)\alpha + \beta \tag{5.3}$$

Using least squares minimization method,

$$(k - (k' - A)\alpha - \beta)^2 = 0$$

$$\Rightarrow [(k - \beta) - \alpha(k' - A)]^2 = 0 \tag{5.4}$$

Differentiating w.r.t. α,

$$\alpha = \frac{\sum (k - \beta)(k' - \alpha)}{\sum (k' - \alpha)^2} \tag{5.5}$$

where A =k'_{min} (5.6)

β is the y intercept and α is the slope.

At k’=k'_{min}, $\beta = k$.

Therefore, $\beta = k_{min}$. (5.7)

Substituting these values in eq (5.1) gives α.

Let k'' denote the calibrated k values for experimental data. Then,

$$k'' = \alpha(k - A) + \beta \quad (5.8)$$

The k'' values were generated for the entire segment by interpolation. The calibration was repeated for different segments of the spectrum and the revised dataset was generated (In Table 5.3, this has been shown for the first segment). The consolidated k'' and corresponding intensities were plotted and compared with the standard spectrum in Fig. 5.5. Clearly, Indus-2 Ni foil data for the selected range now matches with standard Ni foil data. The difference in amplitude is possibly caused by the difference in the qualities of the foils and correspondingly different DWF.

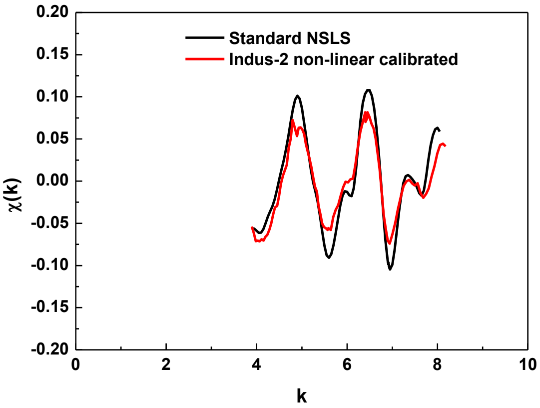

Fig. 5.5: Comparison of standard NSLS data with non-linear calibrated Indus-2 data

5.2.3 Fitting the calibrated (Indus-2) spectrum obtained from 5.2.2

The (non-linear) calibrated Indus-2 spectrum (from 5.3.1.2) was fit for k^w (w=1,2) [to reduce error bars] over k = 3.9-8Å^{-1}, r = 1.2-3 Å. The standard NSLS and linear calibrated Indus2 data were re-fitted over the revised range. The structural parameters obtained are now comparable to those of standard NSLS data. [Table 5.2]

Table 5.3: k'' values generated for the first segment

k	k'	A	α	B	k''
3.9	3.9	3.98	0.86	3.92	3.8942
3.95	3.95				3.9372
4	4				3.9802
4.05	4.05				4.0232
4.1	4.1				4.0662
4.15	4.15				4.1092
4.2	4.2				4.1522
4.25	4.25				4.1952
4.3	4.3				4.2382
4.35	4.35				4.2812
4.4	4.4				4.3242
4.45	4.45				4.3672
4.5	4.5				4.4102
4.55	4.55				4.4532
4.6	4.6				4.4962
4.65	4.65				4.5392
4.7	4.7				4.5822
4.75	4.75				4.6252
4.8	4.8				4.6682
4.85	4.85				4.7112
4.9	4.9				4.7542
4.9	4.95				4.7972
4.95	5				4.89202
5	3.9				4.93192

The selection of points was done manually. Over the selected (short) data range, it is possible to calibrate (non-linearly) Indus-2 data with standard NSLS data. For more complicated analysis involving second neighbors and farther neighbors, extended data range is required. For such cases, a computer program with a Graphical User Interface (GUI) would be necessary.

5.4 High Pressure XAFS at Indus-2

The main effect of high pressure on compounds is reduction in inter-atomic distances, modifying the interaction between atoms. This can lead to phase transformations with large changes in the bonds: breaking of hybridization, delocalization of electrons, metallization of semiconductors, charge transfer between intra-molecular and inter-molecular bonds etc. The study of the structure of high pressure melts is of great interest to the scientific community worldwide, mainly because it would contribute to the understanding of the evolution of the earth, planetary cores and their magnetic fields, and also to the study of hydrothermal solutions in relation with mineral formation. Some chemical reactions need high pressure to occur or are more efficient under pressure, for e.g., large oxygen pressure allows for production of unusual oxidation states. Moreover, structural changes of materials under high pressure have direct bearing on practical applications, where they could be in nano-size and subject to high surface pressure. Additionally, high-pressure studies also provide data for the determination of accurate inter-atomic potentials used for condensed matter simulations.

Systems widely studied under pressure include Negative Thermal Expansion (NTE) materials[2930,98], Fe-based superconductors[31-32], Perovskites[99-100], nanoclusters[101-102], semiconductors[103] etc.. Problems of our current interest involve transitions at <40 GPa pressure. XAFS with synchrotron radiation is used to correlate changes in the local and electronic structures.

High Pressure (HP) XAFS experiments are Diamond Anvil Cell (DAC) based and therefore required highly focused, stable beam spot (described in detail in the following section). Energy Dispersive X-ray Absorption Spectroscopy (EDXAS) is best suited for studies at extreme conditions of pressure using DAC, where the strongly focusing crystal and the absence of movements provide the necessary small and stable focal spot, respectively. Moreover, from a practical point of view, Bragg reflections from the diamond anvils can be removed quickly from the energy range of interest, because the whole spectral range is observed simultaneously. Due to these characteristics, dedicated HP-XAFS beamlines worldwide are based on dispersive geometry, for e.g. ID24 (ESRF, France)[104], D11 (LURE, France).[105]

On the other hand, for high pressure studies using scanning beamline, sharp focussing optics is a pre-requisite for obtaining reasonable signal-to-noise ratio. Thus, in general, while a dispersive beamline is preferred for high pressure XAFS measurements, scanning beamline can also serve the purpose provided suitable focusing optics is available. We have performed one such experiment at the Hard X-ray microprobe beamline (P06), PETRA III synchrotron facility, Germany, by using the KB mirror system available at the beamline (focussed spot size ~ 250nm ×250nm). Our aim was to understand the effect of pressure on the local structure which might have implications on pressure dependent superconductivity in $PrOFe_{0.9}Co_{0.1}As$.[106] As-K edge (11.867 keV) XANES data were recorded as a function of pressure over 0-10 GPa. We have obtained a very good signal-to-noise ratio as shown in Fig. 5.6. Preliminary observations indicate that with increase in pressure, there is drop in intensity and area of XANES features, suggesting decrease in density of unoccupied states at Fermi Level. The most likely reason is charge transfer to As with pressure, resulting in possible change in metallicity across 2 GPa. Complementary studies are underway to corroborate XANES results with theory and pressure dependent T_c measurements. We have also planned to carry out detailed high pressure investigations in future on this system at Indus-2, especially at close pressure steps in the region of transition pressure (2 – 6 GPa) indicated from our preliminary study. In fact, to cater to the large user base of high pressure studies, we have initiated the installation of high pressure XAFS facility at Indus-2.

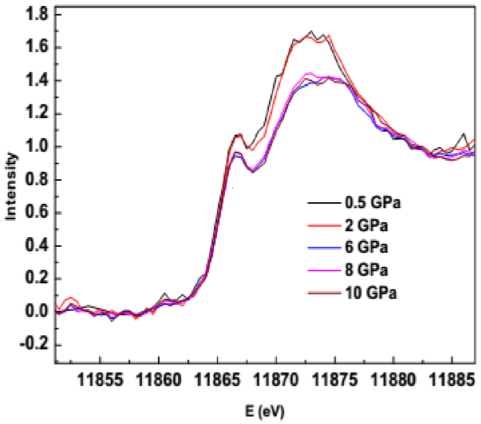

Fig. 5.6: As K edge XANES data on $PrOFe_{0.9}Co_{0.1}As$ as function of pressure

Under the present conditions, considering the lack of focusing optics at BL-09 (scanning type) and the advantages of dispersive geometry, we have utilized BL-08 (dispersive) for our HP-XAFS experiments[107] to the best of our ability. In the next sections, modification of the optical layout of BL-08 to accommodate HP-XAFS experiments is described. In future, we plan to explore possibilities of HP-XAFS experiments at BL-09 and also at Energy Dispersive X-ray Diffraction (ED-XRD) beamline (BL-11), by employing compound refractive lenses that are being developed at BL-07, Indus-2.[108]

5.4.1 Requirements of HP-XAFS

Diamond Anvil Cell (DAC)-based (Fig. 5.7(a)) HP-XAFS experiments have the following requirements:

5.4.1.1 Requirements for diamonds

The use of DACs for HP-XAFS results in distortion of XAFS spectra due to the Bragg reflections from the diamond anvils, restricted sample thickness, and reduced signal quality due to absorption by diamond at low energy (Fig. 5.7(b)). The Bragg reflection of the diamond anvils can suddenly reduce the transmitted intensity and makes a strong contribution to the measured attenuation of x-ray photons, i.e. glitches, at certain x-ray energies and orientations of the diamonds. These DAC Bragg glitches are often more intense than XAFS oscillations and hence spoil the high-quality XAFS data necessary for precise structural information. To counteract these problems, use of the following are recommended: (i) Thin diamonds (≤1mm) to reduce loss of intensity due to absorption by the diamonds (Fig. 5.7(b)). For experiments at energy ≤ 8keV, perforated diamonds (~ 500μm thickness) supported on a backing plate should be used. (ii) Nano-polycrystalline diamond instead of single crystal anvils. This significantly reduces the influence of diamond diffraction on XAFS data[109-110]

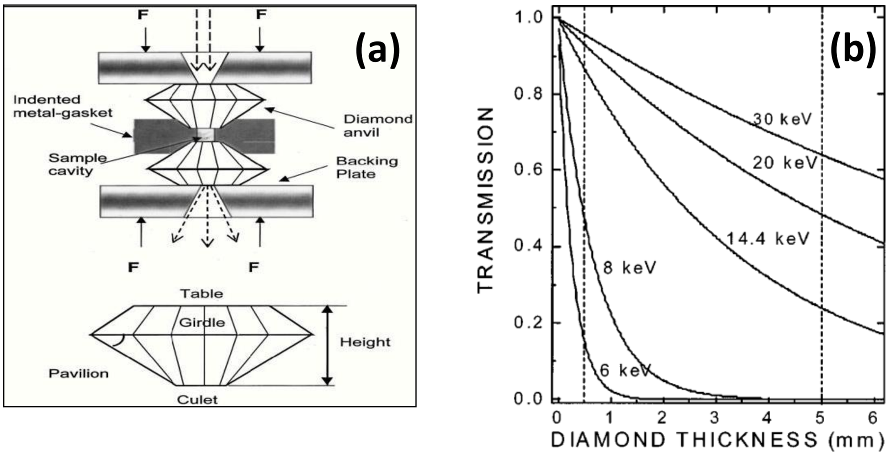

Fig. 5.7 (a) Schematic of Diamond Anvil Cell, (b) Plot of diamond thickness vs transmitted x-ray intensity through diamond.

5.4.1.2 Beam requirements

HP-XAFS experiments have stringent beam requirements:

(i) **Small beam size** to (a) ensure that the beam size is less than size of diamond window and (b) minimize beam footprint on the diamonds. [Characteristics of diamonds for HP XAFS are listed in Table 5.4[111]].

(ii) **Beam stability**-Because of small size of the sample, any movement can lead to reduction in beam intensity; therefore, it is important that the experiment be done under one constant condition.

(iii) **High flux** (~10^{12} photons/sec) to compensate for absorption in diamond window (Fig. 5.7(b)) and small sample size. [Note that signal-to-noise ratio requirement for XAFS: $\left(\frac{S}{N}=10^3\right)$].

Table 5.4: Characteristics of diamonds used for HP-XAFS	
Culet size	150-500µm
Gasket hole size	$\frac{1}{3}\times$ culet size = 50-150 µm
Sample size	30-120 µm

The beamline was originally designed for non-HPXAFS experiments with target spot size $(\sigma_H,\sigma_V)=(18,133)\mu m^2$ [112], assuming ideal source size and polychromator curvature. The target size for HP-XAFS: $(\sigma_H,\sigma_V)=(18,51)\mu m^2$ .by reduction of $\sigma_{V\ Expt}$.[113] However, in the present experimental setup at BL-08, the spot sizes at S_1 are much larger than theoretical values: $(\sigma_H,\sigma_V)=(192,460)\mu m^2$ *i.e.* mismatch factor $F_1\approx(6,3)$ for (σ_H,σ_V). Spot size enlargement could be partly from enlarged source size and scattering from some optical element; $\sigma_{H\ \exp tal}$ particularly increased as the polychromator has been relaxed from ideal curvature to avoid breaking of crystal. In principle, $\sigma_{H\ \exp tal}$ can be reduced by bending the polychromator. However, this is practically not feasible for HP-XAFS at ~10 keV due to space constraint (explained later). On the other hand, $\sigma_{V\ Expt}$ cannot be reduced further in the present setup due to fixed vertically focusing optics (pre-mirror). Reduction of $\sigma_{V\ Expt}$ is possible only with the inclusion of additional focusing element. Employing SHADOW[114] calculations with initial theoretical size $\sigma_V=133\mu m$, we had estimated the attainable spot size for different combinations of optical elements [113],: (i) simply replacing the present spherical pre-mirror

(M) with elliptical ($\sigma_V = 75\mu m$) (ii) elliptical pre-mirror M + elliptical post-polychromator mirror M_1 ($\sigma_V = 27\mu m$) (iii) present spherical pre-mirror M + elliptical post-mirror M1 ($\sigma_V = 51\mu m$).[113] While (ii) provides the ideal spot size for HP-XAFS, we decided temporarily not to disturb the current pre-mirror setup. Instead, we opted for (iii) to be installed between CC and S_1[115] (Fig. 5.8). The elliptical mirror has been designed for variable radii at different energy ranges. Since our starting beam size: $\sigma_{V\,\exp t} \approx 3\times\sigma_{V\,theory}$, it is understood that the targeted focal spot size cannot be attained with the mirror. Nevertheless, we have installed the mirror and discuss the alignment to obtain the best feasible spot size in the current situation.

Table 5.5: Spot size at q_H: H×V = $\sigma_H \times\sigma_V$	
$(\sigma_H \times\sigma_V)_{HP}$	30 μm ×30 μm
$(\sigma_H \times\sigma_V)_{Design}$	32 μm ×133 μm
$(\sigma_H \times\sigma_V)_{Experimental}$ [Ideal]	192 μm ×460 μm

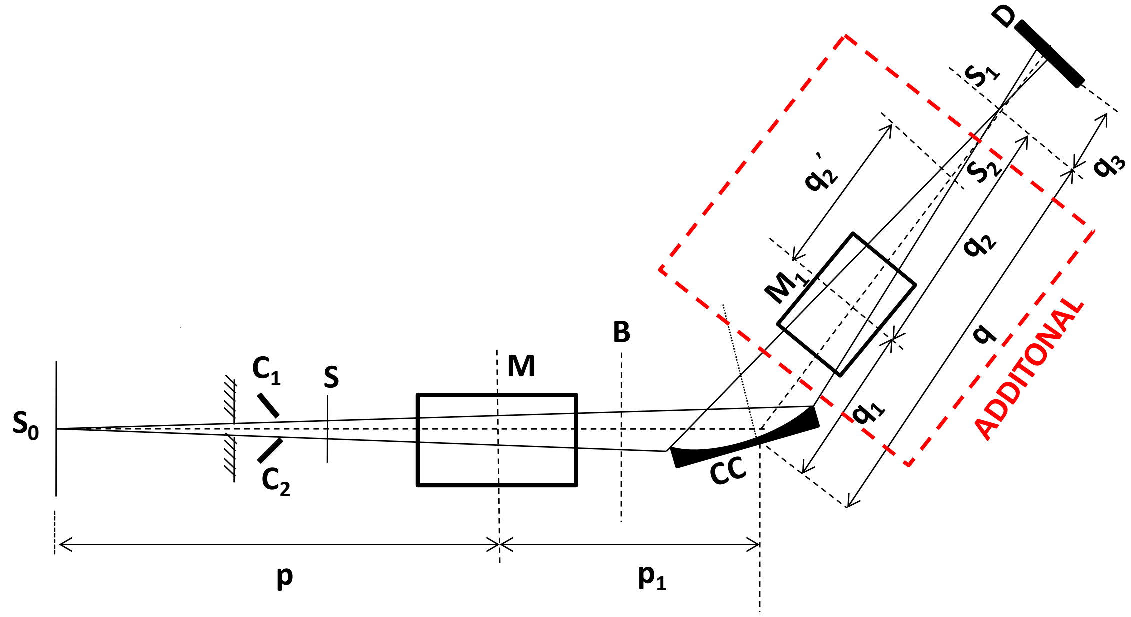

Fig. 5.8: Modified optical layout of BL-08 after inclusion of bendable elliptical post-mirror M_1

5.4.2 Design of post-mirror M$_1$

A major consideration in the design goal has been space-constraint. In this beamline, horizontal and vertical foci (q_H and q_V respectively, *wrt* CC) are non-equivalent, since different focusing elements are involved in horizontal (polychromator CC) and vertical (pre-mirror M) focusing. The function of M$_1$ would be to shift the vertical focal spot to the horizontal focal position so that $q_V^{'} = q_H$. Synchronizing horizontal and vertical foci at the same point would maximize the incident beam intensity. Since q_H is energy-dependent ($q_V = \text{constant}$), $[\frac{1}{p} + \frac{1}{q_H} = \frac{2}{R_{CC}\sin\theta_0}$;$[\sin\theta_0 \propto 1/E_0]$ and q_V energy-independent, M$_1$ radius should be varied accordingly to achieve synchronization at all energies.

$$R_{M1}(E) = \frac{2(q_2 q_2')}{(q_2 + q_2')\sin\theta_{M1}} \tag{5.9}$$

For the selection of geometry of mirror M$_1$, we considered both spherical and elliptical profiles for M$_1$. Ray tracing was carried out using SHADOW ray tracing program[116] for both these cases, and the spot sizes at the final image position S$_2$ were estimated. It was found that the spot size at the final image position was smaller when the post mirror M$_1$ was shaped in the form of elliptic cylinder.[113] Therefore, this particular geometry was selected for M$_1$.

The mirror was procured from SESO (France). Picture of the mirror system is shown in Fig. 5.9. It consists of a parallelepiped shaped mirror with two stepper motors. The system can be kinematically mounted inside a vacuum chamber using the 3 balls provided for mounting. Size and bending radius of the mirror were specified according to the space and focus distance available at the beamline. Substrate material and the location of mirror material on the substrate were customized for mechanical strength. Specifications of the mirror are listed in Table 5.6.

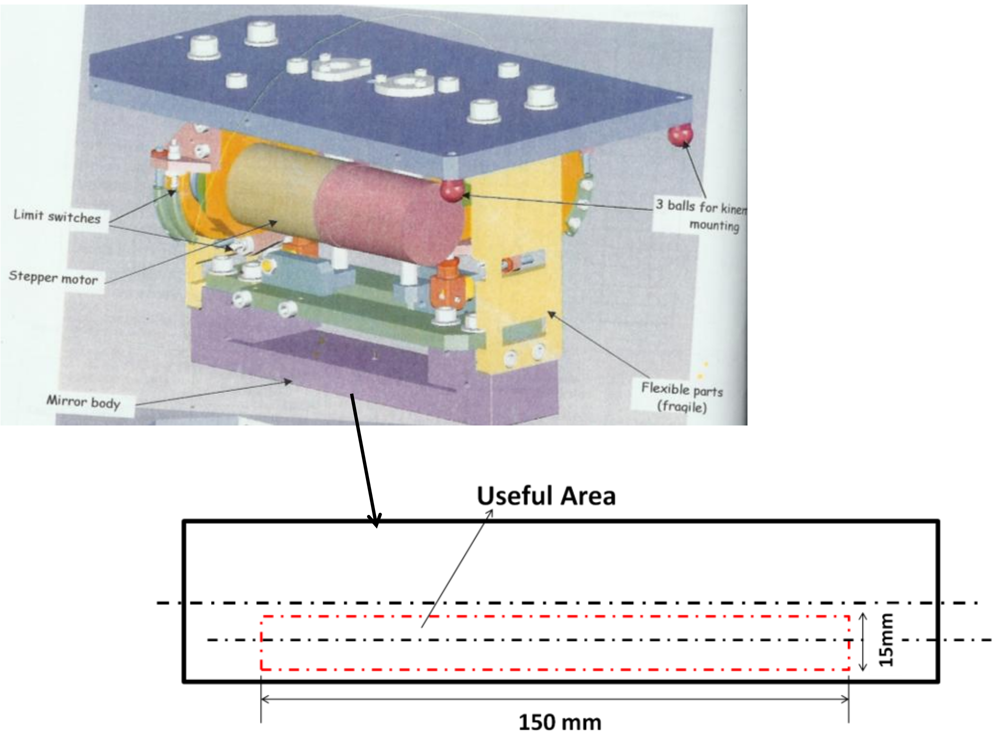

Fig. 5.9: Post-mirror design

Table 5.6: Post Mirror Specifications

Substrate	Glidcop
Coating	Rhodium (~500Å thickness)
Reflecting area	150mm×15mm
Shape	Elliptical cylinder (with bender)
Focus direction	Vertical
Radius (Variable)	0.442km-0.401km
Mirror chamber dimensions	340mm × 275mm

5.4.3 Feasibility tests to check the transmission of synchrotron radiation through diamond

To check the transmission of synchrotron radiation through diamond, feasibility test was performed at Sr K edge (~16 keV) at BL-08 (Beam current = 60mA, Ring energy = 2GeV) without M_1. At this energy, diamond absorption is less[117] (Fig. 5.7(b)). $SrRuO_3$ sample was ground to powder of average particle size ~ 5 μm and pasted uniformly on tape.[49] XAFS was measured both within and without the DAC (2 diamonds, each having thickness = 2mm). A Mao Bell type DAC, with anvil culet of diameter 400μm, was used for this experiment. The optimized spot size in this experiment was 192μm × 460μm (H×V). We obtained reasonable intensity signal for the DAC setup. The decrease in transmitted signal intensity was by ~40% when DAC was used (Fig. 5.10). Installation of M_1 would significantly improve the intensity, due to reduced spot size.

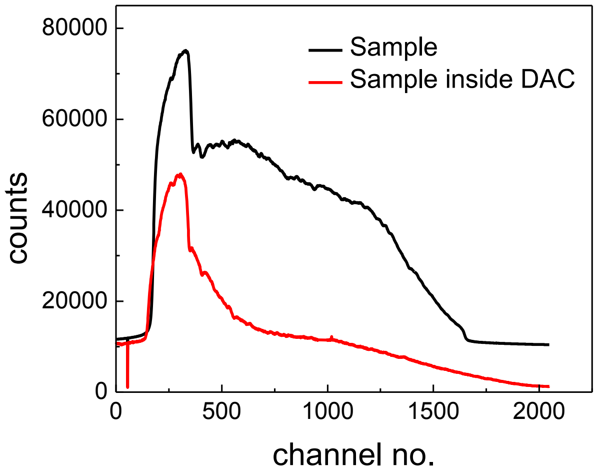

Fig. 5.10: Transmitted intensity through the sample without DAC (black curve) and with DAC (red curve).

5.4.4 Installation of the mirror

For feasibility test, we conducted the installation at the worst possible beamline condition i.e. minimum available space. The installation involved: (i) space estimation, (ii) Characterization of focal spot parameters in the current beamline i.e. without M1, (iii) inserting M1 and characterization of spot parameters at M1, (iv) alignment of M1 without bending, (v) Bending and characterization of final spot parameters.

(i) Estimation of Space availability

Fig. 5.11(a) shows the variation of available space ($= q_H(E)$) between CC chamber and S_1, for ideal focusing condition. The worst space condition corresponds to 0-available space after accommodating M1 chamber viz. $(q_H)_{\min} = 855mm$.[i] [Note that this chamber will be removed for regular / non-HPXAFS experiments so that XAFS at lower energies (< 12 keV) can be performed as per design goal.]

From Fig. 5.11(a), $(q_H)_{\min} = 855mm$ corresponds to $E_0 = 12keV$. Thus, it is clear that M1 can be accommodated without any problem for $E_0 > 12keV$. For $E_0 < 12keV$, additional space would have to be created in order to accommodate chamber M1 by focusing at $(q_H)_{\min}[> (q_H)_{ideal}]$. This would require relaxation of the polychromator (R_{CC}) from its design goal, resulting in compromised energy band Δ*E*. [(ΔE =380 eV, k_{max} = 10 $Å^{-1}$) is sufficient for XANES and first shell EXAFS analysis. Larger energy band (k_{max} > 10 $Å^{-1}$) is encouraged to obtain well-resolved peaks in real space and accommodate more fitting variables for higher shell EXAFS analysis.] To determine the bandwidth (Δ*E*) attainable in the compromised geometry, we have calculated R_{CC} (E) and ΔE (E) for the worst condition ($q_H = (q_H)_{\min} = 855mm$), at E_0= 10keV, from the equations below:

$\Delta E = E_0 l \cot\theta_0 \left[\frac{1}{R_{CC}} - \frac{\sin\theta_0}{p}\right]$, where $\frac{1}{R_{CC}} = \frac{\sin\theta_0}{2}\left[\frac{1}{p+p_1} + \frac{1}{q_H}\right]$, and l = illuminated length of CC.[112] The results are plotted in Fig. 5.11(b); k_{max} = 10 $Å^{-1}$ corresponds to $E_0 = 7keV$. It is clearly possible to carry out XANES and first shell EXAFS analysis for

---

[i] Radius of CC chamber = 400mm, Length of M1 chamber = 340mm, S_1 stage protrusion length = 115mm. Therefore, minimum space condition = (400+340+115) mm = 855mm

$E_0 < 7keV$, which may be sufficient for problems involving catalysts, amorphous alloys. Complicated higher shell EXAFS analysis is possible only for $E_0 \geq 7keV$.

For the first phase of commissioning, we have considered Cu K edge = 8.979 keV. For first-hand experience, we created 200 mm extra (*wrt* minimum condition) space for mirror translation by focusing the polychromator beam at $q_H (=1100mm) > | q_H |_{\min}$. This was achieved by relaxing crystal curvature ($R_{CC} = 0.0105km$), which resulted in compromised energy-bandwidth ($\Delta E = 500eV, k_{\max} = 11.5$ Å^{-1}).

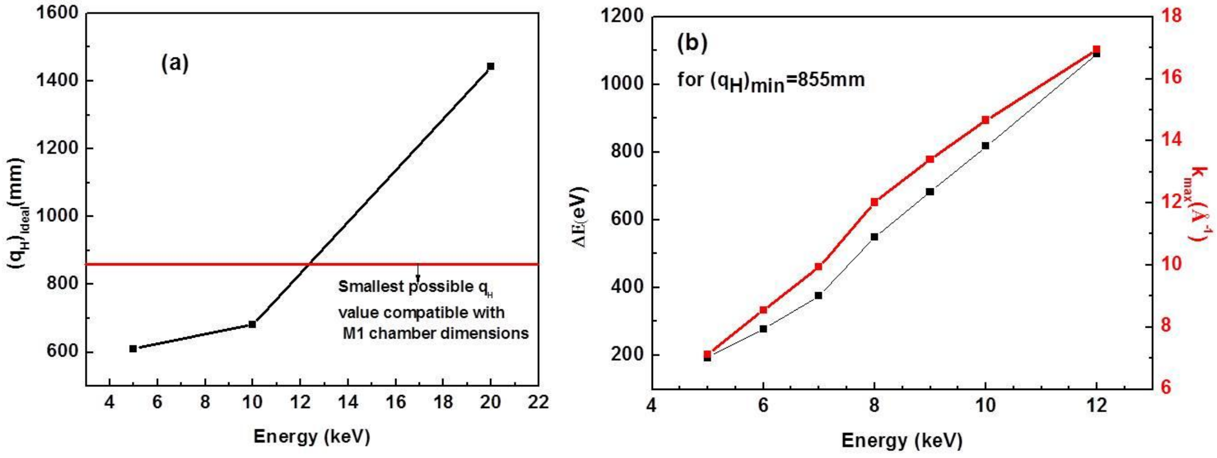

Fig. 5.11: (a) Space available between CC and S$_1$, (b) Plot of ΔE and k_{max} vs E for $(q_H)_{\min}$

Table 5.7: BL-08 parameters at E$_0$=10keV			
	Design	Experimental (Ideal)	Experimental (relaxed polychromator)
Bragg angle, θ_0	11.4°	11.4°	11.4°
Radius of CC, R_{CC}	0.063 km	0.063 km	0.011 km
Energy bandwidth, ΔE	1123 eV	700 eV	500eV
q_H	641 mm	900 mm	1100 mm
σ_H	32 µm	192 µm	338 µm
σ_V	140 µm	460 µm	460 µm

(ii) Characterization of primary focal spot: *Pre-Mirror* (M) and CC

<u>Primary spot parameters</u>:

The spot size was measured in units of number-of-pixels: [$pixel = (13.5,13.5)\mu m^2$]. To locate the primary focal point at Cu *K*-edge, the CCD was translated along the beam direction and spot size was measured as function of q in Fig.5.12. The smallest spot size obtained in the relaxed CC configuration: $\sigma_H = 338\mu m$ at $q_H = 1120mm$ and $\sigma_V = 460\mu m$ at $q_V = 1240mm$. Since the radius of curvature of pre-mirror M is very large, the variation in σ_V with distance is small (within 10 µm). Thus, extra crystal relaxation introduces extra mismatch factor $F_2 = (1.7,1)$. The net mismatch factor after this stage is

$$F_{CC} = F_2 \times F_1 \approx (10,3) \qquad (5.11)$$

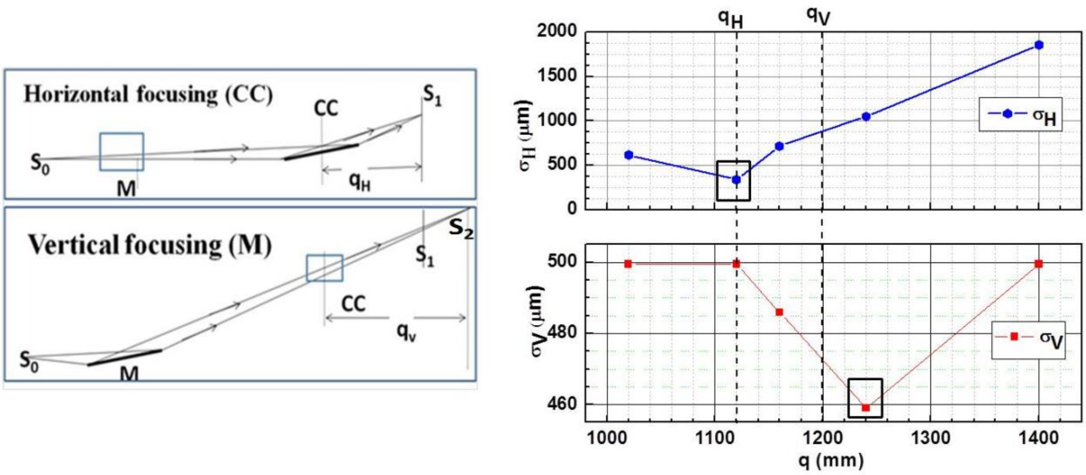

Fig. 5.12: Horizontal and vertical focusing

(i) Post Mirror (M_1): Determining spot parameters at M_1

Post-mirror (M1) was placed between CC and S1 (Fig. 5.13). Accommodating CC and mirror chambers within $q_H = 1120mm$, the allowed q_1-range = 570-835 mm. For convenience, we have placed the mirror at $q_1 = 620mm$.

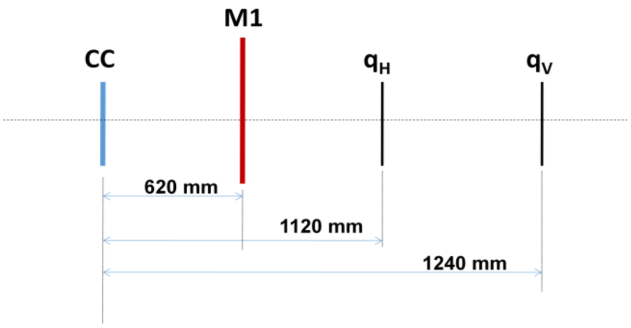

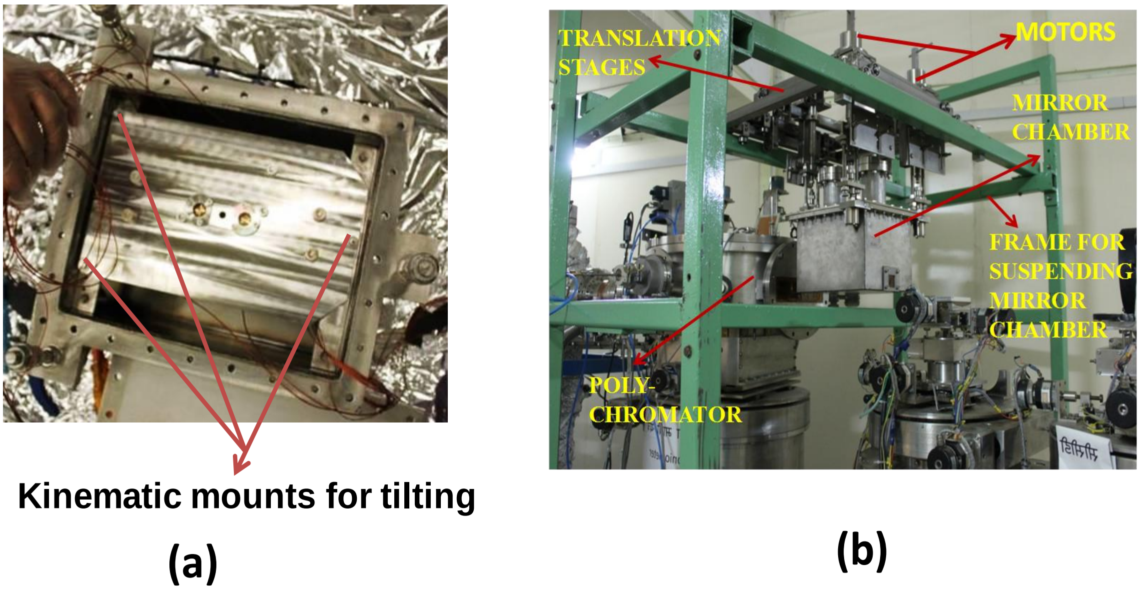

(a)

(b)

Fig. 5.13: Photograph of (a) Mirror chamber with the mirror installed, (b) BL-08 with the post mirror in place

The spot parameters at M_1 were derived from the mirror geometry, shown in Fig. 5.14a.[112.] Post mirror parameters are listed in Table 5.8.

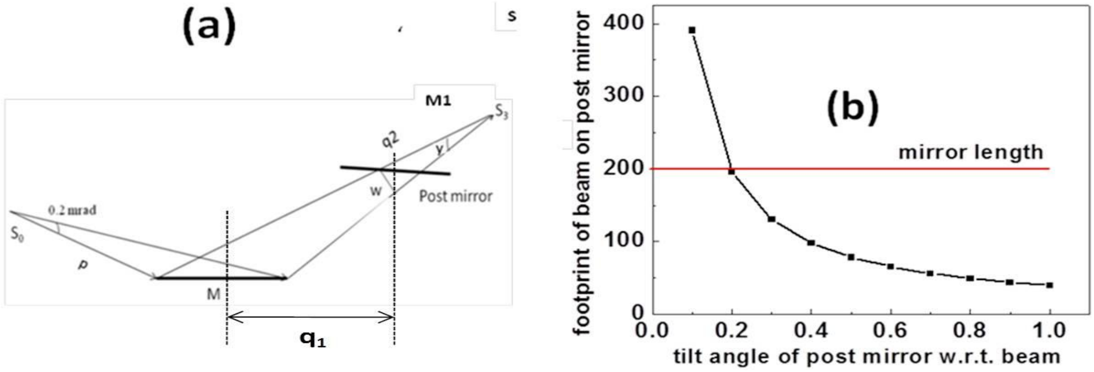

Fig. 5.14 (a) Post mirror parameters, (b) Footprint of beam on the post mirror

Table 5.8: Parameters for post mirror M1		
	Formula used	**Calculated value**
CC-M1 distance (q_1)	q_1	620 mm
$(q_1)_{min}$	Radius of CC chamber (=400 mm)+ 0.5×length of M1 chamber	570 mm
M1-q_v distance	q_v-q_1	620 mm
M1-q_H distance	q_H-q_1=q_2’	500 mm
Vertical angle subtended by pre-mirror at $q_v(\gamma)$	$\frac{p\times 0.2}{(2000+q_V)}$	1.11 mrad
Width of beam falling on M1 (w)	$(q_V - q_1)\times\gamma$	0.68 mm
Footprint of beam on M1 (l)	$\frac{w}{\tan\phi}$	Plotted in Fig. 5.12(b)

Although under these alignment conditions $(q_1)_{\min} = 570mm$, we have placed M_1 at a farther distance so that it can be translated along the beam direction both towards and away from CC. Fig. 5.14b shows the variation of footprint of the beam on M1 as function of ϕ. Clearly, the footprint is larger than the mirror itself for $\phi < 0.2°$. Therefore the mirror must be placed at $\phi \geq 0.2°$ to the beam.

(ii) Post-mirror (M_1) Alignment (0-bending)

While the procurement of automated mirror accessories (e.g. translation stage etc.) is in process, we conducted the alignment procedure with manual setup (Fig. 5.13). The setup consists of a mirror chamber mounted on frame. The mirror was placed inside this chamber on three kinematic mounts, which are used for tilting the mirror *wrt* the beam. There are two stages for translating the mirror perpendicular to and along the beam. The mirror alignment procedure described below and summarized in Table 5.9.

(a) 0-angle alignment *wrt* beam :

The pre-mirror, M, is at angle $\theta_M = 0.2^o$ *wrt* beam. Therefore, beam angle at M$_1$, $\theta_{M1} = 0.4^o$. Desired angle of M1 *wrt* horizontal for 0-angle alignment *wrt* beam = 0.4°. To place the mirror at 0-angle *wrt* the beam, we calculate the height difference (h) between the ends of the mirror corresponding to 0.4° angle:

$$h = l\,(=340\,mm) \times \tan\,(0.4°) = 2.4mm\,, \tag{5.12}$$

where l is the length of the chamber.

Subsequently, the mirror was placed such that its two ends (along the beam axis) had a height difference h.

(b) Bringing mirror down into the beam

Standard half-cut procedure was followed in which M$_1$ was slowly lowered into the beam path until only half of the beam was visible (vertically) on CCD.

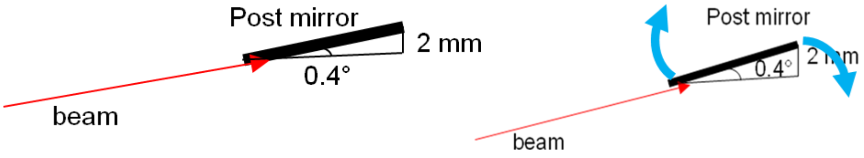

(c) Tilting the mirror

The target tilt angle was set at $\phi = 0.2^O (< \phi_c^{Rh} = 0.4^O)$. Experimentally, ϕ was determined from the vertical separation (= c) between direct and reflected beam spots on CCD:

$$\phi = \tan^{-1}(\frac{c}{q3})\ i.e.\phi = 0.2^O \Rightarrow c = 1500\mu m\,. \tag{5.13}$$

The mirror was tilted until the desired separation was obtained (Fig. 5.15).

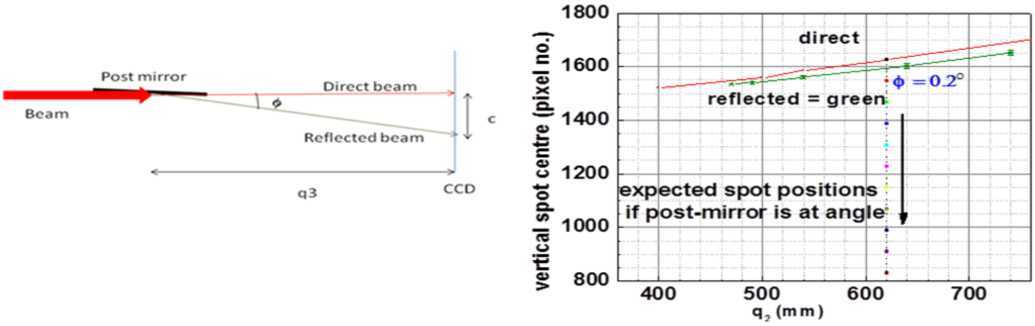

Fig. 5.15: Tilting the mirror

(iii) Bending post-mirror M_1:

Requisite M_1-radius:

$$R_{M1} = \frac{2q_2 q_2'}{(q_2 + q_2')\sin(0.2^\circ)} = \frac{2\times 620\times 500}{1100\times \sin 0.2^\circ} = 0.158km \tag{5.14}$$

Where $q_2 = q_V - q_1, q_2' = q_H - q_1.$ (5.15)

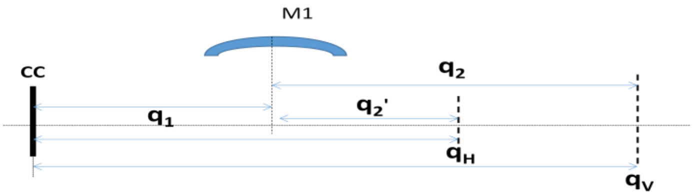

The mirror is bent by two stepper-motor driven actuators (M_A, M_B) [Fig. 5.16].

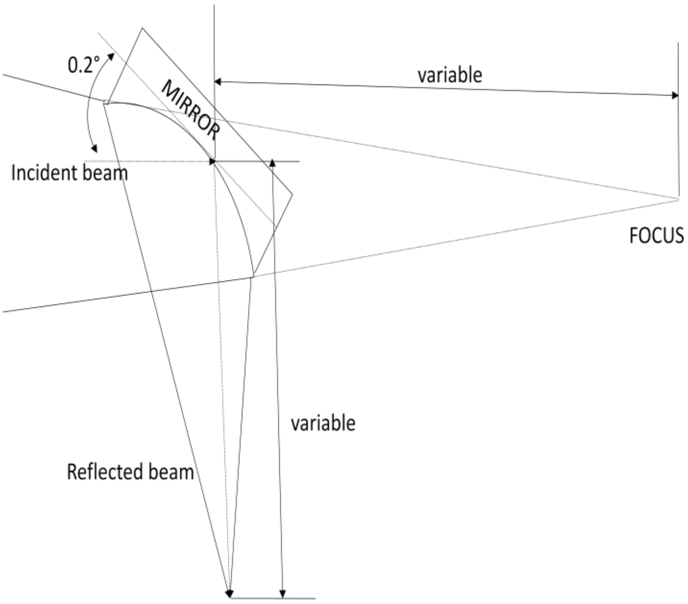

Fig. 5.16: Schematic diagram of elliptically bent mirror

Elliptical shape is represented by

$$z = A1x^2 + A2x^3; \qquad (5.16)$$

$$\begin{aligned} A1 &= K1 + K2(N1 + N2) \\ A2 &= K3 + K4(N1 - N2) \end{aligned}, \qquad (5.17)$$

where (N_1, N_2) = number of half-steps for (M_A, M_B) and (K_1, K_2, K_3, K_4) are mirror constants. ($N_1 \neq N_2 \Rightarrow$ non-spherical shape).

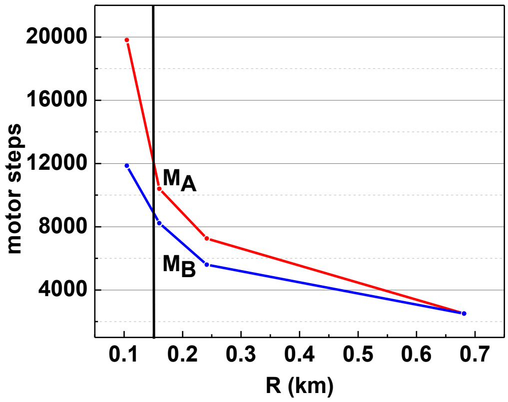

Fig. 5.17: Number of steps required for motors M_A and M_B, to obtain focused spot

From Fig. 5.17, $(N_1, N_2)_{R_1}$ was calculated and input into the motor-control program (developed by M/S SESO). Elliptical surface curvature was confirmed as the spot position remained static while M1 was translated along the beam direction. The final spot S_2 (Fig. 5.18) has size $(\sigma_H, \sigma_V) = (338, 220)\mu m^2$. Bending-induced spot reduction $\sigma_V = 360 \xrightarrow[R_1]{} 220 \mu m$. M_1-demagnification

$$f_{M1} = \frac{q_2'}{q_2} = 0.8. \qquad (5.18)$$

(iv) Recording XAFS spectrum of *Cu* foil

Cu foil was placed at sample position S_1 and *Cu K*- edge (8.979 keV) XAFS spectrum was recorded in transmission mode (Fig. 5.19). The data quality is reasonably good, with Signal-Noise ratio ~ 3×10^2.

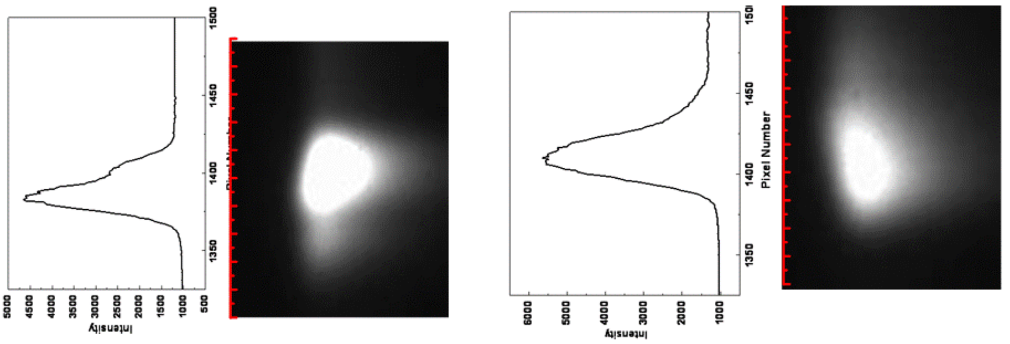

Reflected beam from M

Reflected beam (from M1,without bending)

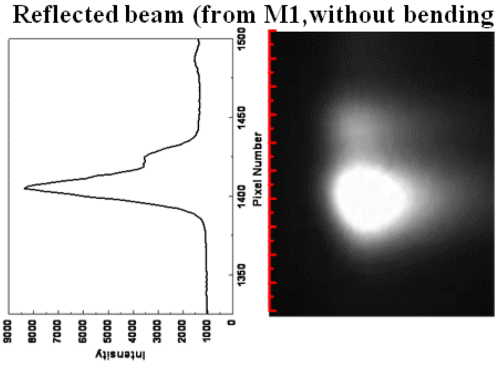

Focused reflected beam (from bent M1)

Fig. 5.18: Focal spot photograph

This was a concentrated sample. For dilute samples, although we expect the data to be noisier, the effect of focusing would be more prominent.

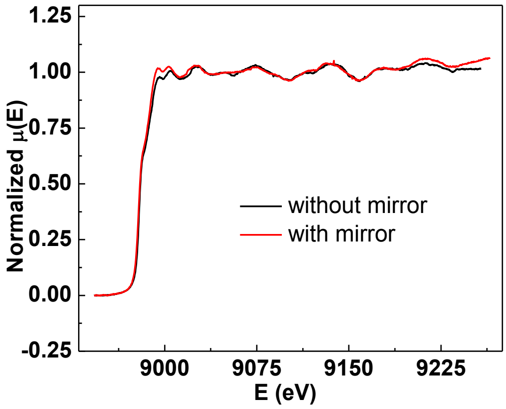

Fig. 5.19: XAFS spectrum of Cu foil

<table>
<tr><th colspan="4">Table 5.9 : Summary of alignment procedure for M1</th></tr>
<tr><td></td><td></td><td>Symbol/Formula</td><td>Value</td></tr>
<tr><td>1.</td><td colspan="3">Zero-angle alignment <i>wrt</i> beam
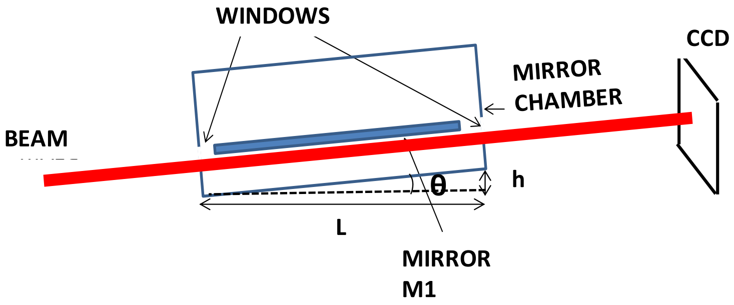

M1 was aligned parallel to the beam</td></tr>
<tr><td></td><td>Pre-Mirror angle <i>wrt</i> beam,</td><td>θ_M</td><td>0.2°</td></tr>
<tr><td></td><td>Post Mirror angle <i>wrt</i> horizontal (for 0° alignment)</td><td>θ_{M1}</td><td>0.4°</td></tr>
<tr><td></td><td>Mirror chamber length</td><td>L</td><td>340 mm</td></tr>
<tr><td></td><td>Height difference between the ends of mirror chamber corresponding to θ_{M1}=0.4°</td><td>$h = L \tan \theta_{M1}$</td><td>2.4 mm</td></tr>
<tr><td>2.</td><td colspan="3">Bringing mirror down into the beam (Half cutting the beam)
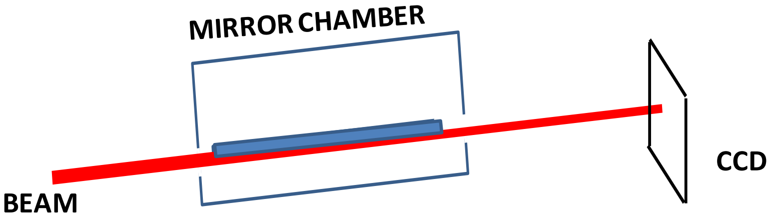
</td></tr>
<tr><td>3.</td><td colspan="3">Centering the beam
The mirror was translated along the beam direction until there was no shift in beam spot position on the CCD. This ensured that the beam was centred on the mirror.</td></tr>
<tr><td>4.</td><td colspan="3">Tilting the mirror <i>wrt</i> the beam
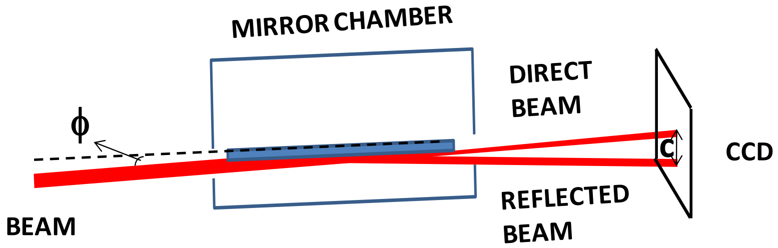

Separation between direct and reflected beam (c) on the CCD determines tilt angle of the mirror. (Tilt angle should be less than critical angle of mirror coating material, $\phi_c^{Rh} = 0.4°$).</td></tr>
</table>

	The mirror was tilted until the desired separation was obtained		
	Table5.9 continued		
	M1-CCD distance	q_3	430 mm
	Separation between direct and reflected spot on CCD	c	
	Desired tilt angle of mirror	ϕ	0.2°
	Desired value of c corresponding to $\phi = 0.2°$	$c = q3 \times \tan\phi$	1500μm (~111 pixels)
	Size of unfocused, reflected beam	338 μm×360μm	
5.	**Maximizing reflected intensity** ϕ was further increased till the intensity started to drop. The value of ϕ corresponding to maximum reflected intensity was just below this angle.		

Table 5.10: Post mirror focusing parameters

	Design	**Experimental**	**Mismatch Factor** $F_{M1} = \frac{(f_{M1})_{experimental}}{(f_{M1})_{design}}$
$(\sigma_V)_{pre-bending}$ [reflected spot]	140 μm	360μm	
$(\sigma_V)_{post-bending}$	40μm	220μm	
$f_{M1} = \frac{q_H - q_1}{q_V - q_1}$	0.35	0.8	2.1

5.4.5 Scope of improvement

$\begin{pmatrix} \sigma_H = 338 \\ \sigma_V = 220 \end{pmatrix}_{expt} = \begin{pmatrix} F_H = 10 \\ F_V = 4 \end{pmatrix} \times \begin{pmatrix} \sigma_H = 32 \\ \sigma_V = 58 \end{pmatrix}_{design}$ *i.e.* the experimental spot size is significantly larger than design goal. The mismatch in horizontal spot size is very large and due to large increase (worst condition) in horizontal focusing distance (q_H). The purpose of extending focal spot farther was to (i) accommodate mirror chamber in limited space and (ii) relax the polychromator crystal and avoid breaking due to bending. In principle, we can moderate the setup (within space constraint) by bringing the horizontal focus closer to design goal viz. $q_H = 920mm$. Recalculation with $q_H = 920mm$ confirms simultaneous reduction of $(\sigma_H, \sigma_V) = (277{,}130)\mu m^2$. By reducing mirror chamber size, we can create extra 140 mm space *i.e.* $(q_H)_{\min} = 715mm$ and obtain $(\sigma_H, \sigma_V) = (215{,}55)\mu m^2$ (Fig. 5.20). This is the best we can achieve in the near future, with design modification and minimal space constraint.

For future, we may consider replacement of spherical pre-mirror with elliptical. As demonstrated from our SHADOW calculations[113] , this would result in $\sigma_V = 27\mu m$. Besides, optics that leads to large initial beam size must be identified and replaced.

Thus, we conclude that for (< 10 keV), the main limitation of spot size will be in the horizontal direction due to space constraint.

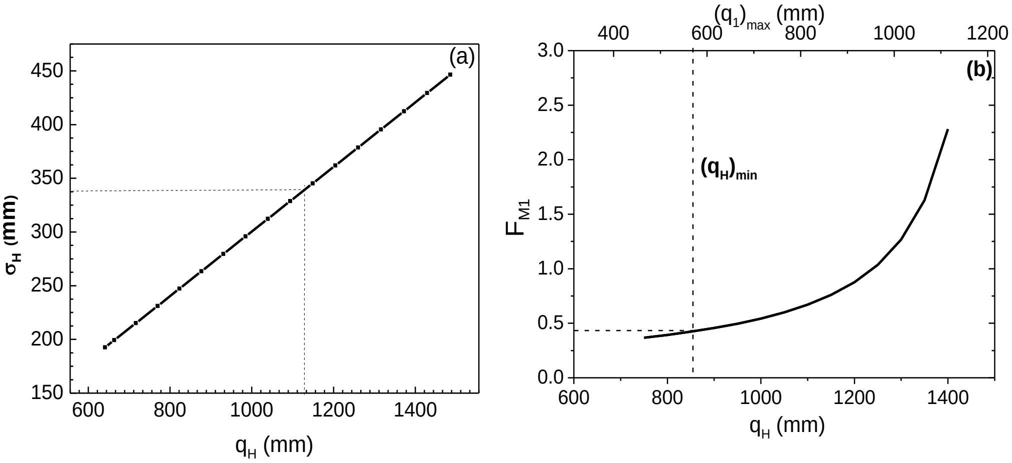

Fig. 5.20: Plot of (a) q_H vs horizontal spot size σ_H, and (b) M1 demagnification vs q_H

5.5 Low Temperature XAFS at Indus-2

Low temperature XAFS experiments have gained impetus over the years, due to the growing importance of understanding short-range-order (SRO) changes across magneto-electronic phase transitions ($T_c << 300K$).[118-122] In Ref. 43, long-range structural phase transition temperature did not coincide with superconducting transition temperature for $La_{2-x}Sr_xCuO_4$. In Ref.44, temperature-evolution of long-range-order could not explain pairing mechanism in $La_{1.6-x}Sr_xNd_{0.4}CuO_4$. These paradoxes could be solved by XAFS detection of distortions on local scale (<5%): viz. changes in disorder, Jahn-Teller distortion, octahedral tilts, buckling angle etc.

To cater to the increasing demand of low-temperature XAFS, low-temperature XAFS-compatible closed cycle displex cryostat [DE-210, Advanced Research System (USA)] has been commissioned at Indus-2 under the initiative of Bhabha Atomic Research Centre (BARC), Mumbai (India) and Raja Ramanna Centre for Advanced Technology (RRCAT), Indore (India). Since XAFS analysis is based on Fourier analysis of oscillations, any noise can lead to spurious peaks in real space and convey false information. Therefore, XAFS has stringent requirement of noise elimination [Signal-to-noise ratio, $S/N = 10^3$]. Design parameters of the cryostat are listed in Table 5.11.

Table 5.11. Specifications of XAFS compatible cryostat

Design Parameter	**Specification**
Vibration Amplitude	15μm
Operational Temperature Range	4.2-300K
Heat Capacity	$0.8W @ 60Hz @ 4.2K$
Windows	Kapton[ii] [<5μm thickness]

We have assessed the feasibility of low temperature XAFS experiments by measuring temperature-dependent XAFS on known system. We discuss the feasibility in

---

[ii] Selected for its x-ray transparency, low coefficient of thermal expansion, mechanical strength, non-toxicity and low cost.

terms of (i) temperature range that can be covered *i.e.* identifying phase transitions with T_c in this range (ii) data quality and reproducibility with international standards (iii) temperature calibration and (iv) temperature resolution with which the phase transition can be mapped (generally, phase transition spreads across 20K).

Most of the phase transitions of our current interest occur in the temperature range 50-250 K [e.g. spintronic material $Sr_{1-y}Ca_yRu_{1-x}Ti_xO_3$ $(T_C = 165K)$[123-125]; Fe-based superconductors $(T_C \sim 55K)$[55,126], spin glass $YBaCo_4O_7$ $(T_c = 65K)$[127-128],half-metallic $CeMnNi_4$ $(T_c = 140K)$.[50] Correspondingly, we have selected standard *Au* foil for feasibility test and standardization, since *Au L3* XAFS shows significant and standardized DWF evolution [$\sigma^2_{Debye}(T)$] in this temperature range. Debye Model predicts $\sigma^2_{Debye}(T)$ function for metals (*Au*). The Debye Temperature, [$(\Theta_{Debye})_{Au} = 165K$], denotes the temperature beyond which $\frac{d}{dT}(\sigma^2_{Debye}(T)$ remains constant. Being metal-specific, it can be used for temperature calibration. Experimental $(\Theta_{Debye})_{Au}$ can be obtained from $\sigma^2_{\exp t}(T)$, by Debye Model fitting (option in FEFFIT) of temperature-dependent experimental XAFS data. The actual temperature (T') of the foil can then be determined and compared with the temperature readout (T_{set}) from sensor. This method of temperature calibration (using XAFS standard Au foil) is unique since it is directly based on the sample and bypasses any error (e.g. loose connectivity) in the electronic circuit of the sensor. Although the cryostat features two sensors (described below in section 5.5.1), this method of calibration would be particularly useful when these sensors fail. Besides electronic error, there could be systematic error in data due to absorption in windows, contraction of windows at low-temperature (though probability is low), condensation of water etc., leading to extra noise in the data. Calibrating with XAFS on standard foil would provide first-hand evaluation of these sources of systematic error.

5.5.1. Closed Cycle Displex Cryostat- Description of Components

Fig. 5.21 shows the schematic diagram (A-E) of the low temperature setup that operates on the principle of Gifford McMahon refrigeration cycle.

A. Expander: Expander (DE210) is the heart of the cryostat where the cooling cycle takes place. Sample holder is mounted on the cold head of the cryostat. Sample holder (Fig. 5.3) is insulated from the atmosphere by radiation shield and vacuum shroud.

B. Compressor: Compressor (ARS-10 HW) provides the requisite He gas flow rate for operating the expander.

C. Sample Holder: Sample Holder consists of two plates made of highly conducting material like Cu to ensure good thermal conductivity. The sample is sandwiched between the two plates. It is mounted on the cold head.

D. Gas lines: Two gas lines connect the expander to the compressor – one supplies high pressure *He* gas to the expander and the other returns low pressure *He* gas from the expander.

E. Chiller: Water-chiller (3TB10WC1X, Werner Finley Pvt. Ltd.) is connected to the compressor to circulate chilled water and maintain the temperature of *He*- gas at 15^{o}C.

F. Temperature controller: Temperature controller (Lakeshore Cryotronics) is connected to the cold head by Cernox sensor (CX-SD, Lakeshore Cryotronics) [Cernox is ideal due to its (i) temperature range 100mK -420K, (ii) high sensitivity at low temperatures (iii) excellent resistance to ionizing radiation.] and to the sample by silicon diode sensor. The controller has closed loop PID (Proportional-Integral-

Derivative) controlled outputs. In this mode, the controller attempts to keep the load at exactly the user defined setpoint, which can be entered in temperature. This is done by using feedback from the control sensor to calculate and actively adjust the control (heater) output.

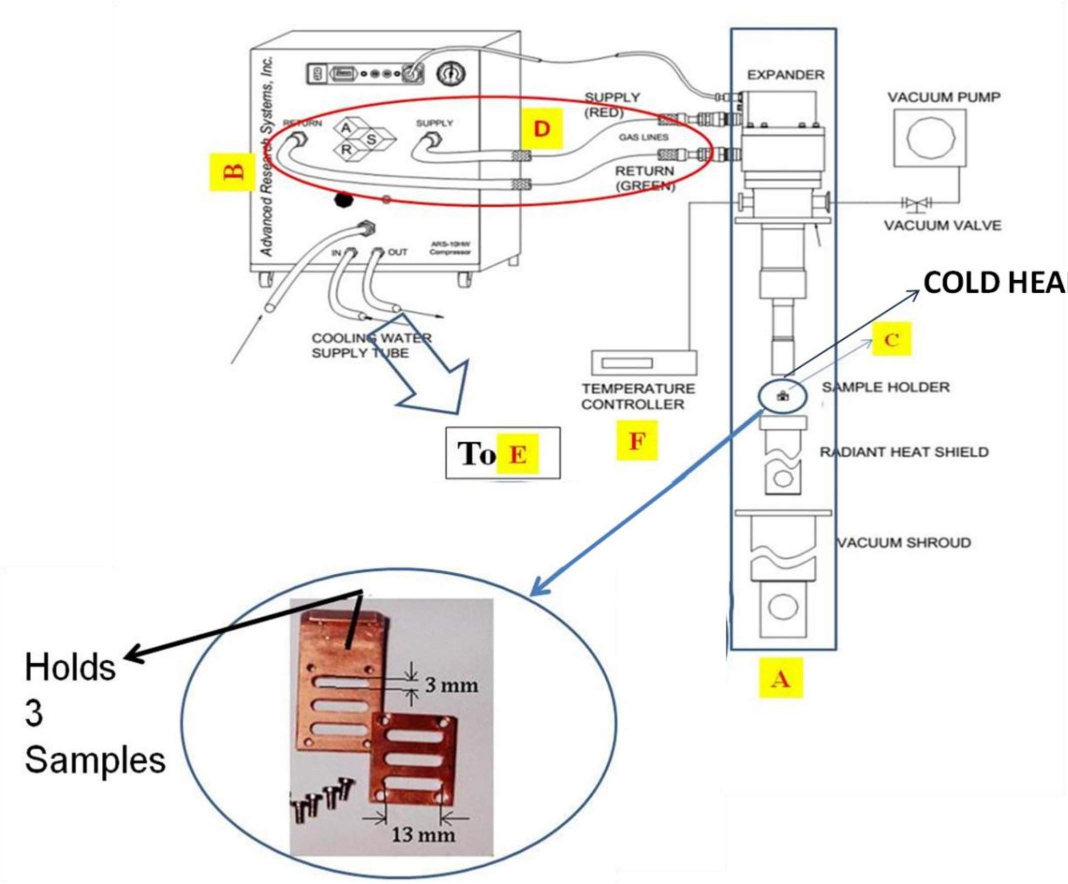

Fig. 5.21: Schematic diagram of low temperature setup

5.5.2. Principle of operation

The cryostat works on the pneumatically driven Gifford McMahon refrigeration cycle (Fig. 5.22), in four main stages:

I. The valve disk rotates, opening the high pressure path and allowing high pressure *He* gas to pass through the regenerating material into the expansion space.[129]

II. The pressure differential drives the piston "up" allowing the gas at the bottom to expand and cool.

III. The valve disk rotates and opens the low pressure path, allowing the cold gas to flow through the regenerating material, hence removing heat from the system.

IV. The pressure differential returns the displacer to its original position, completing the cycle.

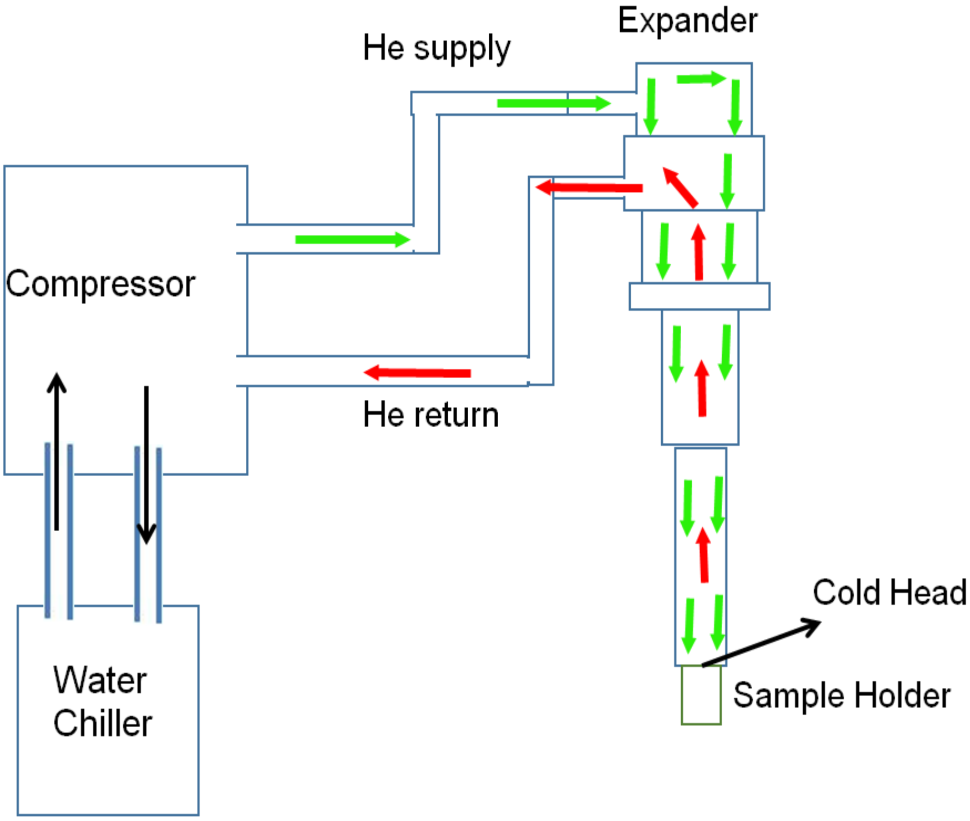

Fig.5.22: Schematic diagram of low temperature setup. Green arrows depict He being supplied to the expander for cooling. Red arrows depict return cycle of He.

5.5.3 Calibration of the Cryostat

Calibration of the cryostat was undertaken at scanning XAFS beamline (BL-09). Fig. 5.23 shows schematic of BL-09. A pair of *Si(111)* crystals in parallel geometry functions as Double Crystal Monochromator (DCM), which is used for energy selection from the white synchrotron beam. A 1.5 m long, Rh/Pt coated horizontal pre-mirror with meridionial cylindrical curvature is used to obtain collimated beam on the first crystal of DCM and to reject higher harmonics from the beam. Incident (I_0) and transmitted (I_t) / fluorescent (I_f) intensities from the sample are measured using N_2/Ar filled ionization chambers. The absorption data for the sample are recorded by scanning the DCM over the entire energy range of interest.

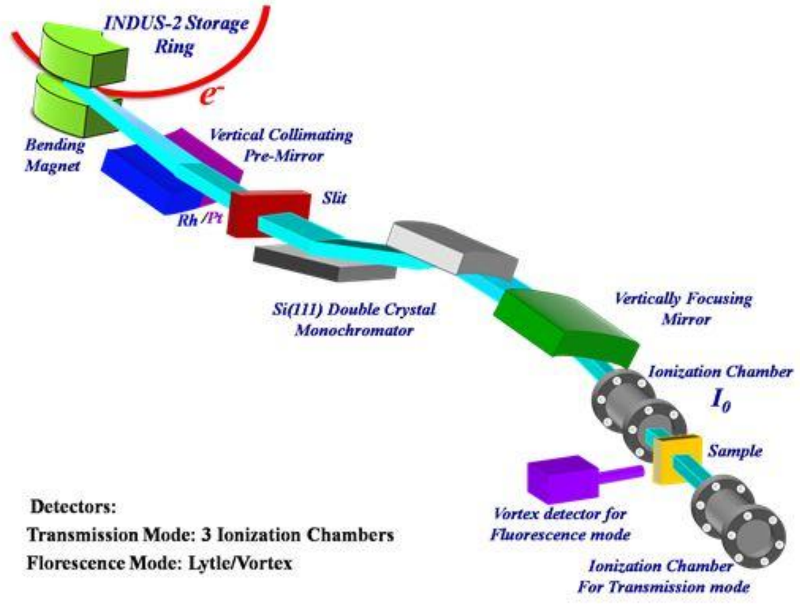

Fig. 5.23: Schematic diagram of BL-09

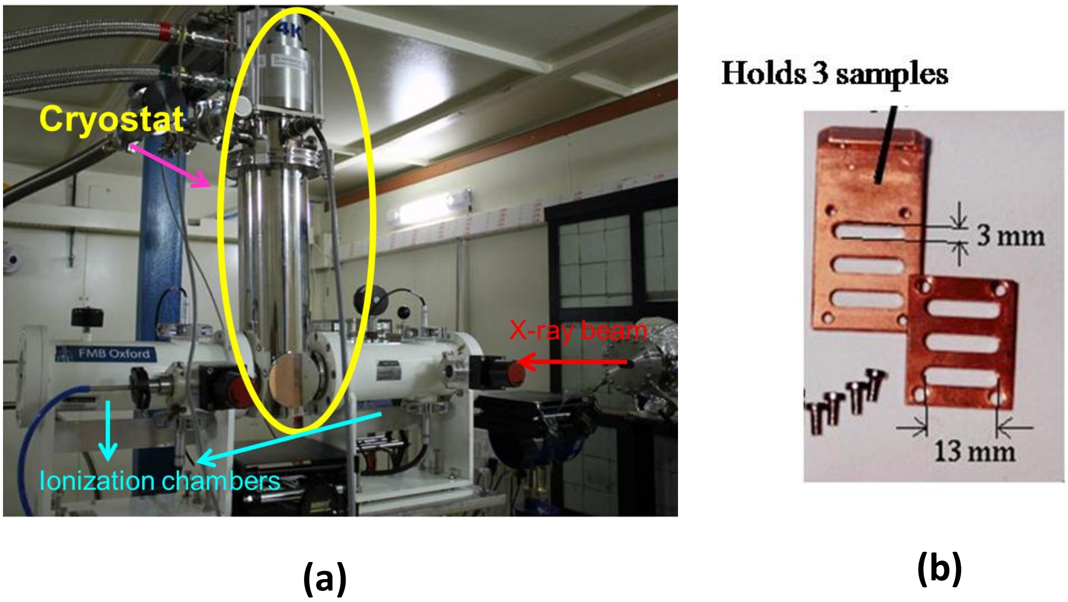

Fig 5.24: Photograph of (a) BL-09 experimental station with the cryostat in place, (b) Cu sample holder

The Au foil (thickness, $t = 5\mu m$) was sandwiched between two plates of *Cu* sample holder (ensuring good thermal contact) (Fig. 5.24(b)), which in turn was mounted on the cold head of the cryostat. The cryostat was mounted at the sample position at BL-09 (Fig. 5.24 (a)). Distance of each ion chamber from the sample was adjusted to minimize leakage of fluorescence photons (from the sample) into the chamber. By optimizing all these factors, we could obtain good signal-to-noise ratio. The size of the *Au* foil [$15mm \times 10mm$] was large enough to utilize the entire beam [$1mm \times 0.2mm$].

First room temperature (RT) data of the foil was measured, both *before* and *after* inserting into cryostat: the spectra were reproducible (Fig. 5.25(a-b)), ruling out any impact of absorption by the cryostat windows. Subsequently XAFS at lower temperatures were measured. The temperature was controlled using the sensor located at the sample holder-cold head interface, since, being closer to the sample, it is a better representation of the temperature at the sample.

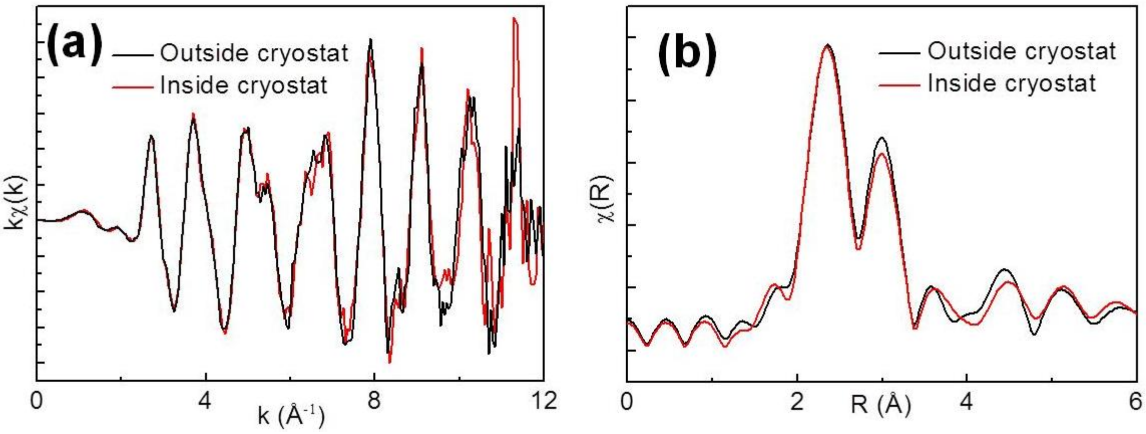

Fig. 5.25: Comparison of Au foil XAFS data recorded outside and inside the cryostat at room temperature in (a) k-space, (b) R-space

Obtaining good quality data with low noise (signal-to-noise ratio ~ 10^3) is very important – in this case, data quality determines the precision of the calibration. Signal-to-noise ratio depends on several factors: (i) gas pressure in the ion chambers, (ii) geometry, particularly the distance between the sample and the ion chambers (iii) beam stability (iv) sample quality. Our initial temperature-dependent data on Au foil was extremely noisy (Fig. 5.26). At higher *k*-range $(> 6\text{Å}^{-1})$, background fluctuations were comparable with reduced data amplitude (due to DWF effect), rendering the data extremely noisy and unusable. When this data was Fourier-transformed, it did not give rise to the expected temperature evolution, leading us to think that the cryostat was not cooling properly. The most likely reasons for poor data quality were (i) inadequate gas (or pressure) in the ion chamber detectors, (ii) fluorescence leakage (due to current space limitations) into the ion chamber. Fluorescence photons add non-trivial background signal that is difficult to remove and causes fluctuation in data (iii) small fluctuations in the beam (iv) sample thickness inhomogeneity. (iv) condensation of water on the cryostat windows.

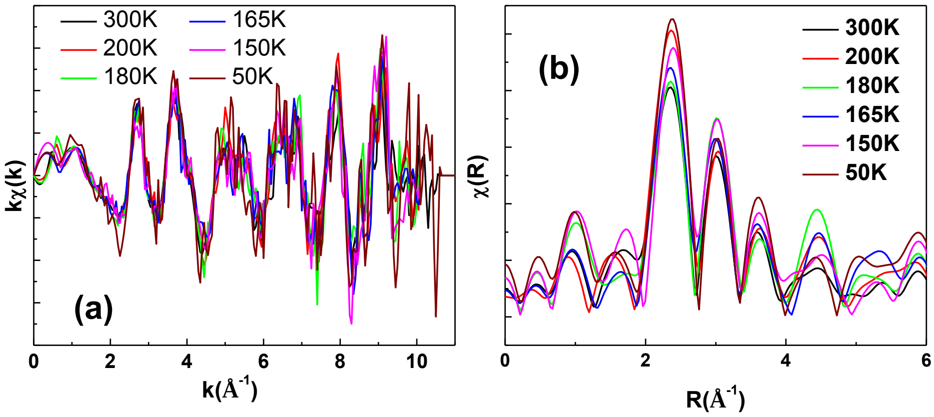

Fig. 5.26: Initial attempt at low temperature data collection

To improve the data quality, the following measures were implemented: (i) The inner components of the cryostat were wrapped with Aluminized mylar sheets to prevent outgassing and absorb any thermal radiation from the shielding materials.[130] (ii) The cryostat windows were removed, greased and re-sealed to prevent vacuum leak (and hence water-condensation). (iii) The second Ionization Chamber (used for measuring transmitted intensity from the sample) was moved farther from the sample to reduce fluorescence leakage (in this configuration, the fluorescence leakage was estimated to be only 0.02% of the total signal). (iv) Both the Ionization Chambers were evacuated and re-filled with appropriate gases. This time, we obtained good quality data for all temperature points in the range 50-300K (Fig. 5.27 (a-b)) [Note that we did not measure *Au* for 10-50K, since no variation is expected for this foil. Earlier, we had tested the cryostat down to 5K]. No condensation was visibly observed on the cryostat windows at low temperatures (In case there is any moisture, we have the option of blowing it away with dry nitrogen gas); no change was observed in the windows (contraction etc.) at low temperature.

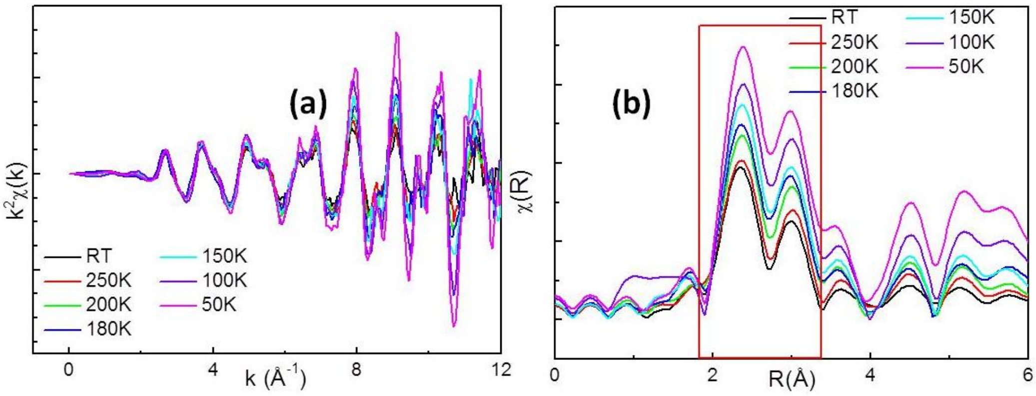

Fig. 5.27: Temperature dependent XAFS data on *Au* foil recorded at BL-09 in (a) k-space, (b) R-space

Au foil data from BL-09 were processed using ATHENA[83] and the extracted XAFS oscillations, $\chi(k)$, were Fourier transformed into real space for fitting. Fitting data involves (i) structural modeling using ATOMS[88] [space group= $fm3m\,(fcc)$, a = 4.08Å], (ii) generation of theoretical XAFS scattering amplitudes and phase shifts using FEFF6[89] (iii) Data fitting with FEFFIT [89] using the scattering parameter output of FEFF6.

We first compared the room temperature XAFS data of *Au* foil (inside/ outside cryostat) with international standard viz. *Au* foil at APS (USA) (Fig.5.28). Indus-2 and APS datasets are slightly phase-shifted relative to each other; this could be due to small optical misalignment at beamline e.g. slight loss of parallelism between the monochromator crystals. Small energy correction ($\Delta E_0 = 3eV$) to APS data, using ATHENA, matches it with Indus-2 data. (Fig.5.29). There is small difference in amplitudes (DWF) of Indus-2 and APS XAFS data, which is due to small variation in foil quality.

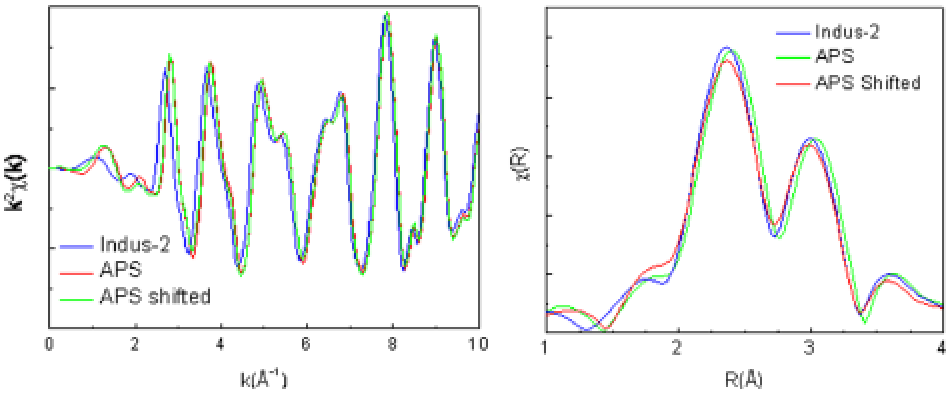

Fig. 5.28: Comparison of RT Au foil data (Indus-2) (blue line) with standard Au foil (RT) data from APS (USA) (green line). Phase mismatch between the two data could be corrected with small energy correction ΔE_0=3eV (red line).

For DWF analysis of our XAFS data, we considered fit range $k-range=2.8-10Å^{-1}, R-range=1.8-3.4Å$, which includes contributions from nearest *Au* neighbors at $R=2.88Å\ (N=12)$. To minimize error bars, eliminate systematic error in analysis (for example, leakage of background into first peak) and perform temperature calibration with maximum accuracy, various comprehensive strategies were employed to fit the temperature-dependent XAFS data unambiguously. These include (i) fitting individual datasets; (ii) simultaneous fitting of datasets for different temperatures, varying common $[S_0^2, R]$ but different DWF between the datasets; (iii) simultaneous fitting of datasets for different temperatures using Debye Model *i.e.* varying common $[\Theta_D, S_0^2, R]$: $\Theta_D = 163K \pm 2K$ was obtained. *R*-factor was considered as an estimate of fit quality[88,97]; comparison between data and fit spectra, for RT and 50K, is shown in Fig.5.29.

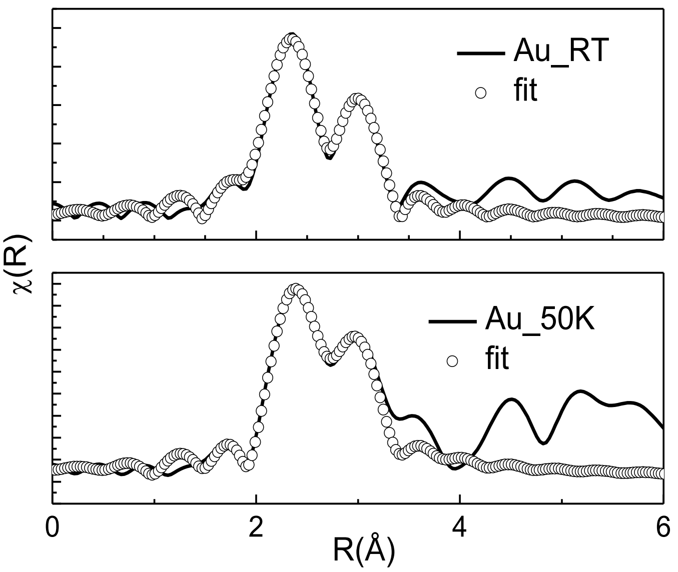

Fig. 5.29: Comparison between data and fit for *Au* foil data at RT and at 50K.

DWF fit results, from strategies (i-iii), are shown in Table 5.12 and plotted in Fig. 5.30(a). The results, from all these strategies, agree with each other within error bars. We have generated theoretical DWF evolution curves from Debye Model (Fig. 5.30(a)), using 'NOFIT' option in FEFFIT[89], for $\Theta_D = 160K, 165K \; and \; 170K.$. We have compared the experimental results from strategies (i-iii) with these theoretical curves. Our XAFS fit results ($\Theta_D = 163K$) match closely with the theoretical curve (Fig. 5.30(a)) corresponding to $\Theta_D = 165K$, assuring credibility of temperature calibration. [Small deviations in $\sigma^2_{\exp t}(T)$ from Debye curve could be due to an-harmonic vibration components present in the foil, which are not taken into account in Debye Model. The deviations are contained within $\Delta\Theta_D = \pm 5K$.]. The error bars in $\sigma^2_{\exp t}(T)$ correspond to temperature uncertainty $\Delta T \leq 5K$ on the same curve. From Θ_D value obtained using strategy (iii), we deduce the relation between the readout temperature of the sensor, $T_{readout}$, and actual temperature of the foil, T': $(\Theta_D)_{Au} = 165K; [(\Theta_D)_{Au}]_{Exptal} = 163K$

$$\Rightarrow T' = T_{readout} - 2K. \qquad (5.19)$$

Fig. 5.30(b) shows the final comparison of our XAFS-derived temperature $T^{'}$ *vs*. readout temperature of the sensor $T_{readout}$.

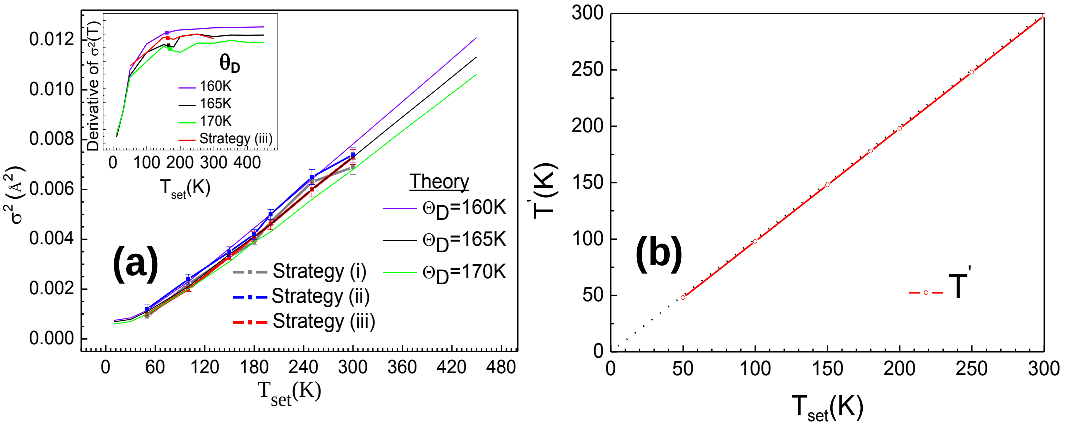

Fig. 5.30: (a). Evolution of DWF with temperature. Strategies (i) and (ii) involve fitting the data without using Debye Model. In (i), datasets for different temperatures were fit individually while in (ii), they were fit simultaneously. Strategy (iii) involved simultaneous fitting of the datasets using Debye Model. [Inset shows the derivative of the theoretical curves for different Θ_D (160K, 165K, 170K). Θ_D(marked by solid square) represents the Temperature beyond which the rate of change of derivative remains constant. (b) Plot of temperature of foil (T$^{'}$) vs temperature readout of the sensor (T$_{set}$)

To summarize, we have obtained good quality XAFS data on *Au* foil in the temperature range 50-300K. The data is free of artifact related to absorption inside cryostat etc., as room temperature XAFS data, recorded inside cryostat, matches well with that measured outside the cryostat and with international data. XAFS-derived $\sigma^2_{\exp t}(T)$ matches well with theoretical Debye model generated $\sigma^2_{Debye}(T)$ and experimental $(\Theta_{Debye})_{Au}$ is determined to be within ± 2K of the theoretical value. The .minimum temperature step size, for low temperature-dependent XAFS experiments, is determined to be $\Delta T = 5K$. We expect the calibration to be as good for metallic samples in general. For insulating samples, adequate temperature accuracy can be attained if thin and uniform samples (on tape / pellets) are sandwiched between the plates of Cu sample holder.[49,50,55,120]

Table 5.12 : XAFS Fit results for Au foil

$T_{set}(K)$	σ^2_{Au-Au}(Å^2)		
	Strategy (i)	**Strategy (ii)**	**Strategy (iii)**
300	0.0069 (2)	0.0074 (3)	0.0073 (3)
250	0.0063 (1)	0.0065 (3)	0.0060 (3)
200	0.0047 (1)	0.0050 (2)	0.0046 (2)
180	0.0039 (1)	0.0042 (2)	0.0041 (2)
150	0.0033 (1)	0.0035 (2)	0.0033 (1)
100	0.0022 (1)	0.0024 (2)	0.0020 (1)
50	0.0009 (0)	0.0012 (2)	0.0010 (0)

Following this commissioning of low temperature XAFS facility at Indus-2, we plan to pursue lower (<50 K) temperature-XAFS of non-standard samples in the future. As mentioned earlier, we had already tested and confirmed temperature stability down to 5 K; XAFS data, at lower temperature, is expected to have large signal-to-noise ratio (*i.e.* very good quality), due to lower DWF. The entire sample series (e.g. different dopant concentrations plus one standard) will be fixed onto vertically separated multi-slot sample holder (Fig.5.23). At each temperature point, all the samples will be measured in turn by vertical adjustment of the sample stage. [Since samples tend to condense at low temperature, sample centers could shift slightly (~0.1mm) and should be re-adjusted at every temperature]. This configuration would not only increase data collection efficiency but maintain the same temperature calibration for all the samples of the series.

5.6 Conclusions

We have commissioned high pressure and low temperature XAFS facilities at Indus-2. For high pressure XAFS experiments at ED-XAS beamline (BL-08), we have installed bendable elliptical mirror M1 designed for the reduction of vertical spot size. We have aligned the mirror at *Cu K* edge (8.979 keV) energy. By combination of pre-mirror, polychromator CC and post mirror M1, we could obtain spot size $338\mu m \times 220\mu m$. We have suggested several corrections for further improvement in the spot size. Overall, the suggested corrections are feasible and we are optimistic about carrying out HP EXAFS experiments for $E \geq 9keV$, and XANES and first shell EXAFS analysis for $5keV \leq E \leq 9keV$.

For low temperature XAFS experiments, we have installed displex closed cycle cryostat. The cryostat was tested down to 5 K. We have critically evaluated the feasibility of performing low temperature XAFS experiments using this cryostat at scanning XAFS beamline (BL-09). For this purpose, temperature-dependent (50-300K) XAFS were measured for standard *Au* foil and $\sigma^2_{\exp t}(T)$ obtained from fitting the data. The highlights of our results are (i) Data are reproducible inside and outside cryostat (thus ruling out systematic error from window absorption etc.) and match well with international XAFS data on Au foil. (ii) Data quality is sufficiently good to reduce uncertainties in fit results. (iii) Our $\sigma^2_{\exp t}(T)$ results matched with standard Debye Model [$\sigma^2_{Debye}(T)$] for Au, thus confirming temperature calibration (±2K) of the cryostat. (iv) Temperature accuracy: $\Delta T \leq \pm 5K$. This demonstrates the feasibility of measuring any structural phase transition over 50-300K and mapping the transition in steps of 5K; in principle, the transition temperature range can be extended down to 5K. Systems with $Z = 26 - 42; \geq 63$ are compatible with the energy range available at BL-09 and should be in pellet/foil/ribbon form for low temperature experiments.

CHAPTER 6

XAFS CHARACTERIZATION OF EMBEDDED BIMETALLIC NANOCLUSTERS IN MULTILAYER FILM

6.1. Background

Bimetallic magnetic NCs embedded in non-magnetic matrix have gained impetus due to their ability wide-ranged applications. The employment of a matrix gives an additional degree of freedom and allows tuning the properties depending on the particle arrangement within the matrix. Additionally, the matrix stabilizes the NCs (even those present in non-equilibrium state), protects them from the environment, arrests their position and prevents coalescence. They are widely employed in (i) opto-electronic devices (for their large third-order susceptibility with pico second response time)[131] ((ii) surface lubricants for MEMS switch contacts; (iii) ultra high density data storage.[132-133] (iv) Catalysis[134-136], including specific reactions like hydrogenation of olefins and structural rearrangement (of Carbon skeleton) in hydrocarbons[137], decontamination of ground water[138], *Metal-filled carbon nanotubes* as electrocatalysts in fuel cells.[139]

Wetting being an issue in electronic devices, a dry method of synthesis would be advantageous. Several dry synthesis methods viz. lithography[140], co-sputtering[141], ion implantation[142], laser ablation[143] have also been used previously for embedded NC synthesis. Over the years, Ion irradiation has gained importance as a method for synthesis/modification/characterization materials depending on the energy of the incident ions (~keV to GeV).[144] Ion irradiation results in a variety of ion-solid interactions, including (i) incorporation of ions into the solid, (ii) creation of vacancies (defects and interstitials), (iii) sputtering (ejection of atoms and molecules), depending on the energy of the incident ion. Energetic ions, during their passage through a material lose energy via two processes: Nuclear energy loss S_n and electronic energy loss S_e. S_n refers to energy loss due to elastic collisions of the incident ions with the atoms in the material, and is dominant at low energies (~ keV to 1 MeV). It results in atomic displacement from their lattice sites either by ejection from the surface or by relocation within the solid. S_e refers to the energy lost by inelastic collisions of the ion with the atoms in the material, leading to ionization or excitation of the atoms. It is dominant at high energies (>>1MeV).

In multilayer (ML) thin films, MeV ion irradiation has been observed to introduce a number of effects with interesting consequences. In magnetic *Co/Pt* MLs, interfacial mixing induced by ion irradiation resulted in spin-reorientation transition, and change of giant magnetoresistance.[145] Small concentrations of magnetic impurity in non magnetic layers of a magnetic ML, which can cause changes in magnetic coupling and magnetoresistance[146], can be introduced in the non-magnetic layers by ion irradiation. In general, irradiation induced inter-layer mixing, interfacial broadening and period dilation is commonly observed in MLs[147-148], as demonstrated in several previous reports.[149- 152]

A *Pt/C* ML has been used as a regular X-ray mirror.[153-154] Addition of a *Ni* layer is expected to extend the functional energy range beyond 80 keV, i.e. beyond the *Pt* K-edge. Ion irradiation of the mirror was intended to simulate the defects that could possibly be induced by high-flux, high-energy X-rays, in order to understand device functionality.

However, the main impact of this work lies beyond mirror assessment in terms of damage. Instead, we explore the possibility/feasibility to synthesize bimetallic (magnetic) *Ni/Pt* clusters on (non-magnetic) *C* matrix by ion irradiation of *Pt/Ni/C* multilayer (ML). *C* is selected for its low density (2.5g/cc) and high stiffness (> glass). Additionally, Carbon can provide magnetic isolation between neighboring clusters, which causes the reduction of inter-particle exchange coupling.

This method would be unique in the sense that, if successful, it would lead to the generation of ML structure which contains alternating layers of magnetic clusters embedded in non-magnetic matrix separated by magnetic layers.

Herein, the control parameter for composition of the bimetallic clusters will not be limited to thermodynamics alone, but can be controlled by collision kinetics, initial thickness of the layers and interfacial integrity.

6.2 Sample Synthesis details

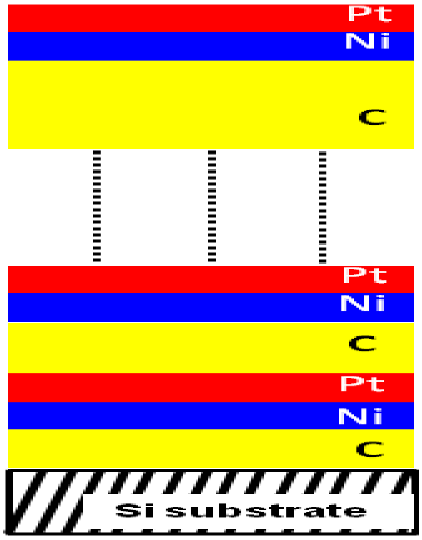

Fig. 6.1: Schematic of the deposited multilayer

A depth graded *Pt/Ni/C* multi tri-layer (15 tri-layers in the multilayer stack), in which the thickness of the *C* layer gradually varies with depth, was prepared by alternate deposition of *Pt, Ni* and *C* layers on a 30mm×70mm float glass substrate by ion beam sputtering technique [155,167] at a low Argon pressure of 0.1 mbar. Tri-layer periodicity, *d* ~ 7 nm. Schematic of the multilayer is shown in Fig. 6.1. 20mm ×4mm pieces of the sample were cut and irradiated with 2 MeV Au^{2+} ions 2×10^{15} ions/cm^2 at the 3MV Pelletron accelerator at the Institute of Physics, Bhubhaneshwar (India).

6.3 Structural characterization of the ML pre-and post-irradiation

Several techniques can be used to probe ion-irradiation induced changes in MLs. Transmission Electron Microscopy (TEM) and Scanning Electron Microscopy (SEM) can be used to gain insight into the multilayer structure. X-ray Reflectivity (XRR) and Neutron Reflectometry can be used to determine roughness and thickness of individual layers. X-ray Fluorescence (XRF) is generally used to detect inter-layer mixing, X-ray Photoelectron Spectroscopy (XPS) can be used to chemically characterize the surface of the ML.

In this work, micro-structural details of the ML were derived using X-ray Reflectivity (XRR), X-ray Fluorescence (XRF) and Transmission Electron Microscopy (TEM).[157]

TEM measurements on the samples[157] revealed well separated Pt, Ni and C layers in the pre-irradiated (pristine) ML (Fig. 6.2). The irradiated ML shows mixing between the layers and some dark spots in the C layers[157], which could be nanoscale particles of higher density material within the C layers. Negative heat of mixing between Ni and Pt favors formation of Ni-Pt alloy. In contrast, positive heat of mixing between Ni and C and Pt and C favors segregation. Therefore, the observed clusters are likely to contain Ni and Pt. The average diameter of the clusters was determined to be ~ 1.7 nm, with size dispersion of ~10 %. The average inter-cluster separation was determined to be ~ 3.6 (0.9) nm and 0.8 (0.1) nm across the plane of C layer.[157]

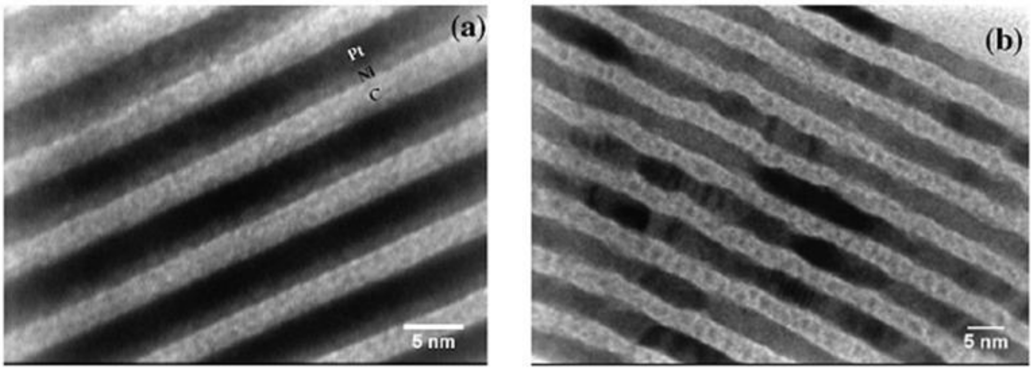

Fig. 6.2: XTEM micrographs of (a) pristine and (b) irradiated (ion fluence = 2×10^{15} ions/cm^2) samples. [157]

XRR and XRF were recorded in X-ray Standing Wave mode to overcome the limitations of conventional XRR and XRF.

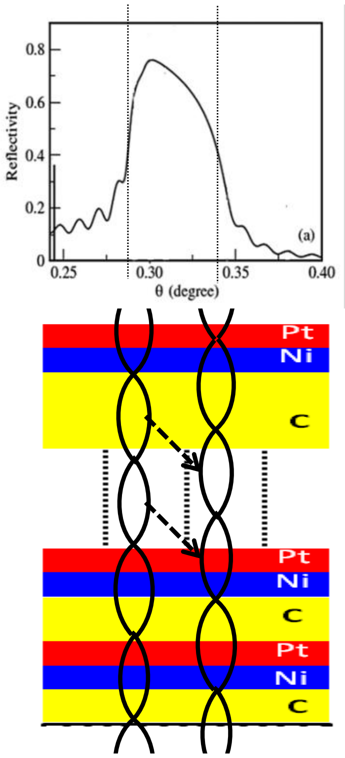

Fig. 6.3: Illustration of formation of standing waves of X-rays in Pt/Ni/C Multilayer. As the angle of incidence increases through the diffraction peak region (top), antinodes move from the low electron-density medium (C layers) to the high electron-density medium (Pt layers) (bottom).

The XSW technique is extensively used in condensed matter science. In a periodic ML, XSW are generated when Bragg diffraction occurs from the

ML.[156] The standing wave pattern has the periodicity of the corresponding diffraction planes (typically 0.2 nm). In this case atomic displacements of typically one-hundredth of this distance (i.e. 2 pm) can be detected, along with details of the displacement direction (inward or outward). Details of XSW technique are given in the next section. Fig. 6.3 schematically shows the formation of standing wave patterns while a first order Bragg diffraction of x-rays occurs from a periodic ML. At the rising edge of the Bragg peak, the antinodes of the standing wave are in the C layers. As the grazing angle of incidence advances through the Bragg peak, the standing wave pattern moves inward finally moving by half the ML period (*d*) at the falling edge of the Bragg peak, where the antinodes coincide with the Pt layers. The intensity of emission of fluorescence is proportional to the intensity of x rays.

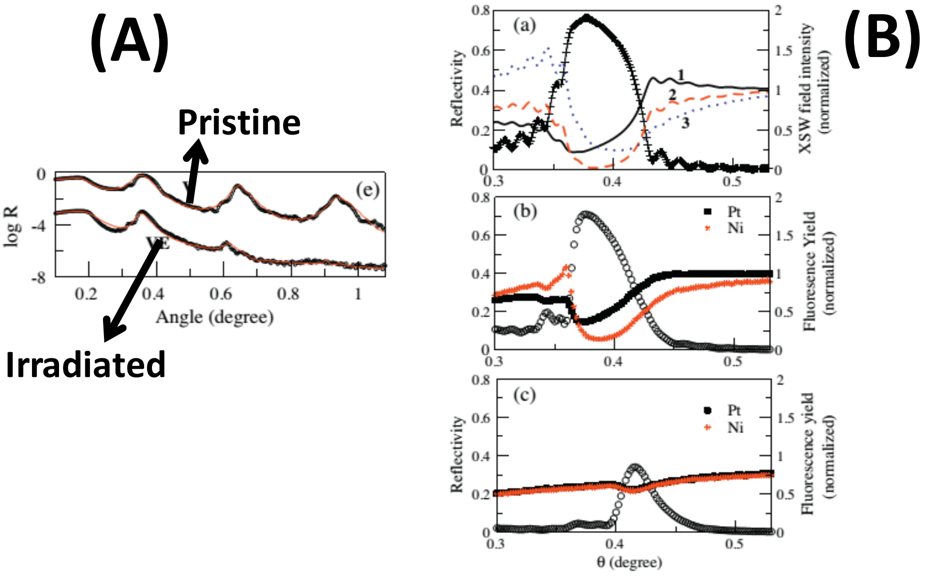

Fig. 6.4: (A) X-ray Reflectivity of pristine and irradiated MLs. (B) (a) Reflectivity under first order Bragg peak and integrated field intensities in 1-Pt layer, 2-Ni layer and 3-C layer. Reflectivity data and fluorescence yield for (b) pristine and (c) irradiated samples.[157]

Fig. 6.4 (A) shows the reflectivity plot for the pristine and irradiated samples.[157] Clearly there is an increase in interlayer roughness with irradiation. Fig. 6.4 (B) shows the fluorescence yields for both the samples. Clearly the Pt- and Ni-fluorescence yields are almost indistinguishable in the irradiated ML (Fig. 6.4 (B) (c)). This indistinguishability implies that the Pt and Ni layers are completely mixed at this ion-fluence.

The knowledge from these structural studies had limitations of cluster details and the origin of assumed cluster configuration. In this context, XAFS would provide first-hand impression[150,157] of the cluster structure, for the given irradiation condition. For example, our results would establish if *Ni* and *Pt* form isolated clusters in *C*-matrix or core-shell structure[158-159] or alloy. These predictions cannot be drawn simplistically from bulk binary phase diagrams since factors such as surface energetics[160], *Ni/C* or *Pt/C* interactions (*i.e.* ternary phase diagrams), could come into play.

XAFS at *Ni K*-edge can (in principle) detect possible *Ni-Pt* alloy formation[161-162] at the *Ni-Pt* interface or *Ni-C* compound formation[163-164] at the *Ni-C* interface. These changes are typically reflected in coordination or bond-lengths in EXAFS results or *whiteline* features (oxidation state) in XANES.

To solve this problem, it is clear that XAFS cannot be measured in normal reflection mode, since it would be impossible to separate information coming from the layers and the interfaces, which is the key to decoding the structure of the ion irradiation generated clusters. The layers and interfaces of the ML can be selectively filtered for information by x-ray standing wave (XSW) technique. The standing-wave field is generated within the periodic ML as a result of a superposition of incident and diffracted waves when x-rays are Bragg reflected by the periodic ML.[165-166] The equi-intensity planes of the standing-wave field are parallel to and have the periodicity of the diffracting planes in the periodic MLs. At an angle of incidence corresponding to the rising edge of the diffraction peak, the antinodal planes of the standing-wave field lie between the diffracting planes. As the angle of incidence increases, the antinodal planes move continuously inward onto the diffracting planes at the falling edge of the diffraction peak. Over the angular region of Bragg reflection, emission of fluorescent X-rays[165-166] from the periodic ML is strongly modulated, being at a maximum (minimum) when the antinodal (nodal) planes coincide with positions of the atoms in the periodic ML. Bragg diffraction is also obtained from a ML with a slightly varying period and consequently XSW is generated in such graded MLs. By scanning across the Bragg angle, we center the antinode successively in each layer. The present system is same as described in Ref. 157 and 167. On the Bragg peak [Fig. 6.5(a)], we select two angles on rising ($\theta = 0.554^o$) and falling ($\theta = 0.638^o$) edges of the Bragg peak which we refer to as "low" and "high" respectively. For the present pristine ML system, although the low angle corresponds to the location of antinodes on the *C* layer, rising edges of the antinodes coincide with the *Ni/C* interfaces [Black curve: Fig. 6.5(b)]. Fluorescence-mode *Ni K*-edge XAFS for this angle, therefore, yields the structural information around *Ni* diffused into *C* layer. At the high angle, the anti-nodes coincide with *C/Pt* interfaces [blue curve: Fig. 6.5(b)]. However, the main contribution to *Ni* fluorescence comes from the relatively denser *Ni* atomic concentration at *Pt/Ni* interfaces as the falling edges of the antinodes coincide with these interfaces [Fig.6.5 (b)]. Therefore, *Ni K*-edge XAFS at high angle reveals the *Ni* environment predominantly at the *Pt/Ni* interface[iii]. Any dissolved *Ni*, although expected to be in very small amount at this interface, can contribute to the observed *Ni* fluorescence. In the irradiated ML, the XSW-pattern shifts due to changes in structure (mixing) and density. At low angle, the antinodes of XSW coincide with the *C* layer of the irradiated ML while the nodes coincide with the *Ni/Pt* interface [or rather, at the

---

[iii] In the system under consideration, the thicknesses of the *Pt* layer and *Ni* layer are 23 Å and 22 Å respectively. The thickness of the *C* layer was varied from 29.7 Å (at the bottom-most layer) to 35.7 Å (at the top-most layer), since the system is a depth graded multilayer. Despite the location of anti-node at interfaces, there will be some contribution to the signal from the non-interfacial regions of the layers.

middle of the mixed *Ni-Pt* layer as in Ref. 157] (Black curve, Fig.6.5 (b)). *Ni K* edge XAFS at this angle, for the irradiated ML, reveals structural information around *Ni* diffused into *C* layer (as in the pristine ML). At high angle, the antinodes of the XSW shift to the *Ni/Pt* interface or the middle of the *Ni-Pt* layer (instead of *C/Pt* interface as in pristine ML) while the nodes are located in the *C* layer [Blue curve, Fig. 6.5 (b)]. Therefore, *Ni K* edge XAFS at this angle reveals the structural information around *Ni* at *Ni/Pt* interface of irradiated ML.

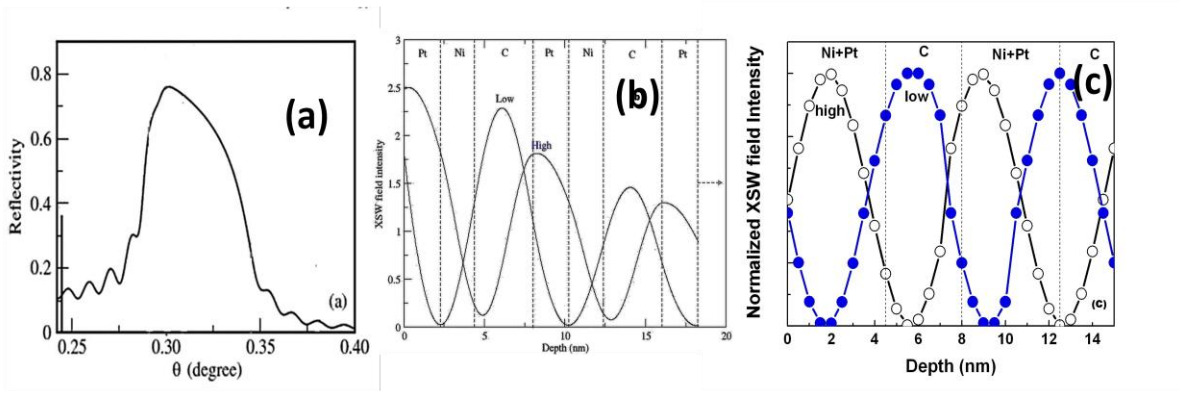

Fig. 6.5: (a) First order Bragg peak; the positions of antinodes and nodes of the X-ray standing wave (XSW) formed within the first few layers (7 consecutive layers from surface) of our graded *Pt/Ni/C* multi-trilayer in (b) Pristine ML and (c) Irradiated ML. The black curve corresponds to the angle chosen in left (lower angle) side of the Bragg peak (BP) while the blue curve corresponds to the angle chosen at the right (high angle) side of the BP.

The structural model is retrieved mainly from the XAFS coordination results. We theoretically calculated the coordination number for various degrees of interfacial mixing and compared with the XAFS results. The theoretical coordination calculation is non-trivial, having to include the variation in field intensity over the individual layers of the ML from XSW pattern (since this causes variation in the number of *Ni* atoms excited in different depths over a period of the ML sample).[iv] With rigorous XAFS analysis, we are able to derive finer (beyond XRR/XRF/XTEM) micro-structural details: e.g. quantification of intermixing, chemical nature of mixing, cluster identification. The most important outcome is the identification of bimetallic nano-clusters formed within irradiated *C* matrix.

6.4. XAFS Experimental details

XAFS data were collected in fluorescence mode at the *Ni-K* edge (8.333 keV) at the ROEMO (E2) beamline at Hamburg Synchrotron Radiation Laboratory (HASYLAB) at DESY, Germany. A pair of Si *(111)* crystals in parallel geometry was used as monochromator to filter out the wavelengths. The first *Si (111)* crystal in the path of the incident beam was given suitable offset (from parallel geometry) to suppress higher harmonics from the monochromator. During energy scan of EXAFS experiments, an appropriate adjustment of the angle of incidence was made in order to maintain the antinodal positions within the sample unchanged. A *Si (Li)* detector was used to collect the fluorescence photons.

6.5. Results and discussion

6.5.1 XAFS results

The XAFS data sets (Fig. 6.6a) were analyzed for the first coordination shell around *Ni*. The rather large noise (possibly due to disordered interface) in the data precluded higher shell analysis. However, the first shell (nearest neighbor) analysis is

---

[iv] The penetration depth of 2 MeV Au^{2+} ions being ~microns ions go through the ML sample and get embedded deep into the substrate; the variation due to ion impact factor is negligible.

found to sufficiently extract the irradiation-induced structural changes (shown below). Correlation-free coordination (N) and Debye Waller Factor (DWF) were obtained by simultaneously fitting each dataset for k^w (w = 1, 2).[v] The data were fit over the k-range 2.2-8 Å^{-1} and r-range 1.2-3.4 Å. The results are listed in Table 6.2. An example of fit quality (R-factor = 0.001-0.014) is shown in Fig. 6.6b.

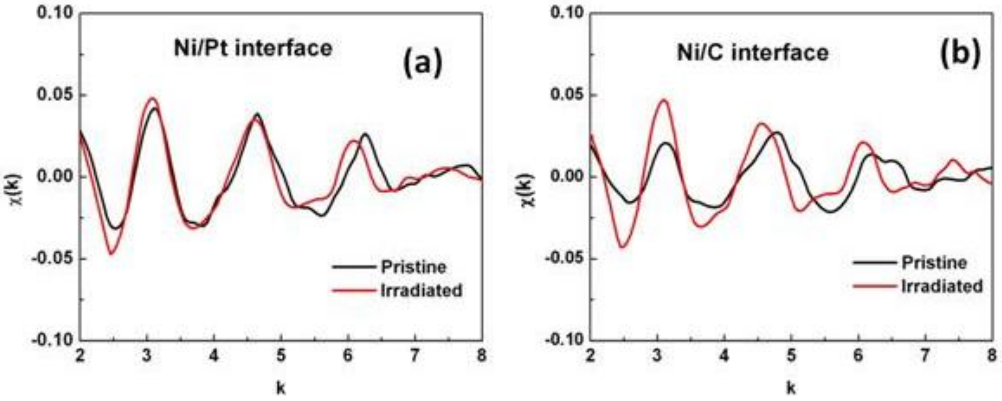

Fig. 6.6a: Comparison of data in k-space before and after irradiation for (a) Ni/C interface and (b) Ni/Pt interface

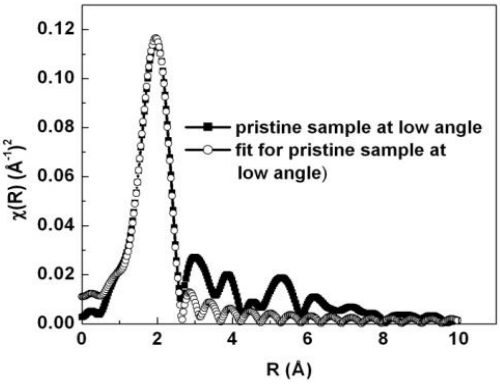

Fig. 6.6b: Comparison of data with fit

Several fitting strategies were considered to test the robustness of the fit parameters, such as (or non-) inclusion of third cumulant[vi] into disorder, (or non-) constraining the coordination number around *Ni* to 12 (fcc) or that between the pristine

---

[v] Simultaneous fitting of the datasets was necessary in order to have sufficient variables for fitting.

[vi] The third cumulant is a measure of the anharmonicity in the atomic distribution.

and irradiated MLs to be the same. The error bars in Table 6.1 reflect the maximum possible variation from all these fits.

6.5.1.1 Low angle (*C* layer and its interfaces with *Ni* and *Pt*)

XAFS data for *pristine* ML at low angle was fit by considering *Ni-Ni* and *Ni-C* scattering paths (any attempt to include *Ni-Pt* path resulted in a bad fit; this is not surprising as there are nodes in the XSW pattern at the *Pt/Ni* interfaces). The large error bars for $N_{Ni\text{-}C}$ are due to the extremely low *Ni-C* coordination.

TABLE 6.1. XAFS fit results for Pt/Ni/C ML

Bond	**ML**	**N**	**σ^2 (Å^2)**	**R(Å)**	**Theoretical R(Å)**
		Low Angle			
Ni-Ni	Pristine	5.46 ± 0.12	0.018 ± 0.0004	2.445 ± 0.003	2.48
	Irradiated	6.24 ± 0.17	0.021 ± 0.0005	2.612 ± 0.001	
Ni-C	Pristine	0.88 ± 0.18	0.016 ± 0.006	1.964 ± 0.007	2.00
	Irradiated	0.33 ± 0.18	0.016 ± 0.006	1.964 ± 0.007	
Ni-Pt	Pristine	-	-	-	2.60
	Irradiated	4.14 ± 0.14	0.024 ± 0.002	2.727 ± 0.007	
		High Angle			
Ni-Ni	Pristine	7.27 ± 1.11	0.021 ± 0.003	2.54 ± 0.01	2.48
	Irradiated	8.49 ± 0.92	0.025 ± 0.003	2.60 ± 0.01	
Ni-Pt	Pristine	3.4 ± .	0.016 ± 0.009	2.72 ± 0.04	2.60
	Irradiated	3.51 ± 0.92	0.02 ± 0.01	2.76 ± 0.03	

From Fig. 6.6(b), it is clear that in the data there are contributions from part of the *Ni* layer, *Ni/C* interface and (possible) diffused *Ni* atoms in the bulk *C* layer. Considering interfacial planes to be {111}/{100}/{110} and taking into account the relative variation in field intensity across the ML (as explained earlier) (Refer Fig. 6.6(b)), the weighted-average Ni-Ni coordination may be formulated as[vii-ix][168-170]:

$$N_{Ni-Ni} = \frac{[(12\times\frac{\int I_{Ni}}{\int I_0}\times N_A)+(8.33\times\frac{\int I_{Ni/C}}{\int I_0}\times N_B)]}{(\frac{\int I_{Ni}}{\int I_0}\times N_A)+(\frac{\int I_{Ni/C}}{\int I_0}\times N_B)} \qquad (6.1),$$

where N_A is the number of Ni atoms in Ni layer, N_B is the number of interfacial Ni atoms, I_{Ni} is the intensity in Ni layer, I_C is the intensity in C layer, $I_{Ni/C}$ is the intensity at Ni/C interface, I_0 is the maximum intensity, in this case, I_C.

The first and second terms in the numerator reflect the contribution from Ni-Ni bonds in Ni layer and at Ni/C interface respectively. (Note that Ni cluster formation inside C layer is excluded preliminarily). The denominator represents the sum of Ni atoms excited in Ni layer and Ni/C interface. Assuming the interfacial roughness (σ_{Ni-C} = 1.7 Å, from reflectivity experiments) to be preliminarily representative of interfacial extent and the thickness of Ni layer = 22 Å, interface-volume ratio $\frac{N_B}{(N_A+N_B)} = 7\%$. However, this ratio should have yielded $N_{Ni-Ni} = 11.63$ from Eq. (6.1) (instead of 5.4 in Table 6.1).

On the other hand, the average interfacial Ni-C coordination (for adsorption) may be formulated as:

$$(N_{Ni-C})_{\max} = \frac{3.67\times\frac{\int I_{Ni/C}}{\int I_0}\times N_B}{(\frac{\int I_{Ni}}{\int I_0}\times N_A)+(\frac{\int I_{Ni/C}}{\int I_0}\times N_B)} \qquad (6.2).$$

[vii] Bulk Ni fcc lattice has 12 neighbors while interfacial Ni has 9 neighbors. 3 missing neighbors correspond to dangling bonds for {111} plane. In the case of {110} and {100} planes, interfacial Ni has 8 neighbors and the 4 missing neighbors correspond to dangling bonds. Since the layers are polycrystalline in the sample, we have to consider an average over these three planes.

[viii] The intensity variation (Figure.1) in the various layers is normalized with respect to the intensity in the (i) C layer for low angle of the Bragg peak and (ii) Pt layer for high angle of the Bragg peak.

[ix] There are no *Ni* atoms at the *C/Pt* interface.

Table 6.2: XAFS coordination analysis steps for Ni/C interface*

1. Using XRR determined roughness layer thickness, calculate fraction of Ni atoms at Ni/C interface
2. From the normalized XSW intensity variation across the ML, extract the no. of x-ray excited *Ni* atoms ((N_{Ni}) ex) (that contribute to XAFS signal), at different locations of the ML.
3. Considering the structure of *Ni* -layer to be *fcc* and the *Ni/C* interfacial plane to be consisting of {111}:{110}:{100} =1:1:1, calculate the weight-averaged surface coordination for *Ni* atoms at this interface.
4. Using equations 6.1 and 6.2, calculate the weighted average $N_{Ni\text{-}Ni}$ and $(N_{Ni\text{-}C})_{max.}$
5. If $(N_{Ni\text{-}Ni})_{calculated} \neq (N_{Ni\text{-}Ni})_{XAFS}$ and $(N_{Ni\text{-}C})_{max.} < (N_{Ni\text{-}C})_{XAFS}$, the interface is not sharp and some Ni atoms are pre-diffused into C layer.
   $(N_{Ni\text{-}C})_{C\ layer} = (N_{Ni\text{-}C})_{XAFS} - (N_{NiC})_{interfacial}$
6. Calculate % of Ni atoms diffused into C layer

*The above procedure is true for all interfaces

From this equation, $N_{Ni\text{-}C} = 0.37$ (instead of 0.879 in Table 6.2). Lower $N_{Ni\text{-}Ni}$ (in Table 6.1) and higher $N_{Ni\text{-}C}$ (compared to calculated results from above eqn.) suggest replacement of some *Ni* near neighbors by *C* atoms, possibly due to additional (random) diffusion of *Ni* into *C* layer (beyond the reflectivity-derived simplistic binary model of layer + interface) (Fig.. 6.7). Solving Eq. (6.2) for XAFS-derived coordination yielded this additional *Ni* proportion to be 26%.[x] Thus, the salient conclusion on the pristine *Ni/C* interfacial structure, from XAFS (and beyond XRR), is the existence of significant proportion of sporadic pre-diffused *Ni* atoms within *C* layer. The implications of this finding will be evident later in this paper.

The nature of *Ni-C* bond is determined to be chemical from XANES: XANES at *Ni K*-edge (Fig. 6.8(a)), for the pristine ML, shows conspicuous (positive) deviation of *Ni*

---

[x] Total $N_{Ni\text{-}C}=0.88$, out of which 0.37 is interfacial. This implies that 0.51 is in C layer. Now, each Ni atom in C layer has 2 C coordination (amorphous carbon). 2×(total no. of Ni atoms) contribute to $N_{Ni\text{-}C}$ =0.51 Therefore % of Ni atoms diffused into C layer = 0.51/2 = 26%.

valence from that of pure *Ni* (i.e. 0 oxidation state). We attribute the integrity of *Ni/C* interface, during irradiation, to this chemical binding.

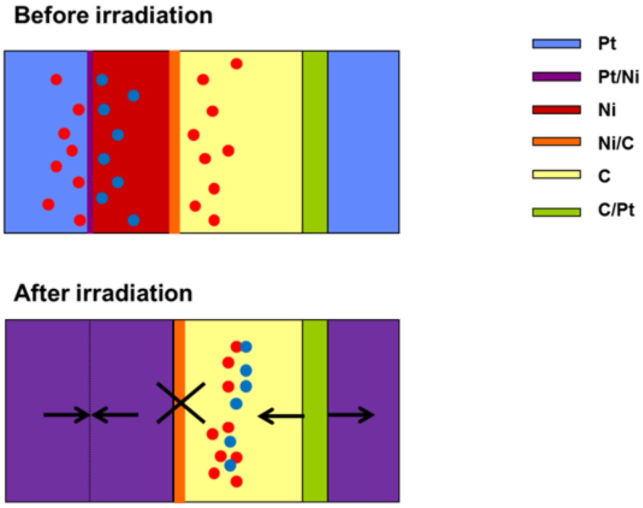

Fig. 6.7: Structural model for the multilayer before and after irradiation.

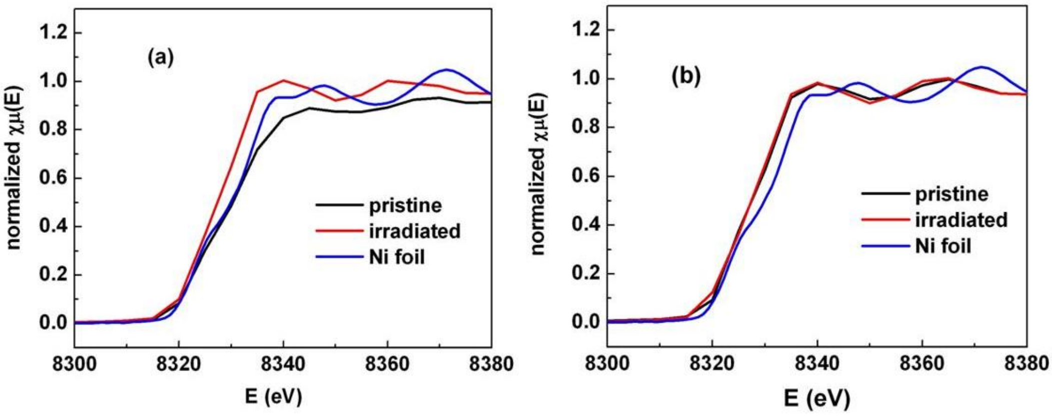

Fig.6.8: XANES at (a) *Ni/C* interface and (b) *Ni/Pt* interface

The data for the *irradiated* ML was best fit by *Ni-C*, *Ni-Ni* and *Ni-Pt* scattering paths (simulations for different values of N_{Ni-Ni} (and N_{Ni-Pt}) reveal resolution limit of $\Delta N = 2$). The emergence of *Ni-Pt* coordination (in contrast to pristine ML) is consistent with XTEM results and due to irradiation-induced diffusion of *Pt* atoms into C layer (suggested by XRR). [*Pt/C* interfaces[171,172] are reported to be vulnerable due to absence of *Pt-C* chemical bond[173], unlike *Ni-C*.[174] This is consistent with increase in roughness with irradiation in Ref. 157: $\sigma_{Pt/C}$ increases by ~ 400% while the corresponding increase in

$\sigma_{Ni/C}$ is by 32%]. The bond-length changes are consistent with the mixing of *Ni* and *Pt.* *Ni-Ni* bond-length (2.44 Å), which is close to the metallic value (2.48 Å) before irradiation, expands (to 2.6 Å) towards *Pt-Pt* bond-length (2.7 Å) after irradiation. This bond-length change is duly directed towards accommodating the larger intercalated *Pt* atoms.

6.5.1.2 Cluster Models

While XTEM indicates the formation of *Pt-Ni* nanoclusters, it is unable to determine their exact configuration. We consider various models of nano-clusters to deduce the configuration of *Ni-Pt* within *C* layer (i) isolated clusters of *Ni* and *Pt*; (ii) *Ni* core - *Pt* shell; (iii) *Pt* core – *Ni* shell; (iv) *Ni*-centered icosahedral bimetallic cluster [Icosahedral model has been considered since this is a highly disordered system. In highly disordered systems (for e.g. metallic glass), such icosahedral structural units have been observed[175]] and (v) *Pt*-centered icosahedral bimetallic cluster. (Fig. 6.9)

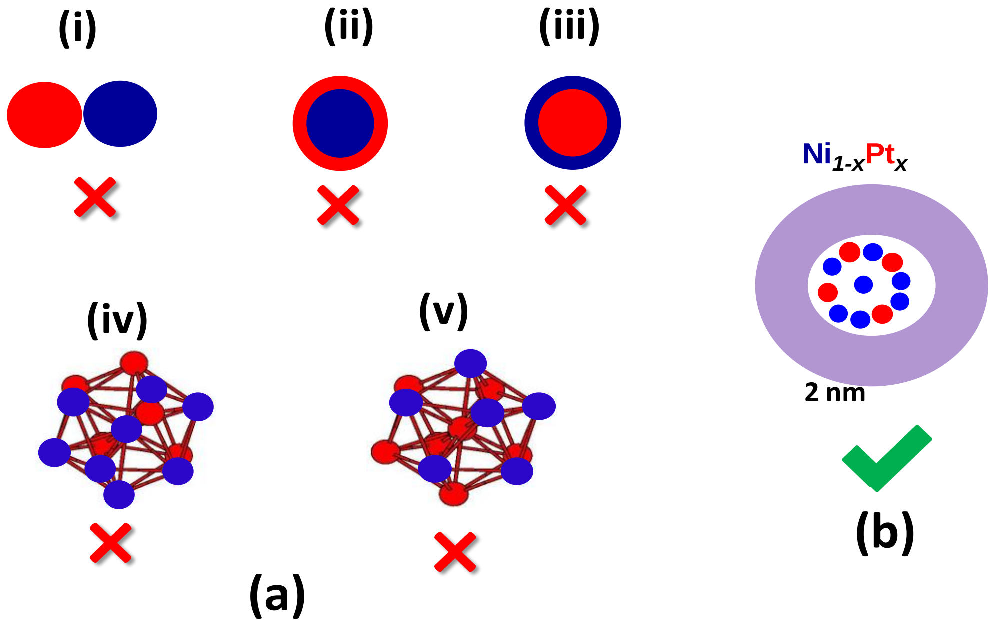

Fig. 6.9: (a) Various cluster models considered, (b) final model for embedded clusters in C layers

For this, the contributions to $N_{Ni\text{-}Ni}$ from *Ni/C* interface, *Ni+Pt* mixed layer and within *C* layer were decoupled.[xi] Subtracting the interfacial contribution and *Ni+Pt* layer contribution from the total in Table 6.2, $N_{Ni\text{-}Ni}$ (from *C* layer) and $N_{Ni\text{-}Pt}$ are calculated to be 6.35 and 3.64 respectively. Next, for models (i-iv) we calculated $N_{Ni\text{-}Ni}$ and $N_{Ni\text{-}Pt}$ for different surface-volume ratios of the number of *Ni* atoms[xii] (*i.e.* different cluster sizes of *Ni*).

Model (i) is ruled out since experimentally-deduced $N_{Ni\text{-}Ni}$ (~6.35) is significantly lower than that for the smallest *Ni* cluster. On the other hand, significant $N_{Ni\text{-}Pt}$ (~ 3.64) rules out isolated *Pt* clusters. The same logistics rule out Model (ii), since the latter would have resulted in a minimum $N_{Ni\text{-}Ni}$ ~ 9. Model (iii) is ruled out since our $N_{Ni\text{-}Pt} > 0.3$.[xiii] Model (iv-v) would have resulted in $N_{Ni\text{-}Ni} + N_{Ni\text{-}Pt}$ ~ 7. The same being ~ 9 from our XAFS results rules out 13 atom icosahedral clusters.

Therefore, *Ni-Pt* bimetallic clusters around *Ni* centre, having *Ni:Pt* = 0.6:0.4, highly disordered beyond the first shell, may be the best representation for the *Ni/Pt* configuration within the *C* layer. The first shell radius of the clusters is estimated to be ~ 0.25 nm, corresponding to *Ni-Pt* bond-length in Table 6.1. The solution is consistent with *Ni-Pt* alloy formation, as indicated by *Ni-Pt* binary phase diagram for this atomic concentration ratio. Previous reports on *Ni/Pt* alloys have shown clusters of this particular composition to be ferromagnetic.[176-178]

[xi] The integrated intensities for each interface and layer were calculated. The total $N_{Ni\text{-}Ni}$ has contributions from *Ni+Pt* mixed layer + *C* layer + *Ni/C* interface.

$$[N_{Ni-Ni}]_{Total} = \frac{N_{Clayer} \times \int I_C + N_{Ni+Ptmixedlayer} \times \int I_{Ni+Pt} + N_{Ni/C} \times \int I_{Ni/C}}{\int I_C + \int I_{Ni+Pt} + \int I_{Ni/C}}$$

[xii] $$N_{Ni-Ni} = 12(1-x) + 9x; N_{Ni-Pt} = 3x$$

[xiii] Pt core, Ni shell would imply that surface Pt atoms see an average of 3 Ni nearest neighbor, assuming the surface to be (111). So each Ni atom will see 1/3 = 0.3 Pt atoms.

6.5.1.3 High Angle (*Ni-Pt interface*)

The data for both the pristine and the irradiated MLs (Fig. 6.10) were best fit by *Ni-Ni* and *Ni-Pt* scattering paths. (Note that any attempt to include *Ni-C* path resulted in bad fit.). Metallic interfaces are generally marked by intermixing[179] between the layers: *Ni-Pt* form alloys[180-181]at very low energies. Lower N_{Ni-Ni} (~ 7.3) and increased N_{Ni-Pt} (~3.4), for the pristine ML, compared to those theoretically calculated [replacing I_C by I_{Pt} (Intensity in *Pt* layer) and $I_{Ni/C}$ by $I_{Ni/Pt}$ (Intensity at *Ni/Pt* interface) in Eqn.(6.1)-(6.2)] for ideal sharp interface[xiv] implies pre-existing intermixing, consistent with XRR. From the coordination ratio N_{Ni-Ni}:N_{Ni-Pt} (and density), the atomic concentration ratio *Ni:Pt* was calculated to be 0.82: 0.16. *Ni-Pt* binary phase diagram suggests the possibility of alloy formation for this concentration ratio.[163] This is further supported by XANES at *Ni K*-edge (Fig.6.8(b)) for the pristine ML, which shows conspicuous (negative) deviation from that of pure *Ni* (i.e.0 oxidation state). It implies charge transfer to *Ni* at this interface, most likely from *Pt*.[182] Therefore, *Ni-Pt* alloy could be reasonably justified structural representation for this interface.

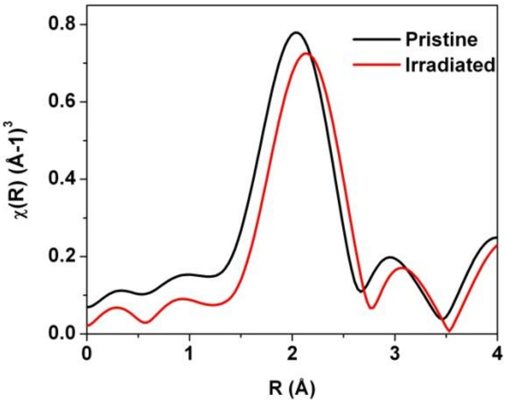

Fig. 6.10: Fourier Transform for both the MLs at *Ni/Pt* interface

For the irradiated ML, N_{Ni-Ni} and N_{Ni-Pt} were calculated for various degrees of interfacial mixing and by including the intensity variation. It is deduced that interlayer

---

[xiv] Ideal sharp interface implies that there is no diffusion between the layers beyond the interface.

diffusion of 54% *Pt →Ni* and 22% *Ni → Pt* best matches with the XAFS coordination.[xv] The asymmetry in diffusion is consistent with pre-existing vacancy in *Ni* layer (due to 26 % *Ni →C* diffusion), which accommodates the apparently extra *Pt* atoms.[xvi]

Comparing the results for pristine and irradiated *Ni/Pt* interfaces, we observe significant enhancement in interfacial broadening (consistent with XRR) due to ion-driven diffusion, depicted in Fig. 6.7. The oxidation state of *Ni* remains unchanged, as confirmed by the similarity in the XANES spectra (Fig. 6.8(b)) for both the pristine and irradiated MLs. Thus, XAFS conclusion of *Ni/Pt* interface (beyond XRR) is the quantification of degree of atomic mixing and alloy composition of the interface.

6.5.2 Cluster Formation Method

We now decouple the role of kinetics, thermodynamics and nature of interfaces in cluster formation. The nature of interface (i.e. chemically bound/physically bound) determines the relative ratio of metallic diffusion into *C* matrix. This in turn determines the composition/density of the bimetallic clusters.

In this case, *Pt/C* is a physically bound interface due to large positive heat of mixing between *Pt* and *C*; hence it is susceptible to ion irradiation.[171-173] On the other hand, *Ni/C* is chemically bound[174] (Ni-carbide compound formation) and hence less susceptible to ion irradiation. *Ni/Pt* is an alloyed interface. As a result, ion irradiation induces diffusion of large number of *Pt* atoms into *C* layer, while the number of *Ni* atoms diffusing from *Ni/C* interface is much lower. (Note that from our XAFS coordination results, *Ni/C* interface is unaffected by ion irradiation).

[xv] The following equations were used to deduce the degree of mixing between Ni and Pt layers:

$$N_{Ni-Ni} = \frac{[(12\times(N_A-\Delta N)\times\frac{\int I_{Ni}}{\int I_0}+(8.33\times\frac{\int I_{Ni/Pt}}{\int I_0})\times N_B}{(\frac{\int I_{Ni}}{\int I_0}\times N_A)+(\frac{\int I_{Ni/Pt}}{\int I_0}\times N_B)}, \quad N_{Ni-Pt} = \frac{(12\times\Delta N\times\frac{\int I_{Pt}}{\int I_0})+(\frac{1}{12}\times\Delta N\times\frac{\int I_{Ni}}{\int I_0})+(3.67\times\frac{\int I_{Ni/Pt}}{\int I_0}\times N_B)}{(\frac{\int I_{Pt}}{\int I_0}\times\Delta N)+(\frac{\int I_{Ni}}{\int I_0}\times N_A)+(\frac{\int I_{Ni/Pt}}{\int I_0}\times N_B)}$$

ΔN = no of *Ni* atoms exchanged, N_A = no. of Ni atoms in Ni layer, N_B = no. of Ni atoms at Ni/Pt interface.

[xvi] Note that total Ni vacancy, due to diffusion = 26 % (Ni→C) + 22% (Ni →Pt) = 48%, is consistent with total Pt → Ni diffusion = 54%

6.5.3 Significance of Cluster Results

A remarkable aspect of these clusters is the presence of large disorder beyond the nearest neighbor, similar to our observation for multi-component metallic glasses. Notably, ordering features persisted up to second nearest neighbor for our bimetallic glasses. The striking difference in the degree of disorder between multi-component and bimetallic glasses is understandably consistent with "confusion principle".[175] In contrast, we observe that the bimetallic clusters formed on *C* matrix (induced by ion irradiation) are far more disordered and resemble multi-component cluster characteristics. Carbon matrix possibly helps the amorphous structure.[183] Highly disordered clusters, resembling glassy structure, find usage as patterned magnetic recording media. Their amorphous nature promotes growth in preferred orientation.[184] Moreover, glasses being defect free, the issue of different bits having different switching fields due to defects can be avoided (during writing).[185] Thus, ion irradiated *Pt/Ni/C* ML offers promise as magnetic device. The subsequent design goal in ion-irradiation based fabrication method should be optimization of the cluster composition (to tune T_c, susceptibility etc.[175]), size and inter-cluster separation (to tune luminescence properties) by selection of matrix and metals, controlling interfacial charge transfer, layer thickness, ion flux etc.

6.4. Conclusion

We have probed the structural changes of a *Pt/Ni/C* multi tri-layer upon ion irradiation, using a combination of XSW and *Ni K*-edge XAFS. Our XAFS (and XANES) analysis detects pre-existing charge and atomic transfer at pristine *Ni/C* and *Ni/Pt* interfaces (directly) and determines the character of *Pt/C* to be physically adsorbed *Pt-C* (indirectly). Metallic diffusion into *C* matrix is observed to be directly correlated with the extent of charge transfer at metal /*C* interface. Physical adsorption (at *Pt/C* interface) evidently encourages interfacial diffusion (*Pt* into *C*). Following irradiation, *Pt* atoms from the disrupted *Pt/C* interfaces migrate towards pre-diffused *Ni* atoms within *C* layer to form *Ni*-centered *Ni-Pt* bimetallic nano-clusters. These clusters having *Ni:Pt* =60:40, are ferromagnetic in nature. The clusters are highly disordered beyond nearest neighbor and resemble the short range order of multi-component glasses. Such disordered clusters on C-matrix have promising applications as magnetic devices.

CHAPTER 7

XAFS CHARACTERIZATION OF BIMETALLIC NANORODS SYNTHESIZED VIA SWIFT HEAVY ION IRRADIATION

7.1 Background

Nanorods possess high aspect ratio $\left(AR = \frac{L}{D} \right)$, which splits the Surface Plasmon Resonance (SPR) along major and minor axes. [186-188] Due to this, they offer enhanced optical-sensitivity due to sharp increase in near-field intensity[189] and high polarization sensitivity. Their high sensing capabilities are best realized when they are parallel aligned. They have interesting applications in a wide variety of fields ranging from electronics[190-191] and optoelectronics to biology[192], for e.g. (i) ZnO nanorod arrays on fluorine doped, SnO_2 coated, glass substrates have been observed to be efficient electrodes for *dye-sensitized solar cells*,[193] (ii) *biomedical applications* – Au nanorods have been used for detecting the target sequences of infecting agents of many diseases, for eg. HIV, based on the electrostatic interaction between DNA and gold nanorods[194], (iii) Tunability with applied electric field: (a) *Display Technologies:* By changing the orientation of the nanorods with respect to an applied electric field, the reflectivity of the rods can be altered, resulting in superior displays, hence radically improved picture quality. Such TVs, known as *field emission TVs*, are brighter since the pixels (picture element) can glow better in every color they take up.[195] This is because they pass though a small potential gap at high currents, emitting electrons at the same time. (b) Nanorod-based flexible, *thin-film computers* can revolutionize the retail industry, enabling customers to checkout easily without the hassles of having to pay cash. (iv) *Humidity monitor*: ZnO nanorod films on Si substrate show high-humidity sensitivity, good long-term stability and fast response time. Further, their resistance decreases with increasing relative humidity. Hence they can be efficiently used as humidity sensors.[196]

Several methods have been used to synthesize nanorods. These include (i) Seed-mediated growth[197]: In this method, metal salts are reduced initially with a strong reducing agent to seed particles. Subsequent reduction of more metal salt with a weak reducing agent, with the presence of structure-directing additives results in the controlled formation of nanorods of specific aspect ratio; (ii) surfactant mediated growth[198-199]; (iii) reduction[200]; (iv) Template based synthesis: The templates provide a regular array of sites with nanometer dimensions to guide the growth of nanorods in an organized fashion[201]; (v) electrochemical deposition; (vi) radiolysis[54,202]; (vii) Lithography; (viii) Oblique angle deposition: This is an electron-beam deposition method. Initially, some amount of metal is deposited at normal incidence with substrate rotation. Following this, the substrate is kept at grazing angle *wrt* the incident beam so that nanorods of *different* lengths are deposited.[203] The most important issues that need to be addressed for selection of the appropriate synthesis method are simultaneous control over morphology, uniformity, aspect ratio and alignment.

Ion beams have been extensively used to tailor the properties of materials and for developing new materials. Ion beams, depending on the energy, can play different roles in material science such as synthesis, modification and characterization.

For heavy ions at high energies, Electronic Energy Loss (S_e) dominates, leading to excitation or ionization of the atoms in the material. At these energies, the velocity of the ion is comparable to or higher than the velocity of Bohr electron. The ions with such high energies are referred to as *Swift Heavy Ions (SHI)*. The deposited energy from the ions generates transient extreme conditions (e.g. $P = 100 MPa, T = 1600^{o} C, H = 10^{19} W$) and melts the material along the path resulting in the formation of ion track $\left(D < 10 nm\right)$. The number / dimensions of these defects depend on the material and can be controlled by the mass/energy/ flux of the ion. There is a material-specific threshold of S_e, beyond which ion tracks form. It can vary from ~eV/Å for polymers and other insulators to keV/Å for metals. This method of defect engineering, called SHI-Irradiation (SHII), could utilize the directional reference of ion track to generate aligned nano-rods in the matrix.[204]

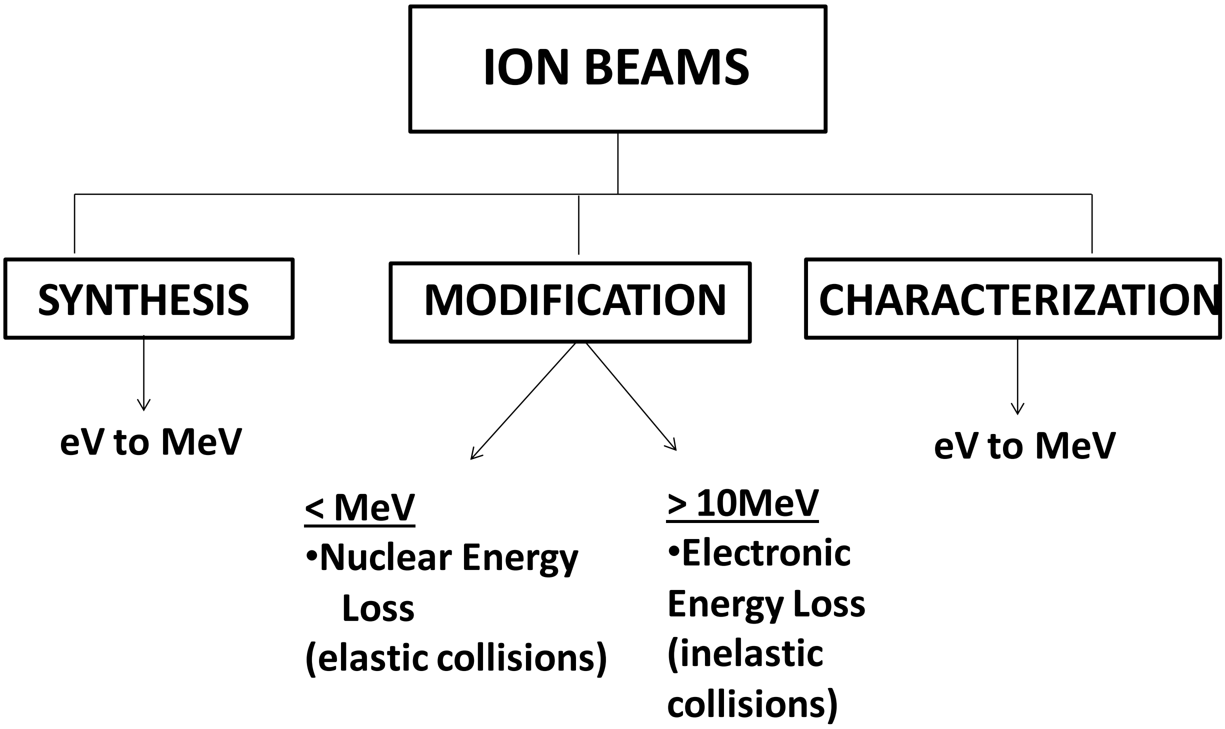

Synthesis of metallic nano-rods: The ion impact in the medium imparts in-plane strain perpendicular to ion path, which acts on the core of any embedded nanoparticles, causing them to flow along the ion path. Rapid $(\sim 10-100ps)$ quenching drives amorphous track formation along ion path, arresting the nanoparticles in deformed state. In principle, the method is comparable to the formation of metallic glasses (Fig. 7.1).

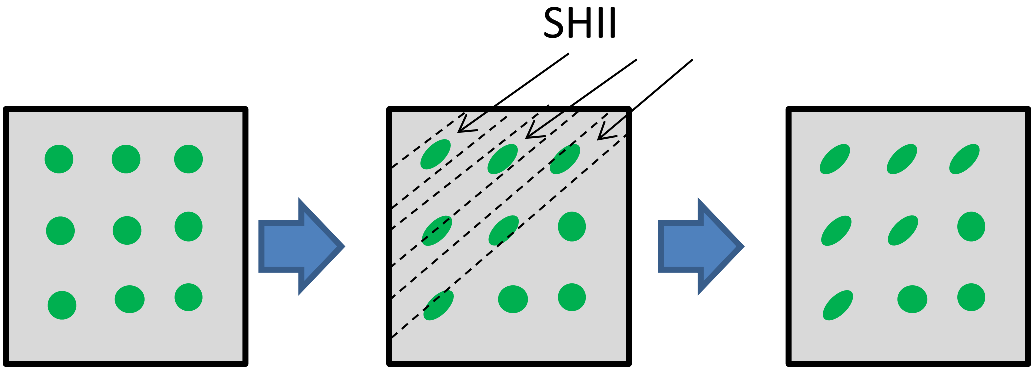

Fig. 7.1: Schematic of SHI induced modification

So far, this method has been extensively used to produce only mono-metallic nanorods.[205-213] Micro-structural characterization (viz. shape, size, amorphous content) of SHII-synthesized monometallic nano-rods is well-established.[214-218] However, multi-metallic (rather than monometallic) nano-rods are the systems of practical interest (e.g. multiplexing, coding, vaccination applications, magnetic tweezers for biophysics applications).[219-230] Degree of alloying is an important control parameter for nano-rods for sensor applications, since it affects the electronic properties of the nanorods by modifying the Fermi level[231], and can be markedly different from bulk phase diagram due to enhanced disorder[232] or surface energetics.[233] During SHII, the local temperature along the ion track rises above the melting points of the substrate and the embedded nanoparticles. This results in molten phase formation along the ion track, which could cause the nanoparticles to 'flow'; hence there is a possibility of alloying. The only reports, on SHII-synthesized multi-metallic nanorods, involve bulk-miscible systems (*Fe*/*Pt*)[234-235]. These cases are not particularly insightful: being thermodynamically favoured, mixing is guaranteed and nano-scale disorder only accelerates the process. On the contrary, immiscible systems are significantly more sensitive to size reduction. Competition between counteractive factors, viz. de-alloying (melting point, surface energy, oxidation or reduction potential) *versus* alloying [disorder], makes the final phase unpredictable. Depending on the relative strengths of de-alloying and alloying factors, immiscible or miscible phase might result. This allows one to identify threshold size/disorder for immiscible → miscible transition and define the comparative-scale for different alloying techniques.

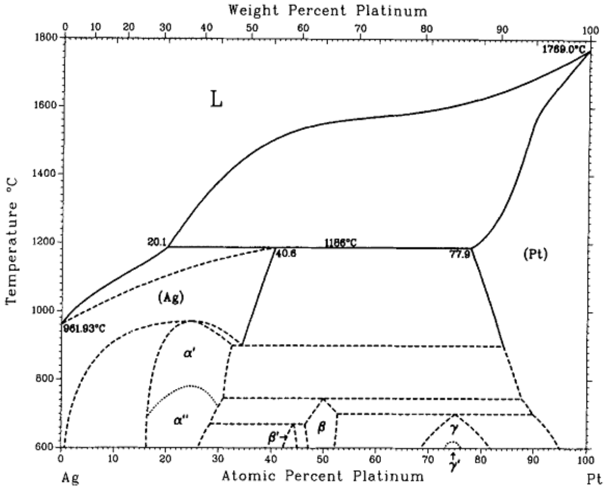

Fig. 7.2: Ag/Pt phase diagram[236]

In this work, we study mixing behaviour in SHII-irradiated [*Au* ions, $E = 100MeV; F = (1-100)\times 10^{12} ions/cm^2$] *Ag*/*Pt* nanoparticles embedded in silica matrix.[237] *Ag*/*Pt* is bulk-immiscible (Fig. 7.2) and from all earlier reports, immiscibility was retained down to the lowest attainable size (2 nm).[54] We expect the miscibility to improve under the extreme synthesis conditions of SHII:

(i) $T_{SHII} = 1700^o C > \{T_m^{Ag} = 600^o C, T_m^{Pt}(nano) = 1200^o C\}$ ensures liquid phase across the entire composition range [Ag/*Pt* bulk phase diagram].[238]

(ii) Local temperature increase in SHI-irradiated *Ag/Pt* leads to formation of molten *Ag/Pt* and rapid quenching [$quenching \;\; rate = 10^9 K/s$] arrests the mixing status of the molten phase.[239]

(iii) In molten state, the problem of preferential *Pt* “surface” segregation becomes irrelevant.

(iv) In synthesis methods involving co-reduction of $\left(Ag^{+}, Pt^{+}\right)$, larger electronegative potential of Ag leads to sequential cluster formation $\left(Ag^{0}, Pt^{+}\right)$ *i.e. Ag* core-*Pt* shell. In contrast, SHII acts upon pre-existing $\left(Ag^{0}, Pt^{0}\right)$clusters so that chemical contribution to de-alloying is eliminated.

(v) $P = 170MPa \Rightarrow$ High defect density ($> 10^{13} / cm^{3}$).[240-242]. Atomic displacement production rate is proportional to incident ion-flux (ϕ), leading to rapid production of point defects and diffusion paths].[243]

In summary, SHII is expected to eliminate de-alloying factors to large extent and promote mixing.

For complete characterization of these Ag/Pt nano-rods, we have employed comprehensive techniques viz. TEM (shape and size), XRD (crystalline content), Optical Absorption (degree of alloying) and XAFS (short-range-order).

Further, we compare our results on Ag/Pt system with those on bulk miscible Ag/Au system.

7.2 Experimental details

Ag/Pt/SiO_2 thin films (thickness = 200nm) were prepared by Ar atom beam co-sputtering (ABS) technique by sputtering Ag, Pt and SiO_2 simultaneously. An inductively coupled ion gun with active neutralization was used to generate neutralized Ar atoms of energy 600eV of current 36 mA with beam area of 40mm. The target was a 3” diameter silica (99.999%) disc on which Ag and Pt metal pieces (99.999%) of 5 mm X 5 mm were placed and the target was rotated continuously during sputtering. The sputtered species were collected on substrates place on a rotating substrate holder. Both incoming beam and the substrate were kept at an angle of 45^{o} with respect to the target surface. The samples were subjected to post-growth annealing at 400°C for 1 hour under flowing Ar gas in a quartz tube furnace. The metal content in the composite thin films was evaluated by Rutherford Back Scattering Spectrometry (RBS) using 2 MeV He beam at Inter-University Accelerator Centre facility. The RBS result shows ~10% Ag and ~10% Pt present in the films. These samples were irradiated with 100 MeV Au ions at Inter-University Accelerator Centre 16UD Pelletron facility. The samples were mounted on a heavy Copper ladder with proper thermal contact and a beam spot of 1 mm diameter was scanned uniformly on the surface using an electromagnetic stirrer. The beam current was ~1 particle nanoampere (p nA) ensuring negligible heating of the sample.

The same procedure was followed for preparation of Ag/Au/SiO_2 samples as well.

7.3 Structural Characterization

7.3.1. Pristine System (Throughout this chapter, pristine system refers to the sample pre-SHII)

7.3.1.1 TEM results

TEM [Fig.7.3(a)] shows well-separated nearly spherical clusters with average diameter 1.5-2.5nm.

7.3.1.2 X-ray Diffraction

XRD pattern [Fig. 7.3(b)] shows no crystalline peaks. Instead it resembles the pattern for metallic glass.[244]

In contrast, XRD pattern for Au/Ag system (inset, Fig. 7.3 (b)) shows peak corresponding to (111) plane of both Ag and Au, suggesting alloy formation.

7.3.1.3 Optical Absorption Spectroscopy

Optical Absorption Spectrum [Fig.7.3(c)] shows no Surface Plasmon Resonance (SPR) band corresponding to either $Ag(\lambda_{Ag} = 400nm)$, $Pt\ (\lambda_{Pt} = 270nm)$ or Ag / Pt. This is in contrast with pristine Au/Ag system (inset, Fig. 7.3(c)), which shows a clear band at $\lambda = 420nm$ corresponding to Au-Ag alloy.

In previous work on metal-silica systems synthesized via ion implantation, significantly larger particle size (~8nm) was observed. The optical absorption pattern showed prominent SPR band. Further, monometallic metal-silica systems synthesized via atom beam co-sputtering also showed prominent SPR band. [212,216,245]

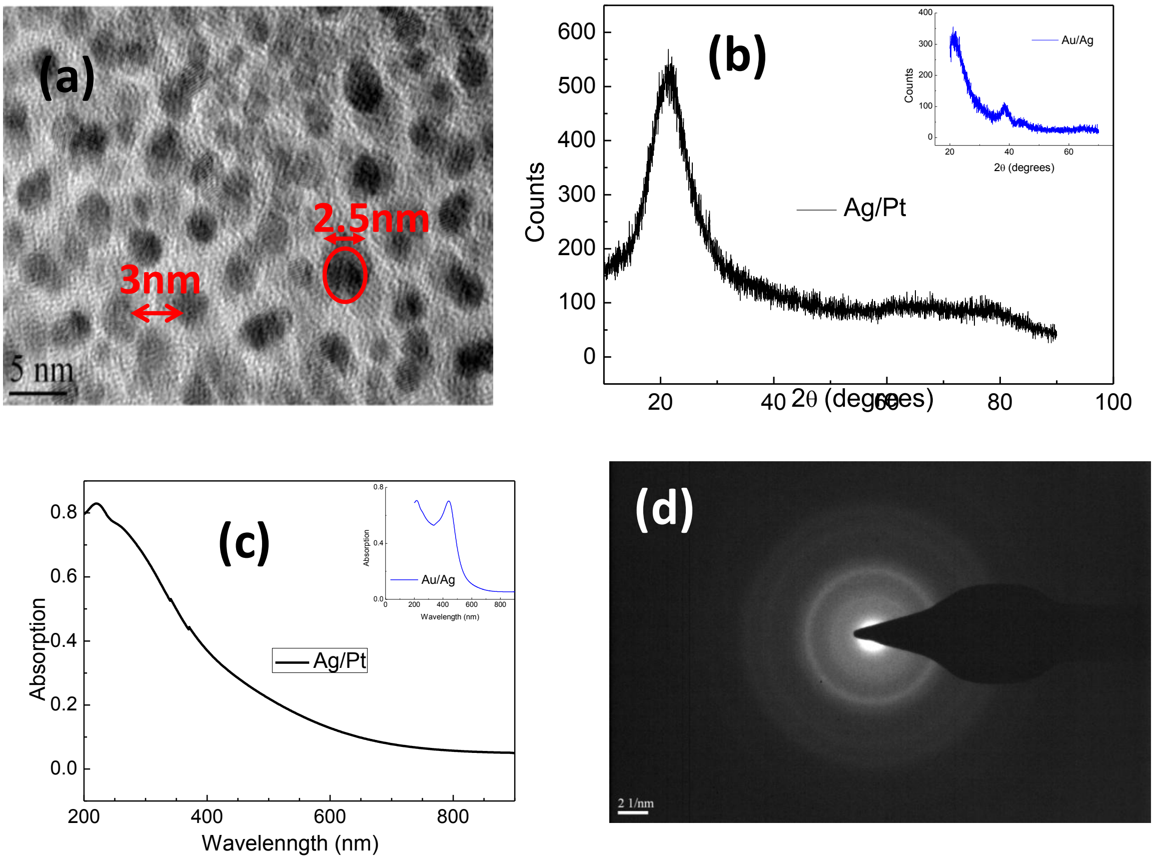

Fig. 7.3: Structural characterization of pristine Ag/Pt system: (a) TEM, (b) XRD pattern, (c) Absorption spectrum, (d) Selective area diffraction pattern

Absence of absorption band implies either amorphous structure or very small clusters (<3nm). Previously, amorphous structure was reported in co-sputtered bimetallic films.[246-249] The amorphization was attributed to difference in radii (>10%) of the metals being deposited. In our case, the size difference is only 4%, yet we observe amorphous structure [$R_{Pt} = 1.38\text{Å}$; $R_{Ag} = 1.44\text{Å}$].

7.3.1.4 Selective Area Diffraction (SAED)

SAED pattern [Fig. 7.3(d)] shows diffuse rings, corresponding to amorphous structure.

Table 7.1: Structural characterization of Pristine System

	Ag/Pt	Au/Ag
Shape	Spherical	Spherical
Size	1.5-2.5nm diameter	2nm diameter
Separation	3 nm	
Structure	Amorphous	Partially crystalline
Alloying	No	Yes

7.3.1.5 XAFS

XAFS experimental details

Fluorescence mode XAFS data was recorded at Pt *L3* (11.562 keV) and Ag-*K* (25.514 keV) edges at 10-ID-MR beamline (MRCAT), Advanced Photon Source, Argonne National Laboratory, USA. Si (111) double crystal monochromator was used for energy selection and Rh coated harmonic rejection mirror was used to eliminate higher harmonics from the spectrum. Incident and fluorescence intensities were measured with Ar filled Lytle detector and multi element Ge detector respectively. The data were processed using ATHENA software. The extracted XAFS oscillations, $\chi(k)$, were Fourier-transformed into real space for fitting. Structural model was constructed, using FEFF6.1. The model parameters were allowed to vary while fitting (using FEFFIT) to yield the best-fit values for bond lengths (r), coordination numbers (N) and Debye–Waller factors (DWF or σ^2). R factor was considered as an estimate of the quality of fit.[97]

XAFS data at *Pt L3* and *Ag K* edges were fit to determine the amorphous short range order in the nanoclusters.

A) ***Pt L3* edge:**

Pt L3 edge XAFS data (Fig. 7.4) was fit over $k = 3.1 - 9.3\,\text{Å}^{-1}; k^{w}(w = 2,3)$; $R = 1.6 - 3.6\,\text{Å}$. The cluster configuration is determined from analysis of the nearest neighbour species:

$$(segregated\ clusters)_{x_{Ag}=0} \rightarrow (AgPt\ \ alloy)_{x_{Ag}\neq 0}$$

$$\Rightarrow\ (N_{Pt})_{Total} = N_{Pt-Pt} \rightarrow [N_{Pt-Pt} + N_{Pt-Ag}]$$

i.e. some of the *Pt* neighbours get replaced by *Ag*. *Pt* and *Ag* neighbours give rise to separate peaks (A, B) in real-space and their intensity ratio (R) can be considered as marker for alloying [Fig.7.4]: $R\left(=\frac{B}{A}\right) \propto \frac{N_{Pt-Ag}}{N_{Pt-Pt}}$. In the rest of this chapter, we use $R_{nor}(F) = \left(\frac{R(F)}{R_{Pt-foil}}\right)$ *i.e.* fluence-dependent *R*-(normalized *wrt* *Pt*-foil):

$$R_{nor}\begin{pmatrix} = 1; x_{Ag} = 0 \\ > 1; x_{Ag} \neq 0 \end{pmatrix}.$$

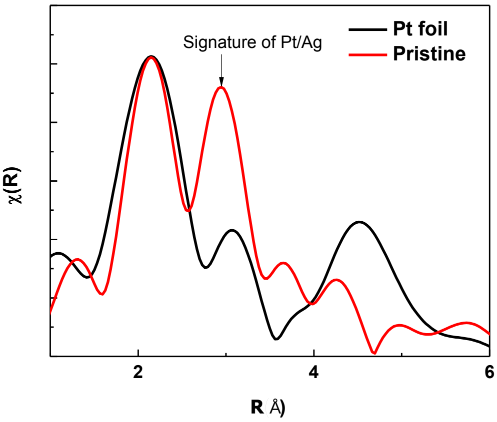

Fig. 7.4: Pt L3 edge XAFS data for pristine Ag/Pt system

From Fig. 7.4, presence of *Ag* neighbors in the pristine system is apparent, since $[R_{nor}(F)]_{F=0} = 1.4$.

Subsequently, fitting strategies were employed to determine *Pt-Pt* and *Pt-Ag* coordination unambiguously. Individual datasets were fit by (i) varying $\left(N_{Pt-Pt}, N_{Pt-Ag}\right)$ separately; (ii) constraining $N_{Pt-total} = 12$ $\left(N_{Pt-total} = N_{Pt-Pt} + N_{Pt-Ag}\right)$ and (iii) constraining $\sigma^2_{Pt-Pt} = \sigma^2_{Pt-Ag}$. Results obtained from fitting strategy (i) are listed in Table 7.2 and plotted in Fig. 7.5 (a-c).

$[N_{Pt-Pt}]_{F=0} = 7;\ N_{Pt-Ag} = 1;\ \Rightarrow.\ N_{Pt}^{total} = 8$. [Fitting strategies (ii) and (iii) degraded the fit quality considerably]. $\boldsymbol{N_{Pt}^{total}} < 9 \Rightarrow$ partially-formed *Pt*-clusters.

Fig. 7.6(a) shows the XANES at *Pt L3* edge. Whiteline feature in Pt results from 2p→6d transition. Lower intensity of XANES features in the pristine sample as compared to Pt foil is signature of disordered structure around *Pt*.

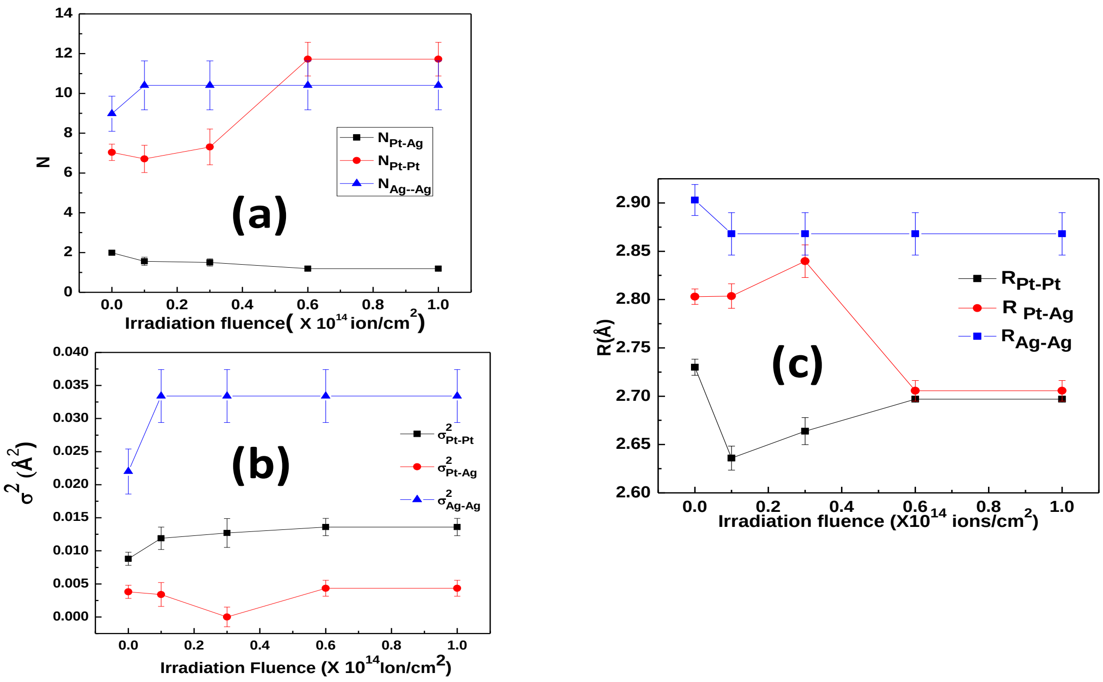

Fig. 7.5 Plot of (a) N, (b) σ^2 and (c) R vs. irradiation fluence for Ag/Pt system

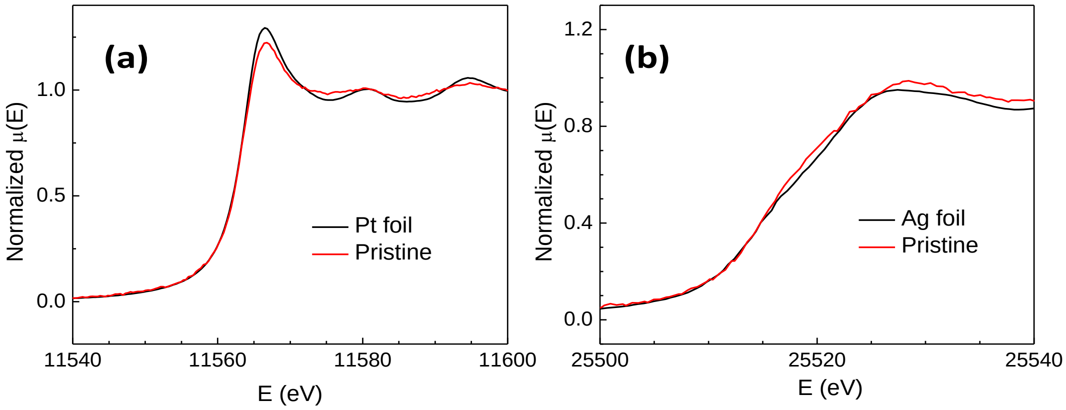

Fig. 7.6: XANES spectra at (a) Pt L3 edge and (b) Ag K edge for the pristine Ag/Pt system

B) Ag K edge

Ag *K* edge XAFS data (Fig. 7.7) was fit for $k = 2.8 - 6\,\text{Å}^{-1}$, $R = 1.5 - 3.8\,\text{Å}$, $k^{w}(w = 0,1)$. [Large amount of noise rendered data beyond $k = 6\,\text{Å}^{-1}$ unusable.] XAFS coordination analysis [$N_{Ag-Ag} = 11; N_{Ag-Pt} \sim 0$] suggests the existence of *Ag*-clusters of size $D = 3nm$. This is supported by XANES results at *Ag* edge (Fig. 7.6(b)), which is similar to *Ag* foil XANES. Further, the absence of data beyond 3.6Å^{-1} suggests that these clusters are highly disordered beyond first nearest neighbor.

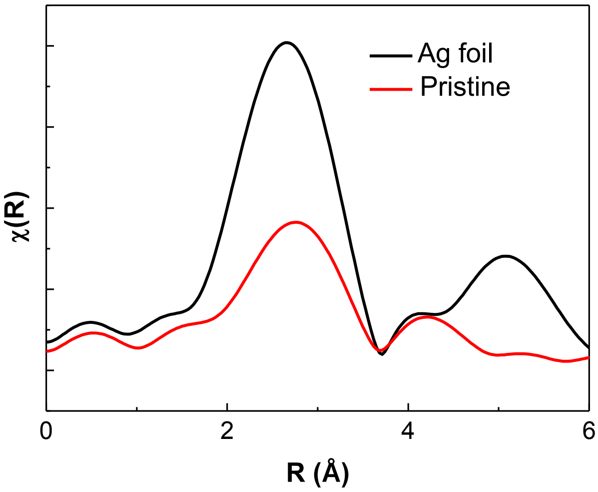

Fig. 7.7: Ag K edge XAFS data for pristine Ag/Pt system

Table 7.2: XAFS fit results

(a) *Pt L3* edge

Irradiation fluence (ions/cm^2)	**N** $_{Pt\text{-}Pt}$	**N** $_{Pt\text{-}Ag}$	$\sigma^2_{Pt\text{-}Pt}$**(Å^2)**	$\sigma^2_{Pt\text{-}Ag}$**(Å^2)**	**R**$_{Pt\text{-}Pt}$**(Å)**	**R**$_{Pt\text{-}Ag}$**(Å)**
0	7.03 (41)	1.987(13)	0.0088(10)	0.0038(10)	2.730(8)	2.803(8)
1×10^{12}	9.73 (82)	1.208(14)	0.0147(16)	0.0011(6)	2.700(9)	2.700(4)
1×10^{13}	6.70(69)	1.561(20)	0.0119(17)	0.0034(18)	2.630(12)	2.803(12)
3×10^{13}	7.31(09)	1.500(18)	0.0127(21)	0.0000(14)	2.660(14)	2.839(16)
6×10^{13}	11.70(84)	1.186(12)	0.0136(13)	0.0043(12)	2.690(2)	2.705(10)
1×10^{14}	11.70(80)	1.186(12)	0.0136(13)	0.0043(12)	2.690(2)	2.705(10)

(b) *Ag* K edge

Irradiation fluence (ions/cm^2)	**N**$_{Ag\text{-}Ag}$	**N**$_{Ag\text{-}Pt}$	$\sigma^2_{Ag\text{-}Ag}$ **(Å^2)**	$\sigma^2_{Ag\text{-}Pt}$**(Å^2)**	**R**$_{Ag\text{-}Ag}$ **(Å)**	**R**$_{Ag\text{-}Pt}$**(Å)**
0	8.98 (88)	-	0.022(3)	-	2.903(16)	-
1×10^{12}	10.41(1.23)	-	0.033(4)	-	2.868(22)	-
1×10^{13}	10.41(1.23)	-	0.033(4)	-	2.868(22)	-
3×10^{13}	10.41(1.23)	-	0.033(4)	-	2.868(22)	-
6×10^{13}	10.41(1.23)	-	0.033(4)	-	2.868(22)	-
1×10^{14}	10.41(1.23)	-	0.033(4)	-	2.868(22)	-

To explain the absence of *Ag-Pt* bonds, we estimated the lower limit of detectable x_{Pt} by generating *Ag K*-edge FEFF simulations $(\chi_{alloy})$for $Ag_{1-x}Pt_x$ alloy ($x = 0 - 0.25$). In contrast to *Pt* L_3-edge, simulated *Ag-Pt* and *Ag-Ag* peaks are not well-resolved at *Ag K*-edge. The only signature of *Ag-Pt* is reduction (Δ) in the net amplitude ($\Delta_{x=0\to0.25} = 0 \to 25\%$) of simulated spectra(χ_{alloy}), resembling DWF-like effect [Fig. 7.8]. We could indeed fit the alloy simulation (χ_{alloy}) with pure *Ag* model coupled with increased disorder. This defines the intrinsic resolution limit for *Pt* detection from *Ag* K-edge analysis: $x_{Pt} = 10\%$ Thus, $N_{Ag-Pt} \sim 0$ does not preclude <10% *Ag-Pt* bonds.

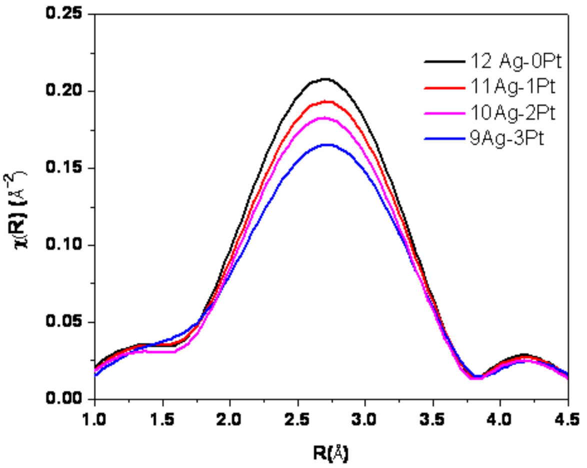

Fig. 7.8: Simulations for fcc structure around Ag with different Ag:Pt ratios

From the above techniques, it is clear that Ag, Pt phase segregate in the co-sputtered film. This is consistent with the fact that substrate temperature (<<1000°C) is much lower than Ag-Pt miscibility temperature (~1700°C) (Fig. 7.2). From XAFS coordination analysis, Ag nearest neighbor coordination is *near-complete* (~12) while Pt coordination is *incomplete* (~7). This implies that Ag forms cluster faster than Pt, which could be consistent with higher reduction potential and higher diffusion coefficient of Ag. [202,27,250-253].

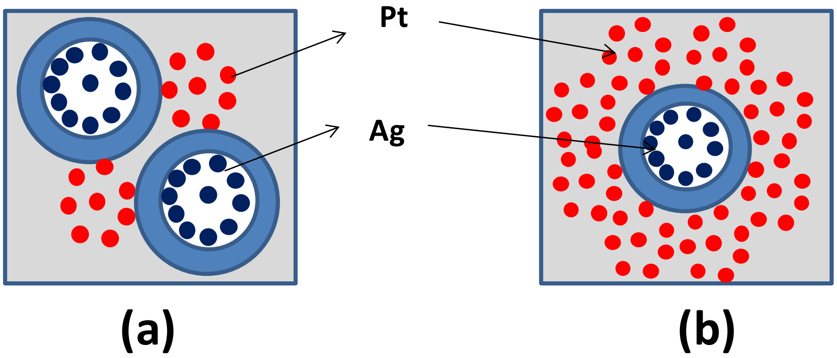

Fig. 7.9: Possible models for the pristine system: (a) Ag and Pt exist as separate clusters, (b) Ag@Pt core-shell. Note that the shell like feature around Ag represents disordered higher shell features of Ag.

Two possible configurations, consistent with XAFS coordination, emerge for the phase-segregated pristine system: (i) Separate clusters (Fig 7.9(a)) and (ii) Ag@Pt core-shell (Fig. 7.9(b)), consistent with lower surface energetics of Pt.[254-256] In the latter model, incomplete Pt coordination (*i.e.* loss of bonds) is consistent with its surface location. It is not possible to resolve between these two models due to amorphous character of the system. In the absence of absorption band, Surface Enhanced Raman Scattering (SERS) is unable to provide any answer.

Summary of structure for pristine Ag/Pt system is highly disordered, phase-segregated configuration.

7.3.1.6 Comparison with pristine Au/Ag system

As mentioned earlier, for the pristine Au/Ag system, (i) XRD spectrum (inset, Fig. 7.3 (b)) shows peak corresponding to (111) plane of both Ag and Au, consistent with Au/Ag alloy; (ii) Optical spectrum (inset, Fig. 7.3(c)), shows a clear band at $\lambda = 420nm$ corresponding to Au-Ag alloy.

Ag K edge XAFS data (Fig. 7.10(a)) were fit over k=2.7-7.7Å^{-1}, R=1.4-3.4Å, k^w(w=2,3). Difference from Ag foil data suggests presence of Au neighbors. Au L3 edge data (Fig. 7.10(b)) were fit over k=2.8-9Å^{-1}, R=1.6-3.4Å, k^w(w=2,3). Comparison with Au foil data reveals presence of Ag neighbors.

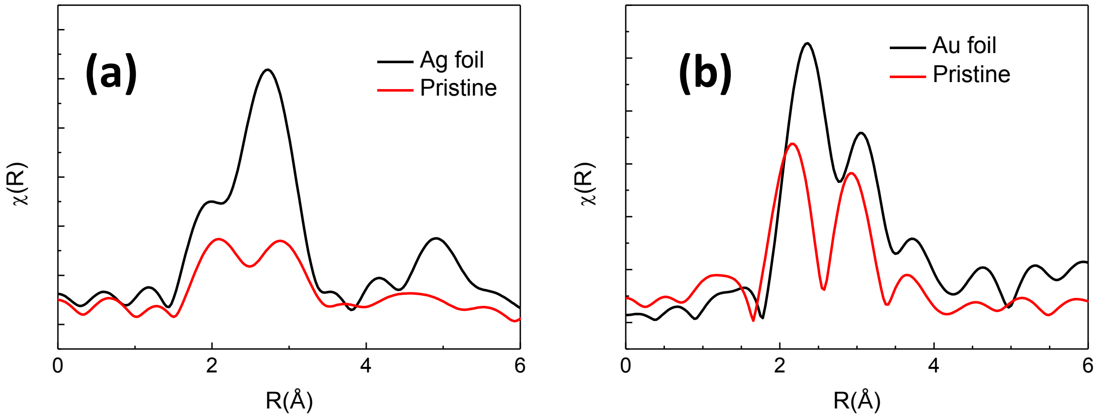

Fig. 7.10: XAFS data for pristine Au/Ag system (a) Ag K edge, (b) Au L3 edge

For both the edges, best fit was obtained when fcc structure was assumed around Ag and Au. The fit results are plotted in Fig. 7.11(a-c). Au/Ag alloy is the best representation for the pristine system.

In summary, both Ag/Pt and Au/Ag co-sputtered systems follow their respective bulk phase diagrams.

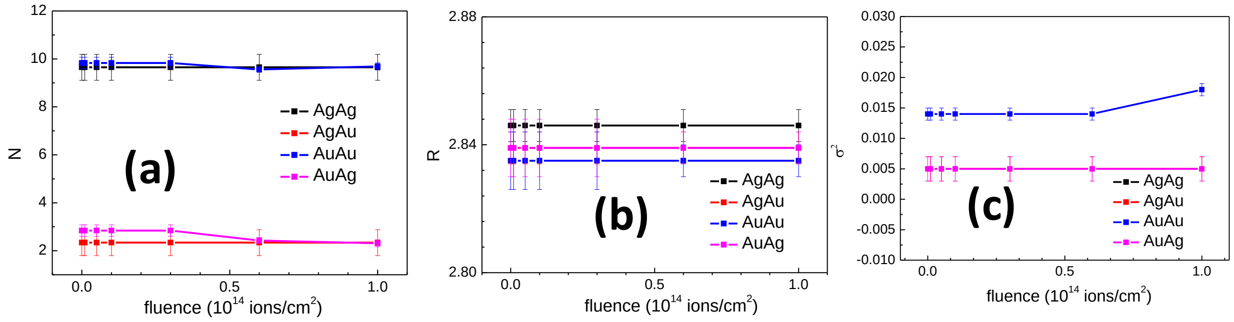

Fig. 7.11: XAFS fit results for Au/Ag system. Plot of (a) N, (b) σ^2 and (c) R as function of SHI fluence.

7.3.2. Post-SHI Irradiation

7.3.2.1 TEM results

Fig. 7.12(a) shows the TEM image of samples irradiated with $1x10^{13}$ ions/cm^2 and $1x10^{14}$ ions/cm^2 respectively. The figures show that size of NCs grows continuously with increasing irradiation fluence mostly due to elongation along ion direction and getting connected to each other. At fluence 1×10^{13} ions/cm^2 and 1×10^{14} ions/cm^2, the aspect ratio (AR=L/D) increases to 3.3 and 5.5 respectively.

7.3.2.2 X-ray Diffraction

XRD pattern [Fig. 7.12(b)] shows no crystalline peaks and continues to resemble the pattern for metallic glass.

In contrast, XRD pattern for Au/Ag system (inset, Fig. 7.12(b)) shows peak corresponding to (111) plane of both Ag and Au, with no change from the pristine sample, suggesting that Au and Ag are alloyed in all the samples.

7.3.2.3 Optical Absorption Spectroscopy

Optical Absorption Spectrum [Fig.7.12(c)] shows no Surface Plasmon Resonance (SPR) band corresponding to either $Ag(\lambda_{Ag} = 400nm)$, $Pt\ (\lambda_{Pt} = 270nm)$ or Ag / Pt. This is in contrast with pristine Au/Ag system (inset, Fig. 7.12(b)), which shows a clear band at corresponding to Au-Ag alloy in both the SHII samples.

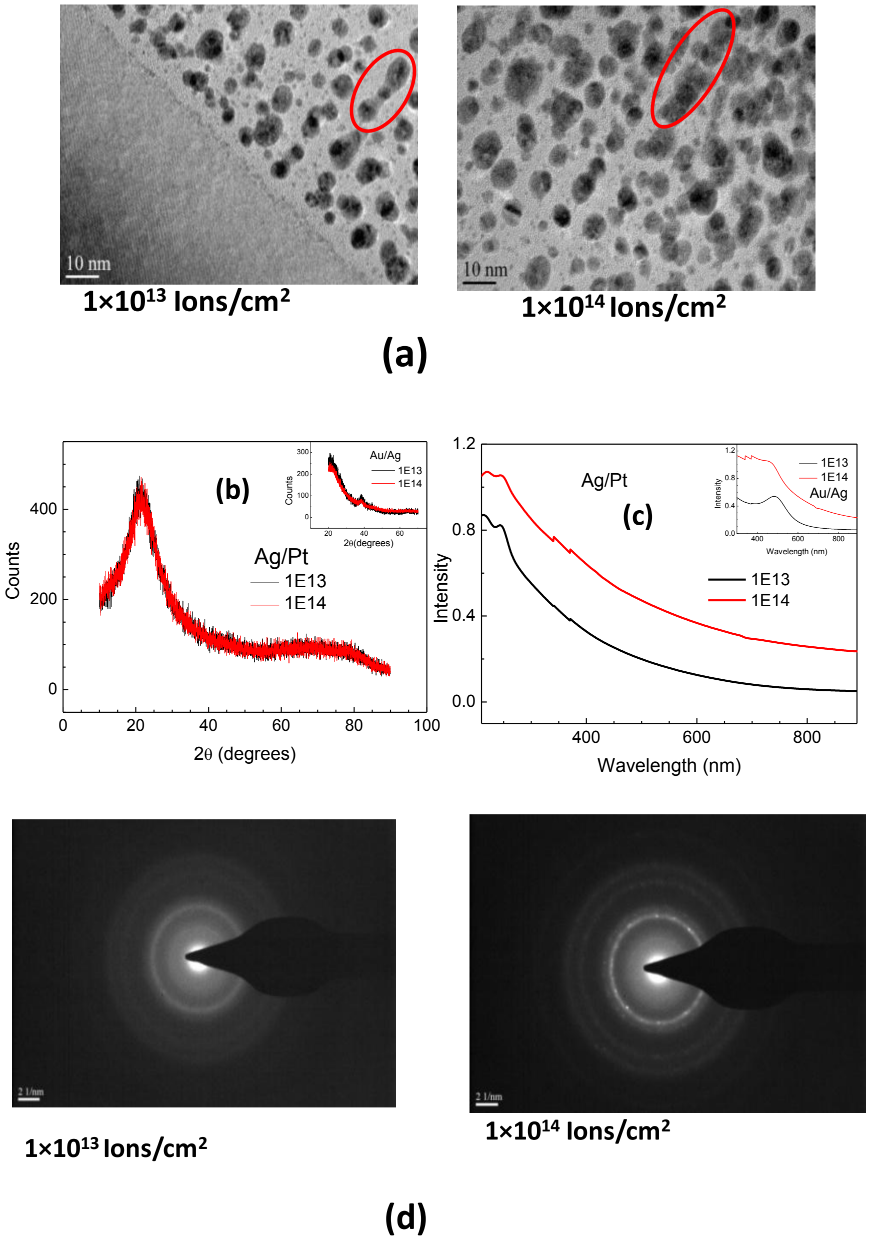

Fig. 7.12: Structural characterization of SHII Ag/Pt system: (a) TEM, (b) XRD pattern, (c) Absorption spectrum, (d) Selective area diffraction pattern

7.3.2.4 Selective Area Diffraction (SAED)

The SAED patterns [Fig. 7.12(d)] show some spots with increasing fluence, suggesting that the samples might contain locally disordered crystals.

Table7.3: Structural Characterization of SHII systems

	Ag/Pt	Au/Ag
Structure	Amorphous	Partially crystalline
Alloying	No	Yes
Shape	Elongated	Elongated (*Not shown in Fig.)
Size	fluence dependent 6nm×20nm @ 6×10^{13} ions/cm^2 8nm44nm @ 1×10^{14} ions/cm^2	
Critical fluence for Pt cluster-formation	5×10^{13} ions/cm^2	-

7.3.2.5 XAFS

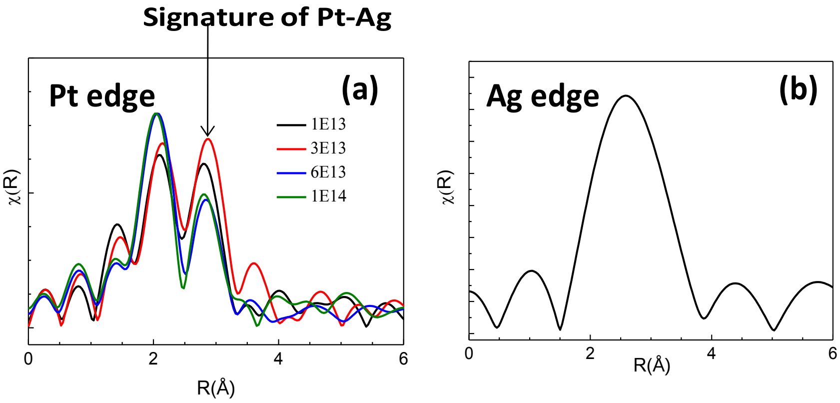

Fig. 7.13: XAFS data for the SHII Ag/Pt samples at (a) Pt L3 edge, (b) Ag K edge

Once again, XAFS data at *Pt L3* and *Ag K* edges (Fig. 7.13 (a-b)) were fit to determine the amorphous short range order in the NCs. The same fitting strategies described in section 7.3.1.5 for the pristine sample were employed to decode the structure of the SHII samples. Note that for Ag edge, the data for all irradiation fluence were similar, therefore all of them were merged together to reduce error bars.

Fit results are plotted in Fig. 7.5 (a-c). Examples of fit quality are plotted in Fig. 7.14 (a-b).

Only $N_{Pt\text{-}Pt}$ increases with SHII beyond critical fluence 5×10^{13} ions/cm^2 and saturates at SHII fluence 6×10^{13} ions/cm^2. This implies SHII-induced growth of the *incomplete* pristine Pt clusters, until it reaches saturation. Pt edge XANES whiteline (Fig. 7.15 (a)) consistently demonstrates signature of "reduction". Its conspicuous deviation *wrt* Pt foil XANES[257-259] suggests that Pt becomes charged beyond critical fluence in the post-SHII samples. Ag edge XANES remains unchanged from metallic state (Fig. 7.15 (b)). Critical fluence could represent the minimum energy deposition per unit length into the system required for Pt reduction and aggregation. XAFS results are consistent with the post-SHII picture of enhanced local crystalline character from SAED.

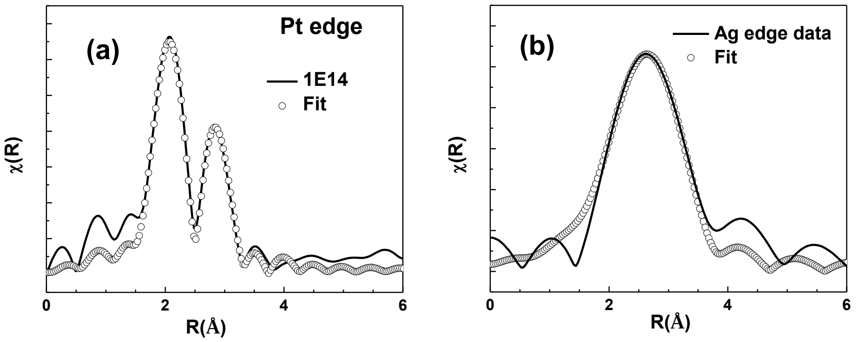

Fig. 7.14: Example of fit quality for (a) Pt edge, (b) Ag edge

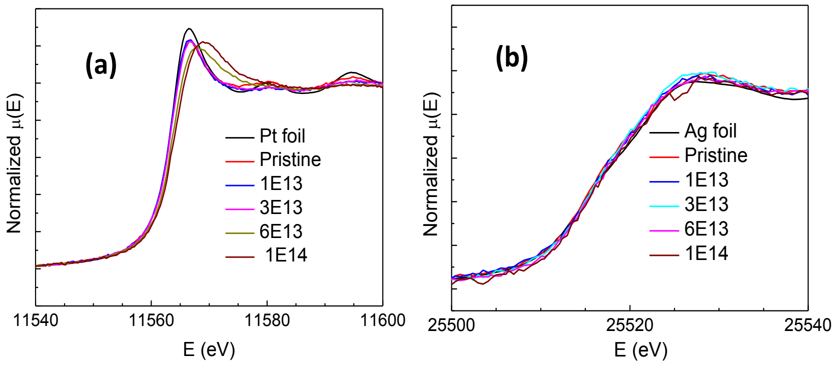

Fig. 7.15: XANES spectra for the SHII Ag/Pt samples at (a) Pt edge and (b) Ag edge

Since SHII is similar to the synthesis method for metallic glass, we considered icosahedral configuration for post-SHII clusters. XAFS coordination (12) is incompatible with site-averaged 13-atom icosahedral coordination $(N = 7)$. To the best of our understanding, the cluster configuration is therefore disordered *fcc*; this is similar to the observation of highly disordered $NiZr_2$ crystalline phase for binary glass $(Zr_{67}Ni_{33})$.[260-261] $R_{Pt\text{-}Ag} \neq R_{Pt\text{-}Pt}$ implies that Pt and Ag have not alloyed with SHII.

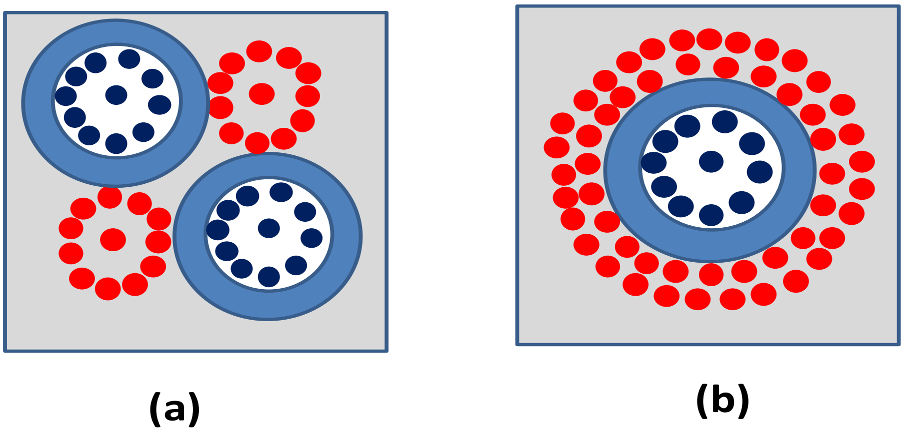

Fig. 7.16: Possible models for the SHII Ag/Pt systems

In section 7.3.1, we had proposed two models for the pristine system: (i) separate Ag and Pt clusters and (ii) Ag@Pt core-shell. Either of these models could explain the increase in $N_{Pt\text{-}Pt}$ while $N_{Ag\text{-}Ag}$ remains unaffected. For Model (i), the insensitivity of Ag coordination to SHII could be because it is already saturated and stable pre-SHII. For Model (ii), it would mean that the Pt shell protects the Ag core from SHI energy; increase of Pt coordination is due to shell thickening. However, XANES clearly shows presence of Pt in charged state beyond the critical fluence. This is possible only in model (ii) (Fig. 7.16 (b)). Therefore the best representation for the SHII systems is Ag@ Pt core-shell.

In summary, the conclusion derived on the role SHII on Ag/Pt system is enhancement of ordering in amorphous system, similar to annealing effect. This is contrary to previous reports where SHII induced amorphization.[262-264] We believe that the difference lies with the pristine system: in previous reports, the pristine crystalline system gets amorphized by SHII, while in this case pristine amorphous system gets annealed by

SHII. Although we had expected Ag and Pt to alloy under the extreme conditions of SHII, it is clear from our analysis that they do not. The main reason is that stable Pt and Ag crystal seeds are pre-formed in the pristine system. SHII is unable to reverse that since it (most likely) does not completely melt Ag and Pt for mixing. Further, the time-scale of SHII (ps) is unable to compete with much faster crystallization kinetics.

These observations yet again point towards the striking similarities of our Ag/Pt system with metallic glass. Similar amorphous to crystalline transition was observed in $Zr_{67}Ni_{33}$ glass[265] with annealing.

7.3.2.6 Comparison with Au/Ag system

For the Au/Ag samples (Fig 7.17), the same fitting strategies described in section 7.3.1.5 for the pristine sample were employed to decode the structure. For each edge, similar datasets were merged together to reduce error bars in fit results. Fit results are plotted in Fig. 7.11(a-c). Clearly, Au/Ag alloy formed during co-sputtering is unaffected by irradiation.

Therefore, only those bimetallic systems for which thermodynamics does not allow alloying are affected by SHII.

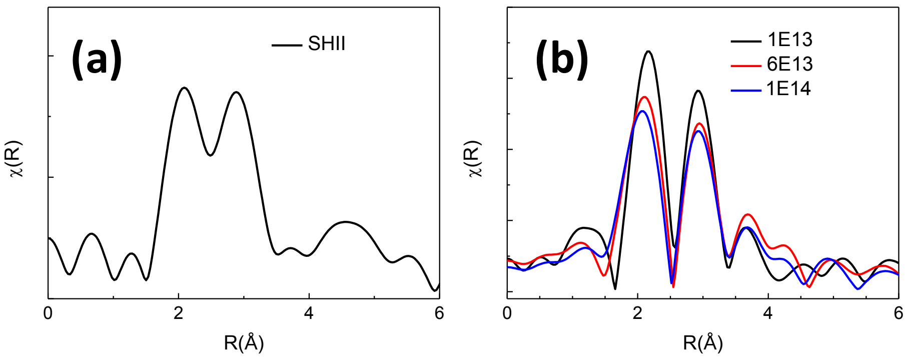

Fig. 7.17: XAFS data for the SHII Au/Ag samples at (a) Ag K edge, (b) Au L3 edge

7.3.3 Implications of our results on sensing ability of Ag/Pt

As observed through optical spectroscopy, Ag/Pt does not show any absorption band. Therefore, using it as optical sensor is not feasible.

Several previous studies have shown that catalytic activity is greatly enhanced with increase in aspect ratio.[266-268] In general, Ag/Pt nanoparticles are popular catalysts for Methanol Oxidation reaction and Oxygen reduction reaction in Fuel cells. [26, 269-270] In our samples, aspect ratio was seen to increase from 1 to 6 with SHII, hence we expect their catalytic activity to improve.

7.4 Conclusions

We have explored the structure of bulk immiscible Ag/Pt system deposited via atom beam co-sputtering and compared it with bulk miscible Au/Ag system synthesized via the same route, using several characterization techniques, viz. TEM, XRD, Optical Spectroscopy, SAED and XAFS. The consolidated result from all these techniques is that Ag and Pt form complete and incomplete amorphous clusters respectively, with no alloying. This inhibits their ability to be used as optical sensors due to lack of any absorption bands. However, this does not affect their catalytic ability. On the other hand, Au and Ag form alloyed clusters, consistent with thermodynamics and bulk phase diagram. SHII induces elongation of the clusters in both systems. In Ag/Pt system, Pt was seen to become more ordered with SHII while Ag was observed to be immune to SHII. Amorphous to crystalline transition was observed in this system, similar to binary metallic glass. In summary, pico-second time scale irradiation is insufficient to cause irradiation induced melting and hence alloying in binary Ag/Pt system. In contrast, Au/Ag system was unaffected by SHII.

To conclude, we would like to say that those systems wherein mixing is not thermodynamically favored tend to form amorphous clusters when co-sputtered. These clusters undergo amorphous to crystalline transition with SHII.

CHAPTER 8

XAFS CHARACTERIZATION OF AYURVEDIC NANOMEDICINE

8.1 Background

The discipline of Indian Ayurvedic medicine is distinctive in that it recognizes the therapeutic potency of heavy metals or their compounds when (i) mixed with organic molecules (herbs) and (ii) processed in prescribed route employing natural products.[271-275] The advantages of Ayurveda over allopathic treatment include (i) cost-effectiveness (due to natural resources),[276] (ii) longer shelf-life (due to presence of metals) and (iii) minimized adverse side effects.[277] In India, Ayurvedic medicine assumes crucial importance in bridging the gap between heavy patient load (rural / poor) and medical accessibility.[278] The scope of Ayurveda in India is aided by availability of abundant medicinal plants.[279-281] Recognizing these facts, the Government of India (GOI) has taken keen interest to regularize Ayurveda as widespread alternative healthcare route. To practically realize this, the GOI has actively invested on Ayurvedic research in several institutes [282-285] with the objective of finding scientific evidence towards non-toxicity, standardization and effectiveness of Ayurvedic medicines.[286-287]

An objection raised against metal-derived drugs of Ayurveda[288-292] is the lack of scientific evidence for its claimed non-toxicity.[293-295] Some reports suggest that toxicity is neutralized by compound formation.[296] However, their synthesis methods do not guarantee (nor experimentally prove) total elimination of metallic phases. In the absence of scientific validation, the present criterion of toxicity (or consequent ban) is defined by the metallic content (and not the chemical or structural forms).[297]

The general Ayurvedic synthesis method (“Bhasmikaran”)[298-299] includes:

(i) Ingredients (metal + organic material): The advantages of metal (or its compounds) are manifold: longer shelf life, small attainable sizes, quick drug release, lower required dosage, size-controlled tunability of Surface Plasmon Resonance for targeted drug delivery.[300]

(ii) Heating: The objective of heating is the formation of metal salts $[M^0 + B^0 \rightarrow M^+(B)^-]; B = S, O$ etc. Toxic reaction of elemental metals (M^0) within body (C, H, O) proceeds by oxidation $[M^0 \rightarrow M^+(C, H, O)^-]$. This is curtailed by pre-forming stable $[M^+B^-]$ compounds before being administered into the body.[301-304] Accomplishing 100% oxidation (zero M^0 remaining) is the most crucial step for non-toxicity of the drug.

(iii) Repeated purification: Impurities / residual metals are removed by controlled heating for prolonged period of time.[305]

(iv) Grinding – reducing the particle size such that end-product ("Bhasma") has very fine texture (Bhasma) and no metallic shine.[306-308]

In modern perspective, this process could be equivalent to the formation of metal-oxide (or compound) nanoparticles,[309-314] that could act as drug-carriers in targeted drug delivery.[315-316]

As mentioned earlier, complete oxidation and quality control of "Bhasma" particles have to be experimentally validated for Ayurvedic bhasmas to be credible and acceptable for use as drugs. Previous research includes reports on elemental analysis[317], toxicology studies[318], heavy metal bioaccessibility tests[319], XRD.[294,317] But none of them could unambiguously establish *complete* oxidation status or account for non-toxicity. In this work, we propose to accomplish this by XAFS-investigation of the structure of α-*HgS*-based *Rasasindura*. The latter is widely prescribed (<125 mg / day) for treatment of certain diseases.[320-325]

Elemental specificity makes XAFS[46] more sensitive to small amounts $(\geq 3\%)$ of defects/ hidden phases that are not detected by X-Ray Diffraction (XRD). Further, XANES at Hg L3 edge contains information of the oxidation state (single or multi-valence).[46] In this case, (i) in the backdrop of primary α-*HgS* phase, there could be minute quantities of segregated chemical phases (pure *Hg*, β-*HgS*) that are undetected by XRD; (ii) identification of core-shell (if) structure of the nanoparticles; (iii) surface segregation (if any) for the nano-crystals and (iv) identification of local defects (pores etc.) / disorder etc within the nano-particle. Each of these parameters, as explained later, is correlated with toxicity.

8.1.1. *HgS*- based *Rasasindura*

Due to high mobility, water-solubility and relative ease of oxidation[326-327], metallic mercury (Hg^0) is one of the most toxic elements known to human; it interacts with human body to form toxic methyl-mercury ($(CH_3)Hg$).[328] While there is worldwide concern against *Hg* contamination in food / water / soil[329-336], it is strange that *Hg-based* medicines are recommended in Ayurveda – often in concentration larger than WHO-permissible limit (> 1 ppm).[337-338] From reported XRD results, the crystal structure of *Rasasindura* is known to be α-*HgS.* Preliminarily, non-toxicity of *Rasasindura*[321] can be correlated with the advantageous properties of bulk α-*HgS*[339]:

(i) Hg has special affinity for *S*[340], resulting in the formation of strong *Hg-S* bond. This is supported by recent experiments on *Hg*-contaminated soil samples[57], where it is observed that binding of Hg^{2+} with sulfur-containing groups (rather than oxygen-containing group) significantly arrests its reduction ($Hg^{2+} \rightarrow Hg^0$).

(ii) Low solubility and bioavailability[319] (0.001g/L) of α-HgS results in low accumulation in the human body (0.2% is absorbed in the gastrointestinal tract and only 0.02% reaches the kidneys).[341-342]

(iii) $Toxicity[HgS] \sim 10^{-4} \times Toxicity[(CH_3)Hg]$ (Ref. 343-346)

(iv) The possibility of $HgS \rightarrow (CH_3)Hg$ conversion by human intestinal bacteria has been ruled out.[347]

However, these advantages may not hold good for nanoparticle form (Bhasma). Surface energetics, increased strain and vacancy defects[348] may lead to the formation of local Hg^0 sites *i.e.* initiate reverse reaction [$Hg^{2+} \rightarrow Hg^0$]. Further, XRD cannot unambiguously rule out the presence of < 5% Hg^0 due to its limited resolution. We need to establish reliably that *Rasasindura* has (i) complete absence of Hg^0 and (ii) robust nano-structure with minimal defects.

8.1.2. Synthesis Method

Rasasindura, like any other licensed and standardised formulation, is subjected to Standard Operating Procedures (SOP), including starting / in-process / finishing quality control (QC) checks. *Rasasindura* was prepared by Arya Vaidya Sala (India) following three distinct steps: (i) pre-treatment of *Hg* and *S* with herbal and milk products: *Hg* was ground with slaked lime on a mortar for three days and filtered through a fine cloth. The filtrate was ground with garlic and rock salt until it turned black in color and then washed in water.[349] *S* was heated with ghee and allowed to drop through a cloth into milk. The resultant granules were collected and washed with water[350]; (ii) mixing of *Hg* and *S* [$Hg:S = 1:1$] along with other herbal ingredients [Aloe vera juice] and ground for five days on electric grinder, resulting in the formation of black-HgS (*Kajjali*)[351]; (iii) thermal treatment at 600˚C of dried *Kajjali*, in porcelain pots, with porcelain lid and totally covered with seven layers of clay smeared cloth. The whole pot is smeared with clay for total sealing. The pots are charged into Open Hearth Furnace (electrically operated) for 24 hours with the temperature being raised from room temperature to 600^0C. After 24 hours, heating is cut off and the pots are allowed to cool down naturally for the next 24 hours. The cooled porcelain pots are opened by cutting open the clay seal. The final product, *Rasasindura,* in the form of fine dust of brick red colour, will be found deposited on the inside roof of the porcelain lid, which is then scraped out.[352] It is triturated in a mortar and pestle and then passed through a fresh nylon cloth of 200-mesh.

Schematically, the entire synthesis process can be thus summarized:

$$[(Hg)+(S)] \rightarrow Kajjali(Black - HgS) \rightarrow \text{Rasasindura}(\text{Red} - HgS)\,. \qquad (8.1)$$

For HgS formation, $S + Hg \rightarrow HgS, \Delta G^\circ = -46\, KJ/mol$. The negative free energy change ΔG° shows feasibility of formation of some amount of HgS even before heat treatment of *Kajjali.*[353] Heat treatment of *Kajjali* is essential to decrease the proportion of unreacted *Sulfur,* and the herbal ingredients provide the acidic medium (catalyst) required for this reaction besides aiding in solidification of *Hg.*[317]

To understand the relative stability and non-toxicity of *Kajjali* and *Rasasindura*, we studied their inorganic counter-parts (viz. Black and Red *HgS*).

8.1.3. *Inorganic* Black-*HgS* and Red-*HgS*

In bulk form, Black and Red *HgS* generally represent the two structural forms of (inorganic) *HgS*:

(a) Symmetry: In bulk form, Black and Red *HgS* represent structural polymorphs *viz.* cubic *β-HgS* (tetrahedral) and trigonal *α-HgS* (octahedral) respectively.

(b) Stability: Black *HgS* is unstable below 600 K (Ref. 354-355), decomposes into Red (α)-*HgS* and is prone to oxidation. Instability of Black-*HgS* may be due to poor packing efficiency for tetrahedral configuration.[xvii,356]

On the other hand, Red (α)-*HgS* is reported to be stable[357] because of its significantly enhanced packing efficiency.[xvii] The smaller misfit factor for octahedral configuration in Red (α)-*HgS* can be accommodated with slight distortion of the octahedron and phase-stabilized.

In summary, $\alpha - phase \rightarrow stability \rightarrow non-toxicity$.

(c) Toxicity: Red (α)-*HgS*, the stable structural form, has not been explicitly reported as toxic in literature[358-360] $Toxicity[\mathrm{Red}\,(\alpha) - HgS] \sim 10^{-4} \times Toxicity[(CH_3)Hg]$ (Ref. 343-346). On the other hand, there are several reports on Black- *HgS* being toxic.[361]

8.1.4. Pre-XAFS characterization of *Rasasindura*

Although colors are strong indicators of structural forms, they could be elusive in this case since Bhasma samples are formed of nano-sized particles where color could be size-dependent. To obtain comprehensive overview of *Rasasindura* structure (in reference to laboratory-based *HgS*), we have employed complementary techniques: XRD/ X-ray Fluorescence (XRF)/ Fourier Transform (FT)-Raman & IR/ Surface Enhanced Raman Scattering (SERS). XRD and XRF experiments were performed at Indus-2 synchrotron source (India), where high-resolution information could be extracted due to very high photon flux ($\sim 10^{11}\, photons/\sec$). SERS, FT-Raman and FT-IR spectra were also recorded at Bhabha Atomic Research Centre (India). The conclusions from these techniques, listed in Table 8.1, unanimously establish that *Rasasindura* has the same structure as Red (α)-*HgS* and additionally, is better ordered.

[xvii] Packing Fraction (P.F.): $P.F._{\beta-HgS} = 32\%$, $P.F._{\alpha-HgS} = 58\%$

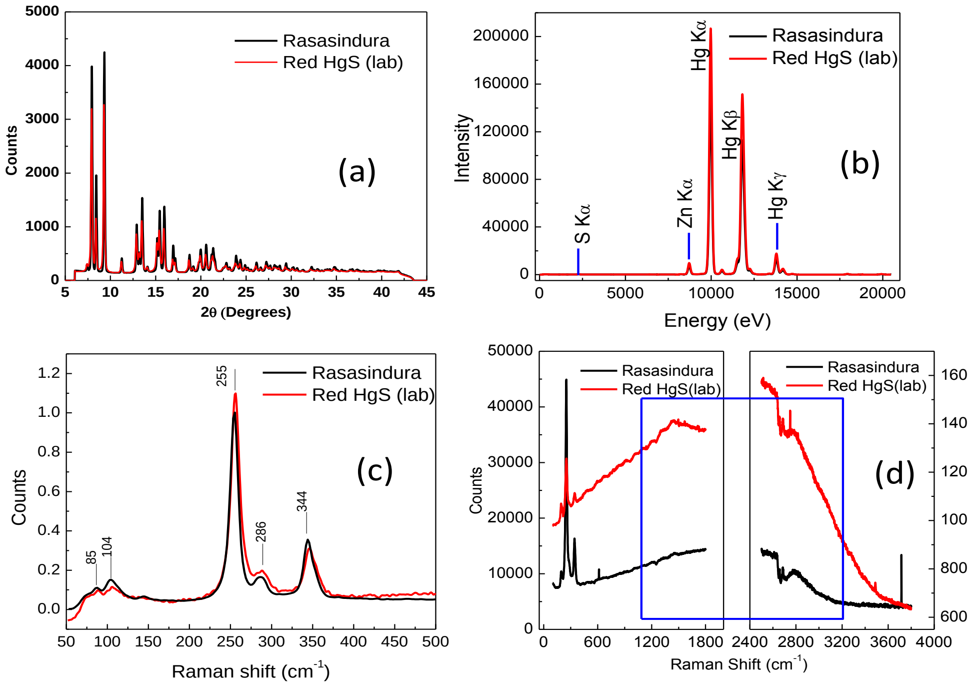

Fig. 8.1: Pre-XAFS characterization of *Rasasindura* in comparison with Laboratory synthesized Red *HgS* using : (a) XRD, (b) XRF, (c) Raman and (d) SERS.

Table 8.1 Characterization of *Rasasindura* and Red *HgS*

Technique		***Rasasindura***	**Red *HgS* (lab)**
XRD (Fig. 8.1 (a))	Form	α-*HgS;* no Hg^0 phase detected.	α-*HgS;* no Hg^0 phase detected.
	Shape	Spherical	Spherical
	Particle size	24nm	18nm
XRF (Fig. 8.1 (b))	Elements	*Hg*, *S* and *Zn* (0.6%)	*Hg*, *S* and *Zn*
		[Note that Zn is reportedly found as impurity in *Hg*]	
	Hg:S ratio	1:1	1:1
FT-Raman (Fig. 8.1 (c))	Form	α-*HgS*	α-*HgS*
	Bonding	Strong *Hg-S* bond	Strong *Hg-S* bond
	Order	Better ordered	
SERS (Fig. 8.1 (d))	Surface organic groups	Absent	Absent
FT-IR	Organic groups	Absent	Absent

8.2 XAFS Experimental details

Transmission mode XAFS was recorded on *Rasasindura* and Red (α)-*HgS* at *Hg L3* edge (12.284 keV) at Scanning EXAFS beamline (BL-09), Indus-2 Synchrotron Radiation Source, RRCAT (India). A pair of *Si* (111) crystals in parallel geometry was used as double crystal monochromator (DCM). 1.5 m long horizontal pre-mirror with meridionial cylindrical curvature was used to obtain collimated beam on first crystal of DCM and reject higher harmonics from the XAFS spectrum. Incident and transmitted intensities were measured using N_2/Ar filled ionization chambers.

XAFS data were processed using ATHENA software. The extracted XAFS oscillations, $\chi(k)$, were Fourier-transformed into real space $\chi(R)$ for fitting. {Structural model was constructed, using FEFF6.1.[89] The model parameters were allowed to vary while fitting (using FEFFIT) to yield the best-fit values for bond lengths (*R*), coordination numbers (N) and Debye–Waller factors (DWF or σ^2). R-factor was considered as an estimate of the quality of fit. [83,97]

8.3 Results and Discussion

XAFS data for *Rasasindura* and laboratory-made Red (α)-*HgS* were fitted for $k = 2.8 - 8.6$ Å^{-1}; $R = 1.1 - 3.4$ Å. In order to reduce error bars and have sufficient number of points for fitting, simultaneous fitting of the data was carried out for different *k*-weights of the transform viz. $\int k^w \chi(k); w = 0{,}1$. Some of the ripples observed in Fig. 8.2 are due to truncation effect from limited data range and do not represent real data. Apparently, features around $2.5 - 3$Å (Fig. 8.2) look less sharp for *Rasasindura*. However, it should not be mis-interpreted for higher disorder; as we note from analysis results (described below), *Hg-S* bond-lengths in *Rasasindura* are displaced relative to each other such that their scattering contributions phase cancel. In fact, *Rasasindura* is found to be better ordered (than Red (α)-*HgS*) from our analysis.

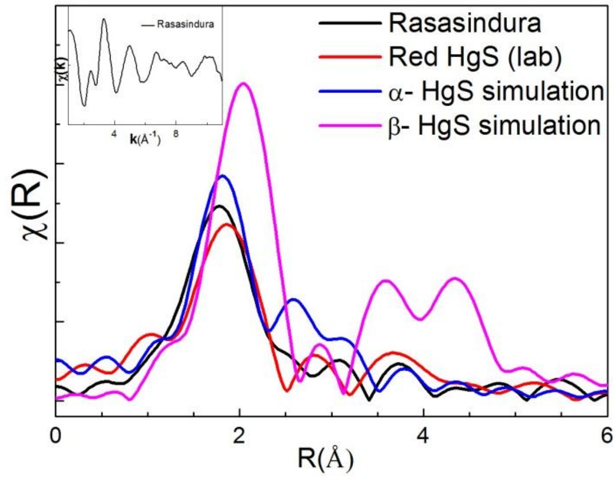

Fig. 8.2 Comparison of *Hg L3* edge XAFS data on *Rasasindura* and Red (α)-*HgS* with simulated XAFS data for *α*- and *β-HgS*. It is clear that the data for *Rasasindura* resembles *α-HgS* (<u>not</u> *β-HgS*).

8.3.1. Phase Segregation

Since changes in XANES are very subtle between *α-HgS* (Hg^{+2}), Hg^0 and *Rasasindura*, we have plotted derivatives of their XANES spectra in Fig.8.3a. XANES derivative features for *Rasasindura* viz. pre-edge (A) and edge position (B) resemble *α-HgS* (Hg^{+2}) (Fig. 8.3a) and are markedly different from Hg^0 (C). Comparison of XANES derivative spectra of *HgS* compounds (*Rasasindura*, α-*HgS*) and Hg^0 clearly reveals[362] (i) shift in edge position (B) towards higher energy ($E_{shift} = 5\,eV$) for (*Rasasindura*, α-*HgS*), due to higher oxidation state (+2) of *Hg* (ii) presence of pre-edge feature (A) in *HgS* due to *S* (*2p*) - *Hg* (*6d*) orbital hybridization, which is absent in Hg^0. The main absorption edge (B) corresponds to intra-site *Hg* (*2p)*→*Hg (6d)* transition, consistent with dipole selection rule $(\Delta l = \pm 1)$. While direct inter-site *Hg (2p)*→ *S (2p)* transition is prohibited by dipole rule, pre-edge feature (A) is indirect signature of *S (2p)* through *Hg (6d)*-*S (2p)* hybridization. Strong pre-edge (hybridization) features confirm strong *Hg-S* covalent bond.

Our next objective is to determine if Hg^0 is *completely* absent or *partially* present. Since our XRD spectrum does not show signature of Hg^0 phase, one can presume that Hg^0 content (x) would be < 5%. On the other hand, XANES derivate spectra show that the amplitudes of (A, B) peaks and their ratio (X) are significantly reduced $\begin{pmatrix} \Delta A, \\ \Delta B, \\ \Delta X \end{pmatrix} = \begin{pmatrix} -33\%, \\ -25\%, \\ -17\% \end{pmatrix}$ in *Rasasindura* $(X = 1.2)$ *wrt α-HgS* $(X = 1.5)$. Since peak "A" (*α-HgS*) is negatively correlated with peak "C" (Hg^0), mixture of these phases (Hg^0, *α-HgS*) could reduce the net amplitude around peak "A" and subsequently, reduce X (as observed for *Rasasindura*). This implies that the reduced features of *Rasasindura* spectra could be consistent with the co-existence of (Hg^0, *α-HgS*) phases. To clarify this ambiguity, we simulated the derivative spectra for different fractions (x_{Hg^0}) of Hg^0 (Fig. 8.3b). For $x_{Hg^0} = 0 \to 30\%$, amplitudes of (A, B) peaks are progressively dampened while their ratio $(X = 1.5)$ remains constant. For $x_{Hg^0} \geq 30\%$, the signature of Hg^0 becomes dramatically conspicuous as the spectra evolve into peaks (A', C') following peaks (A, C); peak B is completely dampened. With increasing Hg^0 content, the positions of (A', C') respectively move away from and towards (A, C) such that the split becomes wider. The spectrum of *Rasasindura* is not consistent with any of these mixed phase features; instead, $(X = 1.3)$ resembles XANES for *Hg-S* bonds in soil, water etc.[363-368]

Reconciling XRD and XANES results, we unambiguously conclude that Hg^0 is absent in *Rasasindura*. Absence of Hg^0 is the most significant evidence towards confirming non-toxicity of *Rasasindura*.

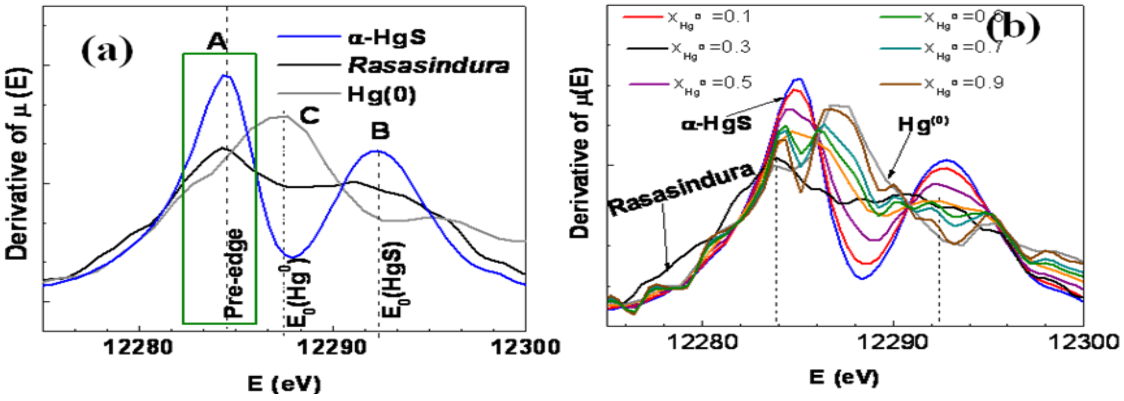

Fig. 8.3 Comparison between (a) derivatives of XANES data on α-*HgS*, *Hg*^{0} and *Rasasindura*. *Rasasindura* closely resembles *α-HgS*. Clearly in *Rasasindura*, (i) edge position is shifted *wrt Hg*^{0} ($E_{shift} = 5eV$) and (ii) pre-edge features are present which are absent in *Hg(0)*. (b) Simulated derivative spectra for different fractions (x_{Hg^0}) of *Hg*^{0}

8.3.2. Crystalline structure details and degree of disorder

In Fig. 8.2, we compared *Rasasindura* / Red (α)-*HgS* data with simulations for *α-HgS* and *β-HgS* crystal structures. Except for larger disorder, near neighbor features ($R < 2.5\,\text{Å}$) of both *Rasasindura* and Red (α)-*HgS* clearly resemble *α-HgS* (in terms of peak position). Theoretical bond-lengths for α-*HgS* are shown in Table 8.2. XAFS fit results (Fig. 3) conform to *α-HgS* configuration for *S* neighbors. [Other models (a) cubic = 6*S* (b) *β-HgS* = 4S ($R = 2.53\,\text{Å}$) yielded bad fit quality.]

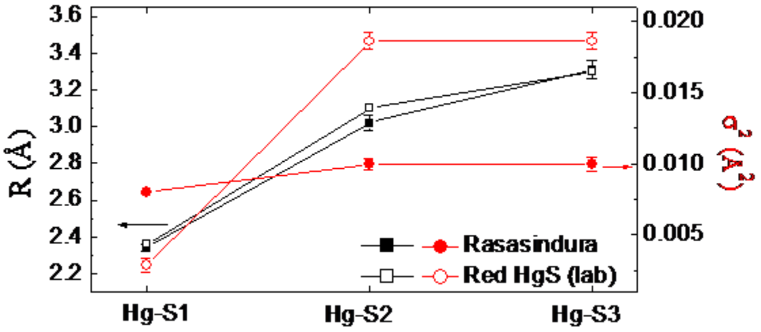

Fig. 8.4a: XAFS fit results for *Rasasindura* and Red (α)- *HgS* (lab). *Rasasindura* is more ordered than Red (α)- *HgS* (lab).

From Fig. 8.4, we observe that *Hg-S* near neighbor configuration is better ordered (lower σ^2) in *Rasasindura* compared to laboratory-synthesized inorganic Red (α)-*HgS*.

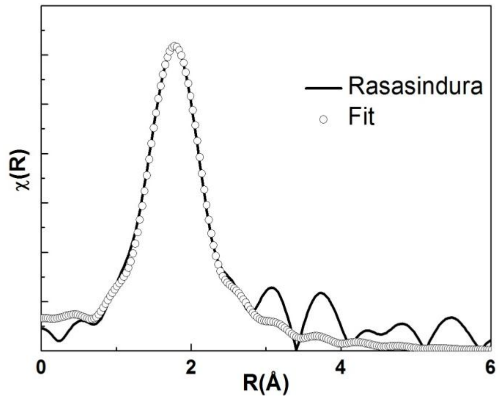

Fig. 8.4b: Comparison of data with fit for *Rasasindura*

Table 8.2 Comparison of bond lengths (*R*)

	Hg-S1	*Hg-S2*	*Hg-S3*	*Hg-Hg1*	*Hg-Hg2*	*Hg-Hg3*
α-*HgS* {theory}	2.36 Å	3.1 Å	3.3 Å	3.79 Å	4.09 Å	4.14 Å
Red (α)- *HgS* (lab) {XAFS}	2.36 Å	3.10 Å	3.30 Å	Absent		
Rasasindura {XAFS}	2.34 (2) Å	3.02 (4) Å	3.31 (5) Å	Absent		

In contrast, *Hg-Hg* bond features ($R > 2.5$ Å) of *α-HgS* are conspicuously absent in experimental XAFS spectra[369-370] (although XRD-generated radial distribution function (using RAD software)[371] clearly reproduces *Hg-Hg* peak). XAFS and XRD experimental results can be reconciled by considering the possible role of *Hg-Hg* disorder (σ^2_{Hg-Hg}). By simulating XAFS for different σ^2_{Hg-Hg}, we determined the critical disorder value for *Hg-Hg* peak suppression to be $\sigma^2_{Hg-Hg} \geq 0.025\,\text{Å}^2$ (Fig. 8.5a). Independently, we simulated XRD patterns with different values of σ^2_{Hg-Hg}. XRD pattern for *Rasasindura* is insensitive to $\boldsymbol{\sigma^2_{Hg-Hg}}$ variation up to $\sigma^2_{Hg-Hg} = 0.035\,Å^2$ **(**Fig. 8.5b). From XAFS and XRD simulations, we thus conclude and clarify that the apparent "absence" of *Hg-Hg* correlation features in experimental XAFS spectrum is actually the reflection of large disorder in *Hg-Hg* bonds. Despite *Hg* being the heavier atom, $\boldsymbol{\sigma^2_{Hg-Hg} >> \sigma^2_{Hg-S}}$ due to strong *Hg-S* covalent bond and relatively weak Van der Waal interaction between *Hg-Hg*. *HgS* structure can be depicted as spiral –*S-Hg-S-Hg-S*- chains (Fig. 8.6a), in which *Hg-S* and *Hg-Hg* bonds are intra- and inter- chain respectively. Any defect in the spiral (e.g. compression / elongation) affects inter-chain *Hg-Hg* bond substantially while strong *Hg-S* bond remains largely unaffected (Fig. 8. 6b). This leads to $\sigma^2_{Hg-Hg} > \sigma^2_{Hg-S}$.

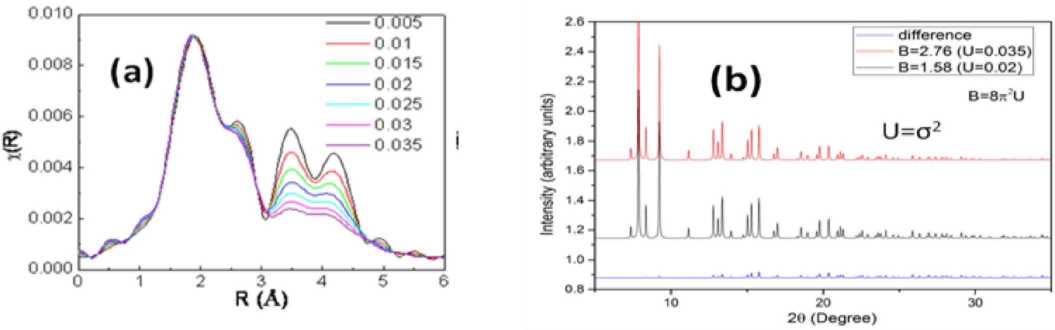

Fig. 8.5: Simulations for different values of σ^2_{Hg-Hg} : (a) XAFS simulations (b) XRD simulations. XRD spectrum is insensitive to σ^2_{Hg-Hg} variation up to $\sigma^2_{Hg-Hg} = 0.035\text{Å}^2$. From XAFS simulations, *Hg-Hg* features are suppressed for $\sigma^2_{Hg-Hg} \geq 0.025\text{Å}^2$

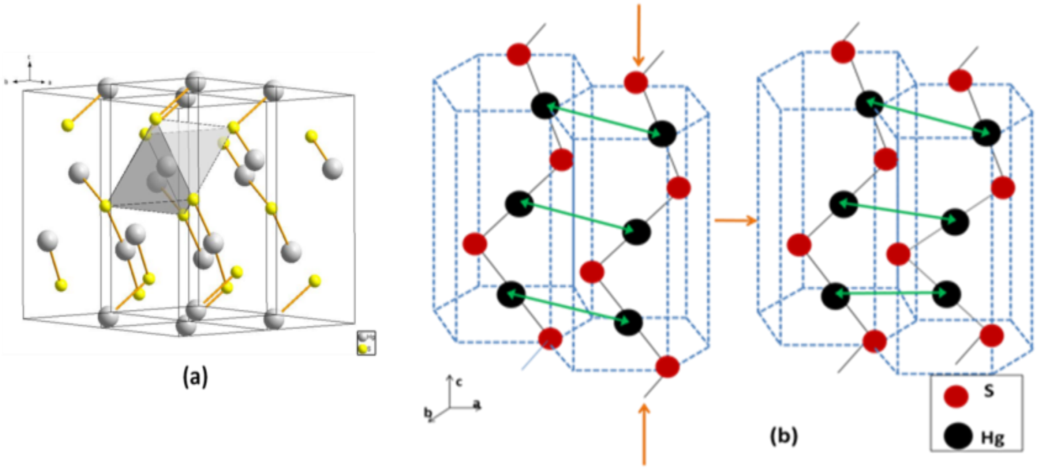

Fig. 8.6: (a) Structure of α-*HgS* comprises of parallel –*S-Hg-S-Hg-S*- chains along c-axis. (b) Compression of one of the chains (defect) affects *Hg-Hg* (green arrows) substantially.

8.3.3. Analysis of the nano-crystal units

For $(D_{Rasa} = 24nm)$, surface-volume ratio of atoms is ~2% $i.e\,(x_{Hg}^{Surface} = 2\%)$. XAFS coordination result $N_{Hg-S} = 6(\pm 3\%)$ is the site-averaged contribution from core $(x_{Hg}^{Core} = 98\%)$ and surface $(x_{Hg}^{Surface} = 2\%)$ sites. Considering coordination loss (ΔN) due to truncation at bare surface, the net (theoretical) coordination for particular bond-length (R=*Hg*-*S* in this case)[372]:

$$N_{nano}(Hg-S) = \left[1 - \frac{3}{4}\left(\frac{2R}{D}\right) + \frac{1}{16}\left(\frac{2R}{D}\right)^3\right] N_{BULK} \approx 6\ (\approx N_{\exp t}) \qquad (8.2)$$

i.e. $\Delta N_{D=24nm} \approx 2\%$ which is less than XAFS resolution $(\Delta N = \pm 3\%)$. Thus, our XAFS coordination result is apparently consistent with theoretical size-dependent coordination loss for chemically homogeneous defect-free nano-crystal. Any defect, if present, has to be accommodated within 3% error bar of XAFS coordination result. We provide defect estimates that are consistent with this constraint.

(a) Vacancy: Vacancy-induced extra coordination loss is not observed; one can rule out the presence of ***(≥ 3%)*** vacancy in the nano-particles.

(b) Surface segregation of *Hg*: Due to insignificant surface-volume ratio (2%), surface contribution to XAFS coordination result is insignificant; hence, XAFS results do not reflect surface coordination unambiguously. [We have calculated the critical core size $(D_{core} \le 4nm)$ for resolving surface coordination.] To estimate the possibility (and fraction) of preferential surface site occupancy by *Hg*, we considered chemical non-uniformity across the nano-crystal and allowed $(x_{Hg}^{Surface} : x_{Hg}^{Core})$ to vary (instead of constraining $x_{Hg}^{Surface} = 2\%$). By re-calculating site-averaged *Hg* coordination as function of $x_{Hg}^{Surface}$, we determined that $x_{Hg}^{Surface} < 6\%$ is consistent with XAFS result.

(c) Organic molecules at surface: Due to insignificant surface-volume ratio and weak backscattering factor of organic elements, XAFS was unable to unambiguously detect the presence of surface organic molecules. We obtained the answer by employing SERS. SERS results convincingly ruled out the presence of organic molecule at surface. This is remarkable since Ayurvedic synthesis method involves organic molecules. We believe that organic molecules were removed during purification steps or heating.

(d) Porosity: To explore the presence of nano-pores (cylindrical) in the particle, we theoretically estimated the average coordination for pore parameters (D_P, H_p, N_p); $D_p =$ pore diameter, $H_p =$ pore-height, $N_p =$ number of pores. By varying one of these parameters $H_p = 1-10\,nm$ (*i.e.* $H_p^{\max} =$ radius of the nano-crystal), we determined the range of $(D_P, N_p)_{H_p}$ [*i.e.* for each H_p] that is consistent with $N_{\exp t} \approx 6\,(\pm 3\%)$. Compiling all these calculation results, we obtained $D_p^{\max} = 10\,nm, N_p^{\max} = 20$, $V_p^{\max} = 7\%$. [Note that $(D_P, N_p)_{H_p}$ are negatively correlated.] $V_p^{\max} = 7\% \Rightarrow$ Pores occupy small volume fraction of the nano-crystal, which is insufficient to generate large disorder and help preserve robust character of the nanoparticle. Minimal defects for these nano-crystals could be correlated with large particle size $(D_{Rasa} \approx 24\,nm)$. Interfacial defects and broadening generally increase significantly for $D \leq 8\,nm$.[16,373-374]

[Note that the above conclusions for *Rasasindura* also hold good for Red (α)-*HgS* due to similar size and coordination results.] These pores could provide the pathway for drug binding.

Summary of nano-crystal coordination analysis is the presence of robust and chemically homogeneous (α-*HgS*) nano-crystal (Fig. 8.7). Including the error bar

$(\Delta N = \pm 3\%)$, we could accommodate possible defects in the particle (viz. vacancy, surface segregation, nano-pore) and determine the upper limit of their content: $(< 3-7\%)$.

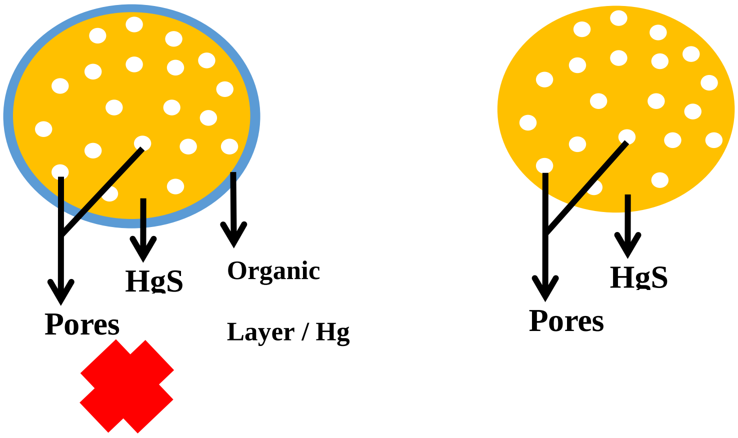

Fig. 8.7: Model of *Rasasindura* nano-crystal with 24 nm HgS core.

8.3.4. Implications of our structural results for toxicity and synthesis route

(i) Toxicity: For successful non-toxic functioning of heavy-metal based Ayurvedic medicine, the most crucial factors (*wrt* toxicity) are (i) complete oxidation of the metals (no remnant of Hg^0-metallic state) before entering human body; (ii) integrated structure of the medicine so that oxide form is retained inside the body (no reduction to metallic form). From our work, we observe that both the criteria are met for *Rasasindura*.

Our main result implying non-toxicity[321] of *Rasasindura* is the absence of metallic Hg^0 [*i.e. Hg* is completely oxidized]. The structural results unanimously establish that *Rasasindura* is composed of robust (minimal defects) single-phase α-*HgS* nano-particle units ($D_{Rasa} \approx 24nm$). As already mentioned above, α-*HgS* is non-toxic which implies the same for *Rasasindura*. Stable α-phase form and robust character of the nanoparticle would help to maintain its integrity during the entire drug delivery process.[375]

Although the implications of size ($D_{Rasa} \approx 24nm$) are not clear at the moment, we would like to cite the correlation between nano-drug and target cell sizes, as in targeted drug delivery [Optimal particle size requirement is target specific].[376-378]

(ii) Synthesis: We compared the structures of *Rasasindura* and Red-*HgS i.e*. end products of organic and inorganic synthesis methods. Interestingly, we found particle size distribution is better controlled in *Rasasindura*[379].The distribution is Gaussian and size-dispersion $(\sigma_D^{Rasa} = \pm 3.5nm;18\%)$. On the other hand, size-distribution of red (α)-*HgS* is non-Gaussian ($D_{peak} \approx 20nm$) and heavily skewed towards higher particle sizes; total size distribution spreads over $(\Delta D = 50nm)$. Better size control in *Rasasindura* could be due to herbal coating - similar to the modern day surfactant- mediated nanoparticle synthesis. Coordination configuration for both show large disorder for *Hg-Hg* bonds but well-defined *HgS* bonds. *Hg-S* coordination distribution is better ordered in *Rasasindura* (Fig. 8.4) which could be due to prolonged annealing.

Thus, our work not only helps understand non-toxicity of *Rasasindura* but also establishes Ayurvedic synthesis method for well controlled end-product.

8.4 Conclusion

We have employed XAFS (coupled with supporting techniques) to investigate the structure of *Rasasindura*. The main results are that *Rasasindura* has the same structure as non-toxic α-*HgS* and elemental Hg^0 is completely absent. Our results also demonstrate that the nano-crystal ($D_{Rasa} \approx 24nm$) units of *Rasasindura* are robust and free of organic molecules. Absence of Hg^0 helps in understanding of non-toxicity and the robust character implies the nano-particle integrity during drug release. Further, we observed that Ayurvedic synthesis yielded better controlled end-product than laboratory-based red (α)-*HgS*: lower size dispersion and better ordered coordination configuration. With all these advantages, *Rasasindura* can be considered for potential therapeutic agent for target cell sizes (~24 nm).

CHAPTER 9

CONCLUSIONS AND FUTURE DIRECTIONS

This thesis has focused on two aspects: (i) XAFS analysis of disordered nanoclusters and (ii) XAFS beamline development program.

9.1 XAFS analysis: In this work, we have characterized the structure of disordered nano-clusters in three unique configurations: (a) Ni/Pt nano-clusters embedded in multilayer film, (b) Ag/Pt and Au/Ag nanorods synthesized via Swift Heavy Ion Irradiation, (c) HgS-based Ayurvedic nano-medicine.

(a) Employing XAFS in grazing-angle X-ray Standing Wave mode, we have characterized Ni/Pt clusters generated by ion irradiation of Pt/Ni/C multilayer. The analysis strategy is challenging since it required decoupling of information from matrix layer, interface and embedded clusters. To the best of our knowledge, this is the first XAFS attempt of decoding the structure of embedded clusters in multi-layers. The clusters are formed by the migration of atoms from interface following ion-irradiation. Our XANES analysis directly establishes the correlation between chemical nature of the interface and the composition of bimetallic clusters. Pre-existing charge transfer at the pristine Ni/C and Ni/Pt interfaces keeps them integrated during irradiation. On the other hand, physically adsorbed Pt/C interface gets disrupted and Pt atoms migrate to C layer. They combine with pre-existing Ni atoms in the C layer to form Ni centered Ni-Pt nano-clusters. These clusters have ferromagnetic composition (Ni:Pt= 60:40) and are highly disordered beyond first neighbor, resembling metallic glasses.

This work is significant for the “dry” synthesis method of amorphous magnetic devices. We demonstrate that the cluster formation / configuration process is not random but can be controlled by manipulating layer (atomic migration length) and interfacial thickness / chemical state.

(b) Amorphous (Ag/Pt, Au/Ag) nano-rods, synthesized via Swift Heavy Ion Irradiation (SHII), were characterized for short-range-order "cluster" configuration. One of the primary interests was to determine whether the extreme conditions of SHII could induce alloying in bulk immiscible Ag/Pt. We realize that segregated seeds of disordered Pt and Ag clusters were pre-formed in the pristine co-sputtered system and SHII only improves the ordering (growth of Pt). The most likely reason for this is that SHII does not completely melt Ag and Pt for mixing. Further, the time-scale of SHII (ps) is unable to compete with much faster crystallization kinetics. [We have compared this case with bulk-miscible Au/Ag system synthesized via the same route. Au/Ag retained its alloyed state and no change in composition / ordering was observed with SHII.]

The implications of the amorphous structure on the applications of these SHII-synthesized nano-rods are: (i) Ag/Pt cannot be used for optical sensing, since it does not give rise to absorption band. However, the high aspect ratio is likely to enhance catalysis due to larger surface area for reactions. Currently, its catalytic activity (methanol oxidation) is under investigation. (ii) Au/Ag exhibits intense absorption band and can continue to be optical sensor despite amorphous character.

(c) We have used XAFS in conjunction with other complementary techniques viz. XRD, Raman, SERS, XRF, to investigate the structure of Hg based ayurvedic drug, "*Rasasindura*". Our XANES results clearly establish the absence of metallic Hg^0 in *Rasasindura*; instead, Hg is present in stable α-HgS nano-crystal form. Non existence of Hg^0 ensures absence of mercury based toxicity; in parallel, stable α-HgS form and robust (<3% defect) nano-particle structure ensure integrity of the drug within human body. Elimination of Hg^0 being the most crucial step in the synthesis, we emphasize strongly on the perfect execution of synthesis process. This is the first report of scientific evidence (and guidance) towards non-toxicity of heavy metal-based Ayurvedic drug. In the backdrop of global interest in Ayurveda vis-à-vis prejudice against heavy metal composition, our results provide significant lead that the chemical form of heavy metal, rather than its content, is the correct parameter to evaluate toxicity of Ayurvedic drugs. This should strengthen credibility of Ayurveda as holistic and cheaper solution. Future of this XAFS work involves binding of *Rasasindura* with human protein in order to understand its actual reaction mechanism within the body.

All of the systems investigated in this thesis are highly disordered clusters beyond first nearest neighbor. In continuation, we are investigating the correlation between glass forming ability and short-range-order in $Zr_{52}Ti_6Al_{10}Cu_{18}Ni_{14}$ glass (in conjunction with ab- initio Molecular Dynamics simulations). Further, we would extend our knowledge of XAFS disorder analysis to decipher the correlation between disorder and Metal-to-Insulator transition in $SrRu_{1-x}Ti_xO_3$.

9.2. Indus-2 XAFS beamline development program: Under XI Plan Project (35.10), we have augmented the XAFS facilities at Indus-2 to accommodate (i) high pressure and (ii) low temperature XAFS experiments. For high pressure XAFS experiments using DAC (sample size=50-80μm), we have installed bendable elliptical mirror to improve vertical focusing of the beam. This new setup has been tested for the worst experimental condition (space limit) and ~ 60% improvement in spot size was attained. Presently, automation of this setup is in progress that will encourage finer optimization of the beam size and efficient data collection.

For low temperature XAFS experiments, we have installed displex closed cycle cryostat, which we have tested down to 5K. We have demonstrated the feasibility of performing low temperature experiments using this cryostat in the temperature range 50-300K by measuring temperature dependent XAFS of Au foil. We have obtained data of reasonable quality, which matches international standard data and is reproducible inside and outside the cryostat. We have calibrated the temperature of the cryostat and observed that the temperature accuracy is $\Delta T \leq \pm 5K$. We now plan to pursue lower (<50 K) temperature-XAFS of non-standard samples.

BIBLIOGRAPHY

[1] Y. Xia, P. Yang, Y. Sun, Y. Wu, B. Mayers, B. Gates, Y. Yin, F. Kim, H. Yan, *Adv. Mat.*, **15**, 353 (2003) and references therein.

[2] H.S. Nalwa (ed.), Handbook of Nanostructured Materials and Nanotechnology, Vol. 1–5. Academic Press, San Diego, USA (2000).

[3] D. Feldheim, *Nature*, **408**, 45 (2000).

[4] M. O. Emeje, I. C. Obidike, E. I. Akpabio, S. I. Ofoefule, Intech, Pg. 69 (2012). http://dx.doi.org/10.5772/51384

[5] A.P. Alivisatos, *Sci. Am.*, **285**, 66 (2001).

[6] A.P. Alivisatos, K.P. Johnson, X.G. Peng, T.E. Wilson, C.J. Loweth, M.P. Bruchez, P.G. Schultz, *Nature*, **382**, 609 (1996).

[7] T.A. El-Brolossy, T. Abdallah, M.B. Mohamed, S. Abdallah, K. Easawi, S. Negm, H. Talaat, *Eur. Phys. J. Special Topics*, **153**, 361(2008).

[8] P.C. Pandey, A.K. Pandey, *Analyst*, **137**, 3306 (2012).

[9] A. Dmitriev, “Nanoplasmonic Sensors”, Springer (2012).

[10] C.R. Henry, *Surf. Sci. Rep.*, **31**, 235 (1998).

[11] D.W. Goodman, *Nature*, **454**, 948 (2008).

[12] D.K. Tiwari, J. Behari, P. Sen, *World Applied Sciences Journal*, **3**, 417 (2008).

[13] G-M Chow, N. Ivanova Noskova, Nano-structured Materials Science and Technology. Dordrecht: Kluwer Academic publishers (1998).

[14] F. Benseba, Nanoparticle technologies: From Lab to Market, Pg. 443 (2012).

[15] A.H. Khan, U. Thupakula, A. Dalui, S. Maji, A. Debangshi, S. Acharya, *J. Phys. Chem. C*, **117**, 7934 (2013).

[16] T. Shibata, B.A. Bunker, Z. Zhang, D. Meisel, C.F. Vardeman II, J.D. Gezelter, *J. Am. Chem. Soc.*, **124**, 11989 (2002).

[17] S. Zhang, X. Y. Cao , Y. M. Ma, Y. C. Ke, J. K. Zhang, F. S. Wang, *Express Polymer Letters*,**5**, 581 (2011).

[18] V. Markovich, R. Puzniak, I. Fita, D. Mogilyansky, A. Wisniewski, Y. Skourski, G. Jung, G. Gorodetsky, *J. Nanopar. Res.*, **15**, 1862 (2013).

[19] M.D. Regulacio, S. Kar, E. Zuniga, G. Wang, Norman R. Dollahon, G. T. Yee,S.L. Stoll, *Chem. Mater*., **20**, 3368 (2008).

[20] F. Michael, C. Gonzalez, V. Mujica, M. Marquez, M. A. Ratner, *Phys. Rev. B*, **76**, 224409 (2007).

[21] I. Žutić, A. Petukhov, *Nature Nanotech.*, **4**, 623 (2009).

[22] I. Žutić, J. Fabian, S. Das Sarma, *Rev. Mod. Phys.*, **76**, 323–410 (2004).

[23] S. Sanchez, L.D. Menard, A. Bram, J.H. Kang, M.W. Small, R.G. Nuzzo, A.I. Frenkel, *J. Am. Chem. Soc*., **131**, 7040 (2009).

[24] S. Roy, J. Ghatak, B.N. Dev, *Appl. Surf. Sci*., **258**, 3967 (2012).

[25] S.M. Heald, J.M. Tranquada, *J. App. Phys*., **65**, 290 (1989).

[26] B. Singh, B. Seddon, E. Dempsey, W. Redington, C. Dickinson, *Electroanalysis*, **26**, 1 (2014).

[27] H. Liu, F. Ye, Q. Yao, H. Cao, J. Xie, J.Y Lee, J. Yang, *Nature*, **4**, 3969 (2014).

[28] C.A. Perottoni,J.A.H. Jornada, *Science*, **280**, 886 (1998).

[29] J. Catafesta, J. Haines, J.E. Zorzi, A.S. Pereira, C.A. Perottoni, *Phys. Rev. B*, **77,** 064104 (2008).

[30] P. Ghalsasi, H.K. Poswal, R. Tripathi, N. Garg, M.N. Deo, S.M. Sharma, *J. Phys.: Conf. Ser*., **377**, 012009 (2012).

[31] Z.-A. Ren, W. Lu, J. Yang, W. Yi, X.-L. Shen, Z.-C. Li, G.-C. Che,X.-L. Dong, L.-L. Sun, F. Zhou, Z.-X. Zhao, *Chin. Phys. Lett*., **25**, 2215 (2008).

[32] Z.-A. Ren, G.-C. Che, X.-L. Dong, J. Yang, W. Lu, W. Yi, X.-L. Shen, Z.-C. Li, L.-L. Sun, F. Zhou, Z.-X. Zhao, *Europhys. Lett*., **83**, 17002 (2008).

[33] A.K. Mishra, K.V. Shanavas, H.K. Poswal, B.P. Mandal, N. Garg, S.M. Sharma, *Sol. State Comm*., 154, 72 (2013).

[34] A.K. Mishra, N. Garg, K.V. Shanavas, S.N. Achary, A.K. Tyagi, S.M. Sharma, *J. App. Phys*., 110, 123505 (2011).

[35] A.K. Mishra, H.K. Poswal, S.N. Acharya, A.K. Tyagi, S.M. Sharma, *Phys. Status Solidi*, **247**, 1773 (2010).

[36] A.K. Mishra, H.K. Poswal, S.M. Sharma, S. Saha, D.V.S. Muthu, S. Singh, R. Suryanarayanan, A. Revcolevschi, A.K. Sood, *J. App. Phys*., **111**, 033509 (2012).

[37] N. Garg, K.K. Pandey, C. Murali, k.V. Shanavas, B.P. Mandal, A.K. Tyagi, S.M. Sharma, *Phys. Rev. B.*, **77**, 214105 (2008).

[38] N.D. Sharma, J, Singh, S. Dogra, D. Varandani, H.K. Poswal, S.M. Sharma, A.K. Bandhopadhyay, *J. Raman Spectros*., **42**, 438 (2011). .,

[39] S. Dogra, N.D. Sharma, J. Singh, H.K. Poswal, S.M. Sharma, A.K. Bandhopadhyay, *High Press. Res*., **31**, 292 (2011).

[40] A.B. Garg, K.V. Shanavas, B.N. Wani, S.M. Sharma, *J. Sol. St. Chem*., **203**, 273 (2013).

[41] K.K. Pandey, N. Garg, A.K. Mishra, S.M. Sharma, *J. Phys.: Conf. Ser*., **377**, 012006 (2012).

[42] H.K. Poswal, S. Karmakar, P.K. Tyagi, D.S. Misra, E. Busetto, S.M. Sharma, A.K. Sood, *Phys. Status Solidi (b)*, 1-8 (2007).

[43] D. Haskel, E.A. Stern, D.G. Hinks, A.W. Mitchell, J.D. Jorgensen, J.L. Budnick, *Phys. Rev. Lett.*, **76**, 439 (1996).

[44] S.-W. Han, E.A. Stern, D. Haskel, A.R. Moodenbaugh, *Phys. Rev. B*, **66**, 094101 (2002).

[45] B. Johanssen, Z.S. Hussain, D.R. East, *J. Phys.: Conf. Ser.*, **430**, 012119 (2013).

[46] D.C. Koningsberger, R. Prins, "X-ray Absorption: Principles, applications and techniques of XAFS, SEXAFS and XANES", John Wiley (1987).

[47] S. Ganorkar, K.R. Priolkar, P.R. Sarode, A. Banerjee, R. Rawat, S. Emura, *J. Phys.: Cond. Mat.*, **24**, 476003 (2012).

[48] S. Chattopadhyay, S.D. Kelly, T. Shibata, R. Viswanatha, M. Balasubramanian, S. Stoupin, C.U. Segre, D.D. Sarma, *AIP Conf. Proc.*, **882**, 809 (2007).

[49] D. Lahiri, *Physica C*, **436**, 32 (2006).

[50] D. Lahiri, S. Khalid, P. Modak, P. Raychaudhuri, S.K. Dhar, S.M. Sharma, *Phys. Rev. B*, **82**, 134424 (2010).

[51] D. Haskel, E.A. Stern, V. Polinger, F. Dogan, *Phys. Rev. B*, **64,** 104510 (2001).

[52] E.A. Stern, S.W. Han, D. Haskel, *J. Supercond.: Incorporating Novel Magnetism*, **17**, 97 (2004).

[53] D. Lahiri, S.M. Sharma, A.K. Verma, B. Vishwanadh, G.K. Dey, G. Schumacher, T. Scherb, H. Reisemeier, U. Reinholz, M. Radtke, S. Banerjee, *J. Sync. Rad.*, **21**, 1296 (2014).

[54] D. Lahiri, B. Bunker, B. Mishra, Z. Zhang, D. Meisel, C.M. Doudna, M.F. Bertino, F.D. Blum, A.T. Tokuhiro, S. Chattopadhyay, T. Shibata, J. Terry, *J. App. Phys.*, **97**, 094304 (2005).

[55] D. Lahiri, S. Khalid, T. Sarkar, A.K. Raychaudhuri, S.M. Sharma, *J. Phys.: Cond. Mat.*, **24**, 336001 (2012).

[56]T. Wichard, B. Mishra, S.C.B. Myneni, J.P. Bellenger, A.M.L. Kraepiel, *Nat. Geosci.*,**2**, 625 (2009).

[57] B. Mishra, E.J.O' Loyghlin, M.I. Boyanov, K.M. Kemner, *Environ. Sci. Technol.*, **45**, 9597 (2011).

[58] D. Lahiri, "XAFS: a versatile technique for sample characterization", IANCAS Bulletin, Vol. 7, pp 59 (2009).

[59] A. Di Cicco, M. Taglienti, M. Minicucci, A. Filipponi, *J. Sync. Rad.*,**1**, 761 (2001).

[60] C. Meneghini, R. Cimino, S. Pascarelli, S. Mobilio, C. Raghu, D.D. Sarma, *Phys. Rev. B*, **56**,3520 (1997).

[61] C. Meneghini, C. Castellano, S. Mobilio, A. Kumar, S. Ray, D.D. Sarma, *J. Phys.: Cond. Mat.*, **14,** 1967 (2002).

[62] N. Mannella, C.H. Booth, C.H. Rosenhahn, B.C. Sell, A. Nambu, S. Marchesini, B.S. Mun, S.-H. Yang, M. Watanabe, K. Ibrahim, E. Arenholz, A. Young, J. Guo, Y. Tomioka, C.S. Fadley, *Phys. Rev. B*, **77**, 125134 (2008).

[63] P.E. Petit, F. Guyot, F. Farges, *J. Phys. IV France***, 7,** C2-1065 (1997).

[64]S. Islam, M.B. Liou, D.J. Fatemi, J.O. Cross, V.G. Harris, W.T. Elam, *J. Sync. Rad*., **6**, 773 (1999).

[65] J.J. Sakurai, Advanced Quantum Mechanics, Addison Wesley (1967).

[66] S.D. Kelly, S.R. Bare, N. Greenlay, G. Azevedo, M. Balasubramanian, D. Barton, S. Chattopadhyay, S. Fakra, B. Johannessen, M. Newville, J. Pena, G.S. Pokrovski, O. Proux, K. Priolkar, B. Ravel, S.M. Webb, *J. Phys.: Conf. Ser.***, 190**, 012032 (2009).

[67] J. J. Boland, S. E. Crane, J. D. Baldeschwieler, *J. Chem. Phys.*, **77**, 142 (1982).

[68] A. Frenkel, E.A. Stern, A. Voronel, M. Quian, M. Newville, *Phys. Rev. Lett*., **71**, 3485 (1993).

[69] T. Shibata, B.A. Bunker, J.F. Mitchell, P. Schiffer, *Phys. Rev. Lett*., **88**, 207205 (2002).

[70] G. Margaritondo, “Introduction to Synchrotron Radiation”, Oxford University Press (1988).

[71] S. Mobilio, F. Boschereni, C. Meneghini, “Synchrotron Radiation Basics, Methods and Applications”, Springer (2015).

[72] J. Schwinger, *Phys. Rev.*, **75**, 1912 (1949).

[73] E.E. Koch, D.E. Eastman, Y. Farges, “Synchrotron radiation—a powerful tool in science”, in *Handbook of Synchrotron Radiation*, ed. by E.E. Koch (North-Holland Publishing Company, Amsterdam, 1983), pp. 1–63

[74] A.Y. Ramos, H. Tolentino, R. Barrea, MCM Alves, MeT-019, http://lnls.cnpem.br/wp-content/uploads/2011/09/met0199.pdf

[75] E.A. Stern, and S.M. Heald, *Rev. Sci. Instrum.*, **50**, 1579 (1979).

[76] G. Bunker, “Introduction to XAFS”, Cambridge University Press (2010).

[77] A.C. Thompson, ‘X-ray Detectors’, X-ray Data Booklet.

[78] W.H. McMaster et al. Compilation of X-ray Cross Sections. Lawrence Radiation Laboratory Report UCRL-50174, National Bureau of Standards, pub. (1969). http://www.csrri.iit.edu/mucal.html ;http://www.csrri.iit.edu/periodic-table.html

[79] B. L. Henke, E. M. Gullikson, and J. C. Davis, Atomic Data and Nuclear Data Tables Vol. 54 No. 2 (1993); http://www-cxro.lbl.gov/optical_constants/atten2.html ;http://www-cxro.lbl.gov/optical_constants/

[80] R.A. Forman, G.J. Piermarini, J.D. Barnett, S. Block, *Science*, **176**, 284 (1972).

[81] R. Kinslow, A.J. Ray *High-velocity impact phenomena*. Boston: Academic Press (1970).

[82] A. Jayaraman, *Reviews of Scientific Instruments*, **57,** 1013 (1986).

[83] B. Ravel, M. Newville, *J. Synchrotron Rad.*, **12**, 537 (2005).

[84] D. Lahiri, Ph.D. Thesis, University of Notre Dame (2003).

[85] M. Newville, P. Livins, Y. Yacoby, E. A. Stern, J. J. Rehr, *Phys. Rev. B*, **47**, 14126 (1993).

[86] S. Kelly, Basics of EXAFS processing, 2009, UOP

[87] J.J. Rehr, J. Mustre de Leon, S.I. Zabinsky, R.C. Albers, *J. Am. Chem. Soc.*, **113**, 5135 (1991).

[88] B. Ravel, *J. Sync. Rad.*, **8**, 314(2001).

[89] M. Newville, B. Ravel, D. Haskel, J. J. Rehr, E. A. Stern, Y. Yacoby, *Physica B*, **208&209**, 154(1995).

[90] M. Newville, FEFFIT tutorial (1998).

[91] M. Quinten, Appendix C: Levenberg–Marquardt Algorithm, in A Practical Guide to Optical Metrology for Thin Films, Wiley-VCH Verlag GmbH & Co. KGaA, Weinheim, Germany (2012).

[92] http://www.cat.gov.in/technology/accel/isrf_index.html

[93] A. Gaur, B.D. Shrivastava, S.N. Jha, D. Bhattacharyya, A. Poswal, *Pramana*, **80**, 159 (2013).

[94] D. Bhattacharyya, A. K. Poswal, S. N. Jha, Sangeeta,S. C. Sabharwal. *Nuc. Insts. Meth. in Phys. Res. A*, **609**, 286 (2009).

[95] D. Bhattacharyya, A. K. Poswal, S. N. Jha, Sangeeta, S. C. Sabharwal, *Bull. Mater. Sci.*,**32**, 103 (2009).

[96] A. Gaur, A. Johari, B.D. Shrivastava, D.C. Gaur, S.N. Jha, D. Bhattacharyya, A. Poswal, S.K. Deb, *Sadhana*, **36**, 339 (2011).

[97] M. Newville, *J. Syn. Rad.*, **8**,96 (2001).

[98] C.A. Perottoni, J.A.H. da Jornada, *Science*, **280**, 886 (1998).

[99] M.K. Jacobsen, R.S. Kumar, G. Cao, J.J. Neumeier, A.L. Cornelius, *J. Phys. Chem. Sol.*,**69**, 2237 (2008).

[100] G. H. Zhong, J. L. Wang, Y. L. Li, Z. Liu, H. Q. Lin, *J. App. Phys.*, **109**, 07E163 (2011).

[101] S.H. Tolbert, A.P. Alivisatos, *Science*, **265**, 373 (1994).

[102] V. Panchal, S. Ghosh, S. Gohil, N. Kulkarni, P. Ayyub, *J. Phys.: Cond. Mat.*, **20**, 345224 (2008)

[103] G. Aquilanti, S. Pascarelli, *J. Phys.: Cond. Mat.*, **17**, 1811 (2005).

[104] http://www.esrf.eu/home/UsersAndScience/Experiments/Beamlines/content/content/id24.html

[105] http://ww1.iucr.org/comm/chp/iucr_hp_facilities.html

[106] J. Prakash, S.J. Singh, D. Das, S. Patnaik, A.K. Ganguli, *J. Sol. St. Chem.*, **183**, 338 (2010).

[107] N. Ramanan, D. Lahiri, N. Garg, D. Bhattacharyya, S.N. Jha, N.K. Sahoo, S.M. Sharma, *J. Phys.: Conf. Series*, **377**, 012011 (2012).

[108] V.P. Dhamgaye, M.K. Tiwari, K.J.S. Sawhney, G.S. Lodha, *Pramana*, **83**, 119 (2014).

[109] M. Baldini et al., *Physical Review B*, **84**, 014111 (2011).[110] N. Ishimatsu, et al., *J. Sync. Rad.*, **19**, 768 (2012).

[111] S. Pascarelli, O. Mathon, G. Aquilanti, *J. Alloys and Compounds*, **362**, 33 (2004).

[112] N.C. Das, S.N. Jha, A.K. Sinha, V.K. Mishra, V. Verma, A.K. Ghosh, A.K., "Optical and Mechanical Design of the Extended X-Ray Absorption Fine Structure (EXAFS) Beamline at INDUS-2 Synchrotron Source", B.A.R.C. Report , E/030 (2002).

[113] N.C. Das, D. Bhattacharyya, D. Lahiri, S.M. Sharma, "Studies on the possibilities of high pressure X-ray absorption experiments using XAFS beamline at INDUS-2 SRS", B.A.R.C. report, E/001 (2007).

[114] http://www.esrf.eu/computing/scientific/raytracing/PDF/shadow_basics.pdf, http://www.esrf.eu/computing/scientific/raytracing/PDF/primer.pdf

[115] X-ray Mirrors, (Thales Seso, 2013), pp 30, http://seso.com/wp-content/themes/theme44938/images/PDF/Brochure/optimise/BROCHURE%20-%20X-RAY.pdf

[116] M. Sanchez del Rio, A. Marcelli, *AIP conf. Proceedings*, **705**, 784 (2004).

[117] A. Dadashev, M.P. Pasternak, G.K. Rozenberg, R.D. Taylor, *Rev. Sci. Inst.*, **72**, 2633 (2001).

[118] H. Oyanagi, C.Z. Zhang, *Adv. Mat. Rev.*, Volume 2010, Article ID 484578 (2010).

[119] X. Tan, T. Yao, R. Long, Z. Sun, Y. Feng, H. Cheng, X. Yuan, W. Zhang, Q. Liu, C. Wu, Y. Xie, S. Wei, *Nature*, **2**, 466 (2012).

[120] M. Fischer, A. Lahmar, M. Maglione, A. San Miguel, J.P. Itié, A. Polian, F. Baudelet, *Phys. Rev. B*, **49**, 12451 (1994).

[121] C. Marini, S. Pascarelli, O. Mathon, B. Joseph, L. Malavasi, P. Postorino, *Europhys. Lett.*, **102,** 66004 (2013).

[122] D. Lahiri, T. Shibata, S. Chattopadhyay, S. Kanungo, T. Saha-Dasgupta, R.S. Singh, S.M. Sharma, K. Maiti, *Phys. Rev. B*, **82**, 094440 (2010).

[123] K.W. Kim, J.S. Lee, T.W. Noh, S.R. Lee, K. Char, *Phys. Rev. B*, **71**, 125104 (2005).

[124] K. Maiti, R.S. Singh, V.R.R. Medicherla, *Phys. Rev. B*, **76**, 165128 (2007).

[125] K. Maiti, *Phys. Rev. B*, **73**, 235110 (2006).

[126] T. Wichard, B. Mishra, S.C.B. Myneni, J.P. Bellenger, A.M.L. Kraepiel, *Nat. Geosci.*, **2**, 625 (2009).

[127] B. Raveau, V. Caignaert, V. Pralong, A. Maignan, *Z. Anorg. Allg. Chem.*, **635**, 1869 (2009).

[128] Y. Jia, H. Jiang, M. Valkeapaa, H. Yamauchi, M. Karppinen, E.I. Kauppinen, *J. Am. Chem. Soc.*, **131**, 4880 (2009).

[129] http://www.arscryo.com/TechNotes/CryocoolerPrincipleofOperation.html

[130] B. Igarashi, T. Christensen, E.H. Larsen, N.B. Olsen, I.H. Pedersen, T, Rasmussen, J.C. Dyre, *Rev. Sci. Inst.*, **79**, 045105 (2008).

[131] Z. Liu *et al.*, *Appl. Phys. Lett*. **72**, 1823 (1998).

[132] M. Yu *et al.*, *Appl. Phys. Lett*. **75**, 3992 (1999).

[133] S. Bera, B. Satpati, D.K. Goswami, K. Bhattacharjee, P.V. Satyam, B.N. Dev *J. Appl. Phys.*, **99,** 074301 (2006).

[134] D. Sengupta, J. Saha, G. De, B. Basu, *J. Mat. Chem. A*, **2**, 3986 (2014).

[135] Y. Wang, H. Zhao, G. Zhao, *Applied Catalysis B: Environmental*, **164**, 396 (2015).

[136] J. Liu, L.L. Zhang, J. Zhang, T. Liu, X.S. Zhao, *Nanoscale*, **5**, 11044 (2013).

[137] N. Toshima, T. YonezawA, *New J. Chem*, 1179 (1998).

[138] M.S. Wong, P.J.J. Alvarez, Y.-I. Fang, N. Akcin, M.O. Nutt, J.T. Miller, K.N. Heck, *J. Chem. Technol Biotechnol*, DOI 10.1002/jctb.2002 (2008).

[139] G. Che, B.B. Lakshmi, C.R. Martin, E.R. Fischer, *Langmuir*, **15,** 750 (1999).

[140] J.H. Choi, C.H. Jung, I.T. Hwang, M.Y. An, B.M. Lee, D.K. Kim, J.S. Lee, Y.C. Nho, K.M. Huh, S.K. Hong, *J. Nanosci. Nanotech*., **10**, 6879 (2010).

[141] D. Kabiraj, S.R. Abhilash, L. Vanmarcke, N. Cinausero, J.C. Pivin, D.K. Avasthi, *Nuc. Inst. Meth. Phys. Res. B*, **244**, 100 (2006).

[142] A.L. Stepanov, *Rev. Adv. Mat. Sci*., **26**, 1 (2010).

[143] V. Amendola, S. Polizzi, M. Meneghetti, *Sci. Adv. Mat.*, **4**, 1 (2012).

[144] E. Knystautas, “Engineering Thin Films and Nanostructures with ion beams”, CRC Press (2005).

[145] D. Weller, J. E. E. Baglin, A. J. Kellock, K. A. Hannibal, M. F. Toney, G. Kusinski, S. Lang, L. Folks, M. E. Best, and B. D. Terris, *J. Appl. Phys.*, **87**, 5768 (2000).

[146] S. S. P. Parkin, C. Chappert, and F. Herman, *Mater. Res. Soc. Symp. Proc.*, **313**, 179 (1993).

[147] S.K. Ghose, D.K. Goswami, B. Rout, B.N. Dev, G. Kuri, G. Materlik, *App. Phys. Lett.*, **79,** 467 (2001).

[148] T. Som, S. Ghosh, M. Mäder, R. Grötzschel, S. Roy, D. Paramanik, A. Gupta, *New J. Phys.*, **9**, 164 (2007).

[149] S. Bera, K. Bhattacharjee, G. Kuri, B.N. Dev, *Phys. Rev. Lett.*, **98**, 196103 (2007).

[150] B.N. Dev, S. Bera, B. Satpati, D.K. Goswami, K. Bhattacharjee, P.V. Satyam, K. Yamashita, O.M. Liedke, K. Potzger, J. Passbender, F. Eichhorn, R. Gröetzschel, *Microelec. Engg.*, **83**, 1721 (2006).

[151] S. Bera, S. Roy, K. Bhatacharjee, G. Kuri, B.N. Dev, *J. App. Phys.*, **102**, 014308 (2007).

[152] S. Bera, D.K. Goswami, K. Bhattacharjee, B.N. Dev, G. Kuri, K. Nomoto, K. Yamashita, *Nuc. Inst. Meth. Phys. Res. B*, **212**, 530 (2003).

[153] B.N. Dev, “Physics at Surfaces and Interfaces”, p. 121, Singapore: World Scientific (2003).

[154] K. Yamashita, P.J. Serlemitsos, J. Tueller, S.D. Barthelmy, L.M. Bartlett, K.W. Chan, A. Furuzawa, N. Gehrels, K. Haga, H. Kunieda, P. Kurczynski, G. Lodha, N. Nakajo, N. Nakamura, Y. Namba, Y. Ogasaka, T. Okajima, D. Palmer, A. Parsons, Y. Soong, C.M. Stahl, H. Takata, K. Tamura, Y.Tawara, B.J. Teegarden, *Appl. Opt.*, **37**, 8067 (1998).

[155] S. Roy, S. Bera, B.N. Dev, *J. Nanosci. and Nanotech.*, **7**, 2182 (2007).

[156] T. W. Barbee,W. K. Warburton, Jr., *Mater. Lett.* **3**, 17 (1984).

[157] S. Roy, J. Ghatak, B.N. Dev, *Appl. Surf. Sci.*, **258**, 3967 (2012).

[158] G. Wang, H. Wu, D. Wexler, H. Liu, O. Savadogo, *J. Alloy Comp.*, **503,** L1 (2010).

[159] W. Li, P. Haldar, *Electrochem. Sol. State Lett*., **13**, B47 (2010).

[160] D. Lahiri, S. Chattopadhyay, B.A. Bunker, C.M. Doudna, M.F. Bertino, F. Blum, A. Tokuhiro, J. Terry, *Physica Scripta*., **T115**, 776–780 (2005).

[161] P. Nash, M.F. Singleton, *Bull. Alloy Phase Diagrams*, **10**, 258 (1989).

[162] H. Okamoto, *J. of Phase Equilibria and Diffusion,* **31**,322 (2010).

[163] M. Singleton, P. Nash, *Bull. Alloy Phase Diagrams*, **10**,121(1989).

[164] E.M. Merschrod, S.H.Tang, R. Hoffmann, *Naturforsch Z.*,**53 b**,322 (1998).

[165] T. Som, S. Ghosh, M. Mäder, R. Grötzschel, S. Roy, D. Paramanik, A. Gupta, *New J. Phys.*, **9**, 164 (2007).

[166] S. Bera, K. Bhattacharjee, G. Kuri, B.N. Dev, *Phys. Rev. Lett*., **98**, 196103 (2007).

[167] S. Roy, B.N. Dev, *Appl. Surf. Sci*., **257,** 7566 (2011).

[168] R. Swaminathan, M.E. Mc Henry, M. Sorescu, L. Diamandescu, S. Calvin, *Ninth International Conference on ferrites (ICF-9)*, 847 (2004).

[169] I.K. Robinson, *Phys. Rev. B*, **33**, 3830 (1986).

[170] T. Fukunaga, K. Itoha, S. Orimo, M. Aoki, H. Fujii, *J. Alloys and Compounds*, **327**, 224 (2001).

[171] G.S. Lodha, K.Yamashita, T. Suzuki, Hatsukade, K. Tamura, T. Ishigami, S. Takahama, Y. Namb, *Appl. Optics*, **33**, 5869 (1994).

[172] B.L. Evans, B. J. Ken, *Appl. Optics*, **26**, 4491 (1987).

[173] K. Albe, K. Nordlund, R.S. Averback, *Phy. Rev. B*, **65**, 195124 (2002).

[174] R.P.W.J. Struis, D. Bachelin, C. Ludwig, A. Wokaun, *J. Phys. Chem. C*, **113**, 2443 (2009).

[175] A.L. Greer, *Nature*, **366,** 303 (1993).

[176] U. Kumar, P.K. Mukhopadhyay, B. Sanyal, O. Eriksson, P. Nordblad, D. Paudyal, K. Tarafder, A. Mookerjee, *Phys. Rev. B*, **74**, 064401 (2006).

[177] U. Kumar, K.G. Padmalekha, P.K. Mukhopadhyay, D. Paudyal, A. Mookerjee, *J. Mag. Mag. Mat*., **292**, 234 (2005).

[178] M. Cadeville, C.E. Dahmani, F.Kern, *J. Mag. Mag. Mat.*, **54-57**, 1055 (1986).

[179] E. Holmström, L. Nordström, L. Bergqvist, B. Skubic, B. Hjörvarsson, I.A. Abrikosov, P. Svedlindh, O. Eriksson, *Proc Natl Acad Sci U S A*., **101**, 4742 (2004).

[180] M. Choi, D.M. Pease, W.A. Hines, G.H. Hayes, J.I. Budnick, S.M. Heald, R. Hasegawa, H.E. Schone, *Phys. Rev. B*, **32**, 7670 (1985).

[181] A.S. Bommannavar, P.A. Montano, M. J. Yacaman, *Surface Science,* **156**, 426 (1985).

[182] N. J. Shevchik, D.Bloch, *J. Phys. F: Metal Phys.*, **7**, 543 (1977).

[183] W-H. Wang, Q. Wei, H. Y. Bai, *Appl. Phys. Lett*., **71**, 58 (1997).

[184] Y. Wang, P. Sharma, A. Makino, *J. Phys.: Condens. Matter,* **24**, 076004 (2012).

[185] Y. F. Xu, M. L. Yan, D. J. Sellmyer, *J. Nanosci. Nanotech*., **7**, 206 (2004).

[186] Kazutaka Baba et. al., *Appl. Phys. Lett*., **62**, 437 (1993).

[187] M. Gaudry et al., *Phys. Rev. B*, **64**, 085407 (2001).

[188] Nicewarner-Pena et al., *Science*, **294**, 137 (2001).

[189] B. Pramanik, A. Patra, *J. Mat. Chem. C*, **2**, 3005 (2014).

[190] S. Tiwari, F. Rana, K. Chan, L. Shi, H. Hanafi, *Appl. Phys. Lett*. **68**, 1377 (1996).

[191] S. Tiwari, F. Rana, K. Chan, L. Shi, H. Hanafi, *Appl. Phys. Lett*. **69**, 1232 (1996).

[192] Park, W.I., Kim, J.S., Yi, G.-C. & Lee, Y.-J. (2005). ZnO Nanorod Logic Circuits. Adv. Mater., Vol. 17, No. 11, (Jun 2005), PP. (1393-1397), ISSN 0935-9648.

[193] O. Lupan, V. M. Guérin, I. M. Tiginyanu, V. V. Ursaki, L. Chow, H. Heinrich, T. Pauporté, *J. Photochem. Photobiol. A: Chem*., **211**, 65 (2010).

[194] W. He, C.Z. Huang, Y.F. Li, J.P. Xie, R.G. Yang, P.F. Zhou, J. Wang, *Anal. Chem.*, **80**, 8424 (2008).

[195] B. R. Mehta, F. E. Kruis. A graded diameter and oriented nanorod–thin film structure for solar cell application: a device proposal Solar Energy Materials and Solar Cells, Volume 85, Issue 1, 1 January 2005, Pages 107-113.

[196] C.M. Chang, M.H. Hon, I.C. Leu .Preparation of ZnO nanorod arrays with tailored defectrelated characterisitcs and their effect on the ethanol gas sensing performance Sensors and Actuators B: Chemical, Volume 151, Issue 1, 26 November 2010, Pages 15-20.[35] Yongsheng Zhang, Ke Yu, Desheng Jiang, Ziqiang Zhu, Haoran Geng, Laiqiang Luo . Zinc oxide nanorod and nanowire for humidity sensor. Applied Surface Science, Volume 242, Issues 1-2, 31 March 2005, Pages 212-217.

[197] Y. Yang, W. Wang, X. Li, W. Chen, N. Fan, C. Zou, X. Chen, X. Xu, L. Zhang, S. Huang, *Chem. Mater.*, **25**, 34 (2013).

[198] B. Nikoobakht, M.A. El-Sayed, *Chem. Mater.*, **15**, 1957 (2003).

[199] C. J. Murphy, T. K. Sau, A. M. Gole, C. J. Orendorff, J. Gao, L. Gou, S. E. Hunyadi, and T. Li, *J. Phys. Chem. B*, **109**, 13857 (2005).

[200] B. Sadeghi (2012). Synthesis and Application of Nanorods, Nanorods, Dr. Orhan Yalçın (Ed.), ISBN: 978- 953-51-0209-0, InTech, Available from: http://www.intechopen.com/books/nanorods/synthesis-and-applicationof-nanorods

[201] G. Cao, D. Liu, *Adv. Coll. Interface Sci.*, **136**, 45 (2008).

[202] C.M. Doudna, M.F. Bertino, F.D. Blum, A.T. Tokuhiro, D.L. Dey, S. Chattopadhyay, J. Terry, *J. Phys. Chem. B*, **107**, 2966 (2003).

[203] M.A. Khan, T.P. Hogan, B. Shanker, *J. Nanosystems and Tech.*, **1**, 1 (2009).

[204] D.K. Awasthi, G.K. Mehta, "Swift Heavy Ions for Materials Engineering and Nanostructuring", Springer (2011).

[205] K. Awazu, X.M.Wang, M. Fujimaki, J. Tominaga, H. Aiba, Y. Ohki, T. Komatsubara, *Phys. Rev. B*, **78**, 054102 (2008).

[206] D.J. Sprouster, R. Giulian, B. Johannessen, C.S. Schnohr, L.L. Araujo, P. Kluth, A.P. Byrne, G.J. Foran, M.C. Ridgway, *Phys. Rev. B*, **80,** 115438 (2009).

[207] P. Kluth, R. Giulian, D.J. Sprouster, C.S. Schnohr, A.P. Byrne, D.J. Cookson, M.C. Ridgway, *Appl. Phys. Lett*., **94,** 113107 (2009).

[208] R. Giulian, P. Kluth, L.L. Araujo, D.J. Sprouster, A.P. Byrne, D.J. Cookson, M.C. Ridgway, *Phys. Rev. B*, **78,** 125413 (2008).

[209] M.C. Ridgway, P. Kluth, R. Giulian, D.J. Sprouster, L.L. Araujo, C.S. Schnohr, D.J. Llewellyn, A.P. Byrne, G.J. Foran, D.J. Cookson, *Nucl. Instrum. Methods B*, **267,** 931–5 (2009).

[210] S. Roorda, T. van Dillen, A. Polman, C. Graf, A. van Blaaderen, B.J. Kooi, *Adv. Mater*., **16,** 235 (2004).

[211] C. D'Orleans, J.P. Stoquert, C. Estournes, C. Cerruti, J.J. Grob, J.L. Guille, F. Haas, D. Muller, M. Richard-Plouet, *Phys. Rev. B*, **67,** 220101 (2003).

[212] H. Kumar, S. Ghosh, D. K. Avasthi, D. Kabiraj, A. Mücklich, S. Zhou, H. Schmidt, J.-P Stoquert, *Nanoscale Res. Lett*., **6**, 155 (2011).

[213] D.K. Awasthi, *Defence Science Journal*, **59**, 401-412 (2009).

[214] Williams, Giordano, *Rev. Sci. Instrum*., **55**, 410 (1983).

[215] US Patent 6444256 issued on Sept 3 2002 – 'Formation of nanometer-size wires using infiltration into latentnuclear tracks'.[216] Y. K. Mishra et. al., *Appl. Phys. Lett*., **91**, 063103 (2007).

[217] P. Stampfli, K. H. Bennemann, *Phys. Rev. B*, **49**, 7299 (1994).

[218] P. Stampfli, K. H. Bennemann, *Appl. Phys. A: Mater. Sci. Process*., **60**, 191 (1995).[219] S. Bera, B. Satpati, D.K. Goswami, K. Bhattacharjee, P.V. Satyam, B.N. Dev, *J. Appl. Phys*, **99**, 074301 (2006).

[220] W. Zhang, J.S. Hu, H.T. Ding, L.J. Wan, W.G. Song, *Anal. Chem*, **81**, 2815 (2009).

[221] N. Chopra, Y. Wu, P.M. Kazmaeir, US Patent Application US 2009/0274834 A1 (2009).

[222] T.C. Deivaraj, W. Chen, J.Y. Lee, *J. Mater. Chem*., **13**,2555 (2003).

[223] J. Prabhuram, T.S. Zhao, C.W. Wong, J.W. Guo, *J. Power Sources*, **134**, 1 (2004).

[224] N. Toshima, T. Yonezawa, *New J. Chem*., **22**, 1179 (1998).

[225] M.S. Wong, P.J.J. Alvarez, Y.I. Fang, N. Akcin, M.O. Nutt, J.T. Miller, K.N. Heck, *J. Chem. Technol. Biotechnol*., **84**, 158 (2008).

[226] G. Che, G.,B.B. Lakshmi, C.R. MartinE.R. Fischer, *Langmuir*, **15**, 750 (1999).

[227] P.M. Wheat, N.A. Marine, J.L. Moran, J.D.Posner, *Langmuir*, **26**, 13052 (2010).

[228] S.T. Patton, J.M. Slocik, J.H. Campbell, R.R. Naik, A.A.Voevodin, *Nanotechnology*, **19**, 05705 (2008).

[229] A. K. Salem, C. F. Hung, T. W. Kim, T.C. Wu, P. C. Searson, K.W. Leong, *Nanotechnology*, **16**, 484-487 (2005).

[230] D. Kilinc, G. U. Lee, *Integr. Biol*, **6**, 27 (2014).

[231] A.Henglein, A.Holzwarth, P. Mulvaney, *J. Phys.Chem*., **96**, 8700 (1992).

[232] D. Alloyeau, C. Ricolleau, C. Mottet, T. Oikawa, C. Langlois, Y. Le Bouar, N. Braidy, A. Loiseau, *Nature Mat*.,**8**, 940 (2009).

[233] M. Hu, K.P. Giapis, J. V. Goicochea, D. Poulikakos, *App. Phys. Lett*., **97**, 153107 (2010).

[234] J C Pivin, F Singh, O Angelov, L Vincent, *J. Phys. D: App. Phys*., **42**, 025005 (2009).

[235] S. Kavita, V. R. Reddy, A. Gupta, D.K. Avasthi, *Nuc. Inst. Meth. Phys. Res. B*, **244,** 19 (2006).

[236] I. Karakaya, W.T. Thomson, *Bull. Alloy Phase Diag.*, **8**, 334 (1987).

[237] J. S. Tsay, Y. D. Yao, C. S. Shern, *Phys. Rev. B*, **58**, 3609 (1998).

[238] T.B. Massalski, J.L. Murray, L.H. Bennett, H. Baker, Binary Alloy Phase Diagrams, American Society for Metals, Metals Park, OH, 1986.

[239] S. Gohil, R. Banerjee, S. Bose, P. Ayyub, *Scripta Materialia*, **58**, 842 (2008).

[240] A. Colder, M. Levalois, and P. Marie, *Eur. Phys. J. AP*, **13**, 89–96 (2001).

[241] J. A. Brinkman, *J. Appl. Phys.*, **25**, 961 (1954).

[242] T.E. Haynes, O.W. Holland, *Appl. Phys. Lett.*, **59** 452 (1991).

[243] J. Ghatak, M. U. Bhatta, B. Sundaravel, K.G.M. Nair, S.-C. Liou, C.-H. Chen, Y.-L. Wang, P V Satyam, *Nanotechnology*, **19**, 325602 (2008).

[244] J. Saida, T. Sanada, S. Sato, M. Imafuku, E. Matsubara, A. Inoue, *Materials Transactions*, **48**, 1703 (2007).

[245] S. Mohapatra, Y.K. Mishra, D.K. Avasthi, D. Kabiraj, J. Ghatak, S. Varma, App. *Phys. Lett.*, **92**, 103105 (2008).

[246] J.H. Hsieh, C. Li, C. M. Wang, Y. C. Liu, Z. Z. Tang, *J. Metastable and Nanocrystalline Materials*, **23**, 211 (2005).

[247] K. Shimamura, Y, Matsumoto, T. Matsunaga, *Surface and Coatings Technology*, **50**, 127 (1992).

[248] Z.Z. Tang, J.H. Hsieh, S.Y. Zhang, C. Li, Y.Q. Fu, *Surface and Coatings Technology*, **198**, 110 (2005).

[249] K. J. A. Mawella, J. A. Sheward, *Thin Solid Films*, **193-194**, 27 (1990).

[250] K. Patel, S. Kapoor, D.P. Dave, T. Mukherjee, *J. Chem. Sci.*, **117**, 311 (2005).

[251] D. Lahiri, V. Subramaniam, B.A. Bunker, P.V. Kamat, *J. Chem. Phys*., **124**, 204720 (2006).

[252] M. He, T.-M. Lu, “Metal Dielectric interfaces in gigascale electronics: Thermal and electrical stability”, Springer (2012).

[253] R. Wolfe, “Applied Solid State Science-Advances in Materials and device research”, Vol.6, Page 19, Academic Press: London.

[254] Z.Y. Duan, J. Zhong, J. G.F. Wang, *J. Chemical Physics*, **133**, 114701 (2010).

[255] Z.Y. Duan, G.F. Wang, *J. Phys.: Cond. Matt.* **23**, 475301 (2011).

[256] Y. Zhang, Z.Y. Duan, C. Xiao, G.F. Wang, *Surface Science*, **605**, 1574 (2011).

[257] T.I. Hyde, P.W. Hash, D.A. Boyd, G. Randlshofer, K. Rothenbacher, G. Sankar, *Platinum Metals Rev*., **55**, 233 (2011).

[258] XAFS reference spectra: http://www.exafsmaterials.com/Ref_Spectra_0.4MB.pdf

[259] http://cars9.uchicago.edu/~ravel/software/doc/Standards/pt.html

[260] H.Y. Yang, S.J. Yang, W.N. Myung, *New Physics*, **27**, 344 (1987).

[261] A. Inoue, A.Takeuchi, *Mater. Trans. JIM*, **43**, 1892 (2002).

[262] H. Amekura, B. Johannessen, D.J. Sprouster, M.C. Ridgeway, *App. Phys. Lett*., **99**, 043102 (2011).

[263] D. J. Sprouster, R. Giulian, L. L. Araujo, P. Kluth, B. Johannessen, N. Kirby, K. Nordlund, M.C. Ridgeway, *Phys. Rev. B*, **81**, 155414 (2010).

[264] W Wesch, C S Schnohr, P Kluth, Z S Hussain, L L Araujo, R Giulian, D J Sprouster, A P Byrne, M C Ridgway, *J. Phys. D: App. Phys*. **42**, 115402 (2009).

[265] G.K. Dey, R.T. Savalia, S.K. Sharma, S.K. Kulkarni, *Corrosion Science*, **29**, 823 (1989).

[266] Y. Liao. L. He, C. Man, L. Chen, M. Fu, J. Wu, D. Ye, B. Huang, *Chem. Engg. J*., 256, 439 (2014).

[267] A. Leelavathi, G. Madras, N. Ravishankar, *Phys. Chem. Chem. Phys.*, **15**, 10795 (2013).

[268] X. Zhan, J. Qin, Y. Xue, P. Yu, B. Zhang, L. Wang, R. Liu, *Nature*, **4**, 4596 (2013).

[269] Y. Feng, H. Liu, P. Wang. F. Ye, Q. Tan, J. Yang, *Nature*, **4**, 6204 (2014).

[270] L. Feng, G. Gao, P. Huang, X. Wang, C. Zhang, J. Zhang, S. Guo, D. Cui, *Nanoscale Res. Lett.*, **6**, 551 (2011).

[271] S. Raha, *J. Ayu. Int. Med.*, **4**, 198 (2013).

[272] http://www.ccras.nic.in/PharmacopoeialWork/Links/Compfom/AyurvedicFarmocopia.pdf

[273] http://www.anh-europe.org/news/the-myth-of-heavy-metal-%E2%80%98camtamination%E2%80%99

[274]http://en.wikipedia.org/wiki/Rasayana

[275] P. Acharya, R. Ranjan, P. Kirar, S. Srivastva P. Singh, *Indian J. Adv. Plant Res.*, **1**, 18 (2014).

[276] http://smallb.in/sites/default/files/knowledge_base/ayurvedic_medicine.pdf

[277] G. Kumar, Y.K. Gupta, *Ayu*, **33**, 569 (2011).

[278] R. Nandha, H. Singh, *Int. J. Green Pharm.*, 173 (2013).

[279] N.B. Raut, U.L. Tiwari, B.S. Adhikari, G. S., Rawat, S. Chandola, *Not Sci. Biol.*, **5,**175 (2013).

[280] M. Panghal, V. Arya, S. Yadav, S. Kumar, J.P. Yadav, *J. Ethnobio. Ethnomed.*, **6**, 4 (2010).

[281] http://web.undp.org/comtoolkit/success-stories/ASIA-india-energyenviron.shtml

[282] http://www.bhu.ac.in/ims/ayurveda/ayurveda_about.htm

[283] http://www.rria.nic.in/

[284] http://www.nia.nic.in/?ref=12&id=6

[285] http://www.ayurvedamanuscripts.com/

[286] M.S. Valiathan, *Curr. Sci.*, **90**, 5 (2006).

[287] A. Bose, V. Saroch, *Int. J. Pharm. Res. Bio Sci*., **1,** 96 (2012).

[288] J. Patwabardhan, *Ayurveda Integr Med*., **2**, 47 (2011).

[289] M.S. Baghel, *Ayu*., **34**, 2 (2013).

[290] R.B. Saper, *JAMA*, **23**, 2868 (2004).

[291] M. Leonti, L. Casu, *Front Pharmacol*., **4**, 92 (2013).

[292] K. Nishteswar, *Ayu*., **34**, 4 (2013).

[293] P.K. Sarkar, S. Das, P.K. Prajapati, *Ancient Sci. Life*, **29**, 1 (2010).

[294] S.U. Kamath *et. al*., *Arch. Toxicol*., DOI 10.1007/s00204-012-0826-2

[295] A.K. Panda, J. Hazra, *Int. J. Res. Ayu. Pharm*., **3**, 772 (2012).

[296] http://sgem.org/sgemlib/spip.php?article1521

[297] R. Singh, N. Gautam, A. Mishra, R. Gupta, *Indian J. Pharmacol*., **43**, 246 (2011).

[298] A. Kumar, A.G.C. Nair, A.V.R. Reddy, A.N. Garg, *J. Radioanal. Nuc. Chem*., **270**, 173 (2006).

[299] M.P. Wadekar, C.V. Rode, Y.N. Bendale, K.R. Patil, A.A. Prabhune, *J. Pharm Biomed. Anal*., **39**, 951 (2005).

[300] H. Liao, C.L. Nehl, J.H. Hafner, *Nanomed*., **1**, 201 (2006).

[301] http://www.slideshare.net/technoayurveda/bhasma-nano

[302] N. Dubey, N. Dubey, R.S. Mehta, A.K. Saluja, D.K. Jain, *Songklanakarin J. Sci. Tech*., **31**, 510 (2009).

[303] A. Chaudhary, *J. Biomed Nanotech*., **7**, 68 (2011).

[304] I. Mukherjee, S. Senapati, D. Mitra, A.K. Rakshit, A.R. Das, S.P. Moulik, *Colloids and Surfaces A: Physicochem. Eng. Aspects*, **360**, 142 (2010).

[305] B. Krishnamachary *et al*., *J. Ethnopharmacology*, **142**, 98 (2012).

[306] N.G. Patel, “Folk Medicine: The Art and the Science”, (ed. Editor R.P. Steiner) 41 (American Chemical Society, Washington, 1986).

[307] K.N. Shastry, “Rasatarangini”, English translation of original in Sanskrit, in “Sadananda” (MotilalBanarasidas Press, Varanasi,1979).

[308] R.E. Svoboda, “Prakriti: Your Ayurvedic Constitution” 169 (Bellingham Sadhana Publications, 1998).

[309] S. Chakrapany, C. Singh, *Am. J. Pharmtech. Res*, **4**, 60 (2014).

[310] P.K. Sarkar, A. Chaudhury, *J. Sci. and Ind. Res.*, **69**, 901 (2010).

[311] S. Kulkarni, *Int. Res. J. Pharm.*, **4**, 10 (2013).

[312] S. Rastogi, *Int. J. Ayurveda Res.*, **1**, 41 (2010).

[313] R. Adhikari,S.Thapa, S. “Ayurvedic Bhasmas: Overview on Nanomaterialistic Aspects, Applications, and Perspectives” in “Infectious Diseases and Nanomedicine I, Advances in Experimental Medicine and Biology” **807,** Pg. 23-32 (Springer, India, 2014).

[314] I. Paur, M.H. Carlsen, B.L. Halvorsen and R. Blomhoff, “Antioxidants in Herbs and Spices” in Herbal Medicine: Biomolecular and Clinical Aspects 2nd edition (ed. Editor Benzie, I.F.F., Wachtel-Galor S) (CRC Press, 2011).

[315] T. Yonezawa, S. Onoue, N. Kimizuka, *Langmuir*, **16**, 5218 (2000).

[316] W.H.D. Jong, P.J.A. Borm*Int. J. Nanomedicine*, **3**, 133 (2008).

[317] S.K. Singh, A. Chaudhary, D.K. Rai, S.B. Rai, *Ind. J. Trad. Knowledge*, **8**, 346 (2009).

[318] N.V. Vardhini, T.N. Sathya, B. Murthy, *Cur. Sci.*, **99**, 1096 (2010).

[319] I. Koch *et. al.*, *Sci. Tot.Env.*, **454–455**, 9 (2013).

[320] Vaidyaratnam P.S. Varier in Chikitsa Samgraham 15th edition, Malayalam, page 148-150 (Arya Vaidya Sala, Kottakkal, India, 1999).

[321] A. Kanojia, A. Sharma, V. Urimindi, V.K. Goecha, *Int. Ayur. Med. J.*, **1**, 1 (2013).

[322] R.A. Gokarn, B. Patgiri, Galib, P.K. Prajapati, *Int. J. Pharm. Bio. Arch.*, **3**, 1360 (2012); B. Patgiri, R. Gokarn, *Ayurpharm. Int. J. Ayur. Alli. Sci.*, **3**, 41 (2014).

[323] R.K. Ingole, *Ayurlog: National Journal of Research in Ayurved. Sci.*, **1**, 1 (2013).

[324] The Ayurvedic Formulatory of India, 2nd ed. Vol.-I, Part-“B”, New Delhi Department of AYUSH, Government of India, page-112 (2003).

[325] S. Mahdihassan, *Ind. J. Hist. Sci.*, **22**, 63 (1987).

[326] http://copublications.greenfacts.org/en/dental-amalgam/l-3/4-health-effects-amalgams.htm

[327] http://web.anl.gov/PCS/acsfuel/maroto-valer.pdf

[328] http://www.cfspages.com/mmercmicro.html

[329] Mercury Study Report to congress, Volume V, “Health effects of Mercury and Mercury Compounds”, United States Environmental Protection Agency, EPA-452/R-97-007 (1997).

[330] http://www.usgs.gov/themes/factsheet/146-00/

[331] http://water.usgs.gov/wid/FS_216-95/FS_216-95.html

[332] http://www.epa.gov/hg/eco.htm

[333] S. Azimi and M.S. Moghaddam, *Env. Ecol. Res.*, **1**, 12 (2013).

[334] Q. Wang, D. Kim, D.D. Dionysiou, G.A. Soriyal, D. Timberlake, *Env. Poll.*, **131**, 323 (2004).

[335] L. Zhang, M.H. Wong, *Env. Int.*, **33**, 108 (2007).

[336] http://www.cseindia.org/node/439

[337] http://en.wikipedia.org/wiki/Mercury_poisoning; http://www.udel.edu/chem/C465/senior/fall00/Mercury/health.htm

[338] http://pib.nic.in/newsite/erelease.aspx?relid=42213

[339] D. Frawlay, ”Ayurvedic Healing : A comprehensive guide” (Lotus Press, Twin Lakes, USA, 2000).

[340] E. Wiberg and N. Wiberg, in Inorganic Chemistry, Pg. 1314 (Academic Press,2001).

[341] Y.M. Sin, W.F. Teh, M.K. Wong, *Bull. Environ. Contam. Toxicol.*, **42**, 307 (1989).

[342] T.S. Yeoh, A.S. Lee, H.S. Lee, *Toxicology*, **41**, 107 (1986).

[343] J.J. Chuu, S.H. Liu, S.Y. Lin Shiau, *Tox. Lett.*, **169**, 109 (2007).

[344] C.-F. Huang, C.J. Hsu, S.H. Liu and S.Y. Lin-Shiau, *J. Biomed. Biotech.*, doi:10.1155/2012/254582 (2012).

[345] J. Liu, J.Z. Shi, L.M. Yu, R.A. Goyer, M.P. Waalkes, *Exp. Biol. Med (Maywood)*, **233**, 810 (2008).

[346] http://aliciac.hubpages.com/hub/Cinnabar-A-Beautiful-But-Toxic-Mineral-Ore-and-Pigment

[347] X. Zhou*et. al.*, *J. Ethnopharmacol.*, **135**, 110 (2011).

[348] J. Deneen, C.B. Carter, *Microscopy and Microanalysis*, **12**, 594 (2006); C.R. Perrey., J. Deneen, C.B. Carter, *Microscopy of Semiconducting Materials, Springer Proceedings in Physics*, **107**, 315 (2005).

[349] S. Sharma, “Rasatarangini”, Pg. 79, Sloka 27-30 (Ed. Sastri, D.) (Motilal Banarasidas, Varanasi) (1979).

[350] S. Sharma, “Rasatarangini”, Pg. 176, Sloka 7-12 (Ed. Sastri, D.) (Motilal Banarasidas, Varanasi) (1979).

[351] S. Sharma, “Rasatarangini”, Pg. 124, Sloka 107 (Ed. Sastri, D.) (Motilal Banarasidas, Varanasi) (1979).

[352] V.P. Hariprapannaji, “Rasayogasagara”, Rasasinduram, Sloka 522-524. (Chowkhamba Krishnadas Acadamy, Varanasi) (2004).

[353] M. Svensson, A. Düker, B. Allard, *J. Haz. Mat.*, **B136**, 830 (2006).

[354] http://www.minweb.co.uk/sulphides/metacinnabar.html.

[355] D. Rickard, “Sulphidic Sediments and sedimentary rocks”, Pg. 178 (Elsevier, 2012).

[356] M. Karkare, R. Bahuguna, in Applied Physics-I, Pg. 39 (I.K. International, 2007). Packing Fraction

[357] V.M. Bhuse, *Archives of Applied Science Research*, **3**, 339 (2011).

[358] DELA Recycling and Umwelttechnik, www.mercurynetwork.org/uk/wp-content/uploads/2009/11/Orthiel.pdf

[359] http://www.hallegeologicalservices.ca/?p=692

[360] A.K. De, Environmental Chemistry 5th Edition, Pg. 100 (New Age International Publishers, 2009).

[361] C.G. Morris, Academic Press Dictionary of Science and Technology, Pg. 1350 (Gulf Professional Publishing, 1992).; http://www.ill.eu/instruments-support/labs-facilities/chemistry-laboratories/list-of-chemicals/dangerous-chemicals/; http://www.lookchem.com/Mercury-II-sulfide/; http://www.answers.com/topic/mercuric-sulfide .

[362] http://ftp.esrf.eu/pub/UserReports/44815_B.pdf

[363] M. Rajan *et. al.*, *Env. Sci. Technol*., **42**, 5568 (2008).

[364] http://doesbr.org/PImeetings/2012/pdf/Tues/NagySBR2012.pdf

[365] S.C. Myneni, B. Mishra,J. Fein, http://www.osti.gov/scitech/biblio/1111104

[366] M.J. Colombo, J. Ha, J.R. Reinfelder, T. Barkay, N. Yee, *Chem. Geo.*, **363**, 334 (2014).

[367] F.E. Huggins *et. al.*, *Env. Bioindicators* , **4**, 291 (2009).

[368] C. Patty *et. al.*, *Env. Sci. Tech.*, **43**, 7397 (2009).

[369] J. Charnock *et. al.*, *Am. Min.*, **88**, 1197 (2003).

[370] C.S. Kim, J.J. Rytuba, G.E. Brown Jr, *App. Geochem*., **19**, 379 (2004).

[371] V. Petkov, *J. App. Cryst.*, **22**, 387 (1989).

[372] S. Calvin, *et. al.*, *J. App. Phys*., **94**, 778 (2003).

[373] R.G. Chaudhuri, S. Paria, *Chem. Rev*., **112**, 2373 (2012).

[374] S. Alayoglu *et. al*., *Nano*, **3**, 3127 (2009).

[375] T. Yoshitomi, D. Miyamoto and Y. Nagasaki, *Bio-Macromolecules*, **10**, 596 (2009).

[376] C. Walkey, E.A. Sykes, W.C.W. Chan, *Hematology*, 701 (2009).

[377] D.M. Smith, J.K. Simon, J.R. Baker Jr., *Nat. Rev. Imm.*, **13**, 592 (2013).

[378] K. Niikura e*t. al.*, *Nano*, **7**, 3926 (2013).

[379] TEM result provided by Prof. Sujit Roy, IIT-Bhubaneswar

APPENDIX A: Levenberg Marquadt Fitting Algorithm

Levenberg-Marquadt (L-M) fitting algorithm is popularly used in the least squares fitting problem.

Consider data points (x_i, y_i) of a set of N measured data. the most likely estimate of the model parameters $a = \{a_1, a_2, ..., a_M\}$ is obtained by minimizing the quantity χ^2 :

$$\chi^2(a) = \sum_{i=1}^{N} (y_i - f(x_i - a))^2$$

(1)

Just like any other numeric minimization algorithm, the L-M algorithm is an iterative procedure. To start a minimization, the initial get for the user provides the initial guess for the parameters vector $a = \{a_1, a_2, ..., a_M\}$

At each iteration step, the parameter vector a is replaced by a new estimate $a + \delta$. To determine δ, the function $f(x, a + \delta)$ is approximated linearly.

$$f(x, a + \delta) \approx f(x, a) + \underline{\underline{J}}.\delta \tag{2}$$

The matrix $\underline{\underline{J}}$ is a Jacobian matrix containing partial derivative of the function f in accordance with the parameter a_j :

$$J_{ij} = \frac{\partial f(x_i, a)}{\partial a_j} \tag{3}$$

Substituting (2) in (1), we get

$$\chi^2(a + \delta) = \sum_{i=1}^{N} (y_i - f(x_i - a) - \underline{\underline{J}}.\delta)^2 \tag{4}$$

The same can be re-written in vector notation as

$$\chi^2(a + \delta) \approx \left\| y - f(a) - \underline{\underline{J}}.\delta \right\| \tag{5}$$

Differentiating *wrt* δ and equating the result to zero, we get

$$(\underline{\underline{J}}^T.\underline{\underline{J}}).\delta = \underline{\underline{J}}^T.(y - f(a)) \tag{6}$$

This is the Gauss-Newton algorithm to solve a set of linear equations for δ. Levenberg replaced this equation by

$$(\underline{\underline{J}}^T.\underline{\underline{J}} - \lambda.\tau).\delta = \underline{\underline{J}}^T.(y - f(a)) \tag{7}$$

where τ is the identity matrix. The non-negative damping factor λ is adjusted at each iteration. If the decrease in χ^2 is rapid, a smaller value of λ can be used and the algorithm is similar to the Gauss-Newton algorithm. If the iteration is low, λ can be increased and the step will be taken approximately in the direction of the gradient.

Marquadt improved the algorithm by scaling each component of the gradient according to the curvature, so that there is larger movement along the directions where the gradient is smaller, thus avoiding slow convergence in the direction of the small gradient. To facilitate this, Marquadt replaced the identity matrix τ with a diagonal matrix consisting of diagonal elements of $(\underline{\underline{J}}^T.\underline{\underline{J}})$, resulting in the L-M algorithm:

$$(\underline{\underline{J}}^T.\underline{\underline{J}} - \lambda.(\underline{\underline{J}}^T.\underline{\underline{J}})).\delta = \underline{\underline{J}}^T.(y - f(a)) \tag{8}$$

The choice of damping factor λ is not obvious. Marquadt recommended starting with a value $\lambda = \lambda_0$ and a factor $\nu > 1$. Depending on the value of χ^2, the damping factor will be replaced after each step by λ / ν or $\lambda.\nu$.

An important point about the L-M algorithm is that it finds only a *local* minimum like all other iterative procedures, not a global minimum.

APPENDIX B: Data and fits

1. Chapter 6: Pt/Ni/C Multilayer system

(i) Low angle

a) Pristine Sample

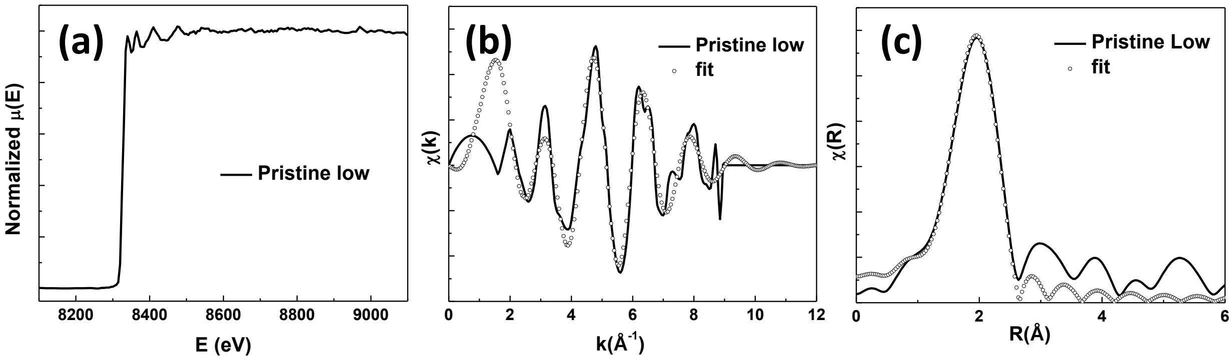

Fig. 1: (a) Ni K edge XAFS data in E space for pristine sample at low angle. Comparison of data with fit in (b) k-space and (c) r-space.

b) Irradiated Sample

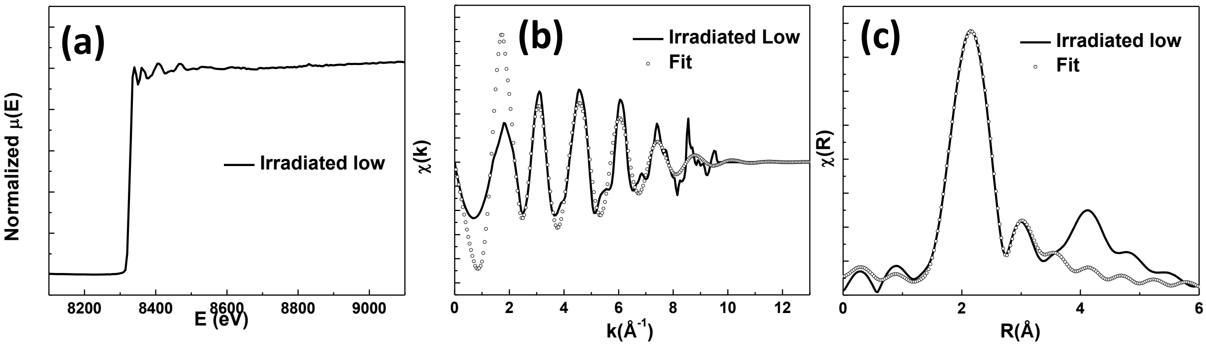

Fig. 2: (a) Ni K edge XAFS data in E space for irradiated sample at low angle. Comparison of data with fit in (b) k-space and (c) r-space.

(j) <u>High angle</u>

a) Pristine Sample

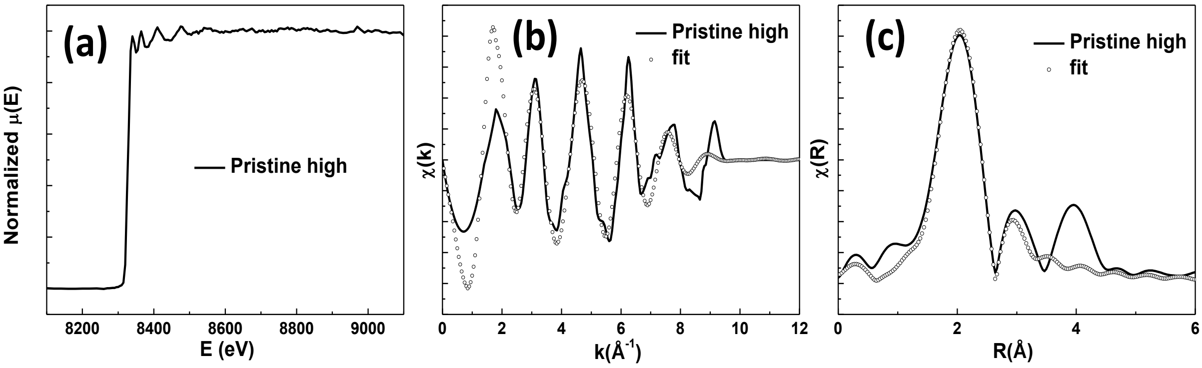

Fig. 3: (a) Ni K edge XAFS data in E space for pristine sample at high angle. Comparison of data with fit in (b) k-space and (c) r-space.

b) Irradiated Sample

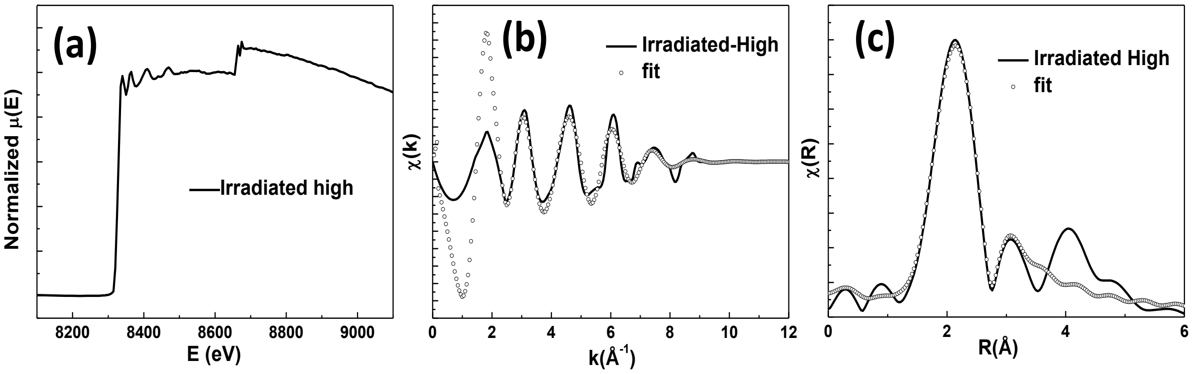

Fig. 4: (a) Ni K edge XAFS data in E space for irradiated sample at high angle. Comparison of data with fit in (b) k-space and (c) r-space.

2. Chapter 7: Ag/Pt nanorods in silica matrix

a) Pristine sample

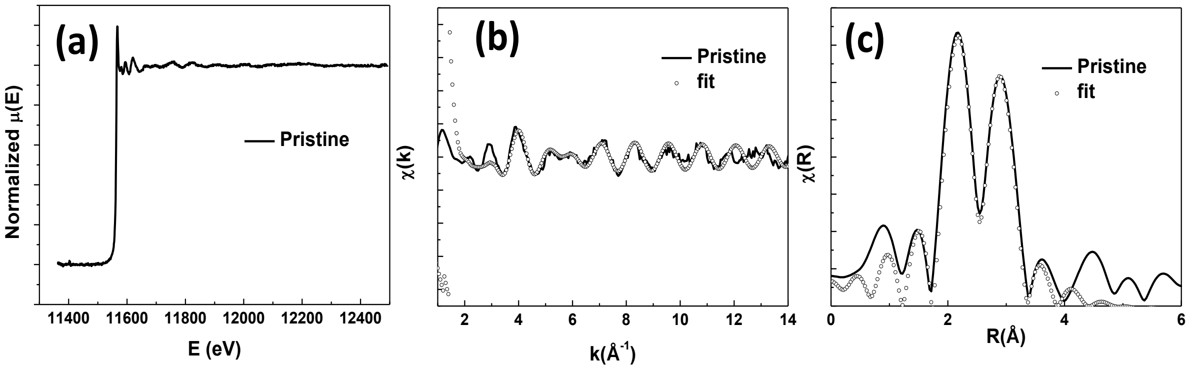

Fig. 5: (a) Pt L3 edge XAFS data in E space for pristine sample. Comparison of data with fit in (b) k-space and (c) r-space.

b) SHI Irradiated samples

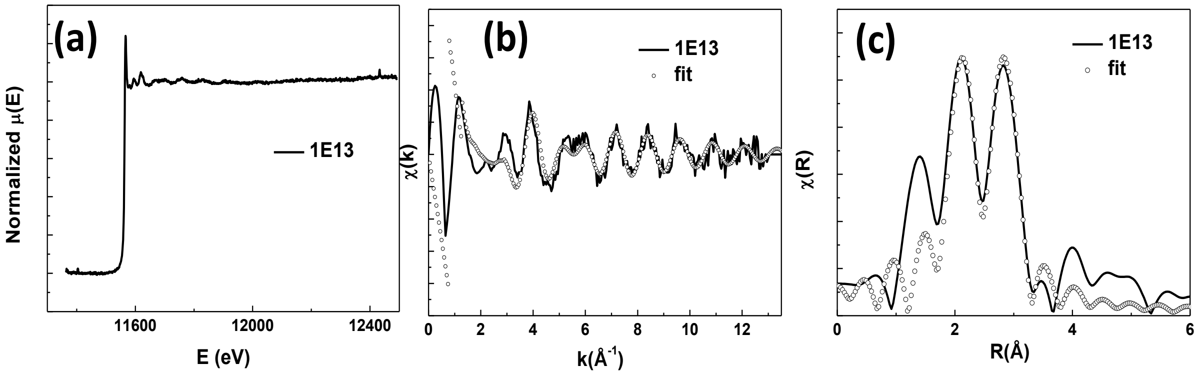

Fig. 6: (a) Pt L3 edge XAFS data in E space for sample irradiated at 1×10^{13} ions/cm^2. Comparison of data with fit in (b) k-space and (c) r-space.

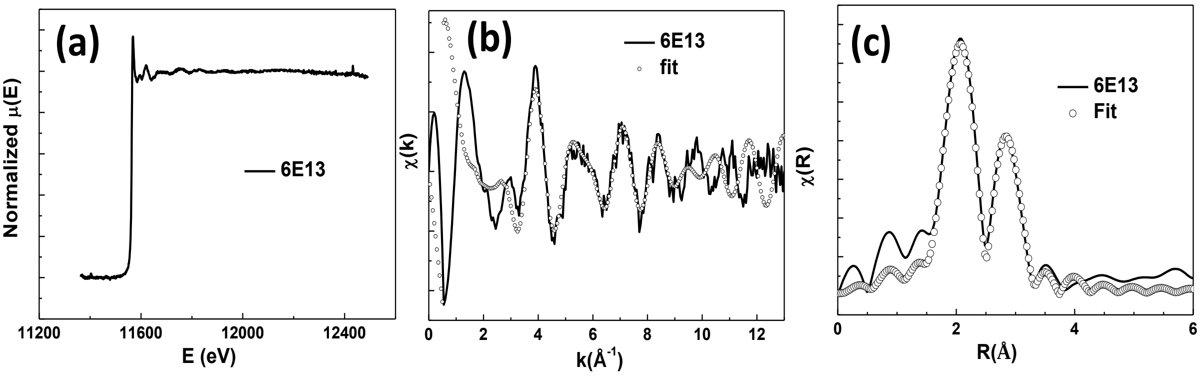

Fig. 7: (a) Pt L3 edge XAFS data in E space for sample irradiated at 6×10^{13} ions/cm^2. Comparison of data with fit in (b) k-space and (c) r-space.

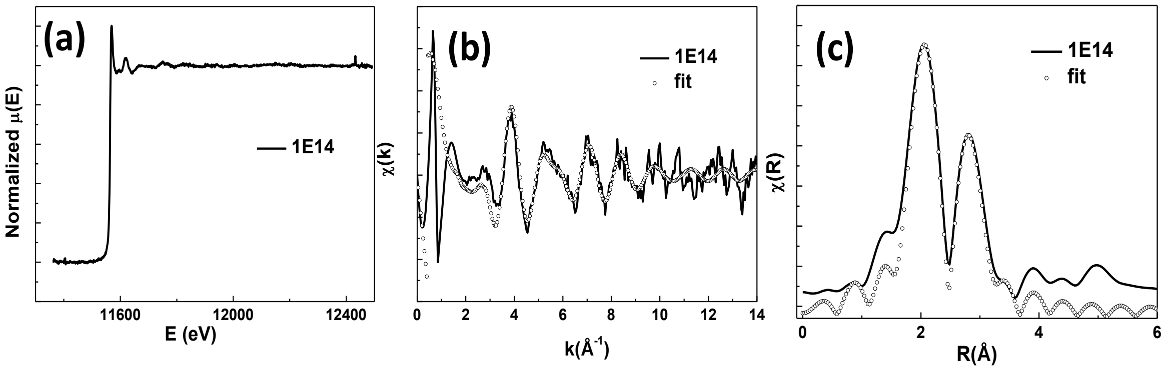

Fig. 8: (a) Pt L3 edge XAFS data in E space for sample irradiated at 1×10^{14} ions/cm^2. Comparison of data with fit in (b) k-space and (c) r-space

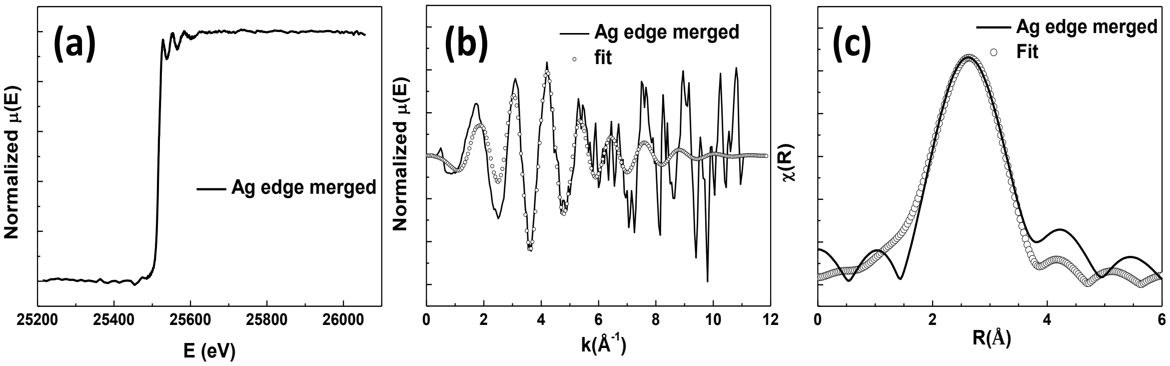

Fig. 9: (a) Ag K edge XAFS data in E space for merged data set of all samples. Comparison of data with fit in (b) k-space and (c) r-space

3. Chapter 8: Ayurvedic nanodrug

a) <u>Rasasindura</u>

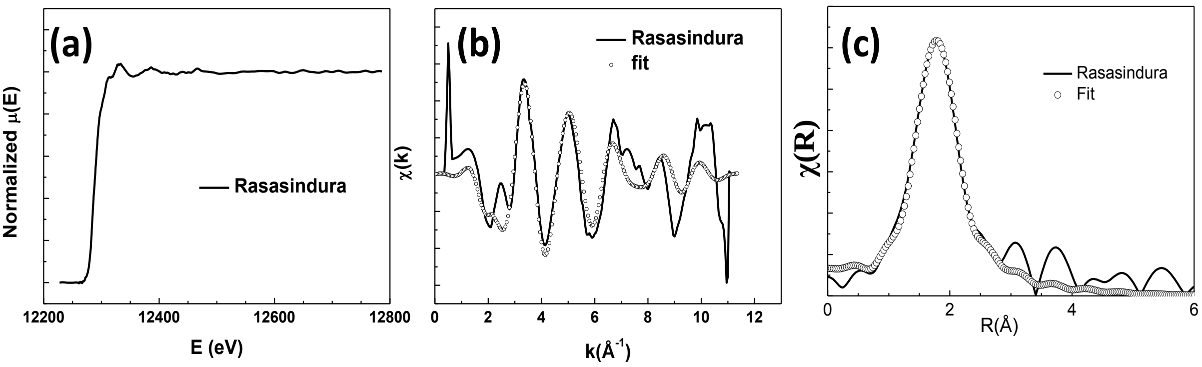

Fig. 10: (a) Hg L3 edge XAFS data in E space for Rasasindura. Comparison of data with fit in (b) k-space and (c) r-space.

b) <u>Red HgS (lab)</u>

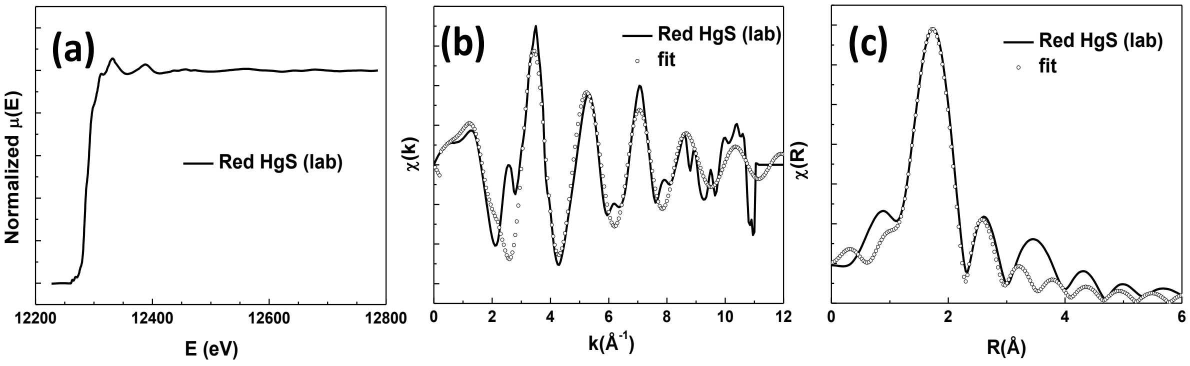

Fig. 11: (a) Hg L3 edge XAFS data in E space for Red HgS (lab). Comparison of data with fit in (b) k-space and (c) r-space.